2008

Enhancement of Mechanical and Tribological Properties of Ti-6Al-4V Alloy

Neda Dalili
University of Windsor

Enhancement of Mechanical and Tribological Properties of Ti-6Al-4V Alloy

By

Neda Dalili

A Thesis

Submitted to the Faculty of Graduate Studies

through Engineering Materials

in Partial Fulfillment of the Requirements for

the Degree of Master of Applied Science at the

University of Windsor

Windsor, Ontario, Canada

2008

Your file Votre référence
ISBN: 978-0-494-82096-4
Our file Notre référence
ISBN: 978-0-494-82096-4

Author's Declaration of Originality

I hereby certify that I am the sole author of this thesis and that no part of this thesis has been published or submitted for publication.

I certify that, to the best of my knowledge, my thesis does not infringe upon anyone's copyright nor violate any proprietary rights and that any ideas, techniques, quotations, or any other material from the work of other people included in my thesis, published or otherwise, are fully acknowledged in accordance with the standard referencing practices. Furthermore, to the extent that I have included copyrighted material that surpasses the bounds of fair dealing within the meaning of the Canada Copyright Act, I certify that I have obtained a written permission from the copyright owner(s) to include such material(s) in my thesis and have included copies of such copyright clearances to my appendix.

I declare that this is a true copy of my thesis, including any final revisions, as approved by my thesis committee and the Graduate Studies office, and that this thesis has not been submitted for a higher degree to any other University of Institution.

Abstract

Incorporation of TiC particle was adopted as one of the available methods to study the enhancement in tribological and mechanical properties of Ti-6Al4V alloy. The mechanical performance of Ti-6Al-4V-10Vol%TiC sample (TMC) was evaluated using tensile and micro-scratch tests. Ball-on-disk tests at various loads revealed that the wear resistance of Ti-6Al-4V was improved via incorporation of TiC provided that the contact pressure remained lower than 0.98 GPa. Thermal oxidation was adopted to improve the high pressure wear resistance of TMCs. The optimum oxidation condition was characterized using XRD, SEM observations, and micro-scratch tests. The fracture toughness of the coatings was measured by micro-indentation tests. Ball-on-disk tests revealed that oxidation at the optimum condition (at 800°C for 20 min) significantly improved the wear resistance of the TMCs compared to uncoated TMCs. The mechanism and the effect of oxidation process were analyzed and the operative wear mechanisms at different loads were discussed.

Dedication

I dedicate this thesis to my first teacher, my mother Haydeh. Her example was my inspiration.

Acknowledgments

I would like to thank my advisor Dr. Afsaneh Edrisy for accepting me as a graduate student. I am practically grateful for her guidance and encouragement during my graduate studies. I would like to acknowledge my thesis committee members, Dr. A.T. Alpas and Dr. D. Ting, for their valuable suggestions.

Thanks are sent out to Mr. John Robinson for his assistance in X-ray diffraction analysis, secondary electron microscopy and metallographic preparations. Special thanks are also extended to Mr. Patrick Seguin and Mr. Andy Jenner for their great technical assistance. The administrative assistance of Mrs. Barbara Denomey is also appreciated. I would also like to thank all my fellow graduate students, especially Mr. Ronholm and Mr. Shafiei.

I would like to also acknowledge the support extended by CANMET/MTL, specifically by Dr. Jason Lo and Ms. Ruby Zhang. Without their technical support and useful discussions, this project would not have been possible.

The financial support of the Natural Science and Engineering Council of Canada (NSERC) and the University of Windsor are graciously acknowledged.

Table of Content

Nomenclature

at.	atomic
BCC	Body Center Cubic
BSI	Back Scattered Image
C/S	Chrome Steel
COF	Coefficient of Friction
CRSS	Critical Resolved Shear Stress
CTE	Coefficient of Thermal Expansion
EDS	Energy Dispersive Spectrometer
FIB	Focused Ion Beam
HCP	Hexagonal Close Packed
ICL	Indentation Cracking Length Method
LEM	Lawn, Evans and Marshal Method
MIM	Metal Injection Moulding
OL	Oxide Layer
ODZ	Oxygen Diffusion Zone
PBR	Pilling-Bedworth Ratio
RH	Relative Humidity
SEM	Scanning Electron Microscope
TMC	Titanium Matrix Composite
TO-TMC	Thermally Oxidized Titanium Matrix Composite
TO	Thermal Oxidation
Vol	Volume
Wt	Weight
XRD	X-ray diffraction

List of Symbols

$a_{element}$	Activity of the element
A	Indentation half-diagonal
A_r	Real area of constant
C	Crack length from the center of indentation
D	Depth of penetration during wear test
E	Elastic Modulus
E*	Reduced elastic modulus
ΔG°	Standard enthalpy of formation
G	Shear Modulus
Hv	Vickers Hardness
K	Coefficient of wear
K_{IC}	Fracture toughness
k_p	Parabolic rate constant of oxidation
L	Crack length from the corners of indentation
μ	Coefficient of friction
P	Indentation or wear load
P_o	Maximum contact pressure
Q	Activation energy for oxidation
R	Molar gas constant, or radius of the wear track
R	Ball or indenter radius
r_P	Indentation plastic zone radius
σ_R	Residual stress
T_f	Flash temperature
τ_c	Peierls-Nabarro force

Θ	Half-diffraction angle
V	Volume loss during wear
V	Sliding speed
Y	Poisson's ratio
W	Wear rate
Z_c	Critical thickness of oxide

List of Figures

List of Tables

Chapter 1

1 Introduction

Interest in the properties of titanium alloys started after the Second World War in the late 1940's and early 1950's. Especially in the USA, major U. S. Government sponsored programs led to the installation of large capacity titanium sponge production plants [1]. High strength, low density, a modulus of elasticity very close to that of bone and excellent corrosion resistance are the main properties that make titanium attractive for a variety of applications. Examples include aerospace components, automotive, chemical and medical applications.Ti-6Al-4V is one of the most widely used titanium alloys. It is an $\alpha+\beta$ alloy whose typical applications include pressure vessels, aircraft gas turbine disks, cases and compressor blades, and surgical implants [2]. Biomedical devices and the parts for aircraft gas turbine are subjected to action of sliding contact of surfaces during their service [3]. Titanium alloys are, however, known for their poor tribological properties, including high and unstable friction coefficients, severe adhesive wear, susceptibility to fretting wear, and a strong tendency to seize [4]. Over the past 20 years many attempts have been made to improve the tribological performance of the titanium alloys by means of two methods, namely surface engineering techniques and incorporation of ceramic particles into the matrix. The developed surface engineering techniques have met more or less with success, but most of them are not cost effective for mass production. A novel surface engineering method has been recently developed by Dong et al [5]. In this process—designated as TO process—Ti-6Al-4V samples are thermally oxidized in an air furnace at 600°C for 65 h followed by furnace cooling which has indicated considerable promise in vivo and in car race industries [4-6].

Discontinuously reinforced titanium shows very attractive structural properties and is currently used commercially in automotive valves for the Toyota Altezza. Research and development of titanium matrix composites (TMCs) for aerospace applications show that this composite has the potential of exceeding the structural efficiency of all metallic materials, and of cross-plied graphite/epoxy. Such reinforcements can be synthesized in-situ in Ti and its alloy matrices via exothermic reactions of the constituent elements

during high temperature processing. The reinforcements can also be directly introduced to the matrix during processing. The resultant titanium matrix composite (TMC) will be called "ex-situ" composites. The in-situ fabricated TMCs generally have a clean particle/matrix interface, thereby promoting strong interfacial bonding [7]. Among the existing ex-situ processes, metal injection moulding (MIM) is a near net shape process which eliminates most of the secondary and machining processes, and it, therefore, offers a low cost alternative for hard to machine materials such as TMCs [8].

1.1 Scope and Objective of This Study

Intake and exhaust valves coordinate the transportation of the air fuel mixture for combustion and the exhaust gases in automotive engines. Both parts are subjected to cyclic mechanical loading, and the exhaust valves operate in gas temperature as high as 900°C, so good fatigue and creep resistance are required. The valves must also possess good resistance to sliding wear in the valve guide. Automotive valves are typically produced from austenite steel. TMCs have been used as automotive valves since 1998 and allow a direct weight saving of 40% compared to a full steel valveset, which together with the reduced spring mass makes a total weight reduction of 56% [9] Incorporation of the ceramic particles to Ti and its alloys increases the high-temperature tensile strength and stiffness of the material at the expense of tensile ductility and fracture toughness at ambient temperature [7]. It has been frequently observed that there is a limit of pressure and sliding speed where the TMCs lose their wear resistance due to debonding and/or fracture of the particles [10-12]. The occurrence of debonding or particle fracture depends on many factors such as the fabrication method, the volume fraction of the particles and the size of the particles. According to author's knowledge, there exists no comprehensive study that covers the tribological performance of TMCs and excavates the role of TiC particle in sliding contact. Thereby, the first part of the present study focuses on the mechanical and sliding wear properties of TiC-reinforced Ti-6Al-4V matrix—fabricated in CANMET MTL, which has been fabricated for the first time by MIM method, and the effect of contact pressure on the success or failure of particles in improvement of sliding wear has been revealed.

It is known that the atmosphere of the exhaust gas is oxidizing, so that the exhaust valves must have good oxidation resistance. A number of studies, therefore, have been performed on the oxidation behaviour of TiC-reinforced Ti alloys to shed light on their high temperature oxidation resistance [13-17]. So far, it is discussed that thermal oxidation process can be employed as a cost-effective method to improve the tribological properties of Ti-6Al-4V [5].This process, however, has never been adopted as a surface engineering method for improvement of tribological properties of TMCs. Therefore, the second part of this study focuses on characterizing an optimum thermal oxidation condition for TMCs and evaluating the performance of these thermally oxidized TMCs during sliding contact.

1.2 Organization of Thesis

This thesis is composed of five chapters. Chapter 1 is an introduction to this study and the objectives of the thesis. A review of the literature on the properties of Ti and its alloys and the available methods for enhancing their tribological and mechanical properties is presented in Chapter 2. Chapter 3 describes the materials and experimental procedure employed in this study. The results of the experimental studies are presented in Chapter 4. This chapter covers the results of thermal oxidation of Ti-6Al-4V and Ti-6Al-4V-10Vol%TiC, and also the results of evaluation of mechanical and tribological performance of both composite and oxidized samples. The experimental results are discussed in Chapter 5. Chapter 6 comprises the summary and conclusions of this thesis.

Chapter 2

2 Literature Survey

Titanium alloys are an important class of lightweight engineering materials used not only for aerospace components, but also for automotive, chemical and medical applications, which makes their tribological behaviour and mechanical properties a major concern. They display an inferior wear resistance and considerable loss in mechanical strength at high temperatures that restrict potential applications in many areas. A variety of surface modification methods or incorporation of ceramic particles into Ti alloy, as an alternative method, have been utilized to combat the poor tribological properties of titanium alloys. The thermal oxidation process is one of the available surface modification methods that has proven to be a cost effective way to improve the tribological behaviour of Ti alloys.

This chapter reviews the existing literature on the properties of titanium alloys, particularly Ti-6Al-4V alloy. Section 2.1 presents a description of the alloying, processing, deformation modes and wear behaviour of titanium alloys. Section 2.1.5 introduces the general sliding wear properties of materials then highlights the specific wear characteristics of titanium alloys. Section 2.2 focuses on the available methods for improving the tribological and mechanical properties of titanium alloys, including the thermal oxidation process and titanium matrix composites. This study uses the fracture toughness measurement provided by indentation technique as a way to characterize the oxide coatings. With this in mind, the literature on this measurement technique is presented in section 2.3.

2.1 Titanium and Titanium-Based Alloys

Titanium is a low-density element (4.5 g/cm^3 or approximately 60% of the density of steels and superalloys) that can be significantly strengthened by alloying and deformation processing. The Ti alloys' other attractive properties include: good heat transfer, low coefficient of thermal expansion (half of Al), the ability to passivate and a high degree of immunity against attack by mineral acids and chlorides [18]. This excellent corrosion resistance and biocompatibility, coupled with good strength make

titanium and its alloys particularly useful in chemical and petrochemical, marine environment and biomaterial applications. The combination of high strength, stiffness, toughness, low density and superior corrosion resistance displayed by various titanium alloys at very low to elevated temperatures meets weight savings efforts in aerospace and other high performance applications [2] The basic characteristics of Ti and its alloys are compared to other Fe, Ni and Al-based alloys in Table 2.1.

Table 2.1. Some important characteristics of titanium and titanium based alloys as compared to other structural metallic materials based on Fe, Ni, and Al [1].

Properties	Ti alloys	Fe alloys	Ni alloys	Al alloys
Melting temperature of the pure metal (C)	1670	1538	1455	660
Room temperature E of the pure metal (GPa)	115	215	200	72
Yield strength level (MPa)	400-1400	200-2000	200-1400	120-500
Density of the pure metal (g/cm^3)	4.5	7.9	8.9	2 7
Comparative corrosion resistance	Very high	Low	Medium	High
Comparative reactivity with oxygen	Very high	Low	Low	High
Comparative price of metal	Very high	Low	High	Medium

Titanium has an HCP crystal structure at room temperature, which is referred to as the "α" phase. This structure transforms into a BCC crystal structure known as the "β" phase at 882°C. The hexagonal unit cell of the α phase exhibit a c/a ratio of 1.587. which is smaller than the HCP crystal structure's ideal ratio of 1.633 [1]. The basic characteristics of Ti are explained in the following sections.

2.1.1 Alloying and Phase Diagrams

The alloying elements present in most of titanium alloys can generally be divided into α stabilizers or β stabilizers. The β transus temperature can be defined as the lowest equilibrium temperature at which the material is 100% β, as shown in the 3-dimentional phase diagram illustrated in Figure 2.1. β stabilizers such as Mo, V, Ta, Cb, Mn, Fe, Cr, Co, Ni and Cu stabilize the BCC crystal structure by lowering the transformation temperature. On the other hand, α stabilising elements including Al, Ga, Ge, C, N and O

favour the α crystal structure by raising the β transus temperature [2]. The transition between β phase and α phase in Ti can either occur martensitically, or by a diffusion-controlled nucleation and growth process, depending on cooling rate and alloy composition. This hexagonal martensite is designated as α' and observed in two morphologies: massive (lath or packet) martensite and the so-called acicular martensite. The former occurs only in Pure Ti, very dilute alloys and alloys with a high martensitic transformation temperature [1].

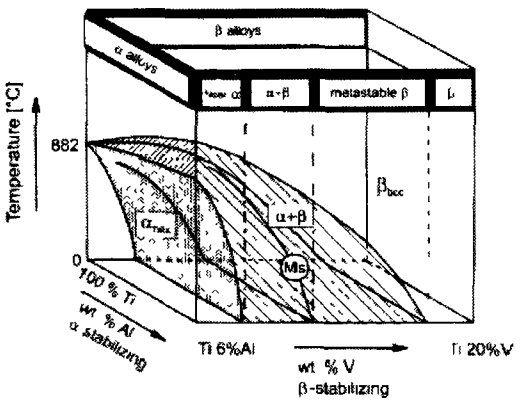

Figure 2.1. The Schematic three-dimensional phase diagram to classify Ti alloys; the diagram is a combination of two phase diagrams with α and β stabilizing elements [19].

It is common to separate the alloys into four categories that refer to the phases that are normally present, namely α, near α, α+β and β (with further subdivision into near- α and metastable β). These are shown schematically in Figure 2.1. The α alloys consist of the commercially pure Ti and alloys with α stabilizers or neutral elements while near α alloys include alloys with minor fraction of β stabilizers. The α+ β alloys, the most widely used alloy group, have an α/β volume fraction ranging from 5 to 40%. In the class of metastable β alloys, the BCC structure no longer transforms to the HCP martensite upon fast quenching.

The properties of titanium alloys are primarily determined by the arrangement, volume fraction, and individual properties of the two phases α and β. Compared with the BCC β, the hexagonal α is characterized by the following properties:

- higher resistance to plastic deformation,
  reduced ductility.

- anisotropic mechanical and physical properties,
  a diffusion rate which is at least two orders of magnitude lower,
- higher creep resistance [20]

Consequently, α+β-Ti alloys have generated increasing interest in many applications due to their relatively low modulus (lower than α alloys), fairly high tensile strength (higher than α-alloys), corrosion resistance (better than β alloys) and ductility (higher than both β and α alloys) [21]. Among α+β-Ti alloys, Ti-6Al-4V is the most widely used and is commonly considered the "workhorse" of the titanium alloy family. It is an α+ β type containing 6 wt% Al and 4 wt% V the properties of [19] which are further described in section 2.1.2.

2.1.2 Ti-6Al-4V Alloy

For the majority of the last half of the twentieth century, Ti-6Al-4V accounted for about 45% of the total weight of all shipped titanium alloys. This alloy is ideal for aircraft structural parts as well as the rotating and non-rotating parts in aero-engines because of its improved corrosion resistance and higher modulus of elasticity, in addition to higher yield and fatigue strength compared to competing materials like Al alloys. Another application for Ti-6Al-4V is in the power generation field as low pressure steam turbine blading material. The Ti-6Al-4V alloy offers a lower modulus of elasticity combined with better seawater corrosion resistance than competing steel materials in offshore oil and gas production. Another major application of this alloy is in the biomedical field where corrosion resistance, biocompatibility, bioadhesion (bone ingrowth), a modulus of elasticity close to that of bone, fatigue strength, and good processibility including joining and casting are the properties of interest[1,2].

Al and V are the most frequently used substitutional alloying elements. Al partitions selectively to the α phase, and provides solid solution strengthening. The most important and by far the most intensively investigated titanium phase diagram is the system Ti-Al, shown in Figure 2.2 [20]. The Al concentration is usually held to 6 wt% (maximum 6.75%) to avoid the formation of an ordered structure of DO_{19} known as α_2 that degrades ductility, stress corrosion resistance and toughness [19]. The ternary

additions of V (maximum 4.5 wt.%) slow this precipitation reaction significantly compared to binary Ti-Al alloys. It also decreases the solubility of Al in α phase. This alloying element is rejected from the α phase because of its low solubility in this phase, and will be concentrated in small regions of the β phase [22].

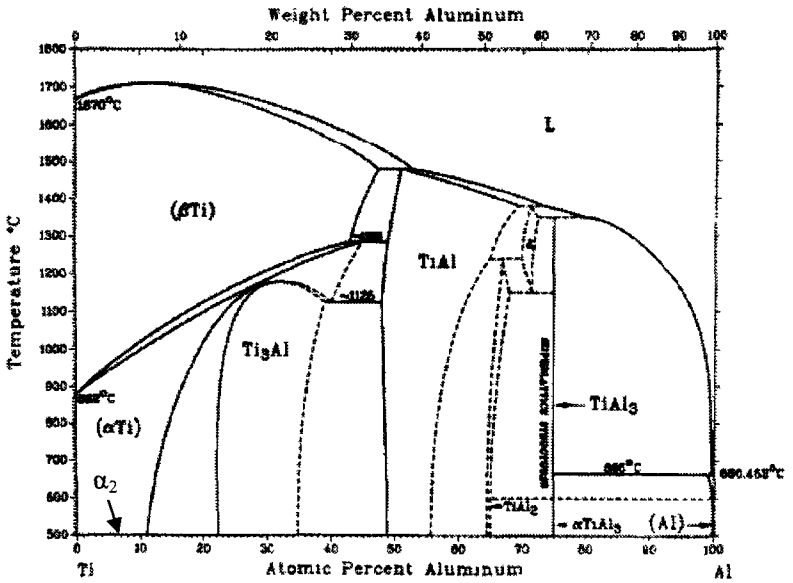

Figure 2.2. The Ti-Al phase diagram [20].

2.1.3 Processing and Microstructure

Microstructure has a substantial effect on the properties of Ti alloys. The microstructure of α+β Ti alloys strongly depends on both processing history and heat treatment. In general, three distinctly different types of microstructures can be obtained by changing the thermo-mechanical processing: fully lamellar, fully equiaxed and bi-modal (duplex) [23].

A central point for thermomechanical treatment is the β -transus temperature (982-993°C for Ti-6Al-4V), since it separates the β phase field from the two-phase α+β field. Lamellar microstructures are the result of cooling from temperatures above the β-transus temperature (such as 1050-1065°C for Ti-6Al-4V). Once the temperature falls below the transus temperature α nucleates at grain boundaries and then grows as lamellae into the (prior) β grain. Slow cooling—with 1°C/min—from the β phase field results in pure lamellar microstructures with the lamellae becoming coarser in tandem with a reduced

cooling rate (Figure 2.3). Rapid cooling—with 8000 °C/min—leads to a martensitic transformation of β, resulting in a very fine needle-like microstructure. For Ti-6Al-4V this change occurs at cooling rates faster than 1000 °C/min. Unlike steels, however, the hardening effect observed for titanium alloys on martensitic transformation is only moderate [20].

Unlike lamellar microstructures, equiaxed microstructures are the result of a recrystallization process, so the alloy must first be highly deformed in the α+β field to introduce enough cold work into the material. The applied plastic deformation should be as high as possible but at least high enough to obtain complete recrystallization of the α and β phases during the next step. Subsequent solution heat treatment at temperatures in the α+β field (950-955 °C for 10 min for Ti-6Al-4V) produces a recrystallized and equiaxed microstructure (Figure 2.4). Extended annealing coarsens the equiaxed microstructure and the solution heat treatment temperature determines the volume fraction of the primary α. Solution heat treatment just below the β-transus temperature (950-955 °C for Ti-6Al-4V) results in bimodal microstructures that consist partly of equiaxed (primary) α in a lamellar α+β matrix. Bimodal microstructures can be considered a combination of lamellar and equiaxed microstructures (Figure 2.5) [20].

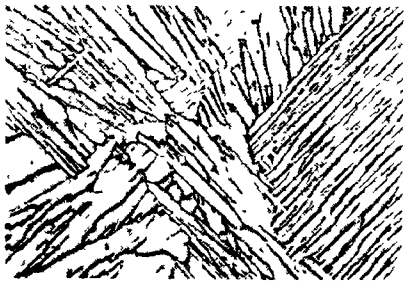

Figure 2.3. Widmanstätten Microstructure of an α+β Ti alloy (Ti-6Al-4V) after slow cooling from above the β transus. The white plates are α, and the dark regions between them are β. Optical micrograph. 500x [1].

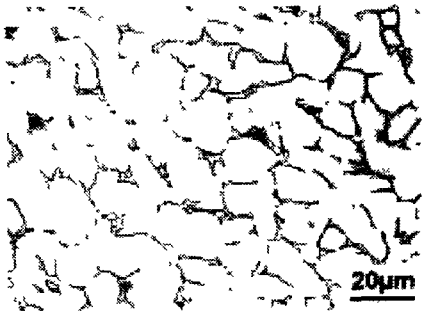

Figure 2.4. Fully equiaxed microstructure of an α+β Ti alloy (Ti-6242) slowly cooled from the α+β two phase region. The white plates are α, and the dark regions between them are β [1].

Figure 2.5. Bimodal microstructure of an α+β Ti alloy (Ti-6Al-4V). The white regions are α, and the regions between them are the lamellar α+β phase [1].

2.1.4 Deformation Modes

The main slip directions for α-Ti are the three close-packed directions of the type $< 11\bar{2}0 >$. The slip planes containing these directions that make the main slip systems are (0001), $\{10\bar{1}0\}$, and $\{10\bar{1}1\}$ ($< a >$ slip systems)—basal, prismatic and pyramidal planes, respectively [1]. These slip systems only offer 4 independent systems and the von Mises criterion requires at least five independent slip systems for the homogenous plastic deformation of metals, meaning that the operation of a slip system from the Burgers vector type $\langle c + a \rangle$ with the slip direction of $\langle 11\bar{2}3 \rangle$ and pyramidal type slip planes of $\{10\bar{1}1\}$ and/or $\{11\bar{2}2\}$ should be activated. These slip systems are schematically shown in Figure 2.6. These latter systems are called first and second order pyramidal slip systems, respectively [1,24]. Most of the studies performed on α-Ti crystals have proven that the relative ease of slip systems activation increases in the order of pyramidal, basal and prismatic systems [25-28]. The fact that the in the absence of

impurities the dislocations movement is easier and friction force is lower for prismatic planes, may be explained by the fact that for the HCP structure of α-Ti the c/a ratio is 3% lower than the ideal lattice (1.633). On the basis of a hard sphere model, this leads to a larger spacing between prism planes and the packing density of the prism planes will increase relative to the basal planes [20,28]. The friction force, or Peierls-Nabarro force, is the stress required to move dislocation through a crystal lattice in a particular direction (τ_c) which is given by,

$$\tau_c = \frac{2G}{1-\upsilon} e^{-[2\pi a/(1-\upsilon)b]} \qquad \text{Equation 1.1}$$

Where a is the distance between slip planes and b is the distance between atoms in the slip direction. Increasing a or decreasing b will decrease the friction force of prismatic planes in Ti relative to the basal planes [29].

The ductile behaviour of HCP-α-Ti, especially at low temperatures, results from the activation of twining deformation modes in addition to conventional slip by dislocations. The main twinning modes for α-Ti are $\{10\bar{1}2\}$, $\{11\bar{2}1\}$ and $\{11\bar{2}2\}$, with additional non-preferred twinning modes of $\{11\bar{2}3\}$, $\{11\bar{2}4\}$, and $\{10\bar{1}1\}$. The BCC β phase also shows twinning in addition to slip. The main slip systems in the BCC β-phase are $\{110\}$, $\{112\}$ and $\{123\}$, all with the same Burgers vector of the type $< 111 >$ It should be noted that the occurrence of twining is limited to the single phase state and decreases with increasing solute atoms [30,31].

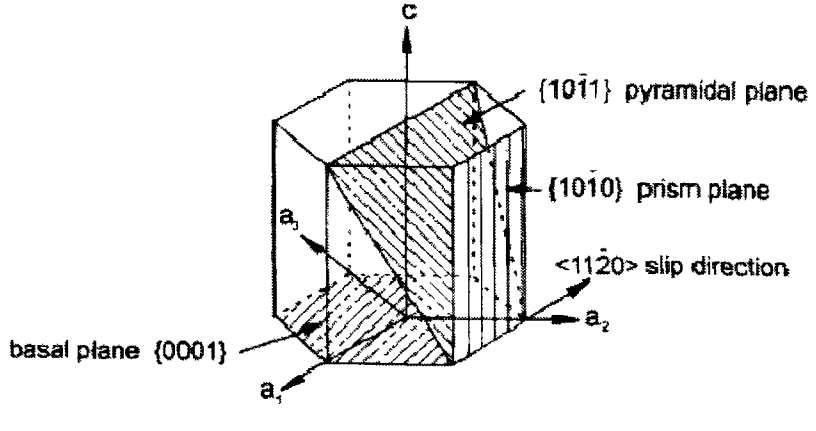

Figure 2.6. Schematic illustration of the slip systems of HCP lattice [20].

2.1.5 Mechanical Properties

With a strength-to-density ratio of $25 \times 10^6 mm$, Ti-6Al-4V is an effective lightweight structural material and has strength-toughness combination between those of steel and aluminum alloys. The effect of prior processing and microstructure on mechanical properties is quite varied. The strength advantage and disadvantages of the two microstructures of equiaxed and Widmanstätten are as follows:

- Equiaxed: higher ductility and formability, higher threshold for hot-salt stress corrosion, higher strength (910 MPa compared to 875 MPa for Widmanstätten), better hydrogen tolerance, and better low-cycle fatigue properties.
- Widmanstätten: Superior creep resistance and higher fracture toughens values.

Therefore, α+β alloys are generally annealed just below the transus temperature to produce a maximum of acicular beta with approximately 10% of equiaxed α to take advantage of a combination of the superior mechanical properties of both microstructure [2].

The typical mechanical properties of a bimodal microstructure of Ti-6Al-4V at room temperature and at 316 and 427°C are listed in Table 2.2 The mechanical properties of Ti and its alloys are generally very sensitive to temperature and the tensile strength is decreased from 827 MPa at room temperature to 563 MPa at 316°C and to 521 MPa at 427°C [23]. The ductile nature of Ti and its alloys, on the other hand, is attributed to the increased number of slip systems caused by the lower c/a ration of the HCP lattice [20].

Table 2.2. Typical mechanical properties of bimodal microstructure of Ti-6Al-4V alloy [23].

Properties	Yield strength (MPa)	Ultimate strength (MPa)	Elongation (%)	Modulus of elasticity (GPa)	Fracture toughness ($MPa\sqrt{m}$)
At 25°C	827	896	10	113	44-110
At 316°C	563	663	17	—	—
At 427°C	521	609	18	—	—

2.1.6 Wear Behaviour of Titanium and Titanium Based Alloys

Sliding wear of metals involves complicated phenomena such as metal transfer and formation of surface layers by mechanical mixing as well as large plastic deformation at and beneath the surface. A general description of the sequence of events occurs during sliding is given in section 2.1.6.1, while the factors motivating the poor tribological properties of Ti alloys, the wear mechanisms and existing methods for improving their wear behaviour are described in section 2.1.6.2.

2.1.6.1 Sliding Wear

Material transfer and surface damage are the inherent sequence of unlubricated sliding systems or the systems with failed lubricants. Local contacts cause large plastic strains in either or both solid components and material transfer occurs due to adhesion and plastic deformation. The transferred material becomes mixed with the matrix and/or environmental components to produce a fine-grained transfer layer, i.e. tribolayer. The plastic deformation imposed on the surface causes a change in the material structure at and beneath the surface. Loose debris is commonly derived from the tribolayer or the highly deformed material. The series of events that lead to the formation of a tribolayer and loose debris are given in this section, together with a general description of wear rate equations (The Archard equation).

Archard Wear Equation

The Archard equation is a simple law for describing the volume of wear due to adhesion in sliding contact. It is based on the assumption that the wear particles are comparable in size to the junctions existing between sliding surfaces. According to this equation the volume of wear per sliding distance (W) has the following form:

$$W = \frac{KF}{H} \qquad \text{Equation 1.2}$$

Where F is the total normal load and H is the indentation hardness of the surface that is worn away. The constant K is called the coefficient of wear [32] and expresses the probability of forming wear particles [33]. According to this equation, if K is constant for

a given sliding system under constant load (F), then the volume of material removed by wear should be proportional to the sliding distance and sliding wear is in equilibrium condition. Wear as a function of operating time or sliding distance, however, also depends on the predominant wear mechanism, with three different periods commonly observed in wear loss-sliding distance curves like Figure 2.7 (a). The running-in period (I) is characterized by a progressive increase in wear loss. In the equilibrium (II) period, which is the regime that satisfies the conditions of equation 1.2, the wear rate is constant. During period III, the system enters a new sliding regime and wears loss increases progressively with sliding distance until failure occurs [34].

The following factors should be considered when using the Archard wear equation to identify the different wear regimes:

- According to Archard and Hirst [32] the linear dependence of wear rate on sliding distance holds true only for the equilibrium stage of the wear which should be distinguished from the periods I and III when interpreting the volume loss data.
- According to this equation, the wear rate depends only on the hardness and normal load. The hardness of the material changes during the course of sliding, however, as tribolayers form on the surface or the temperature varies as a result of variations in sliding velocity [35].

Therefore, microscopic observations and the wear rate measurements based on the Archard equation can be utilized to characterize the mechanisms responsible for material removal in the equilibrium sliding wear.

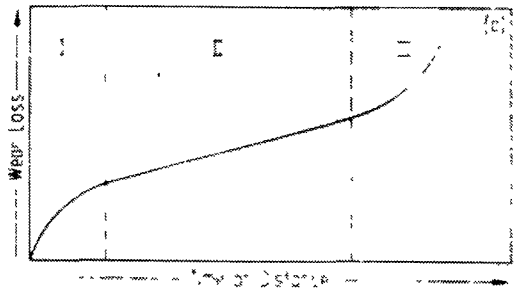

Figure 2.7 Schematic representation of the wear loss plot as a function of operating time or sliding distance showing the general progress of wear [34].

Formation of Transfer Layer

In the early stages of sliding, material transfer occurs as a result of adhesion and asperities interaction After prolonged sliding, long enough to produce shear instability regions, transfer can occur due to crack nucleation and propagation in the subsurface region, which becomes instable due to shear [36] The tribolayer material commonly contains at least one second phase source of which can be from the counterface material, a coating or the environment This layer's grain size is typically 10-50 nm, although grains as small as 3nm have also been observed [37,38] The frequently-observed sharp boundary between the tribolayer and the highly deformed substrate material suggests the involvement of a mechanical mixing process [36-46] The observed small grain size is consistent either with a fracture model, a deformation model, or recrystallization [44,47] and it is generally known that a structure with very fine grain size may be unstable because of grain boundaries that can induce grain growth to minimize the Gibbs free energy of the system The grain growth, however, can be impeded by incorporation of a second phase which provides microstructural stability by acting as pinning points for grain boundaries The ultrafine microstructure of the wear debris or the tribolayer is, therefore, attributed to the existence of a mixture of phases (such as oxides) [37,38,44,45]

There is some evidence for the formation of tribolayers whose microstructure and even composition are different than those of the sliding pair The inter diffusion of atoms due to elevated local temperatures can result in the formation of supersaturated solid solutions and/or intermetallic compounds [38,48] Another frequently observed phenomena is temperature or deformation-induced phase transformations that lead to a fine-grain martensitic layer observed on ferrous materials [49], or a tribolayer that consists mainly of an α phase on an $\alpha+\beta$ base Ti alloy [50]

Formation of Wear Debris Particles

Loose debris can originate from the transfer layer or the bulk material by different mechanisms that depend on sliding condition, relative hardness of transfer material and adjacent substrate and the microstructure and mechanical properties of the sliding

materials [51]. According to Rigney et al [44], wear debris usually falls into two categories, plate like and non-plate like. The former is a result of asperity deformation and fracture, and/or ploughing by hard entrapped particles or hard asperities [52]. There are several mechanisms proposed to describe the formation of loose debris from the highly deformed material of the tribolayer or subsurface, such as the damage accumulation model, the delamination model, the shear localization model, the oxidation model, and others, which are described here.

The damage accumulation model was first proposed by Zhang and Alpas [43] then modified using finite element analysis by Akarca et al [53]. According to this model, the critical depth of crack propagation is determined by the opposing effect of plastic strain (flow stress σ_f) and hydrostatic pressure (σ_H), which both reach a maximum at the surface. As Figure 2.8 shows, the critical depth at which these two stresses will be equal is probably the depth at which the damage growth rate (D) is at its maximum, since the hydrostatic pressure inhibits void growth and its magnitude on the surface is higher than the flow stress. Estimating critical depth this way is in accordance with the thickness of plate-like debris produced from the sliding of an Al-7%Si alloy.

According to the delamination model—proposed by N. P Suh [52]— large incremental plastic strains caused by cyclic loading of asperities can promote the nucleation of cracks at different depths below the surface. Further loading and deformation then causes the cracks to propagate parallel to the surface with the propagation of the crack that is nearest to the surface as the rate controlling process. When the tip of the crack enters the tensile region, it propagates towards the surface perpendicular to the maximum tensile stress direction [52]. The shear localization model is based on the formation of adiabatic shear bands, which are formed due to both large scale strains and strain rates where work hardening and strain rate hardening compete with high-strain softening and thermal softening. This model describes conditions in which a critical temperature at the asperities or bulk material must be overcome before the occurrence of delamination [40].

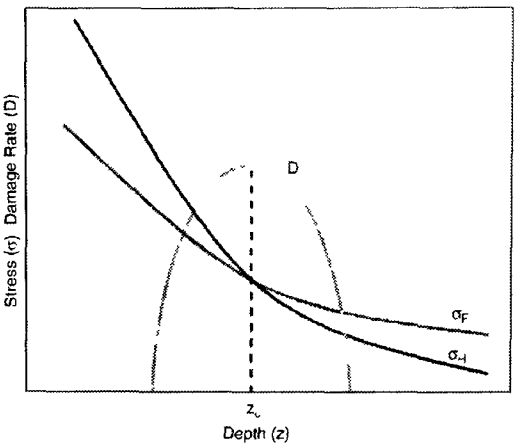

Figure 2.8. Schematic distribution of hydrostatic pressure, σ_H and the flow stress σ_f that create a subsurface damage gradient D (Z_c is the location of the highest damage) [53].

Lim and Ashby's [54] has summarized and discussed the models of oxidation based on the sliding wear of steels. According to this model an oxide layer will grow on the asperity tip at elevated flash temperature until it reaches a critical thickness and spalls off to form fine oxide particles. A new oxide layer then forms on the next asperity contact. A schematic representation of this model is presented in Figure 2.9 [54]. At higher temperatures, due to higher sliding velocity and load, islands or layers of oxide forms on the surface that can be homogeneous oxide layers growing by tribochemically enhanced oxidation, as shown in Figure 2.10. This is associated with both general oxidation and the oxide becoming plastic and melting locally to a viscous liquid that can flow under the sliding action [54]. Another possible mechanism for the formation of an oxide layer is the agglomeration of fine particles generated at asperities contacts as shown in Figure 2.11 [55]. In this latter mechanism, the oxide particles are retained within the wear track where they are comminuted and fractured by repeated plastic deformation while moving freely between the sliding surfaces. Once the particles are small enough, they are agglomerated due to adhesion forces arising from the surface energy, and they form the compact layer. This reduces material loss, since newly formed debris particles are recycled into the layers. As sliding continues, the rates of two processes determine the wear rate: the breakdown of the layers and the formation of the oxide layer by severe or mild oxidation. For example, if the particle layers are not very well compacted, the particle will be removed faster and the wear rate will be higher [55].

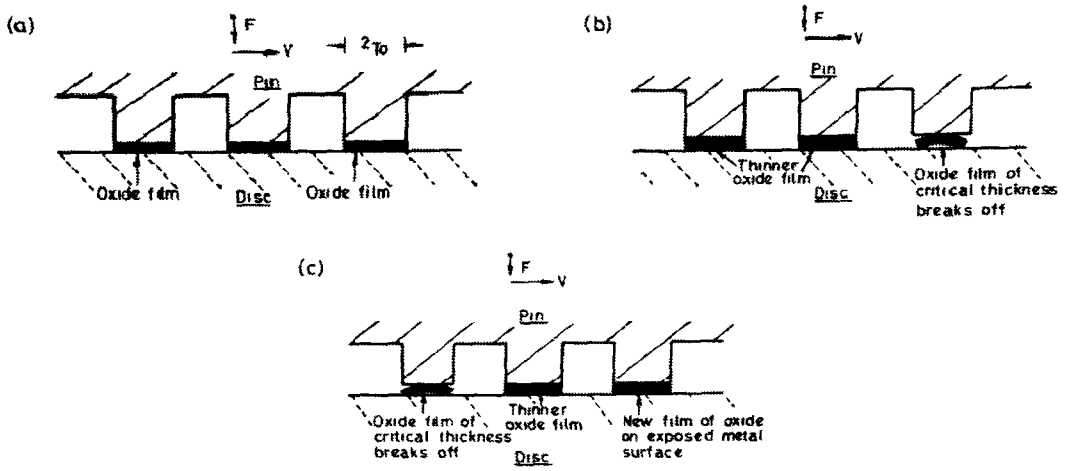

Figure 2.9. Schematic representation of idealized mild-oxidational wear model for pin-on-disc specimen configuration; (a) Oxide films grow on the asperity contacts. (b) The critical oxide film thickness is attained on one of the contacts and the oxide layer breaks off as wear debris. (c) New oxide grows on the metal exposed following loss of the oxide film while the oxide film on another asperity reaches the critical thickness and breaks off [54].

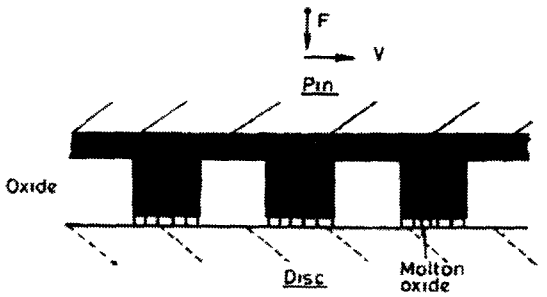

Figure 2.10. Schematic representation of idealized severe oxidational wear model for pin-on-disk specimen configuration [54].

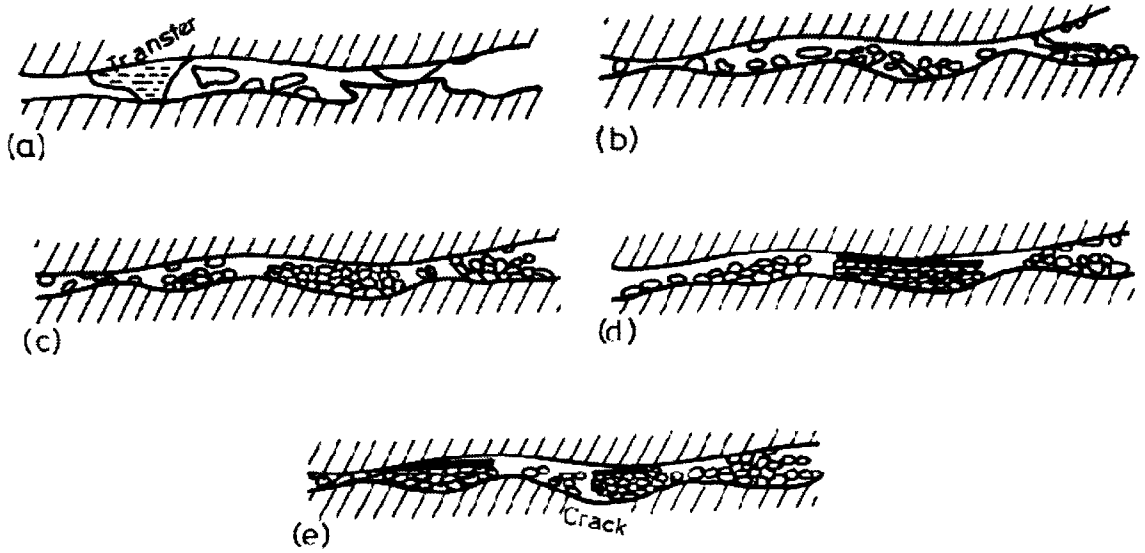

Figure 2.11. Schematic representation of a model for the development of wear-protective oxide layers from wear debris particles. (a) Generation of metallic wear debris. (b) Comminution, oxidation and agglomeration of debris particles. (c) Compaction of agglomerated debris particles. (d) Development of 'glaze' layer over compacted particle layer under some conditions. (e) Breakdown of wear-protective layers and development of new protective layers in other areas [55].

2.1.6.2 Wear Behaviour of Titanium and Ti-6Al-4V

The sliding wear behaviour of Ti alloys reveals poor tribological properties, including high and unstable friction coefficient, severe adhesive wear, susceptibility to fretting wear, and a strong tendency to seize. Dong and Bell [4] correlated this characteristics of Ti alloys with their electron configuration, crystal structure and lubrication characteristics.

- Electron configuration: since Ti has the lowest d-bond character (27%) and is extremely active, it produces a high coefficient of friction and is ready to alloy with other materials.
- Crystal structure: as mentioned in section 2.1.4, the c/a ratio for α-Ti is less than the ideal for HCP structures. This leads to an increase in the number of possible slip systems. Since junction growth requires slip on different slip planes (lower resistance to plastic shearing and low work hardening), it will be promoted by the increased number of possible slip systems.

- Lubrication characteristics: all conventional lubricants are reported ineffective when applied to Ti alloys, with an explanation being the low heat conductive nature of Ti [4,56].

The low heat conductivity of Ti also leads to high flash temperatures induced by friction during sliding as well as the formation of surface oxides. This oxide is thin and easily removed, and does not protect the subsurface layers against wear [4,56].

Many studies have focused on the characterization of the wear mechanisms for Ti and Ti-based alloys in reciprocating or dry sliding contact against various counterfaces [50,57-61]. Metal and ceramic counterfaces were observed to produce a friction coefficient in the range of 0.34-0.5 with relatively large fluctuations, while the polymeric counterface (PTFE) generated a fairly smooth friction trace [61]. It is proposed that the wear rate of a Ti-6Al-4V alloy is determined by the ductility of the material, the existence of oxidation as a competing process and by the local plastic shear strain (by surface temperature). Molinari et al [58] and Straffelini and Molinari [50] conducted a comprehensive study on the dry sliding wear mechanism of Ti-6Al-4V against Ti-6Al-4V and M2 steel counterfaces, and proposed a wear map as shown in Figure 2.12. The bold curve indicates the boundary between two areas where distinct wear mechanisms predominate; namely the oxidative and the delamination wear. The other curve—the thin line— represents the minimum value of wear rate which lies in the region of delamination very close to the boundary between the two regimes. The typical wear rates were between $(2.8 - 11.2) \times 10^{-6} mm^3/mm$ for oxidative wear and $(17.0 - 45.2) \times 10^{-6} mm^3/mm$ for delamination wear.

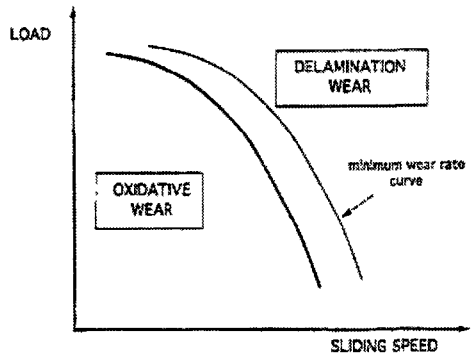

Figure 2.12. Qualitative wear map representing the results of (Ti-6Al-4V) disk against (Ti-6Al-4V or M2 Steel) disk wear tests and predominating wear mechanisms, normal load: 35-200N and sliding speed: 0.3-0.8 m/s [58].

Surface and subsurface observations at lower speed and loads reveal that the dominant wear mechanism is oxidative wear. Lim and Ashby [54] described mild oxidation wear (as described in section 2.1.6.1), with the following equation:

$$W_{0x} = \frac{A_r C^2 A}{v Z_c} \times \exp\left(\frac{-Q}{RT_f}\right) \qquad \text{Equation 1.3}$$

where W_{0x} is the oxidative wear rate, A_r is the real area of contact, C is a material constant, A is the Arrhenius constant for oxidation, Z_c is the oxide critical thickness, Q is the activation energy for oxidation, R is the molar gas constant, T_f is the flash temperature and v is the sliding speed [54]. The oxide formed in-situ on Ti-6Al-4V is brittle and, not supported by the substrate with a very low critical thickness (Z_c). On the other hand, Ti has a low activation energy for thermal oxidation (Q). Titanium oxide is therefore not protective and the resulting wear calculated by equation 1.3 is severe [50,58].

The first factor in equation 2.2 represents the contact time between the sliding surfaces, while the exponential factor represents the role of the flash temperature on the oxidation rate. As the velocity increases the time available for the out-of-contact oxidation decreases and the first factor decreases. The contribution of thermal activation, on the other hand, increases as the sliding velocity increases; as a consequence, the oxidative wear presents a maximum as shown in Figure 2.13. Likewise an increase in the surface temperature induced by a higher sliding velocity increases the contribution of

metallic wear produced by the delamination of the mechanically mixed layers (Figure 2.13). The diagram resulting from the combination of oxidative and delamination wear is drawn in Figure 2.13. The minimum in the wear in correspondence to the transition from oxidative to delamination is then justified [50,58].

The dynamic recrystallization [62] or the shear localization models [63] described in section 2.1.6.1 explain the increase in the wear rate as the sliding velocity increases. Molinari et al [58] correlated the increase in wear rate at a critical load and speed with a change in wear mechanism from oxidative to delamination wear. The observed delamination wear was accompanied by abrasive grooves, smooth plastically deformed layers and an increased amount of Ti-6Al-4V material transferred to the counterface as shown in Figure 2.14.

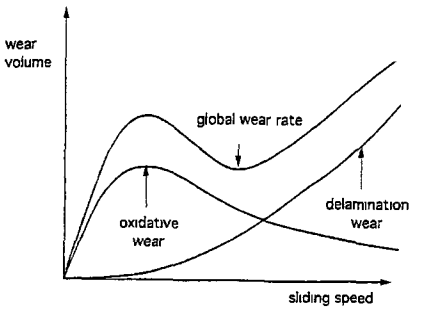

Figure 2.13. Schematic representation of the contribution of oxidative and delamination wear on the sliding wear volume vs. sliding speed of Ti-6Al-4V [58].

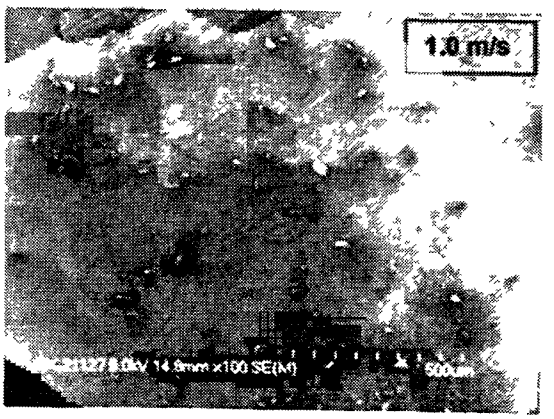

Figure 2.14. Extensive transfer of Ti to the 440C steel ball as a result of sliding against Ti-6Al-4V [61].

The poor tribological properties of Ti alloys, therefore, are associated with their inherent surface characteristics. As a result, in an attempt to modify the surface properties of these alloys, the incorporation of high strength ceramic particles to the bulk material or a variety of surface treatment methods have been frequently adopted to improve the wear resistance of Ti alloys. Existing surface treatments include the thermal oxidation process (TO), a novel method, first developed by Dong et al [4]. A comprehensive study of the detailed characteristics of the oxide formed under TO condition has not been performed. An alternative method for modifying the bulk and surface properties of a Ti matrix is to fabricate titanium matrix composites (TMCs). TO treatment and the incorporation of TiC particles were adopted in this research to study any improvement in mechanical and tribological properties of Ti-6Al-4V matrix, described in detail in section 2.2.

2.2 Available Methods for Enhancing the Tribological and Mechanical Properties of Titanium Alloys

A wide variety of surface treatment methods, as well as the incorporation of different types of ceramic particles or fibers have been employed to improve the mechanical and sliding wear properties of Ti alloys. Some of these surface treatments include: i) anodizing, ii) anodizing and Mo_2S co-deposition, iii) ion implantation, iv) plasma nitriding, v) laser nitriding, vi) laser alloying electron beam nitriding, vii) diamond coating, viii) plasma spray, physical vapour deposition and ix) thermal oxidation (TO) process [58]. Most of these existing surface engineering techniques (except for the TO process) are not cost effective for mass production, and while ion implantation and TiN coatings have proven unsatisfactory in-vivo, the in vivo corrosion studies of the thermally oxidized samples showed no pitting or blistering of the oxide coating [6]. The TO process was first developed by Dong et al [4], who based their work on the thermal oxidation of Ti-6Al-4V samples in an air furnace. The thick, adherent oxide layer formed by this method significantly improved the dry and lubricated sliding wear and corrosion wear resistance of the Ti alloy matrix [4,5,56]. The details of this process are further described in section 2.2.1 .A thorough study of oxidation characteristics of Ti alloys is given in section 2.2.1.1 to clarify the series of phenomenon that happen during the TO process. An alternative method for modifying the surface and bulk properties of the Ti

matrix, as previously mentioned, is to incorporate ceramic reinforcements, which is described in section 2.2.2.

2.2.1 Thermal Oxidation (TO) Process

The thermal oxidation or TO process was first adopted by Dong et al [5] for modifying the surface characteristics of Ti-6Al-4V alloy, and has been successfully used for the surface treatment of Ti components for off-shore gas/oil and car race industries [5]. The compound layer that formed on the surface was, essentially, a rutile form of TiO_2 with a 2μm thickness supported by a hard layer formed by diffusion of oxygen into Ti matrix (ODZ), which was 20 μm thick as shown in Figure 2.15. The isothermal oxidation treatment was performed in an air furnace at 600°C for 65 hours. An Al-rich layer at the outer surface of the oxide was observed [4,5,64]. The oxidation kinetic in air follows a parabolic relationship that changes to an almost linear relationship at temperatures higher than 650°C. This change in oxidation kinetic was correlated with the stratification of the oxide formed at high temperatures [65,66], making the choice of the TO process condition consistent with literature data on the effect of temperature on oxide scale quality. A review on the oxidation characteristics of Ti alloys and the relevant effective parameters is provided in the following sections.

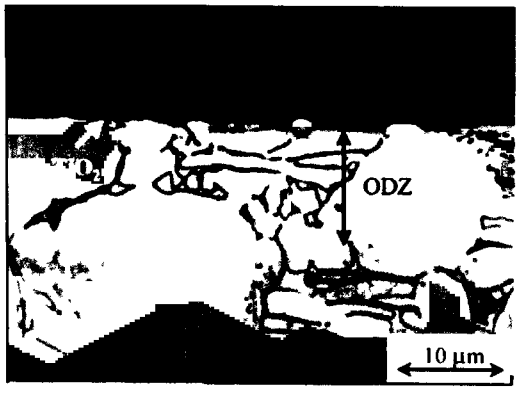

Figure 2.15. Cross-section of oxidized Ti-6Al-4V showing the exterior TiO_2 layer and adjacent ODZ [6].

2.2.1.1 Oxidation of Titanium and Titanium Based Alloys

It is difficult to completely eliminate oxygen from Ti, due to its large chemical affinity to Ti, confirmed by Ti-O bond energy of 2.12 eV compared to the Ti-Ti bond

energy of 2.56 eV [67]. As previously described in section 2.1.1, oxygen is an α phase stabilizer that shifts the β transus to higher temperatures to an extent that prevents the formation of the β phase even in dilute solutions, as shown in the Ti-O phase diagram in Figure 2.16. Consequently, penetration of oxygen into Ti readily establishes a solid solution layer referred to as α-case or an oxygen diffusion zone (designated as ODZ hereafter). The limiting solid solubility of oxygen below 800°C is reported to be constant at 33.9 at% (Figure 2.16) [68], although other magnitudes of 30% [69] and 34% [70] have also been reported. The oxygen atoms occupy octahedral interstitial sites in HCP-Ti, with distribution that can be either random or in ordered arrangements. In the α-phase region ordered structures based on the compositions Ti_2O, α′, Ti_3O, α'' and Ti_6O, α''' have been reported [71].

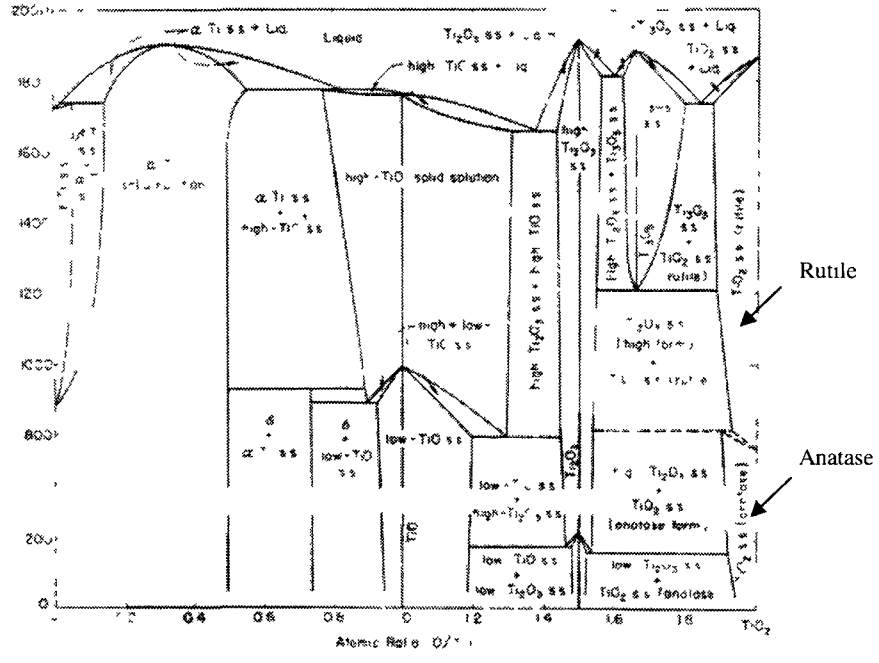

Figure 2.16. Titanium-Oxygen phase diagram [72]. The arrow indicates the stability region of TiO_2 phase.

The Ti-O system has several compounds—TiO_2, Ti_3O_5, Ti_2O_3 and TiO [66]—which can be seen in Figure 2.16. The nature, composition and thickness of the oxide formed depend on environmental conditions. The most important Ti oxide is the dioxide TiO_2 which crystallizes in three structural forms: brookite, anatase and rutile. Rutile is the most stable or thermodynamically preferred and highly crystalline form, while anatase is

metastable and more amorphous, and is only synthesized at relatively low temperatures. Brookite is formed only in extreme conditions and is rare as a mineral [73,74]. Table 2.3 provides some of the physical properties of the anatase and rutile phases.

The anatase to rutile transformation is irreversible and generally occurs at temperatures higher than 700 to 800 °C [73,74]. Nevertheless, these values are reliable in the equilibrium condition of transformation, which is not the condition for the extreme, high temperature conditions of thermal oxidation [74]. Since the focus of this study is on the oxidation behaviour of a Ti-6Al-4V alloy at high temperatures and the mechanical performance of the resulting scale, the effect of interstitials on mechanical properties, diffusion mechanisms, the parameters affecting oxidation behaviour—including alloying elements—and the composition of oxide layers are discussed in the following sections.

Table 2.3. Some physical properties of anatase and rutile [73]

Physical property	Anatase	Rutile
Crystal structure	Tetragonal	Tetragonal
c/a ratio	2.51	0.64
Density (Kg/m^3)	3890	4260
Melting point (°C)	Converts to rutile at 700-800°C	1830-1850
Hardness (HV)	669-817	1161-1364
Corrosion resistance[1]	High	Low

1. The corrosion resistance data are taken from [3]

Diffusion Mechanisms

Once the metal surface is completely covered with a thin oxide layer and thus separated from the gaseous environment, further growth of the scale is controlled by mass transport through the oxide scale. Mass transport can happen through micro/macro cracks and voids, grain boundary diffusion or volume diffusion. The volume diffusion mechanism is dominant at higher temperatures, and is closely linked to the disorder of the reaction products. During oxidation either stoichiometric or non-stoichiometric products can be formed. For oxides that deviate from stoichiometric composition, maintaining

electroneutrality dictates electron disorder in addition to ion disorder, practically making these compounds semiconductors. Such semiconductors are divided into the following groups:

- Electron excess conductors (n-conductors) with
    - Metal excess (metal ions located at interstitials)
    - Non-metal deficit (non-metals ion vacancies)
- Electron defect conductors (p-conductors) with
    - Metal deficit (metal ion vacancies)
    - Non-metal excess (non-metal ions located at interstitials) [20]

The dependency of the vacancy concentration on the oxygen partial pressure for both of these types of conductors can be calculated by:

n-conductors: [vacancies]$\approx P_{O_2}^{-1/v}$

p-conductors: [vacancies]$\approx P_{O_2}^{1/v}$

The value of v depends on the composition of the oxide formed, and is typically between 2 and 8, and as a result the disorder of the oxide determines which species are mobile in the course of action. The diffusion's driving force is the concentration gradient of the vacancies in the oxide. Oxides that grow at the metal/oxide interface by anion conductivity lack the ability to heal cracks, while oxides that grow at the gas/oxide interface by cationic diffusion have the ability to heal cracks [20].

According to Leyens [20], the disorder of TiO_2 is strongly dependent on environmental conditions. The types of defects observed correspond to n-type conductors. At low pressures and high temperatures, interstitial titanium ions are major defects, while at high oxygen pressure and low temperatures, disorder is dominated by oxygen anion vacancies—which means that—the composition of titanium oxide can be described more generally as $Ti_{1+x}O_{2-y}$. On the other hand, according to theoretical considerations, the interstitial diffusion of oxygen in Ti is more rapid than anion vacancy diffusion in rutile, which would offer an explanation for the observed early establishment of an oxygen solution in the metal phase (ODZ) during the oxidation reaction [70,71].

Effect of Interstitial Atoms on Deformation Behaviour of Ti

The effect of an oxygen solution on the preferred slip systems of Ti has been the subject of many investigations [25,26,28,75,76]. As described in section 2.1.4, the primary slip for pure Ti happens on the prismatic planes rather than the basal planes due to the lower c/a ratio of Ti compared to the ideal HCP lattice. The dissolution of oxygen in Ti increases the critical resolved shear stress (CRSS) of all the slip systems. Addition of low amounts of oxygen to Ti, as low as 1000 ppm [75] or 0.1 Wt% [28] or 0.19 Wt% [76], however, increases the CRSS for prism planes more than for other systems. This accounts for the preference of pyramidal and basal planes over prismatic planes.

The lower increase in CRSS of pyramidal plane that accounts for their preference is explained based on the geometrical considerations concerning interstitials and slip planes. As mentioned before neutral O atoms occupy the interstitial octahedral positions in the HCP lattice of α-Ti. Solubility limit, i.e. 33.9 at% and lattice parameter changes corresponds approximately to one –half of these sites to be occupied. Consider a model of the hexagonal lattice in which the atoms are hard spheres. If we examine a $(11\bar{2}0)$, as shown schematically in Figure 2.17, in this model it can be seen that two of the three slip planes, $(10\bar{1}0)$ and $(10\bar{1}1)$, have corrugated repeat layers, while the atoms in the basal layers are all coplanar. The positions of the interstitial sites are such that atoms occupying these are not coplanar with either the (0001) or the $(10\bar{1}0)$ layers and therefore provide obstacles to the movement of adjacent layers of this type over one another. However, interstitial atoms occupying the $(\frac{1}{3},\frac{2}{3},\frac{1}{4})$ positions are coplanar with the $(10\bar{1}1)$ layer but not the $(\bar{1}011)$ layers, while atoms in the $(\frac{1}{3},\frac{2}{3},\frac{3}{4})$ positions are coplanar with $(\bar{1}011)$ layers but not with $(10\bar{1}1)$. At low oxygen concentrations, it is unlikely that adjacent sites of the two types will both be occupied. In a random distribution of oxygen atoms, one would expect only one-half of these to act as obstacles to the passage of dislocations and consequent relative displacement of $(10\bar{1}1)$ planes. On the other hand, as both types of site interfere with the displacement of all planes of the (0001) and $(10\bar{1}0)$ types all the O atoms will be effective obstacles to slip on these planes. The mean free path of a

dislocation will therefore be much greater in the $(10\bar{1}1)$ plane than either a basal or a $(10\bar{1}0)$ plane [28].

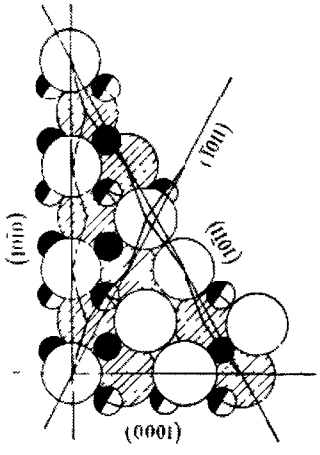

Figure 2.17. A section in the $(\mathbf{11\bar{2}0})$ plane through a ball model of the close-packed hexagonal lattice. The bounding surfaces are the repeat layers of the $(\mathbf{0001})$, $(\mathbf{10\bar{1}0})$, and $(\mathbf{10\bar{1}1})$ planes. The two positions for the interstitial atoms are shown by small circles [28].

Several other models, such as the non-planar core structure of $\langle a \rangle$ type screw dislocations [76], or the ordering of oxygen atoms on slip planes [25] were suggested also for justifying the observed change in the preferred slip system.

Plastic deformation by twinning has been observed to be completely suppressed as the oxygen content of Ti increases, and this can be explained based on the hindrance of zonal dislocations whose existence and movement is mandatory for the twins in an HCP structure to form [26,77]. The significant hardening effect of oxygen as it dissolves in titanium structure is explained in terms of interaction with dislocations in the following ways:

Tetragonal interaction: Weissmann et al [69] analyzed the strain imposed on the Ti lattice as a result of oxygen dissolution, and observed that the strain distribution tends to become axisymmetric in respect to the c-axis of the HCP structure. Two factors were considered to contribute to the resulting overall strain configuration: one arising from the preferred ordering of the O atoms and the other from the oblate geometry of octahedral sites. The unusual hardening associated with the oxidation of Ti was attributed to the ordering of oxygen atoms with the concomitant tetragonality strains—the latter being due

to the fact that lattice defects with tetragonality strains interact with the shear part of the stress field of a dislocation to give rise to large interactions with both screw and edge dislocations [69]. Tyson et al [78] and Naka et al [25] disputed this model, suggesting that the contribution of elastic interaction of oxygen to titanium is low since the magnitude of the strains calculated by this model are too low to explain the large hardening effect.

Chemical reaction: This model was first proposed by Zaefferer [26], and is based on the non-planar core structure of $\langle a \rangle$-type screw dislocations. It suggests that oxygen atoms may have some tendency to form pairs or clusters in α-Ti specimens with oxygen content as low as 9 at% and along a preferential direction of $\langle 11\bar{2}3 \rangle$. According to this model oxygen dissolution induces asymmetric geometry in the dislocation core structure, increasing the energy required for the sessile to glissile transition compared to the pure, symmetric core structure—impeding dislocation movement [26]. It should be noted, however, that the explanation for interstitial hardening in terms of a chemical interaction is valid only for a relatively high concentration of interstitial impurities [25].

Short and long range order interactions: According to Welsch [76], the ordering of oxygen has been reported to occur over nearly the entire O concentration range up to the maximum solubility, i.e. 33.9 at%. The long-range ordering tendencies exhibited in more concentrated solutions (higher than 22.5 at% [68]) are preceded by short-range ordering in more dilute solutions. The most frequently observed ordered structures in the α-phase region are based on the compositions Ti_2O, α', Ti_3O, α'' and Ti_6O, α''' The α'' and α''' structures may be regarded as super-lattices of the α' structure, formed by an ordering of vacancies in the layers of O atoms [68,70]. The strengthening characteristics of short- and/or long-range orders can be assumed to be due to the reduced degree of the local order produced by the movement of a dislocation through the ordered region. This process of disordering causes an increase in the energy of the alloy that is then followed by a hardening effect [29]

Electrical interaction: Studies suggest that solid solutions of oxygen in Ti have metallic characteristics and that promote resonating metallic covalent bonding [28]. The incorporation of covalent bonding is considered partly responsible for the large increase in the CRSS of slip systems, no matter which one is activated first. This effect arises from

the fact that some of the charge associated with solute atoms of dissimilar valence remains localized around the solute atom, making the solute atoms charge centers that can interact with dislocations with electrical dipole. This latter factor makes a much lower contribution to the hardening effect of O atoms, compared to the other effects mentioned [29].

Effective Parameters on Oxidation Behaviour of Titanium

A wide range of parameters can affect oxidation behaviour, resulting in various oxide compositions and configurations. Sample condition and oxidation environment are the two major categories for these parameters. Sample condition includes parameters such as alloying elements and primary microstructure and phases. Oxidation environment includes oxidation temperature, time and pressure as well as oxidation atmosphere. These parameters are further described in the following sub-sections.

Effect of Alloying Elements on Oxidation Behaviour

The influence of adding Al on the oxidation mechanism of Ti has been studied extensively. Chaze et al [79,80] studied the effect of 1.65, 2, and 10 wt% Al on the oxidation of Ti in both air and oxygen environments at temperatures between 550 and 700°C. They observed that the presence of Al promotes a decrease in the amount of oxygen dissolved in the metal phase, except for the lowest Al content (1.65 wt%). Meanwhile, the ratio of oxygen diffused in the form of solid solution to total oxygen increased as the Al content increased. Other studies focused on the effect of Al in binary Ti alloys. Ignatov et al [81] studied oxidation of Ti alloys with 6, 8, 10, and 14 wt% Al in air at 800 and 1000°C for 25 h. They observed an enhancement in oxidation resistance at higher Al contents [81]. The same protective role was witnessed for Ti-5 wt% Al alloy oxidized at temperatures between 650 and 850°C for 8h in a purified oxygen atmosphere, once an initial period of 5h had passed [82]. It must be considered that the duration of oxidation in the latter study was too short to be compared to similar cases.

The majority of workers agreed that the addition of Al to Ti enhanced the oxidation resistance, since the solubility of oxygen in Ti was reduced from 34 at% to 13 at% at 700 °C and a number of alumina layers were found at the surface and in the

sublayers [83]. The following are the factors through which Al contributes to Ti oxidation:

- Al goes into substitutional sites in the Ti lattice and causes lattice contraction that leads to a reduction in the volume of interstitial sites available for oxygen in ODZ [80].
- Al enhances the interatomic force of the bond of a solid solution on an α-Ti base, and the solubility of oxygen in these alloys diminishes [84].

  The interstitial solution of Al in the TiO_2 lattice reduces the concentration of anion vacancies which in turn decreases the inward diffusion of oxygen through rutile. This corresponds to better crack healing properties for the oxide through the promoted outward diffusion mechanism [20,65].
- Depending on the amount of Al, either a continuous alumina layer or a dispersion of alumina particles within the rutile phase can form during oxidation. Since the ionic conductivity of alumina is lower than rutile this layer can act as a diffusion barrier. On the other hand, the addition of alumina to rutile leads to an overall decrease in the thermal expansion coefficient of the oxide, modifying the layer's plasticity [65,79].

Nevertheless, cations with a lower volume like Al^{3+} compared to Ti increase the vacancy concentration in rutile, given that they occupy the titanium sites instead of the interstitial sites. This latter phenomenon, which is called "doping", can describe the accelerating effect of Al on oxidation when the Al content is too low to form enough alumina [20]

Investigation of the effect that ternary addition of alloying elements has on the oxidation behaviour of Ti-Al alloys has not been as comprehensive as that of binary Ti-Al alloys. Rudinger et al [84] studied the oxidation behaviour of different Ti alloys air oxidized at 400-1000°C for 5 to 4000 h. Oxidation resistance increased among the alloys investigated in the order of: β-alloys, Al free-α+β alloys, α-alloys and α+β-alloy contained Al beyond 6%. They observed that both the ODZ thickness and increase in hardness were at their maximum for CP-Ti and then Ti-6Al-4V The only data on modifying effect of vanadium on Ti-6Al-4V oxidation resistance is reported by Frangini

et al [65], who studied the oxidation behaviour of bimodal Ti-6Al-4V in air at temperatures of 600, 650 and 700°C. Generally, the addition of vanadium to Ti-Al alloys prevents the formation of an alumina barrier, as observed for the binary Ti-Al alloys [83-86]. The neutralizing effect of V is also related to an increase in anion vacancies in the rutile structure, which leads to the enhancement of oxygen diffusion through the rutile lattice. Consequently, the scale that formed on the vanadium-containing alloys displayed numerous cracks [84,85].

Effect of Primary Microstructure and Phases

The diffusion coefficient and maximum solubility of O in Ti alloys varies depending on their constituent phases. The solution of O in α-Ti is exceptionally large (34 at.%, compared to 4 at.% dissolution in β-Ti) [66,80]. In contrary, bulk interstitial diffusion in the β-Ti proceeds at a rate of one to three orders of magnitude higher than in the α-Ti [87], making the oxidation resistance of α-Ti superior to that of β-Ti, and the β-transus temperature of an alloy as a safe upper temperature limit for the alloy's high temperature applications [85].

Diffusion initially occurs in parallel through the α and β grains and along associated grain boundaries [87]. As the oxygen concentration increases above that needed to convert the β grains to α, the ODZ layer is formed. Diffusion then occurs through the α-layer and into the mixed α/ β layer. The primary microstructure of the sample can only affect the diffusion rate at the very beginning of the test. The diffusion rate through ODZ itself and through the oxide layer is independent of the constituent phases, and will be the controlling rate once the ODZ layer is established [82,87]. To the author's knowledge, there is a lack of evidence regarding the effect of primary microstructure on oxidation behaviour, as well as on changes in microstructure due to oxidation.

Effect of Oxidation Temperature and Time

Growth of the oxide scale as a function of time can be described by growth laws. For diffusion-controlled scale growth, a parabolic dependency is dominant:

$$x^2 = k_p + C$$ Equation 1.4

where x is the thickness of the oxide scale, k_p is the parabolic rate constant, and C is an integration constant. These values depend on the type of oxide and the oxidation condition. In practical applications, a number of different growth laws such as linear, cubic, and logarithmic are reported. The temperature dependency of the reaction's rate constant, k, can be described with an Arrhenius law:

$$k = k_0 e^{-(\frac{Q}{RT})}$$ Equation 1.5

where k_0 is a temperature-independent pre-factor, Q is the activation energy of equilibrium oxidation, R is the gas constant, and T is the absolute temperature [20]

Most studies have recorded a parabolic behaviour for the oxidation of Ti and its alloys at lower temperatures, while at temperatures around 650-700 °C a transition occurred, in time, to a linear behaviour [65,66]. This behaviour was correlated to the observation that the oxide layers on Ti show an increasing tendency to be stratified above 700°C. The formation of cracks within the oxide prohibits diffusion through the oxide layer and hinders the diffusion-controlled (or parabolic) oxidation. This high temperature oxidation was believed to be the result of a change in the relative diffusivities of anions and cations in the rutile scale. The promotion of cationic diffusion dominates oxidation at the oxide/gas interface, which in turn promotes increased crack healing ability [71,85].

The abovementioned scaling happens when the oxide layer grows beyond a certain maximum thickness, and since the plastic flow of the oxide scale is limited, cracks could form between the oxide scale and the substrate due to the growth stresses built up at the interface and within the oxide. These cracks can propagate during the cooling process [71,83]. The most frequent explanations for oxide stratification are as follows:

> The Pilling-Bedworth ratio (PBR, the ratio of oxide-to-metal molar volumes) is high for rutile to Ti, i.e. 1.75, which produces compressive stresses in oxide and tensile stresses in metal at the interface. These stresses increases until a bearable maximum value is reached (at a critical thickness), at which the crack nucleates. It should point out that the observation of the stratified morphology is not specific to

reactions where PBR>1 since a stratified scale is also found during oxidation of iron pyrite to hematite (PBR<1).

- A great variation in the lattice parameters appears in the Ti-O solid solution at 25.9 at% of oxygen. Stress that has built up in the solid solution due to variation in the lattice parameter will lead to the detachment of solid solution, which will be followed by a fast oxidation.
- The ratio of coefficient of thermal expansion for Ti to rutile is 1.3, which further contributes to interfacial stresses during the cooling down process especially with a high cooling rate.

  The internal morphology of the scale is always observed at room temperature after cooling. The cooling period can generate some transformations in the structure of oxide scale. This, however, can only explain the formation of random cracks [70,71,88].

Effect of Oxidizing Atmosphere

The oxide layers formed on Ti alloys in air were generally thinner, more adherent and more compact than the scale formed in oxygen [70,79,89]. Chaze et al [80] observed a large decrease in oxygen dissolution when they studied α-alloys oxidized at 550-700°C in air, compared to a pure oxygen atmosphere. This behaviour was designated the "nitrogen effect" and believed to be the result of the formation of TiN as a border at the metal/oxide interface. For nitrides, the octahedral interstitial sites in the cubic sodium chloride type lattice are filled with N atoms, making the diffusion of oxygen through the lattice lower than that of rutile [66]. The thermodynamic stability of oxides is superior to that of nitrides and nitrogen and other diffusing species are much less active than oxygen. The diffusion coefficient of N in Ti is also about ten times lower than that of oxygen. Therefore, the presence of nitride layer at the interface can be questioned from a thermodynamic point of view. These comparisons are reliable in the equilibrium state of oxidation, however, which is not the condition for high temperature oxidation [80,87].

Oxide Compositions and Sublayers

The composition of the oxide layers formed on the Ti surface is still a matter of controversy, and strongly depends on the parameters mentioned in the previous section. Ti, Al and V elements were found in the oxide layers formed on the Ti-6Al-4V alloy [65,85]; with Ti in the form of TiO_2 and Al in the form of Al_2O_3. The X-ray diffraction results [65] revealed that vanadium oxide was in the form of VO_2 (for Ti-6Al-4V oxidized at 600-700°C for up to 300 h) while the others [85] found reflections of V_2O_5 when analyzed Ti-6Al-4V oxidized at 900°C for 170 h. The distribution of the oxides was complex depending on the oxidation condition and alloying elements. Frangini et al [65] observed that the ternary addition of V to Ti-6Al-4V alloys hindered the formation of alumina and promoted the formation of vanadium oxides. Du et al [83] and Garbacz and Lewandowska [86] observed no vanadium oxide in the scale formed after oxidation in 650-850°C for up to 100h in air, but they also noted the same multilayered structure of alumina and rutile. To the author's knowledge, most of the Ti-Al alloys studied showed that Al was concentrated locally in a narrow region of the scale near the external interface, sandwiched between two rutile layers [79,81]. The number and distribution of alumina and rutile scales, however, can be altered with oxidation temperature and time.

Several types of titanium oxides were observed during the high temperature oxidation of commercially pure or high purity Ti. The presence of a non-stoichiometric titanium oxide in addition to the stoichiometric rutile with different colours has been revealed by many investigators through X-ray diffraction studies [70,71,88]. Other titanium oxide forms such as TiO [66] and Ti_2O_3 [66,90] are also infrequently observed in the scale. Nevertheless, to the author's knowledge, none of the studies performed on the oxidation of Ti and its alloys with Al and V has witnessed the formation of the anatase form of TiO_2 instead of rutile [66,71,81,89,91].

The stability of different oxides as defined by standard enthalpy of formation (ΔG^o) and correlated to the oxygen partial pressure (P_{O_2}) by the following equation, can be compared by using the plot shown in Figure 2.18.

$$\Delta G^o = RTLnP_{O_2}$$ Equation 1.6

As this Figure shows, the stability of Al_2O_3 and TiO_2 are very similar, but the non-equilibrium state of alloy oxidation, the oxidation kinetic of each element and their activity can be such that the less stable oxide form first [20].

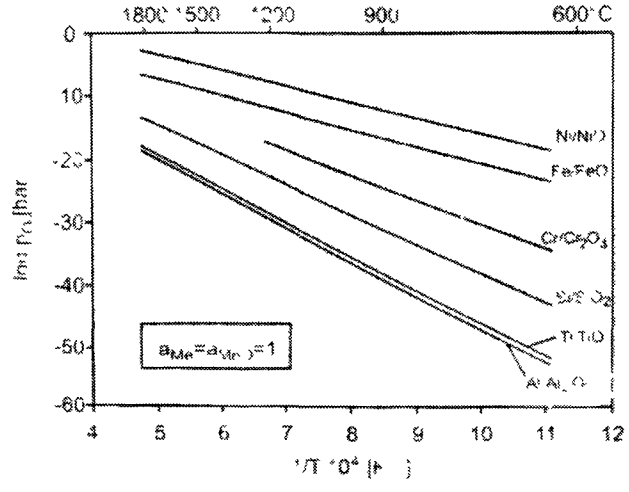

Figure 2.18. Dissociation pressures of selected oxides vs. temperature. As it is evident curves for TiO and Al_2O_3 are close together [20].

According to Leyens' experimental investigations [20] of the phase equilibriums in the Ti-Al-O system, Al_2O_3 is more stable than TiO_2. Du et al [83] and Ignatov et al [81], however, suggested that the activation of Al (a_{Al}) is about 4 orders of magnitude smaller than that of Ti (a_{Ti}) for binary Ti-Al alloys. They assumed that at the initial stages of oxidation, Ti and Al both diffuse outward from the substrate while oxygen diffuses inward, and the addition of V reduces the Al activity to an even smaller value in the ternary alloys. Therefore, Ti reacts with oxygen and would be trapped at the metal/oxide interface, allowing more Al to diffuse outward, making it more kinetically favourable for an alumina layer to form at the gas/oxide interface [81,83].

It is important to note that at least 8 intermediate sub-stoichiometric Ti oxides exist between Ti_2O_3 and TiO_2, and most of these anion-vacancy-poor defect structures should exhibit high shear strengths, but the narrow range of $TiO_{1.98}$ and $TiO_{1.93}$ develop planar defect structures that impart the lowest possible shear strength to the rutile surface at temperatures below 0.7 times its melting point. If the stoichiometry of rutile can be

confined to this desirable (but narrow) range, then the flow pressure of the softened oxide film at high asperity pressure could be reached, and, ideally, the oxide surface should deform before the entire compacted flake column delaminate from the substrate [70].

2.2.1.2 Sliding Wear Behaviour of Thermally Oxidized Titanium Alloys

The success of the TO process in improving the wear resistance of Ti alloys varies with the loading conditions. Dong and Bell [4] studied the lubricated wear behaviour of TO-Ti-6Al-4V against an M40 steel counterface in a wheel-on-wheel configuration (under constant sliding ration of 10%) and evidenced that transfer from the counterface to the thermally oxidized sample happened at low pressures (300 MPa), wear proceeded by deformation and removal of the asperities as well as local breakdown of the oxide layer. At a higher normal pressure (650 MPa), interfacial fatigue and subsurface cracking modes dominated [4,5]. The TO-Ti-6Al-4V showed an improvement in reciprocating dry wear against alumina balls and followed a similar wear mechanism [4]. The TO process also retarded the corrosion-wear and corrosion for both CP-Ti and Ti-6Al-4V samples [3,6]. A local breakdown of the oxide layer is feasible to happen; but the underlying ODZ is proved to successfully restrict further progress of wear, corrosion-wear or corrosion [3-6].

According to Dong et al [4,5], several factors contribute to the reduction in wear rate of thermally oxidized material:

Strong decrease in severe adhesion due to ceramic/metal contact instead of metal/metal contact. Since the adhesion of contact surfaces is related to their metallurgical compatibility and deformation behaviour, a much lower elastic modulus to hardness ratio for TO samples (E/H:13.8 vs. 26.9) can promote elastic deformation, and a reduction in the adhesion wear rate can be anticipated.

- It is known that the boundary lubricating effect is associated with the wettability of the surfaces in contact to the lubricant which is closely related to the degree of ionic character of the surface. Formation of the rutile layer enhances the ionic character of the surface. All commercial lubricants, on the other hand are ineffective on the surface of uncoated Ti alloys. The enhancement in surface wettability when the Ti alloys are thermally oxidized—associated with ionic

characteristic of rutile—leads to the superior performance of the commercial lubricant.

- The support provided by the high hardness of ODZ (~1000 HV) for the oxide scale prevents the hard oxide layer from bending in and penetrating the ductile Ti alloy [4,5].

Therefore the TO process is cost effective and produces a low friction, high corrosion resistant (as listed in Table 2.3) layer of rutile supported by a hard ODZ for improvement in sliding wear and corrosion of the Ti matrix. This process, compared to the other energy beam liquid phase surface alloying methods, produces a homogeneous, composition-controlled and highly reproducible alloyed surface [56]. Among the surface treatments, the ion implantation and TiN coatings have proven unsatisfactory in-vivo, while the corrosion studies of TO-Ti-6Al-4V samples (the samples were deliberately damaged by prior abrasion) showed none of the pitting or blistering of prevalent in the case of TiN-coated samples [6].

2.2.2 Titanium Matrix Composites (TMCs)

The inferior wear resistance of titanium alloys (discussed in section 2.1.6.2) as well as their considerable loss of mechanical strength at high temperatures makes it necessary to improve the mechanical properties of the bulk material to avoid plastic deformation and retard thermal softening. One method is to incorporate high strength and high stiffness ceramic reinforcements into the ductile matrix [7]. Reinforcements can be in the form of continuous fibers or discontinuous whiskers or particles. Several factors, such as the high price of the fibers and, the costly and complicated fabricating process in addition to the high residual thermal stresses and highly anisotropic mechanical and physical properties have severely limited the field of applications for composites reinforced with continuous fibers. Such drawbacks have, in turn, increased the interest in research and development of particulate reinforced titanium matrix composites, which will be referred to as TMCs hereafter [10].

Ceramic particles can be synthesized in-situ in Ti or its alloy matrices via the exothermic reactions of the constituent elements during high temperature processing. The reinforcements can be also directly introduced to the matrix during processing. The

resultant TMCs will be called "ex-situ" composite [7]. The in-situ process results in a lower finished product cost and stronger reinforcement-matrix interface bonding. The latter is believed to be due to the lower amount of contamination on the reinforcement's surface. The main drawback of producing the ex-situ TMCs is the high cost of Ti powders and ceramic reinforcements. This problem can be overcome by the recent developments in Ti processing, which forecasts the availability of lower-cost Ti [61].

For many years, powder metallurgy has been used to fabricate ex-situ TMCs, but, recently metal injection moulding (MIM)—a near net shape process that eliminates most of the secondary and machining processes for complex components and is adaptable to a high production rates—has been used successfully to fabricate ex-situ produced Ti-based alloys. In this method, the powders of the raw material are first mixed with a wax binder in an extruder to produce pellets. The pellets are then heated to and injection moulded to form the green parts. After binding, the binder in the green part is removed using a solvent debinding process. Eventually the debound parts are sintered to produce the final part [8]. A part of this study focuses on the TMC samples produced by MIM method, and the details of this process are given in section 3.2.

Nitrides, carbides and borides are commonly used as reinforcements in TMCs [92]. Most ceramic reinforcements, such as SiC, Al_2O_3 and Si_3N_4, can form reaction products at the interface. A strong reinforcement/matrix interface is needed to produce a high strength composite, which may not be obtained if there is an extensive interaction at the interface during processing [92]. In this respect, the most promising particles are TiC and TiB_2, due to their good thermal and chemical compatibility with Ti [7,12,93]. On the other hand, the inherent high-temperature stability of TiC makes it attractive for use in elevated-temperature applications, where high strength, stiffness, and creep resistance are required [9].

Particulate-reinforced titanium matrix composites have been used commercially as exhaust and intake valves since 1998 in the Toyota Altezza because of their inferior high temperature specific strength which results in a total engine weight reduction of 381 g compared to the typical austenite steel valves. Research and development of TMCs for aerospace applications show that this material has the potential of exceeding the structural

efficiency of all metallic materials, and of cross-plied graphite/epoxy. Examples include engine pylon structures for transport in aircrafts and aft fuselage structure for fighter aircraft where the engine is embedded in the fuselage. In both cases conduction and radiation from the engine heats the surrounding structures. TMCs provide a significant cost and weight penalty compared to the competing Al alloys, and so is an important target for these applications [9].

Both intake and exhaust valves are subjected to cyclic mechanical loading, sliding wear (in the valve guide), high temperatures and high frequency hammering forces. These valves must therefore possess good high-temperature tensile strength, fatigue strength, and resistance to creep, oxidation, sliding wear and galling adhesion [9]. As with Al matrix composites, the incorporation of ceramic particles increases fatigue and tensile strengths, and modulus of the Ti matrix, but at the expense of the ductility. The strengthening effect is retained at high temperatures which is not unexpected as the ceramic particles maintain their properties to higher temperatures better than the matrix. Incorporation of TiC particles also improves the low pressure wear resistance of the matrix alloy. The tensile ductility of these composites, however, tends to increase with increasing temperature; for example the tensile elongation of cold and hot isostatic pressed 10 Wt.% TiC/Ti-6Al-4V composites was 0.3% at room temperature and increased to 2.32% at 200°C [7]. The brittle nature of the reaction products at the interface, the homogeneity of the reinforcement dispersion, the surface properties of the particles, the cleanness of the interface, and the magnitude and inhomogeneity of the internal stresses (such as thermal stresses) can adversely affect the ductility of the composite [92]. It has been frequently observed that the large size of the TiC particle enhances the role of particles as stress raisers during mechanical loading, and promotes premature failure of TMCs via particle cracking. Decreasing the size of particles, consequently can lead to substantial improvement in mechanical performance of TMCs [7].

Part of the research performed in this study is on oxidation and wear behaviour of TMC which is then compared to wear behaviour of oxidized TMC samples. A brief

description of the wear behaviour of TMCs is therefore given in section 2.2.2.1, while Section 2.2.2.2 focuses on the oxidation behaviour of TMCs.

2.2.2.1 Wear Behaviour of TMCs

It has been frequently reported that the volume fraction of the reinforcement must be higher than a critical amount in order to make a considerable improvement in the wear resistance of a Ti matrix. This critical amount for Ti-6Al-6V—2Sn/TiC, Ti6Al-4V/SiC [10] fabricated by cold and hot isostatic pressing (CHIP), Ti/TiC and Ti/TiB_2 (fabricated by cold isostatic pressing and vacuum sintering [93]), Ti-6Al-4V/TiC (fabricated by direct laser method) [11] was reported to be in the range of 15-20 Vol.%. This is believed to be the result of particle precipitation along the grain boundaries at the lower volume fractions, which leaves the soft grain of Ti or its alloy unprotected [11,12].

Poletti et al [10] studied the wear behaviour of TMC pins against 52100 steel disks and suggested the wear mechanism map illustrated in Figure 2.19 (a). The tests were performed under normal pressure of 0.6-4.8 MPa and the sliding speed from 0.1 to 1.5 m/s. The wear rate map was obtained as the 3D interpolation of the experimental values. They observed that there is a limit of pressure and sliding distance where the composites lose their wear resistance due to the debonding of the particles, and the wear loss values become higher than those of the matrix. The wear mechanism observed at low load and sliding speed was tribochemical wear, induced by the formation of a lubricant layer of iron oxide resulting from the abrasion of the counterface by TiC particles. At the highest load and sliding speed (zone *IV*), abrasion was observed on both surfaces resulting from the debonded particles which act as third-body abrasives. Zone *IIIa* also presents debonding of the particles, but here the high speed breaks the oxide layer, while in zone *IIIb* the high speed breaks the oxide layer [10]. The wear process in zone *I* is compare with zones *IIIa* and *IIIb* in Figure 2.19 (b) and (c), respectively.

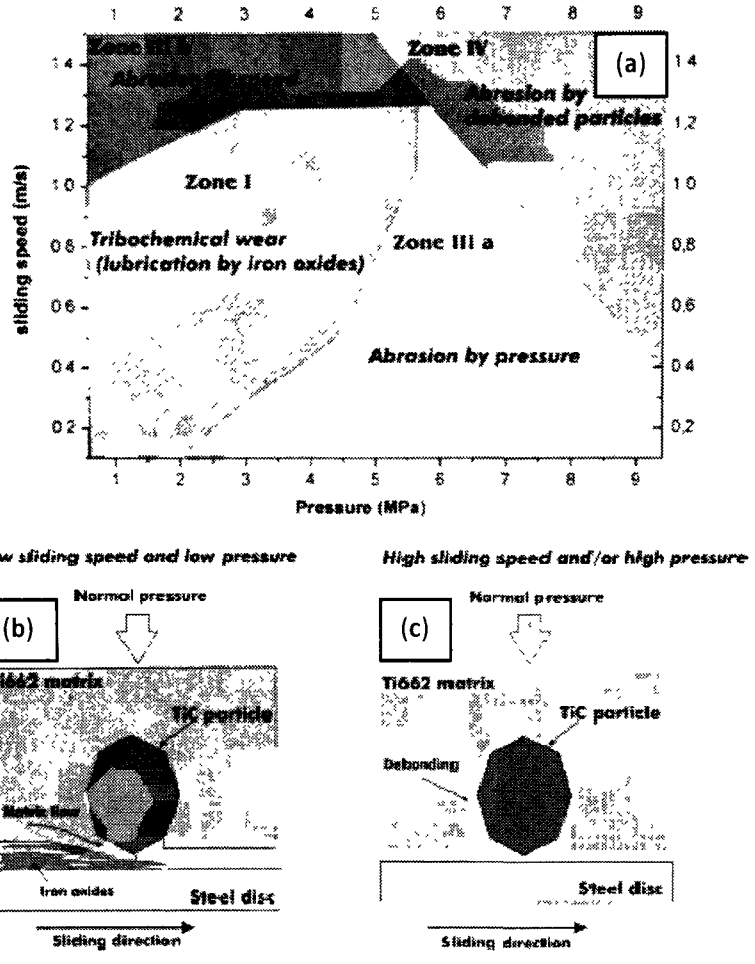

Figure 2.19. (a) Wear mode map for the dry sliding of Ti662/TiC on 52100 steel in the pin on disk configuration [10]. The schematic illustration of the material removal by abrasion process (b) with oxides and (c) without iron oxides are also shown.

Other researchers observed also the abrasion of the steel counter face by TiC particles followed by oxidation of iron, which can either lubricate the contact interface or in turn cause more abrasion, depending on load and velocity. Broken or extracted TiC particles particularly in a low volume fraction of reinforcements induced higher abrasion and increased the wear rate over the Ti alloy matrix [11,94]. It must be noted that comparisons of the reported wear rates and mechanisms must be made cautiously, since dissimilar interfacial bonding strengths can be caused by various fabrication methods employed.

2.2.2.2 Oxidation Behaviour of TMCs

This section reviews the existing literature regarding the oxidation of TMCs. To clarify the effect of incorporating TiC particles into the Ti matrix, the principles of TiC oxidation are provided initially, followed by the oxidation behaviour of Ti-TiC composites.

Oxidation of TiC

Titanium carbide, like the carbides of the other early transition metals, has a NaCl type structure [95]. The oxidation of TiC powder or sintered pellets in dry oxygen happens according to the following chemical reaction:

$$1/2TiC + O_2 \rightarrow 1/2TiO_2 + 1/2CO_2 \qquad \text{Equation 1.7}$$

Oxidation begins at 320°C, with a rate that increases as the temperature increases, but the acceleration is only considerable at temperatures higher than 1000°C [96,97]. The oxidation of TiC occurs parabollicaly under intermediate oxygen pressure (several to 100 KPa) and temperatures of 600-800°C, in contrast to linear oxidation, which is observed at high temperatures and oxygen pressures [96,97]. Lavrenko et al [96] studied the Arrhenius plots of *Ln(k)* vs. *1/T*, and observed a change in their slops at temperatures around 800-900 °C, while Shimada et al [97] observed the same change within temperature range of 410-450°C. They both correlated these changes to a change in the diffusion mechanism. The oxidation process at low temperatures is determined by the contribution of an inward diffusion of anions, accompanied by the outward diffusion of carbon. At higher temperature, an ambi-polar diffusion of both titanium and oxygen ions is expected [96,97].

Lavrenko et al [96] studied the composition of the oxide layer that formed on titanium carbide pellets in oxygen within a temperature range of 600-1200 °C. The reaction product formed within temperatures lower than 800°C, consisted of a very thin, single layer of rutile and lower titanium oxides (Ti_2O_3), while at 900-1200°C, a two-layer scale of dense stoichiometric and porous non-stoichiometric rutile was formed [96]. In contrast, TiO, Ti_3O_5 and Ti_4O_7 oxide compositions were identified in the scale formed at

the early stages of TiC pellets oxidation at 410-450°C, as performed by Shimada et al [97]. An amorphous anatase scale was developed from the suboxides during continuous oxidation, followed by crystallization and subsequent cracking. In any case, formation of rutile rather than anatase was promoted by higher temperature oxidation [97].

An interesting phenomenon observed by the latter researchers was the formation of amorphous carbon layer as the TiC pellets oxidized in water, a process that should be associated with a low oxygen pressure at the reaction interface that cannot oxidize the carbon component of TiC, but does oxidize Ti [97].

The lattice constant of the TiC layer directly under the oxide scale is frequently observed to be less than that of the original unoxidized TiC [96,97]. Researchers have proposed that atomic oxygen can be substituted for the carbon present in the interstitial vacancies of the TiC lattice, forming oxicarbides according to the following chemical reaction:

$$TiC + O_2 \rightarrow Ti(C_xO_y) \qquad \text{Equation 1.8}$$

Therefore, the observed lower lattice constant and the parabolic character of the oxidation were attributed to the dissolution of oxygen in the lattice, and the formation of oxicarbides [96,97].

Oxidation of TiC reinforced Ti

A number of studies have been performed on the in-situ produced TiC as well as the TiC and TiB reinforced Ti composites, in order to characterize their high temperature performance [13-17]. The oxidation behaviour of in-situ produced 5 and 8 vol.% TiC/Ti within 550-650 °C, 10 vol.% TiC/Ti-6Al within 600-800 C and 5 and 8 vol.% TiC+TiB/Ti6242 within 550-650 °C obeyed a parabolic law. The activation energy obtained from the Arrhenius plots was within 249-256 KJ/mol for these TMCs which was slightly higher than that of pure Ti (239 KJ/mol) but much lower than that of TiC powder (837 KJ/mol) [13,14,16,97].

The oxidation behaviour of TiC has been discussed in the previous section where TiO_2 and carbon oxide were the main oxidation products. Ti and Al oxidize according to the following chemical reactions [98]:

$$Ti + O_2 \rightarrow TiO_2 \qquad \text{Equation 1.9}$$

$$4/3Al + O_2 \rightarrow 2/3AlO_2 \qquad \text{Equation 1.10}$$

The Gibbs free energies corresponding to each chemical reaction are as follows:

$$\Delta G^o_{1.7} = -577464 + 85.02T \qquad \text{Equation 1.11}$$

$$\Delta G^o_{1.9} = -943500 + 179.1T \qquad \text{Equation 1.12}$$

$$\Delta G^o_{1.10} = -1115500 + 209.2T \qquad \text{Equation 1.13}$$

These equations reveal that the Gibbs free energies are negative at the temperatures studied so far indicating that these reactions are thermodynamically favourable to occur, but the Gibbs free energy for reaction (1.7) is obviously higher than for reactions (1.9) and (1.10). This difference should result in the preferential oxidation of Ti and Al in the composite, a result that is in complete agreement with results obtained by Y. Qin et al using high temperature, in-situ microscopy [14,16,17]. The latter studied the oxidation resistance of TiC/Ti and TiC+TiB/Ti6242 composites within a temperature range of 550-650 °C, and observed that the oxidation commenced at the crystal boundaries, followed by intra-crystalline oxidation and, lastly, the reinforcements were oxidized. Nevertheless, it is apparent that in any case the oxidation of the composite would be inhomogeneous.

Y Qin et al [14-17] explored the composition and morphology of the oxide scale that formed on the Ti/TiC, Ti/(TiC+TiB), Ti-7.26Al/(TiC+TiB) and Ti-6Al-2Sn-4Zr-2Mo/(TiC+TiB) composites within the temperature range of 550-650°C for 300 h. Partial oxidation of the particles with the formation of an outermost rutile scale was evidenced, as well as an aluminum rich layer laid on the rutile layer in the case of Ti-Al and Ti6242 matrices. Adding TiC to the Ti matrix decreases the coefficient of thermal expansion (CTE) for the whole TMC. As the CTEs of the scale and the substrate are closer, so the

thermal stresses would be lower and just as the plastic deformation of the scale is enhanced by the fine oxide grains formed on the TMCs, the growth and thermal stresses would be effectively released—avoiding cracking and spallation. Additionally, the in-situ TiC particles can act as vacancy annihilation sites. Consequently the oxide formed on TMCs was thinner and denser [14-17]. X. N. Zhang et al [13], however, did not observe the formation of an integrated scale on the whole surface of TiC-reinforced Ti-6Al at temperatures lower than 800°C. In the oxide islands that formed at 700°C, the composition included Ti, Al, O and carbon, while no carbon was found on the scale formed at 800°C [13].

The diffusion mechanisms responsible for the oxidation of TMCs have not been studied as comprehensive, although, based on the corrugated interface of the scale, Y Qin et al [16] concluded that the growth was promoted by the inward diffusion of oxygen anions.

2.3 Fracture Toughness Measurement Based on Indentation Techniques

The fracture toughness or critical stress intensity factor is a material property that is not affected by specimen dimensions or loading type. The oxide phases formed during thermal oxidation have substantially lower fracture toughness than the underlying substrate which can adversely affect the wear performance of the components [99]. A well-known method for estimating the fracture toughness of brittle materials is to measure the length of the cracks emanating from the corners of a sharp indenter. This method has several advantages: the specimen preparation is simple, it can be used on a wide range of sample sizes and the sharp indenter needed is usually a standard item [99,100].

There are two basic cracking modes that can result from the sharp indentation of brittle materials: radial and lateral cracks. Lateral cracks are side edge and side face circular cracks, while radial cracks start from the corner points of the indenter and are oriented perpendicular to the surface so that they can be classified into two groups. Palmqvist cracks start from the corners of the sharp indenter and propagate to a relatively low depth (Figure 2.20 (a)), while the radial-median cracks in Figure 2.20 (b) are much deeper cracks and derives from the subsurface median cracks, then extend into the

material in a semi-circular manner (half-penny shaped crack). Depending on the material, radial cracks are formed during indentation, or/and during relief, by the action of the residual stress field [100,101].

Palmqvist cracks are typically observed in brittle material in a low-load regime, while median cracks only formed at high loads. Studies also confirmed that the transition load depends on the toughness of the material, and for reasonably-tough materials like WC-Co composites with more than 6 Wt% Co, the radial cracks that formed at low to high loads were associated with Palmqvist cracks [102-104]. Numerous, semi-empirical equations relating material fracture toughness (K_{IC}) to measured indentation parameters like, load (P), indentation diagonal (a), crack length from the center of indentation (c), crack length from the corners of indentation (l) and some material properties like Young's modulus (E), Vickers hardness number (Hv) and Poisson's ratio (v) have been developed based on the experimental observations and/or theoretical considerations. A review of these models, which focuses on the radial-median and Palmqvist crack geometries, is provided in sections 2.3.1 and 2.3.2, respectively.

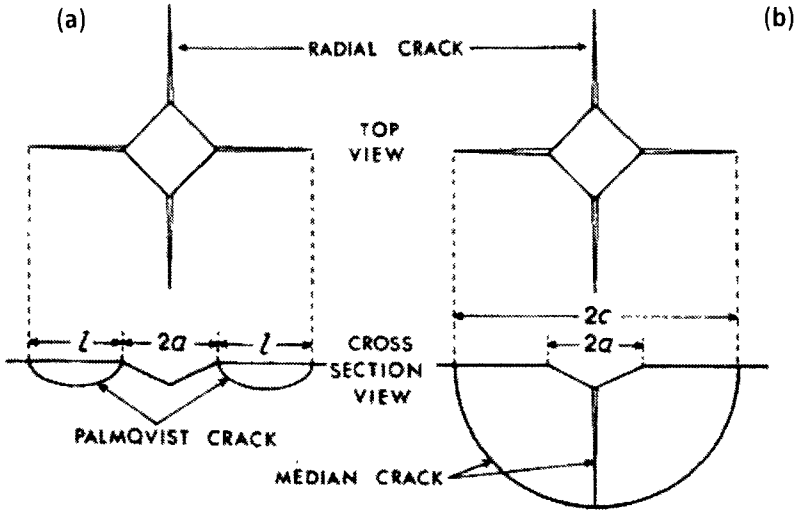

Figure 2.20. Schematic representation of geometries of two types of radial cracks, which include (a) Palmqvist and (b) median cracks observed around Vickers indentation [102].

2.3.1 Models Based on Radial Median Crack Geometry

Evans and Wilshaw [105] conducted a dimensional fracture mechanics analysis of indentation fracture mechanics and found the following equation:

$$\frac{K_{Ic}}{\sigma_Y a^{\frac{1}{2}}} = F_1\left(\frac{c}{a}\right) F_2\left(\frac{r_p}{a}\right) F_3(\vartheta) F_4(\mu) \qquad \text{Equation 1.14}$$

where σ_Y is the uniaxial yield stress, r_p is the indentation plastic zone radius and F_1, F_2, F_3 and F_4 are empirically determined functions. The validity of the proposed functional relationships was further investigated by Evans and Charles [106]. They assumed that the influence of v on c/a was not significant and that a dependence of μ on hardness was not likely. Assuming that r_p/a was proportional to a power function of E/σ_Y, they found the following equation:

$$\frac{K_{Ic}\emptyset}{H a^{\frac{1}{2}}} = F_1\left(\frac{c}{a}\right) F_2\left(\frac{E\emptyset}{H}\right) \qquad \text{Equation 1.15}$$

where $H/\sigma_Y=\Phi$ and $Hv=0.9272H$. The following equation was derived by taking $\Phi=2.7$:

$$K_{Ic} = 0.0824P/c^{3/2} \qquad \text{Equation 1.16}$$

Several other authors employed the Evans and Charles model (equation 1.15) and curve-fitted the fracture toughness data collected from other methods to the indentation test results to disclose numerous semi-empirical equations [100,107].

Evans [108] extended the elastic-plastic model of indentation fracture caused by a sharp indenter and resolved the elastic-plastic stress field into a reversible elastic component and an irreversible residual component. The residual component is derived from the wedging action of the deformation zone, and provides the primary driving force for the half-penny crack configuration. Based on this model, Lawn et al [109] derived the following equation, which is the most commonly used relationship for the formation of radial-median cracks:

$$K_{Ic} = 0.0139\left(\frac{E}{Hv}\right)^{\frac{1}{2}}(P/c^{3/2})$$ Equation 1.17

This equation was shown to be valid for $c/a > \approx 2$, and the constant 0.0139±0.002 was determined empirically. Anstis et al [110] modified equation 1.17 and found a value of 0.016±0.004 for the calibration constant.

2.3.2 Models Based on Palmqvist Crack Geometry

Niihara [102] proposed a model based on fracture mechanics in which he considered the Palmqvist cracks as semi-elliptical surface cracks that are mainly nucleated and propagated by unloading residual stress. Assuming that the maximum crack depth produced by the end of unloading is approximately in the order of the indentation depth, the following equation was derived:

$$K_{Ic} = 0.0122\left(\frac{E}{Hv}\right)^{\frac{2}{5}}P/(al^{\frac{1}{2}})$$ Equation 1.18

The results of this analysis confirmed the empirical equation formerly developed by Niihara et al [103], which was obtained by a best-fit-based on equation 1.14—where they found an empirical constant of 0.0089 instead of 0.0122 for equation 1.18. Shetty et al [104] carried out a fracture mechanics analysis based on the assumption that the Palmqvist cracks are two-dimensional through cracks rather than three-dimensional surface cracks, and derived the following equation:

$$K_{Ic} = 0.0319P/(al^{\frac{1}{2}})$$ Equation 1.19

The constant in this equation is calculated analytically and depends on the geometry of the Vickers indenter and the Poisson's ratio of the material. This equation does not require prior knowledge of the material's elastic modulus (E) and hardness. Another semi-empirical equation derived for Palmqvist cracks is the following equation, derived by Laugier [111]:

$$K_{Ic} = 0.0143\left(\frac{E}{Hv}\right)^{\frac{2}{3}}\left(\frac{a}{l}\right)^{\frac{1}{2}}\left(\frac{P}{c^{\frac{3}{2}}}\right)$$ Equation 1.20

Li et al [112] and Milekhine et al [113] compared the fracture toughness values calculated from the Vickers indentation with the values determined by conventional measurement methods and it confirmed that for the groups of materials studied (FeSi, FeSi2 and Mg2Si) and (α-SiC), both equations 1.18 and 1.19 give fracture toughness values in agreement with conventional measurement techniques.

Equations 1.14-1.19 suggest that the two crack system can be distinguished by load, P, and crack length, c or l, relationships—$c = AP^{2/3}$ for the median cracks and $l = BP$ for the Palmqvist cracks. These relationships provide the criterion for identifying the type of cracks formed under indentation. Shetty et al [104], Li et al [112] and Ponton et al [107] confirmed the applicability of this method through experimental observations, so that if an experimental plot of *ln P* versus *ln c* produces a slope between 1 and 2, radial-median cracks are expected, whereas if an experimental plot of *ln P* versus *ln l* gives a slope between ½ and 1, then Palmqvist cracks are expected.

It must be noted that the hardness value in the aforementioned fracture toughness equations is a material property and should be constant, while for the definition of hardness $Hv = 0.4636P/a^2$, there exists a dependence of the apparent hardness on the applied indentation load, which is known as indentation size effect (ISE) [114]. The physical basis of ISE is uncertain but it can be related to surface tension, crack formation, dislocation activity and elastic recovery [112]. Li et al [112] proposed a model to relate the true indentation hardness to the load and indentation size as follows:

$$P = \alpha_1(2a) + \alpha_2(2a)^2$$ Equation 1.21

where α_1 and α_2 are constants and α_2 is related to true hardness (H) by the following equation:

$$H = k\alpha_2$$ Equation 1.22

where k is a constant dependent on the indenter shape, k=1.8544. Incorporating the true hardness value of material into equations 1.14-1.19 provides a better correspondence between the fracture toughness values obtained by the indentation method and conventional measurement methods [112,114].

Marshal et al [115] analysed the effect of surface residual stress—caused by transformation toughening, surface preparation or the formation of a film on the surface—on the stress intensity factor for a radial-median crack configuration. They rewrote equation 1.17 as follows:

$$K = X\frac{P}{c^{\frac{3}{2}}} - 2m\sigma_R(\frac{c}{\pi})^{1/2} \qquad \text{Equation 1.23}$$

Equation 1.17 defines how in the first term, X is $0.016(\frac{E}{Hv})^{1/2}$, and in the second term—which represents the residual resistance force—m is a dimensionless modification factor whose value can be taken as unity when free-surface effects and stress gradients over the prospective crack depth are neglected. This model predicts that the indentation of a compressively stressed surface should lead to a linear plot of positive slope for ($P/c^{2/3}$) versus $c^{1/2}$ [115].The slope of this plot, however, depends on both the equation used to calculate K_{Ic} data, and the material. There is, additionally, no apparent relationship that defines the effect of surface residual stresses on the fracture toughness data calculated from the Palmqvist crack models [107].

In the case of a thin, brittle layer on a relatively tough substrate, many of the assumptions made in developing the aforementioned equations may not be entirely valid. In order to determine the fracture toughness of hard, brittle films on metallic substrates, many workers [116,117] utilized the equations based on the radial-median cracking mode, although this was not explicitly stated. D. Nolan et al [99] suggested that for thin, brittle films on tough substrate it is reasonable to assume that the Palmqvist morphology dominates as this type of cracking initiated at the surface where the material is more brittle, rather than at a depth [99].

2.4 Objective of This Study

This thesis investigates the tribological and mechanical behaviour of Ti-6Al-4V-10Vol%TiC fabricated by MIM method in an effort to evaluate this process as a cost-effective and near net shape method for incorporation of TiC particle. It has been observed that there is a limit of contact pressure where TMCs lose their wear resistance (section 2.2.2.1). This study, therefore, examines, in detail, the pressure dependence of the deteriorating role of TiC particles during sliding wear. As described in section 2.2.2.2, a number of studies have been performed on oxidation behaviour of TMCs to shed light on their high temperature oxidation resistance. The improvement in tribological behaviour of Ti-6Al-4V, on the other hand, has been achieved by thermal oxidation as described in section 2.2.1. This process, however, has never been adopted as a surface engineering method for improvement of tribological properties of TMCs. The following sections in this thesis will provide an understanding of the mechanical and sliding wear properties of Ti-6Al-4V-10Vol%TiC fabricated by MIM, followed by the oxidation behaviour of this alloy to illustrate whether or not it is beneficial to apply thermal oxidation on TMC samples.

Chapter 3

3 Materials and Experimental Procedures

3.1 Introduction

In this chapter the experimental methods and the materials used in this study are described. The mill-annealed Ti-6Al-4V—with a bimodal microstructure—was heat treated to obtain a Widmanstätten microstructure. The Widmanstätten and bimodal microstructures were thermally oxidized at 600°C for 65 h in order to study the effect of microstructure on oxidation behaviour of Ti-6Al-4V alloy. The optimum condition for oxidation of TMC samples was, additionally, determined based on thermal oxidation at various time and temperatures. The oxide characterization was performed by microstructural analysis, micro-indentation on the tapered cross-section, micro-scratch test, compositional analysis and measurement of fracture toughness by indentation crack length (ICL) method.

The sliding wear tests were performed using a ball-on-disk tester under different loading conditions. The methods used in sample preparation and in determination of wear rate are presented. Analytical methods to identify the wear mechanism and effect of oxide coating are also described.

3.2 Materials Tested

The alloys used in this study were mill-annealed Ti-6Al-4V, metal injection moulded (MIM) Ti-6Al-4V and metal injection moulded Ti-6Al-4V-10 Vol% TiC (TMC). Titanium carbide was selected as the ceramic reinforcement due to their good thermal stability and chemical compatibility with Ti matrix [10]. Chemical composition in weight of the mill-annealed alloy provided by the supplier (GoodFellow Corporation) is listed in Table 3.1. The as-received material was in the rod form with 25mm diameter and 200 mm length with a bimodal microstructure which details are described in section 3.2.2. In order to generate a Widmanstätten microstructure, the as received samples were heat treated. The details of the heat treatment are given in section 3.2.1.

The MIM samples were provided by CANMET/MTL. The raw materials for Ti-6Al-4V samples were a mixture of a gas atomized pure Ti powder and a 60Al40V master alloy powder; both powders were less than 45 μm with a wide size distribution. TiC powder with an irregular shape and size range from 1 to 10μm was used as reinforcement for the Ti-6Al-4V-TiC composite. In this method, metal powders were first mixed with a wax-based binder system in a Tumbler mixer for 30min and then hot mixed in a twin-screw extruder at 130°C to produce the feedstock. The feedstock was then heated and injection moulded with a 35 ton injection moulding machine at 135°C to form green tensile samples. After moulding, the binder in the green samples was removed by a debinding process under the vapour of Heptane for 5 hours and most of the backbone polymers were burnt out by heating the samples after solvent debinding to 400°C for 1 hour under flowing feedstock Argon. Eventually, the debound samples were sintered in a tube vacuum furnace under vacuum range of $2-3\times10^{-6}$ torr at the temperature of 1250°C for 2 hours. The MIM samples were in the form of coupons with 13.5mm radius and 3.5mm thickness.

Table 3.1. Composition of mill-annealedTi-6Al-4V as provided by the supplier (GoodFellow Corporation)

Element	Al	V	Fe	C	H	N	O	Ti
Weight %	6	4	0.003	0.0022	0.001	0.001	0.0065	Balance

3.2.1 Heat Treatment Procedure to Obtain Widmanstätten Microstructure

The mill-annealed Ti-6Al-4V in the form of rod was cut perpendicular to the cylinder axis into coupons with 5mm thickness. The coupons were then encapsulated in a quartz capsule under vacuum of 10^{-4} torr to prevent oxidation of Ti-6Al-4V during heat treatment. The β-transus temperature of this alloy is in a range of 982-993°C [118]. The encapsulated samples were then subjected to a heat treatment at 1050°C for 80 min followed by air-cooling (~ 52°C/min). Therefore, the annealing treatment was performed in the β-phase field to change the as-received bimodal (α+β) structure to β phase. The cooling rate controls the size of the microstructural features such as α-colony size or the

length of α-plates. The cooling rate also determines the change from a Widmanstätten to a martensitic structure, and in order to avoid the nose of the CCT diagram the rate of cooling should be lower than 1000°C to prevent the formation of any martensitic structure [23]. The formation of martensitic structures was then avoided by air-cooling since the presence of α′ or α'' would add to the complexity of the diffusion problem in the oxidation step.

3.2.2 Microstructure Observation

Three types of samples were prepared for microstructure evaluation, which were mill-annealed Ti-6Al-4V, heat treated Ti-6Al-4V and TMC samples. The samples were wet ground using SiC abrasive papers from 240 grit size to 4000 grit size. After grinding, polishing was performed using 0.1 and 0.05 μm alumina suspensions on rotating polishing wheel covered by microcloths. Finally, after polishing, the samples were etched by immersing in Kroll's solution which consisted of 2 ml HF, 4.5 ml HNO_3 and 100 ml H_2O. The immersion time was between 10 to 20 seconds. Microstructural observation of the polished surface was performed under a JEOL scanning electron microscope. The SEM micrographs of the Ti-6Al-4V microstructures, which correspond to bimodal and heat treated samples to give a Widmanstätten microstructures, are shown in Figure 3.1 (a) and (b), respectively. The recrystallized equiaxed primary α together with the recrystallized β phase, i.e. $(\alpha+\beta)_p$, as well as the lamellar α+β colonies are marked on the SEM micrograph of bimodal microstructure (Figure 3.1 (a)). Figure 3.2 illustrates the microstructure of the TMC samples. The micrograph shows the TiC particles within the equiaxed and plate-like α+β phase together with intergranular β phase. The volume fraction of the micro-pores was 5-6 Vol% as measured by image analyzing techniques. The majority of pores were concentrated at the particles/matrix interface.

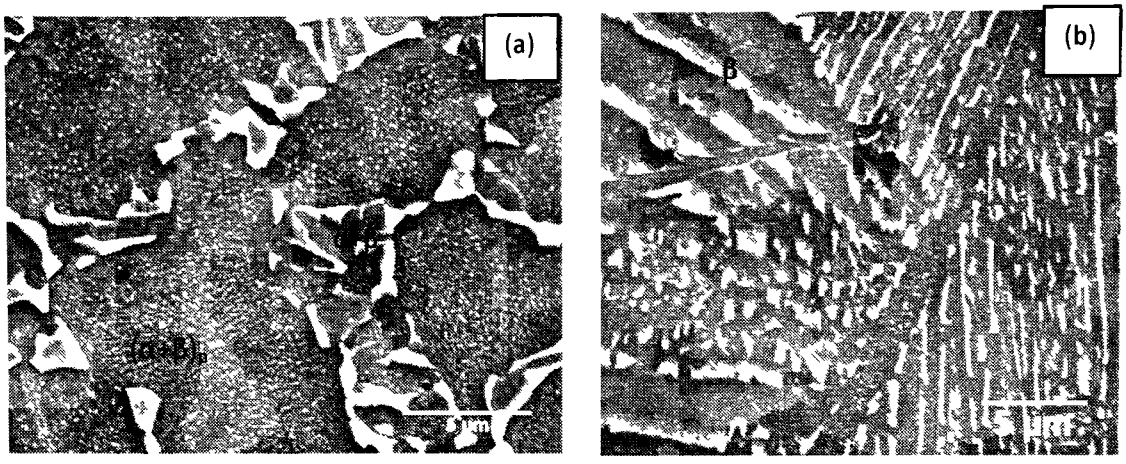

Figure 3.1. The SEM micrograph showing (a) bimodal and (b) Widmanstätten microstructures of mill-annealed Ti-6Al-4V sample. The lamellar α+β colonies together with the recrystallized α and β ($(\alpha+\beta)_p$) phases are marked.

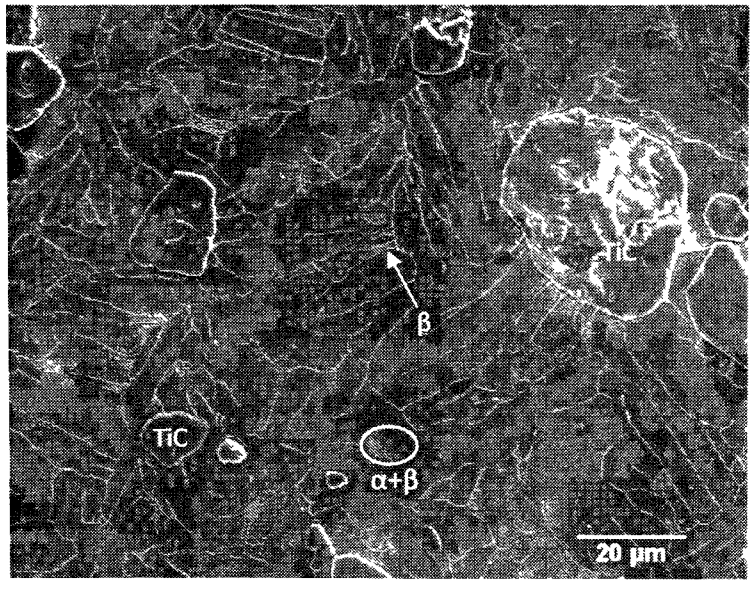

Figure 3.2 The SEM micrograph of the mirror-polished and etched surface of TMC sample. The intergranular β phase and the recrystallized α+β phases are marked.

3.3 Thermal Oxidation Procedure

Thermal oxidation process was performed on Ti-6Al-4V and TMC samples. The condition of TO process—described in section 2.2.1—was adopted for oxidation of Ti-6Al-4V samples. Whereas, due to the effect of TiC on oxidation resistance of TMCs [96,97], the optimum condition to achieve an adherent oxide on TMC substrate had to be

decided. Sample preparation process and the oxidation process for both types of material are described in this section.

3.3.1 Sample Preparation for Thermal Oxidation Process

The samples prepared for the oxidation process were in the form of coupons. The diameter of the mill-annealed Ti-6Al-4V and the TMC samples were 25 and 27 mm, respectively. The specimen surfaces were wet ground using SiC abrasive papers progressively from 240 to 2400 grit. This procedure resulted in an average surface roughness 0.04 μm for Ti-6Al-4V and 0.4 μm for TMC samples as measured by an optical profilometer. The average height distribution of the TiC particles over the Ti-6Al-4V matrix was 1.25 μm. The samples were then rinsed with ethanol, washed ultrasonically for 6 min in acetone and dried in hot air prior to the oxidation process.

3.3.2 Thermal Oxidation Process

Isothermal oxidation was conducted in an electric muffle furnace with static ambient atmosphere. The Ti-6Al-4V samples were oxidized at 600°C for 65 h followed by cooling in the furnace. The condition of the thermal oxidation process is adopted from the literature where it is suggested that the most adherent oxide with optimum corrosion resistance and dry and lubricated wear resistance can be produced. Higher temperatures produce poorly adherent oxide and at lower temperatures formation of a continuous, relatively thick oxide for tribological purposes is not observed [3-5,56,64].

TMC samples were thermally oxidized in the same furnace at 600 and 800°C for 20 min, 20 h and 60 h followed by furnace cooling. These temperatures were chosen as Qin et al [14-16] observed formation of a continuous oxide on TiC/ Ti-6Al-4V, TiC+TiB/ Ti, TiC+TiB/Ti-Al and TiC+TiB/Ti6242 composites within the temperature range of 550-650°C, While Zhang et al [13] did not observe formation of an integrated scale on the whole surface of TiC reinforced Ti-6Al at temperatures lower than 800°C. The quality of the oxide scales formed was investigated by several experimental methods, which are described in detail in section 3.4. The optimum oxidation condition was decided to be at 800°C for 20 min.

3.4 Oxide Characterization Procedures

In order to characterize the composition, mechanical properties and microstructure of the oxide and oxygen diffusion layer (ODZ) formed during thermal oxidation process; several tests were performed on the oxidized Ti-6Al-4V and TMC samples which are described in this section.

3.4.1 Compositional Analyses by X-ray Diffraction Method

A Rigaku DMAX-1200 X-ray diffractometer with Cu K_α radiation was used for phase identification of the oxidized surface. The glancing incidence XRD technique was used with an incident beam angle of 2° The diffraction angle (2θ) was between 10°and 150°and the scanning step was 0.02° for counting time of 1s at each step. The data were collected by a computer and the possible matches were analyzed by the software. It should be noted that the oxide scale was not detached from the substrate for the purpose of XRD analysis and the test was performed on the oxidized coupons, therefore X-rays can penetrate the Ti-6Al-4V or TMC substrate.

3.4.2 Microstructure Observations

Microstructural examinations were conducted by a JEOL and a FEI Quanta 200 FEG scanning electron microscope on the cross-sections of the oxidized samples. In order to measure the oxide and ODZ thickness and evaluate the oxide/substrate interface, samples of the cross-sections of oxidized Ti-6Al-4V and TMCs were cut perpendicular to the oxide surface. The cut surface was at a distance remote enough from the edges of the coupon to exclude the effect of sideway diffusion. The cut samples were Ni-doped coated prior to metallographic preparation, in order to preserve the oxide scale. The solution used was the standard electroless-Ni solution in which the samples were immersed at 90 °C for 45 min. In order to make the samples conductive, the oxidized samples were gold-sputtered prior to Ni-Coating procedure. Finally, the cross-sections were prepared using conventional metallographic methods for Ti alloys mentioned in section 3.2.2 and etched using Kroll's reagent.

3.4.3 Hardness Measurement on Tapered Subsurface

To facilitate the precise microhardness measurements for evaluating the thickness of ODZ layer, the oxidized specimens were taper-sectioned by grinding and polishing. For this purpose, the oxidized samples were glued to an Al stand which is shown in Figure 3.3. The top face of the stand was cut at an angle of about 5.7° which provides a 10 times magnification of the subsurface zone. The sample accompanied with the stand was then mounted and polishing was started from the top face of the sample, as depicted in Figure 3.3.

The microhardness measurements were performed on the tapered sections of bimodal and Widmanstätten Ti-6Al-4V and TMC samples utilizing a Micro-Combi CSM instrument with a diamond Vickers indenter. The elastic modulus and Poisson's ratio of the indenter were 1141 GPa and 0.07, respectively. The instrument allows the measurement of the evolution of force as a function of penetration depth during the indentation process. The elastic modulus and hardness of the material can be estimated from the slope of the unloading curve calculated by Oliver and Pharr method (Appendix A) [119]. The maximum indentation load used was 400 mN with loading and unloading rates of 800 mN/min and an average of 5 indentations were performed at each depth. The Poisson's ratio of the coating was assumed to be 0.3.

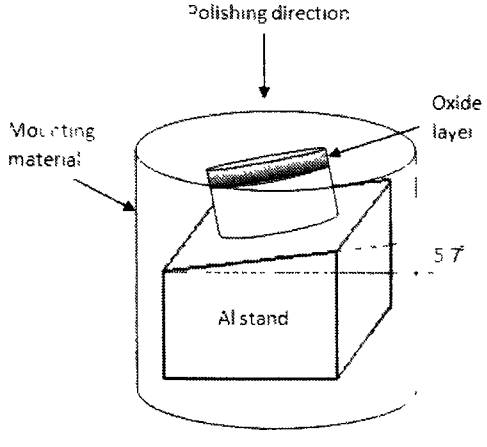

Figure 3.3. Schematic representation of the Al stand cut at an angle of 5.7° with the oxidized sample placed on top; the top arrow shows the direction of grinding and polishing.

3.4.4 Micro-Scratch Test on the Oxide Surface

In order to evaluate the oxide coating formed and also the composite samples single pass scratch tests were performed on Ti-6Al-4V, TMC sample, Ti-6Al-4V sample oxidized at 600 for 65h (TO process), TMC sample oxidized at 600 for 65 h (TMC-6-65h) and TMC sample oxidized at 800 for 20 min (TMC-8-20min). The two latter oxidation conditions were selected based on the cross-sectional microstructural evaluations explained in section 3.4.2.

The surfaces of the TMC and Ti-6Al-4V samples were mirror-polished using the aforementioned conventional metallographic techniques and washed ultrasonically in acetone for 6 min prior to the scratch test. The surface of the oxidized samples were washed and rinsed with acetone and dried in hot air. A single pass scratch test was performed on each sample under progressive load of 1 to 20 N with a loading rate of 6 N/min and the scratch length of 6mm. A Micro-Combi CSM instrument was used which allowed the friction force and the penetration depth to be recorded. The diamond sliding stylus was a micro-Rockwell type indenter of 200 μm tip radius. Characteristic features of the scratch grooves were revealed by a JEOL scanning electron microscope.

3.4.5 Measurement of Fracture Toughness by Indentation Crack Length (ICL) Method

In order to compare the fracture toughness of the oxide scales formed on TMC-6-65h and TMC-8-20min samples indentation crack length method was adopted. The surface of the samples were rinsed with acetone and dried in hot air prior to the indentation tests. A Micro-Combi CSM instrument with a diamond Vickers indenter was utilized to perform indentation at maximum loads of 0.75, 1, 1.25, 1.5, 1.75, 2 and 3 N. An average of 30 indentations was made at each load and the details of each indentation were studied under a FEI Quanta 200 FEG scanning electron microscope. The indentation marks which were relatively symmetric and adequately far from the TiC particles were selected for crack length measurements. The crack lengths from the corners of the indentation mark (l), the crack lengths from the center of the indentation marks (a), and the indent half diagonal were measured by Omnimet image analyzing software. The

measured values were used to determine the type of cracking and the fracture toughness of each oxide coating as described in section 2.3.

3.5 Tensile Testing Procedure

Tensile tests were carried out by CANMET/MTL to evaluate the bulk mechanical properties of Ti-6Al-4V and TMC samples prior to any further surface evaluations. The tensile samples were fabricated by a metal injection moulding process. The tests were performed at three different temperatures of 25°C, 250°C and 400°C. The 25°C tests were performed at a stain rate of $6.6 \times 10^{-5} s^{-1}$ and the 250°C and 400°C tests were run at a strain rate of $1.3 \times 10^{-4} s^{-1}$ An average of 5 tests was performed at each condition which was continued up to the fracture of the tensile samples. The load and elongation of the samples were recorded during the test and the yield strength, the ultimate tensile strength and the final elongation of the samples were reported after each test.

3.6 Laboratory Wear Testing Procedure

3.6.1 Description of Ball-on-Disk Tribometer

The dry sliding wear tests were carried out on a Universal Micro-tribometer using ball-on-disk configuration as shown in Figure 3.4 (a). The tribometer consist of a 2D force sensor and a precision spindle. The ball counterface is mounted to the force sensor (marked as "1" in Figure 3.4 (a)) using a stainless steel ball holder (marked as "2" in Figure 3.4 (a)). This sensor senses the vertical or loading force and the lateral drag or friction force. The loading force sensor is used as feedback for the vertical carriage positioning system to maintain a constant loading force. The combination of loading force and friction are used to calculate the coefficient of friction. Mounted to the force sensor is a suspension (marked as "3" in Figure 3.4) which allows the upper specimen to follow variations in the height of the lower specimen as it rotates. The precision spindle rotates the disk (marked as "4" in Figure 3.4 (a)) at adjusted velocity. The apparatus has a PC-based motor-control and data acquisition.

The tribometer comprises a removable plastic chamber (marked as "5" in Figure 3.4 (b)) which can be installed around the force-sensor and spindle chamber to isolate the

test configuration from the surrounding environment and run the tests under controlled environment condition as shown in Figure 3.4 (b). The disk chamber is connected to a humidifier and dehumidifier system which is capable of controlling the relative humidity (marked as "6" in Figure 3.4 (b)). Wear tests were performed at ambient condition, i.e. room temperature and 40% controlled relative humidity and using normal loads of 2, 3.5, 5, 7 and 10 N. During the test, the disk sample was rotated at 477.5 rpm, which yielded a linear velocity of 0.3 m/s at the periphery of the 6mm radius wear track. Each test involved a total sliding distance of 1000m, which proved to be sufficient for the attainment of a steady-state situation in all tests.

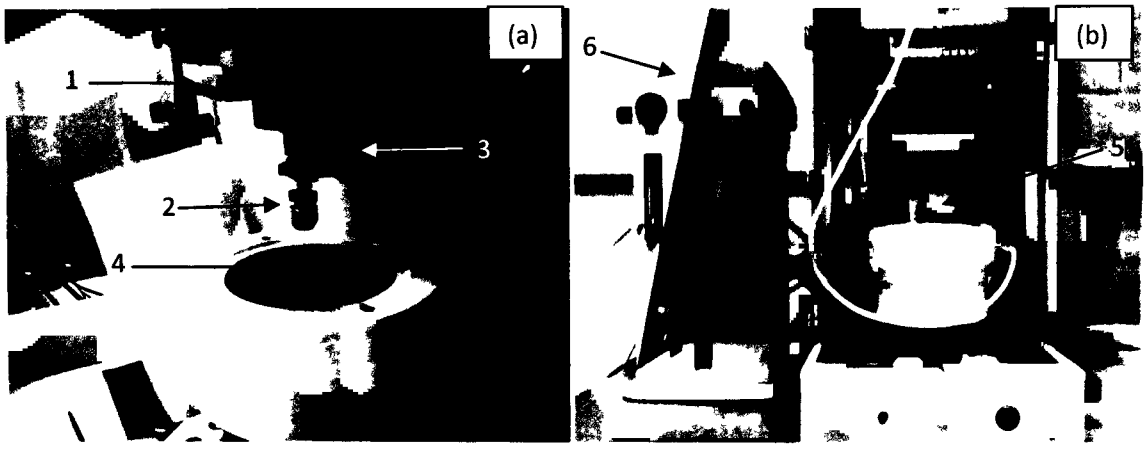

Figure 3.4. Photographs showing (a) the ball-on-disk Universal Micro-Tribometer (b) the humidity chamber; "1" is the force sensor, "2" is the stainless steel ball holder, "3" is the force suspension, "4" is the disk sample, "5" is the humidity chamber, and "6" is the humidity controller.

3.6.2 Wear Test Sample and Counterface Preparation

The MIM-fabricated Ti-6Al-4V and TMC samples were tested in as polished condition using the conventional metallographic techniques described in section 3.2.2. This resulted in an average surface roughness of 0.04 and 0.4 μm for Ti-6Al-4V and TMC samples as measured by optical surface profilometery. The TMC-8-20min samples were tested in the oxidized state without further polishing.

The counterface material was 6mm diameter chrome-steel (C/S) ball which chemical composition in weight is given in Table 3.2 as provided by the supplier. The Vickers hardness of the chrome-steel balls was 700 HV Prior to wear test the C/S balls

and the un-oxidized disks were degreased and washed ultrasonically in acetone for 6min and dried in hot air, while the oxidized samples were only rinsed with acetone in order to avoid any deteriorating effect of ultrasonic washer on the oxide coating.

Table 3.2. Composition of the Chrome-Steel counterface balls

Element	C	Mn	Si	P	S	Cr	Fe
Atomic %	0.95-1.10	0.2-0.45	0.25-0.35	0.25 Max	0.25 Max	1.30-1.60	Balance

3.6.3 Measurement of the Wear Loss

The wear loss of Ti-6Al-4V and TMC and oxidized TMCs were measured base on both mass loss and changes in the depth of the wear track. The tested samples were rinsed with acetone to remove any loose debris. The weight of every coupon and ball were measured using a high precision scale (10^{-5} g) before and after the wear test. At least three tests were carried out for each set of conditions and the average value was taken for the calculation of mass loss. The measured mass loss was converted to volume loss using the density of each sample. The material removed from the oxidized sample was mainly rutile and therefore the density of rutile type of TiO_2 (i.e. 4.26 gcm^{-3}) was used to calculate the volume loss in the case of the TMC-8-20minh samples. The volume loss values were divided by the total sliding distance, i.e. 1000 m, to obtain the amount of wear rates. The wear rates were also measured using the suspension mounted to the force sensor of the tribometer which allowed the height of the lower specimen in relation to the upper ball to be recorded during the wear test. Therefore, it was possible to trace the changes in the depth of penetration of the ball into the disk samples as the sliding proceeded. The volume loss of the samples (V) were calculated using the values of depth change by means of the following equation according to ASTM G99

$$V = 2\pi R\, r^2 \left(\theta - \frac{sin2\theta}{2}\right) \qquad \text{Equation 3.1}$$

where r is the radius of the ball, i.e. 3mm, and R is the radius of the wear track, i.e. 6mm and θ is the half angle of the wear track which is given by the following equation:

$$\theta = cos^{-1}(\frac{r-d}{r})$$ Equation 3.2

where d is the depth change given by the machine. In order to measure the wear rate based on the depth data, the measured volume loss values were plotted against sliding distance. According to the definition of wear rate given in section 2.1.6.1 the slope of these plots yielded the value of wear rate at each load.

3.6.4 Examination of the Worn Surface, Cross-Sectional Subsurface and Wear Debris

The morphology of the worn surface, the mirror-polished cross-sectional subsurface and the wear debris were elucidated using a JEOL scanning electron microscope equipped with an energy dispersive spectroscope (EDS). Before examination in the SEM, the worn surface of the samples was rinsed with acetone. The surface and subsurface layers were also examined microscopically on cross-sectional samples. For this purpose, the worn samples were cut parallel to the sliding direction and Ni-doped coated prior to metallographic preparation in order to preserve any layer on the surface. The coated samples were then mounted and mirror-polished. The details of the metallographic preparations and Ni-coating procedure are given in section 3.2.2.

Chapter 4

4 Results

4.1 Introduction

In this chapter the results of thermal oxidation performed on bimodal and Widmanstätten Ti-6Al-4V, and TMC samples along with the tensile test and the wear test are presented. Ti-6Al-4V samples were oxidized at 600°C for 65 h, which has been designated as TO-condition by Dong et al [5]. SEM observations (section 4.2.1) as well as micro-indentations (section 4.2.2) were performed on the oxide cross-sections. These observations confirmed the similar nature of oxide and oxygen diffusion zone formed on both microstructures. The EDS mapping results, presented in section 1.1.1, together with the X-ray analysis, given in section 4.2.3, confirmed that an alumina layer is formed at the gas/oxide interface. The micro-scratch test results are described in section 4.2.5, which confirmed the outstanding adherence of coating to the substrate.

Prior to any surface characterization and surface treatment, tensile tests at various temperatures (25-400°C) were performed on TMC and Ti-6Al-4V samples to characterize the mechanical properties of the bulk material (section 4.3). TMC samples were thermally oxidized at various temperatures and durations of time. Based on the adhesion strength, morphology and mechanical properties of the oxide scale the optimum oxidation condition was determined (section 4.4). The ball-on-disk configuration was adopted to perform wear tests on Ti-6Al-4V, TMC and thermally oxidized (TO)-TMC samples. The wear rate measurements and SEM observations on worn surface, subsurface and wear debris of TMCs and TO-TMCs are presented in sections 4.5.1 and section 4.5.2 respectively. The ball-on-disk tests performed on TO-TMC samples revealed that this surface treatment significantly improved the tribological behaviour of TMC samples.

4.2 Thermal Oxidation of Ti-6Al-4V Alloy

In this section the results of thermal oxidation (TO) process performed on Ti-6Al-4V alloy are presented. The main aim of these experiments was to evaluate the oxide composition, mechanical properties and the diffusion mechanisms that are responsible for

the formation of oxide scale and ODZ. The mill-annealed bimodal samples were heat treated under vacuum at 1050° C for 80 min and then air-cooled to form Widmanstätten microstructure. The heat treated microstructure is illustrated in Figure 3.1. Thermal oxidation was performed in an air furnace at 600°C for 65 h followed by cooling in the furnace. The oxide scale formed was characterized by SEM observation of the cross-section, micro-indentation on tapered cross-section, X-ray diffraction, and micro-scratch test on the surface under progressive normal load. The results of these experiments are discussed in the following sections.

4.2.1 SEM Observation of the Oxide Cross-Section

The SEM micrographs of the cross-section of the oxide scale formed on bimodal and Widmanstätten samples are shown in Figure 4.1 and Figure 4.2 respectively. The cross-sections were prepared by conventional metallographic methods. The thickness of the oxide scale and the oxygen diffusion zone (ODZ) were measured by Ominimet image analyzer at least at 20 points and the average of the measured valued together with their standard deviation values are tabulated in Table 4.1. The ODZ layer is defined as the zone within which the recrystallized equiaxed β (β_p) is transformed into α since oxygen is a strong α-stabilizer that increases the β-transus temperature as shown in O-Ti phase diagram in Figure 2.16. However as can be seen in these figures a fraction of the lamellar β phase is retained in ODZ layer despite of the oxygen dissolution. Pitt and Ramulu [87] observed that diffusion occurs simultaneously through the α and β grains and along phase boundaries. However, the existence of retained lamellar β phase in Figure 4.1 and Figure 4.2 verifies faster diffusion along equiaxed α+β compared to lamellar α+β. The thicknesses of the oxide scale and ODZ formed on both microstructures were, however, similar. The thickness of the ODZ zone and the hardening effect of oxygen dissolution were studied by micro-hardness test on tapered cross-section which is described in section 4.2.2.

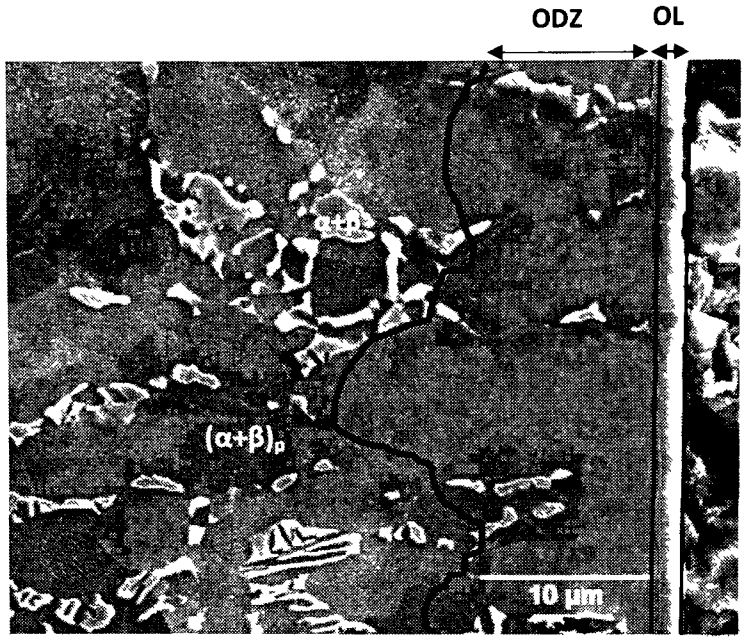

Figure 4.1. Cross-sectional SEM micrograph of Ti-6Al-4V sample with a bimodal microstructure oxidized at 600 C for 65h showing the oxide layer (OL) and the oxygen diffusion zone (ODZ) established as a result of oxygen dissolution.

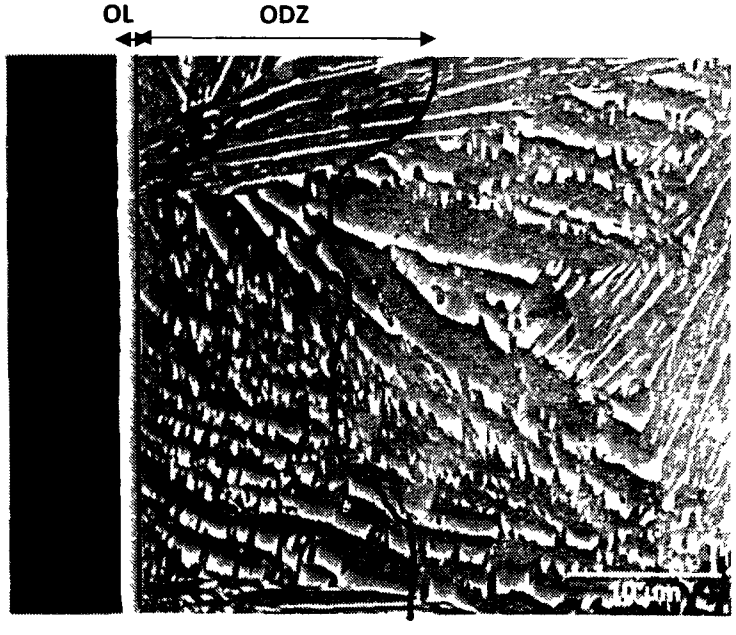

Figure 4.2. Cross-sectional SEM micrograph of Ti-6Al-4V sample with a Widmanstätten microstructure oxidized at 600 C for 65h showing the oxide layer and the oxygen diffusion zone (ODZ) established as a result of oxygen dissolution.

Table 4.1. The thickness of oxide and ODZ layers as measured from the SEM micrographs

Microstructure	Thickness of oxide scale (μm)	Thickness of ODZ (μm)
Bimodal	1.7±0.3	16.4±3.8
Widmanstätten	1.3±0.1	16.9±3.6

4.2.2 Micro-Indentation on Tapered Cross-Section

The tapered cross-sections were polished at an angle of 5.7° to the oxide surface as shown schematically in Figure 3.3 and provided a 10 times magnification in the cross-section. A series of micro-indentation tests were performed on the tapered cross-sections of oxidized bimodal and Widmanstätten samples, starting at 5μm distance from the interface, with a 5 μm step and a total distance of 60 μm. The indentation load was 400 mN with an average of 5 tests at each distance. The hardness values were calculated from the load-penetration depth data utilizing Oliver and Pharr method [119] according to Appendix A. The variations of the measured microhardness of both microstructures as a function of depth below the oxide/ODZ interface is shown in Figure 4.3. The microhardness plot depicted the gradual decrease of surface hardness through the bulk material where the depth of the ODZ can be estimated as 17 μm for both microstructures. This in agreement with the results of the microscopic depth measurements conducted on the cross-sections (Figure 4.1 and Figure 4.2). The ODZ is defined as the depth where the hardness-depth plot levels out and becomes equal to the bulk hardness. The hardness of bimodal and Widmanstätten samples adjacent to the interface (at a 5μm distance) were 989 and 1072 (Hv). This higher hardness for Widmanstätten samples was observed over the whole range of distances studied which can be explained in terms of the hardening effect of the martensitic structure formed during heat-treatment within β-phase field [1], which is described in section 2.1.3.

One of the most effective solid solute atoms in titanium is oxygen. The highest concentration of oxygen in the solid solution occurs at the area adjacent to the oxide interface where the microhardness of both microstructures were measured to be around twice as high as the bulk hardness. The solid solution strengthening of oxygen is explained in section 2.2.1.1 in terms of the increase in the critical resolved shear stress of

slip planes [28] and hindrance of twining [26,77]. Based on the interaction of oxygen interstitials with dislocations, several mechanisms are proposed to explain the strong strengthening effect of oxygen interstitials, some of these mechanisms are: i) the asymmetric core structure of $\langle a \rangle$-type screw dislocations induced by oxygen solute atoms [26], ii) the ordering of oxygen atoms and the oblate geometry of octahedral sites with the concomitant tetragonality strains (the lattice defects with tetragonality strains interact with the shear part of the stress field of a dislocation to give rise to large interactions with both screw and edge dislocations) [69], iii) the partial covalent characteristics of the oxygen solid solution and the associated interaction with dislocations with electrical dipole [28], and iv) the long-range ordering of oxygen observed at higher than 22.5 at% preceded by short range ordering in more dilute solutions [68,76]. In any case, the high strength of the ODZ can provide an excellent support for the oxide scale laid on top of it during any type of sliding contact.

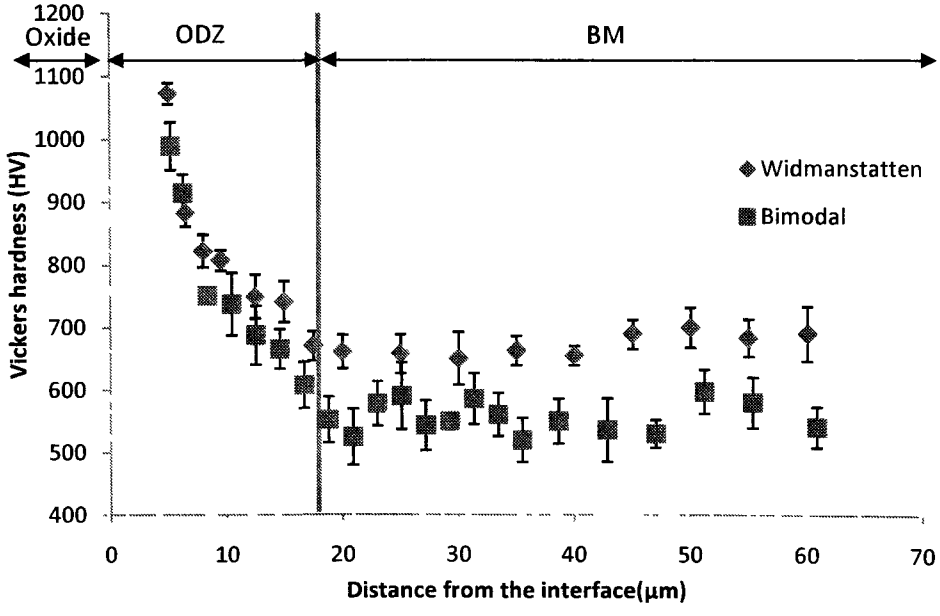

Figure 4.3. The micro-hardness vs. depth profile of the bimodal and Widmanstätten samples oxidized at 600°C for 65h showing the solid solution hardening effect of oxygen in titanium (ODZ: oxygen diffusion zone and BM: bulk metal).

4.2.3 X-Ray Diffraction of the Oxide Scale

The XRD pattern of the oxide layer developed by oxidation of bimodal sample in air is presented in Figure 4.4. The major phase formed during oxidation at 600°C was

rutile form of TiO_2, though the rutile layer formed was so thin that the X-rays penetrated the α-phase of ODZ beneath the oxide. Other possible compounds were TiO and anatase form of TiO_2. However, the presence of TiO can be questioned since its most intensive peak located at 2θ=36.06 overlapped with the peak of rutile and the peak located at 2θ=52.56 overlapped with the peak of α-Ti. On the other hand, the pattern obtained for anatase was weak and incomplete, with many of the high intensity reflections absent, such as the peaks with relative intensities (I) of $\frac{I}{I_1} = 35, 20, 20$ where I_1 is the intensity of the strongest peak. Nevertheless, the only possible match for the peaks located at 2θ=25.26 and 74.80 was anatase, therefore the existence of anatase cannot be ruled out. Apparently, the lower oxides of titanium and aluminum and vanadium oxides are either unstable under these oxidation conditions or they are formed in exceedingly small quantities and/or they are in amorphous or nanocrystalline form.

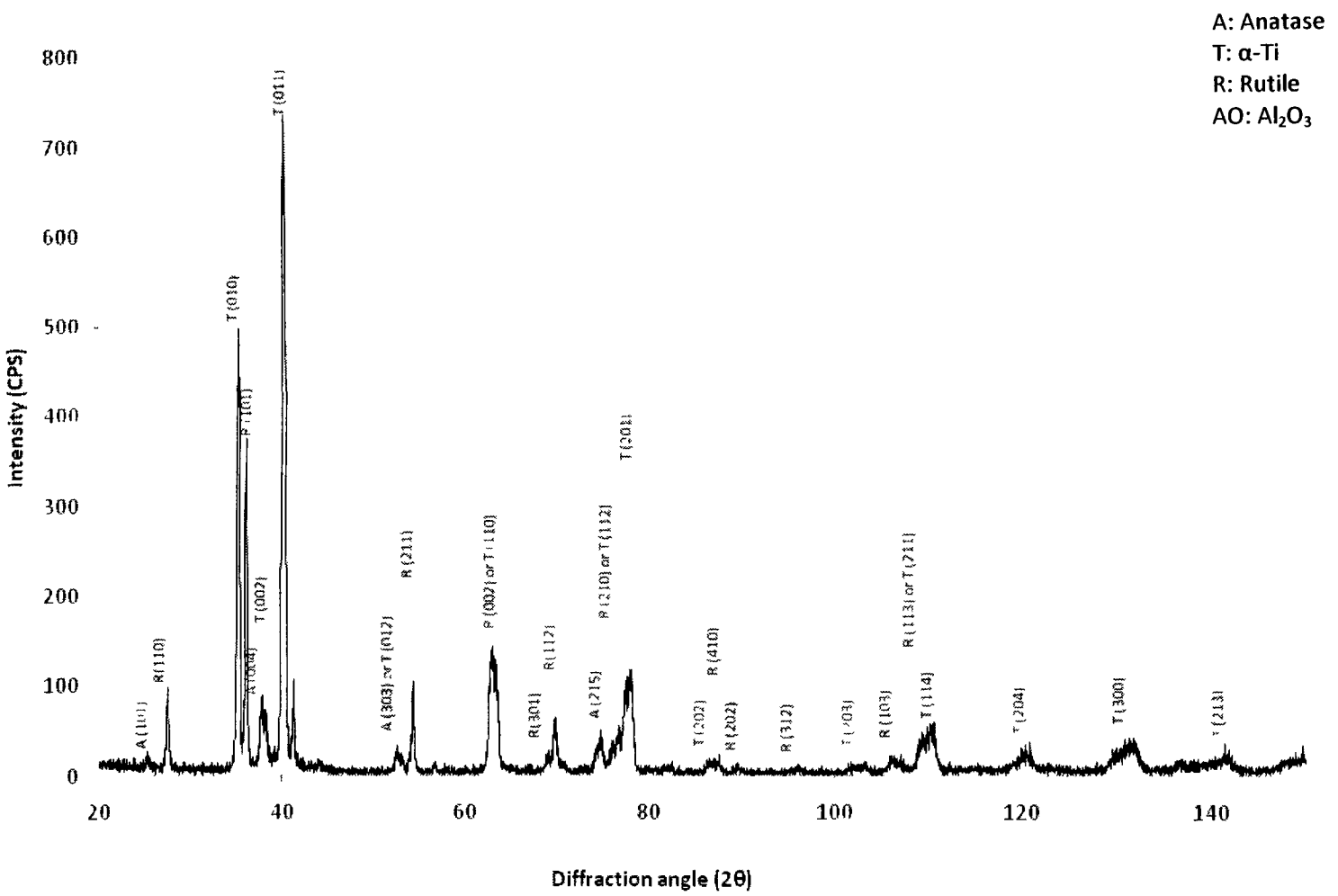

Figure 4.4. XRD pattern for Ti-6Al-4V coupons oxidized in air at 600°C for 65h

4.2.4 EDS Mapping on Oxide Cross-Section

The distribution of the elements in the scale formed on Ti-6Al-4V by TO process was studied by EDS mapping of the oxide cross-section which was sectioned and observed using a dual beam machine combining a high resolution FIB column and an SEM column. Figure 4.5 shows the compositional profiles of Ti, Al, V and O elements. It is noteworthy that an Al-rich layer formed at the gas/oxide interface, while a Ti-rich layer existed at the interface of oxide scale and substrate. The inner Ti-rich scale consisted mainly of TiO_2 as confirmed by XRD results presented in the previous section. The contribution of the external Al-containing compound to the X-ray diffraction peaks, however, was extremely minor, which was either due to its small quantity or amorphous form. The oxidation process had no particular effect on distribution of vanadium in the compound layer as can be seen in Figure 4.5 (d).

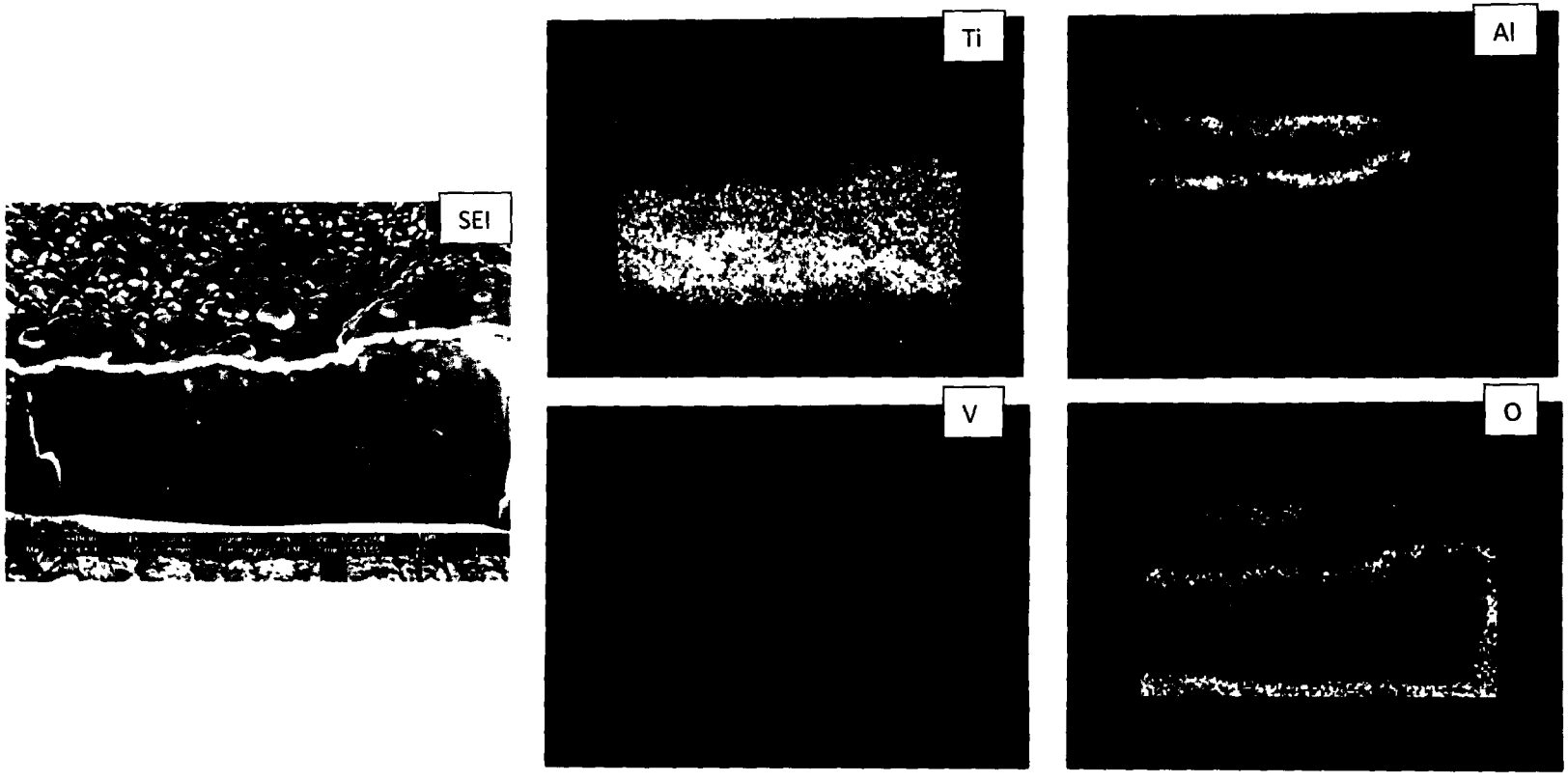

Figure 4.5. EDS distribution maps of elements within the oxide scale formed by TO process on Ti-6Al-4V and sectioned with FIB. The secondary image (SEI) along with the compositional profiles of Ti, Al, V, and O are shown.

4.2.5 Scratch Test Results on Oxide Scale

The scratch test method is generally accepted as an efficient method to evaluate the interface adhesion and the fracture toughness of coated surface In this test the usual procedure is to move the scratch tip across the coated surface under an increasing normal load until failure is observed The load at which this happens is called the critical normal load It is generally accepted that the test is suitable for coatings of thickness ranging from 0 1 to 20 μm [116,120], which includes the coating thickness of this study (1 7 μm) In this study a Rockwell C type diamond indenter with 200 μm tip radius was used to perform scratch test under increasing normal load between 1-20 N The maximum contact pressure at the center of the spherical indenter (P_o) can be calculated based on the the Hertzian theory as follows

$$P_o = \left(\frac{6WE^{*2}}{\pi^3 R^2}\right)^{1/3} \qquad \text{Equation 4 9}$$

where W is the normal load, R is the indenter radius and E^* is the reduced elastic modulus given by the following equation

$$\frac{1}{E^*} = \frac{1-\vartheta_1^2}{E_1} + \frac{1-\vartheta_2^2}{E_2} \qquad \text{Equation 4 10}$$

where E_1 and E_2 are the elastic modulus and ϑ_1 and ϑ_2 are the Poisson's ratios of the substrate and the indenter, respectively It has been shown [121] that the effect of tangential force on the normal pressure and contact area is generally small, particularly when COF is less than 1 Therefore equation 4 9 was employed to estimate the maximum contact pressure under the spherical indenter during scratch test Ascribing $E_{TiO_2} = 192\ GPa$ (measured by microindentation under 200 mN) , $\vartheta_{TiO_2} = 0.3, E_{Diamond} = 1141\ GPa$ and $\vartheta_{Diamond} = 0.07$, the contact pressure produced under indenter of 200 μm radius and increasing normal load of 1-20 N was 5 33-14 47 GPa The loading rate was 6 N/min and the length of the scratch was 6 mm

The typical coefficient of friction (COF) vs normal load plot for Ti-6Al-4V and TO-Ti-6Al-4V samples is shown in Figure 4 6 The recorded fiction data is the sum of

adhesion and ploughing friction [33]. The coefficient of friction was generally higher for Ti-6Al-4V sample with large fluctuations around an average value of 0.37 The large fluctuations confirm the high adhesion tendencies of Ti matrix which is caused by its electron configuration and crystal structure. COF increased gradually for the coated sample as the normal load increased with a discontinuity observed around 12 N or 12.206 GPa, which is marked as "2" in Figure 4.6. Despite this increase, a lower COF was achieved for oxidized samples compared to the un-oxidized sample for all the loads. In order to better explain the COF behaviour, the scratch groove formed on thermally oxidized sample was studied under SEM.

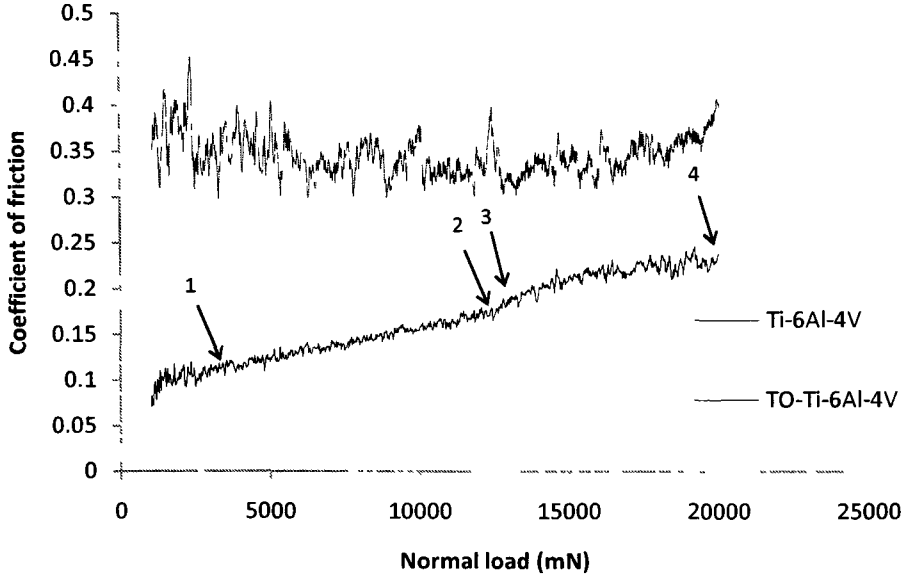

Figure 4.6. Variation of Coefficient of friction with normal load of Ti-6Al-4V and TO-Ti-6Al-4V samples recorded during scratch test under increasing normal load of 1-20N. The scratch length was 6 mm.

The overall view of the scratch groove is shown in Figure 4.7. It is clear that the width of the scratch groove increases with an increase in normal load. Holmberg et al [120] classified the type of failure that happens in coatings during scratch test into 6 groups (shown in Figure 4.8) which can be categorized as (a) angular cracks, (b) parallel cracks, (c) half-circular or half-cone cracks, (d) coating chipping and (f) coating break trough. The failure modes and the value of critical load depends on various parameters, namely the properties of coating, and substrate, the strength of coating/substrate interface,

the coating thickness, the shape of the tip of the indenter, the loading rate, and the friction between coating and scratch tip. Basically, two types of failures can be distinguished, cohesive failure of coating or substrate (such as (a), (b) or (c) type failure), and interfacial failure of coating/substrate interface (such as (d), (e) and (d) type failure) [116].

The occurrence of cohesive and interfacial failure under scratch test was elucidated by closer examination of the scratch groove shown in Figure 4.9. Figure 4.9 (a) illustrates the SEM micrograph of the first failure happened under 8.02 GPa (3.4 N) contact pressure and matched with the angular cracking type. This point is marked as "1" on the COF plot shown in Figure 4.6 from which it is clear that no particular change in COF curve occurs due to cohesive failure of the coating. The discontinuity in COF curve, which is marked as "2" in Figure 4.6, corresponded to the first interfacial failure at the edges of scratch groove that is shown in Figure 4.9 (b). This interfacial failure occurred under 12.2 GPa contact pressure and according to the aforementioned classification corresponded to (d)-type failure shown in Figure 4.8. The half-cone-type cracks, whose SEM micrograph is shown in Figure 4.9 (c), were formed under 12.4 GPa contact pressure. Neither of coating breakthrough type failure nor chipping in front of the sliding stylus ((f)-type failure in Figure 4.8) were evidenced at the tip of the scratch tip, which is depicted in Figure 4.9 (d).

The occurrence of half-cone cracks on the coating surface (type (c)) can be described by Hertz theory which applies to the case of frictionless spherical indentation of an elastic monolithic material. This solution gives a maximum tensile stress on the surface at the perimeter of the contact as shown in Figure 4.10. This stress may lead to cracking in the form of cones starting from the surface. If a tangential load is applied to the indenter, the cone crack can rotate along its axis and a partial cone crack can form due to the shift in maximum tensile stress to the trailing edge of the indenter as shown in Figure 4.10 for μ=0.25, 0.5 [121]. The formation of partial cone cracks repeats with a regular interval which depends on the load, the critical flow size and fracture toughness [122,123]. These cracks start from the surface and therefore, in the case of a brittle coating on a ductile substrate, their average interval provides a criterion for the qualitative evaluation of the fracture toughness of the coating.

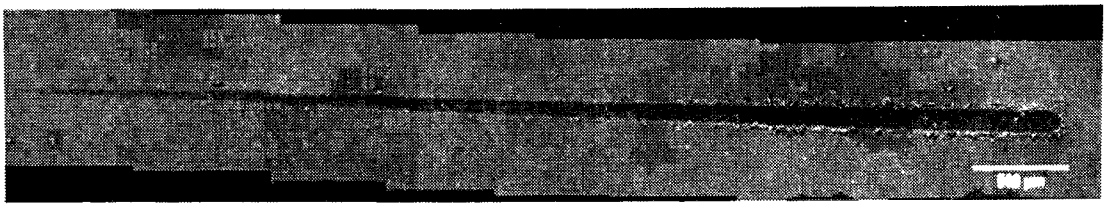

Figure 4 7 SEM micrograph of the scratch groove on TO-Ti-6Al-4V sample The length of the scratch is 6 mm while the normal load was increased linearly from 1 to 20 N

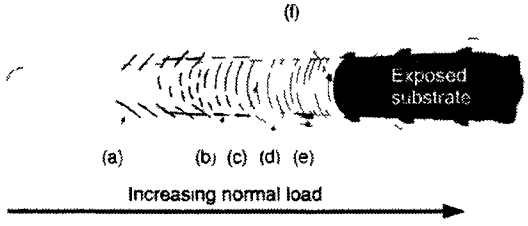

Figure 4 8 Schematic illustration of the possible failure types in a scratch test (a) angular crack, (b) parallel crack, (c) transverse half-cone cracks, (d) coating chipping, (e) coating spalling, and (f) coating breakthrough [120]

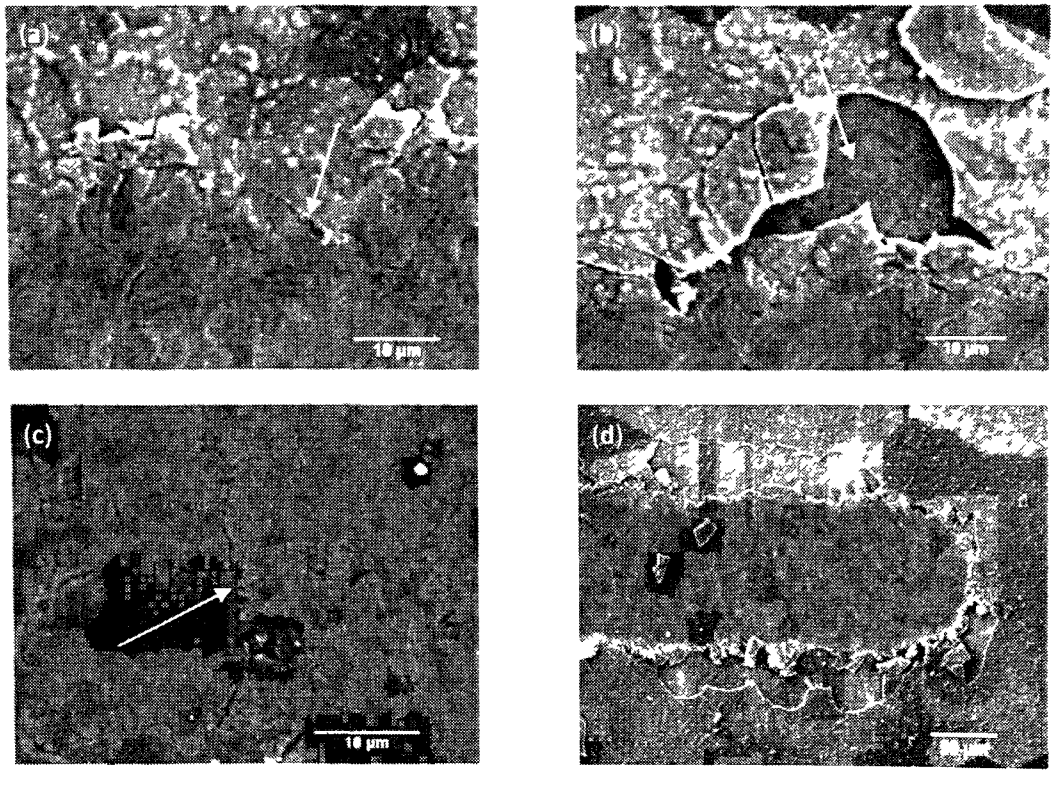

Figure 4 9 SEM micrograph of the various types of cohesive or interfacial failures happened during scratch test on TO-Ti-6Al-4V sample The loads corresponding to these micrographs are marked as 1 to 4 on the COF plot shown in Figure 4 8 (a) angular cracking at 8 02 GPa, (b) coating spalling at 12 2 GPa, (c) half-cone cracking at 12 4 GPa, and (d) the scratch tip where no coating breakthrough was observed at 14 5 GPa

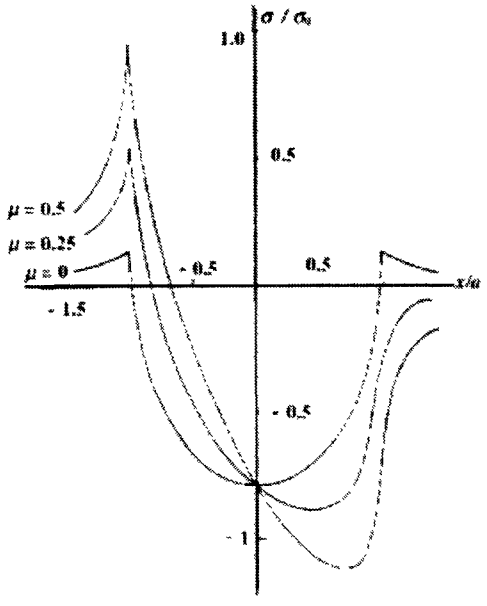

Figure 4.10. Ratio of tensile stress σ to normal stress σ_0 vs. the position x relative to the contact radius a for elastic sliding with a spherical indenter [121].

In summary, all of the following types of failure were evidenced when the diamond stylus was drawn over the TO-Ti-6Al-4V sample: angular cracking, parallel cracking, half-cone cracking, and coating chipping at the edge of scratch. Coating chipping in front of the sliding stylus, however, was not observed, which confirms that the oxide/substrate interfacial bonding withstand the bending stresses at the leading front of the indenter, in spite of the porous interface evidenced by FIB sectioning shown in Figure 4.5. Additionally, the coating chipping was accompanied by a sudden increase in the coefficient of friction.

4.3 Tensile Test Results

In this section the results of tensile tests, which were carried out on Ti-6Al-4V and TMC samples are presented. The tensile samples were produced by MIM process, and the tests were performed at three different temperatures of 25°C, 250°C and 400°C. An average of 5 tests was performed at each condition. The values of yield strength, tensile strength and ductility (elongation) of Ti-6Al-4V and TMC sample are compared in Figure 4.11 for three different temperatures. The results show higher yield strength for the TMC samples compared to Ti-6Al-4V samples at all the temperatures especially at higher

temperatures (Figure 4.11 (a)). The tensile strength of the TMC sample at room temperature was similar to Ti-6Al-4V sample. When tested at 400°C, the tensile strength of both of the TMC and Ti-6Al-4V samples decreased; however, the incorporated particles improved the high temperature strength of the composite to a degree that its tensile strength was 113 MPa higher than the Ti-6Al-4V sample (Figure 4.11 (b)). Figure 4.11 (c) reveals the deteriorating effect of particles on the low temperature ductility of Ti-6Al-4V matrix. The ratio of the elongations of TMC samples to Ti-6Al-4V samples that were tested at 25, 250 and 400°C were respectively 3.3, 2.7 and 2.3, and the inferior ductility of the TMC samples to the matrix alloy at low temperature was compensated by the enhanced ductility of the composite alloy at higher temperatures. Figure 4.12 illustrates the SEM micrograph that was taken from the fracture surface of the TMC sample tested at 25°C. This micrograph revealed that the fracture mechanism consisted of particle fracture as a result of the load transfer from the matrix to the reinforcement followed by the ductile fracture of Ti-6Al-4V matrix (dimpled rupture or cup-and-cone fracture) [29]. The fracture of particles occurred by a brittle mechanism of cracking within the particle but not at the particle/matrix interface. These results confirmed that the particle/matrix interfacial bonding achieved by MIM process endured the tensile stress and the load was completely transferred to the particles, and postponed the void coalescence mechanism within the ductile matrix.

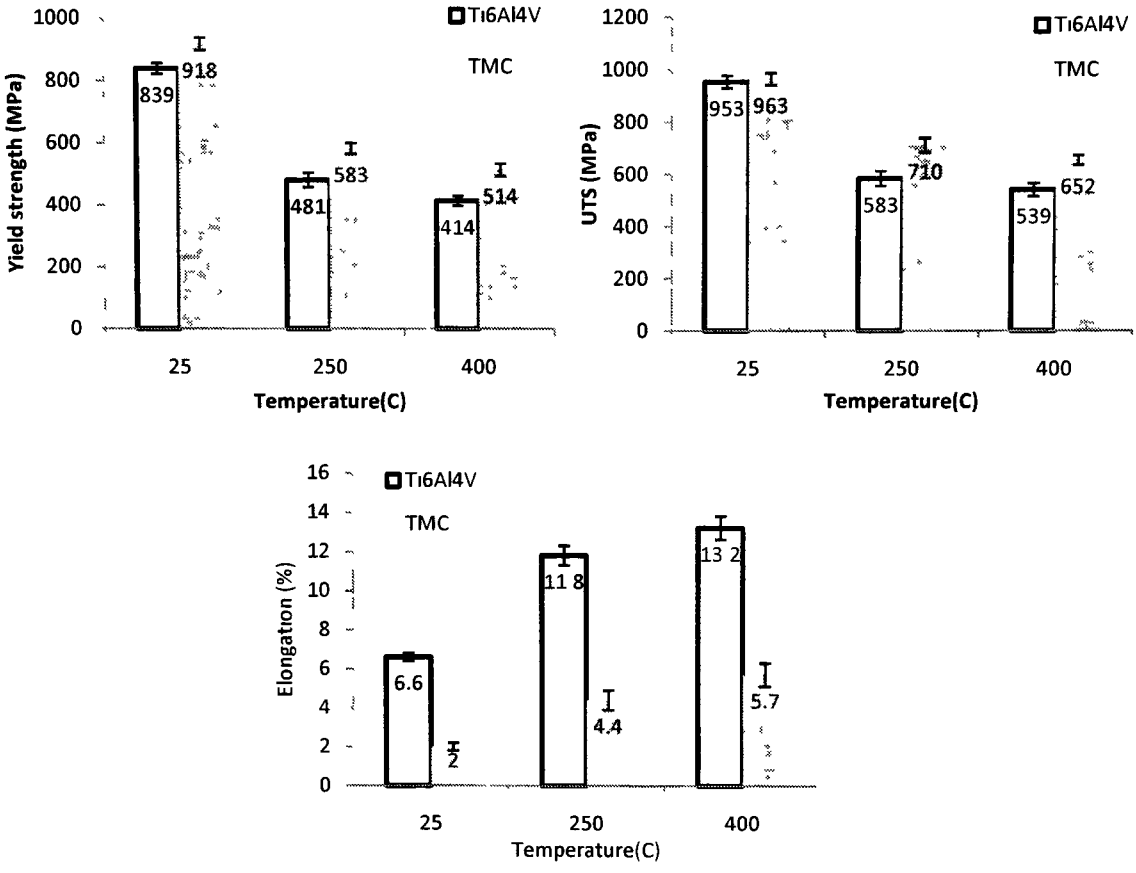

Figure 4.11. A comparison of the mechanical properties of the Ti-6Al-4V and TMC samples measured by tensile tests performed at 25, 250 and 400°C

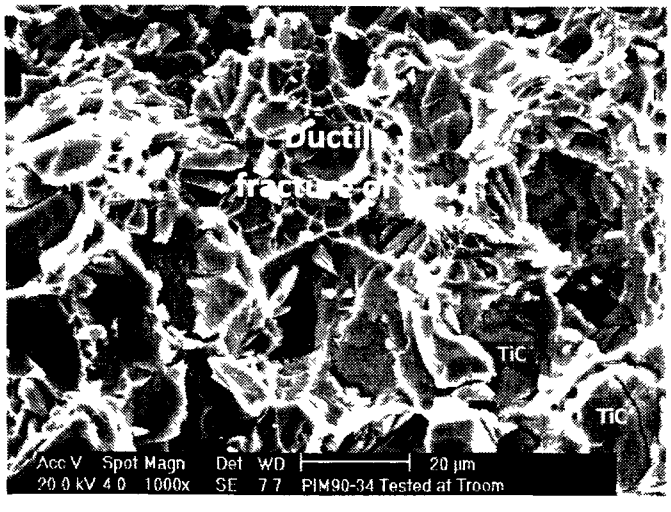

Figure 4.12 Fracture surface of the TMC sample tested at room temperature showing cracking within the TiC particles and ductile fracture of the matrix.

4.4 Thermal Oxidation of TMCs

In this section the results of thermal oxidation of Ti-6Al-4V-10 Vol%TiC composites are presented. The main aims of these experiments were to determine the optimum oxidation condition in terms of temperature and time, and to evaluate the oxide composition, mechanical properties and the diffusion mechanisms responsible for the formation of oxide scale and ODZ. The TMC samples were thermally oxidized in an air furnace at 600 and 800°C for 20 min, 20 h and 65 h followed by cooling in the furnace. The oxidation procedure performed at 600°C for 65 h and at 800°C for 20 min resulted in an integrated and relatively adherent scale. The oxide scales formed as a result of oxidation at these conditions were characterized by SEM observation of the cross-section, X-ray diffraction, and micro-scratch test performed on the surface, and under progressive normal load. The fracture toughness of the scale formed was determined by indentation crack length (ICL) method. The results of these experiments are discussed in the following sections.

4.4.1 SEM Observation of the Oxide Scale

TMC samples were thermally oxidized at temperatures of 600 and 800° C for periods of 20 min, 20 h and 65 h. The SEM micrograph of the cross-sectional microstructure of the scale formed after oxidation at 600° for 65 h is shown Figure 4.13. A continuous oxide scale was not visible on the samples oxidized at 600°C for 20min and 20h, which confirmed that the duration of oxidation was too short. A continuous oxide scale, however, formed at 600°C when prolonged oxidation was performed for 65 h. While the thin scale (0.7 μm) formed on the Ti-6Al-4V substrate (marked as OL_1) was adherent, a visible crack existed within the thick scale (4.4 μm) on TiC particles which is marked as OL_2. This crack caused the spallation of the scale on the particles as is evident in the image of the oxide surface taken when the stage was tilted 50° relative to the beam under SEM (Figure 4.14). Figure 4.15 illustrates the BSE and SEM micrographs of the cross-section of the oxide scale formed during thermal oxidation at 800°C for 20 h and 20 min respectively. As can be seen, when oxidation prolonged for 20 h or longer, the scale was exfoliated (Figure 4.15 (a)). The oxide scale formed at 800°C after 20 min uniformly covered the surface and no evidence of cracking and/or spallation was observed (Figure

4.15 (b)). With these in mind, the following oxidation conditions were selected as the main focus of this study: at 800°C for 20 min and at 600°C for 65 hours. Hereafter the TMC samples oxidized at these conditions are referred to as "TMC-8-20min" and "TMC-6-65h" respectively.

The thickness of the oxide scale which formed on the substrate and TiC particles, and the thickness of ODZ layer were measured separately for 6-65h and 8-20min oxidation conditions at 20 different points using an Ominimet image analyzing software. The average value of these measurements together with the associated standard deviation values are tabulated in Table 4.2. The thickness of ODZ is defined as the zone within which the recrystallized equiaxed β (β_p) is transformed into α since oxygen is a strong α-stabilizer. The thickness of ODZ at 8-20min condition exhibited a large value of standard deviation which was due to the role of TiC particle as diffusion barrier. This is evident from Figure 4.15 (b) where the recrystallized equiaxed β (β_p) were not transformed into α where there was a TiC particle on the diffusion path.

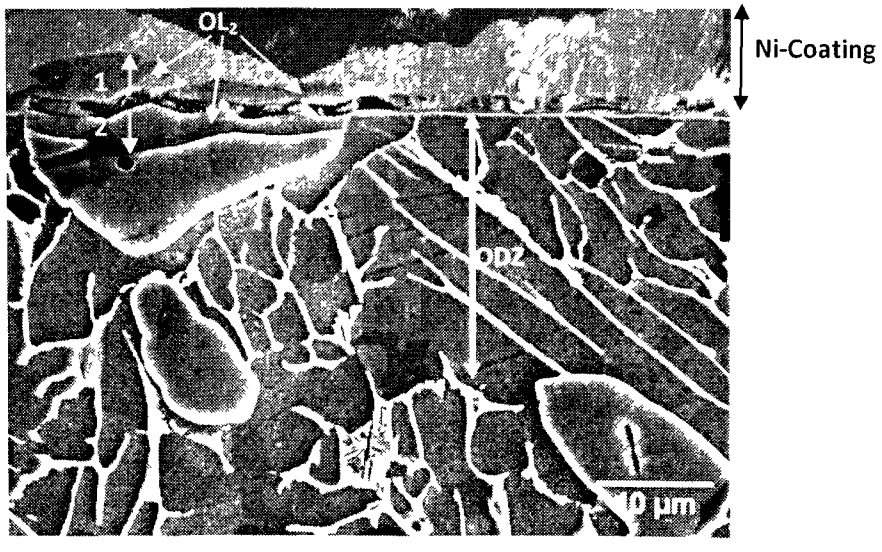

Figure 4.13. Cross-sectional SEM micrograph of TMC sample oxidized at 600°C for 65h showing the oxide layer formed on Ti-6Al-4V substrate (OL_1) and the spalled oxide layer on TiC particles (OL_2). The oxygen diffusion zone is marked as ODZ. A crack is visible within the oxide formed on the TiC particle.

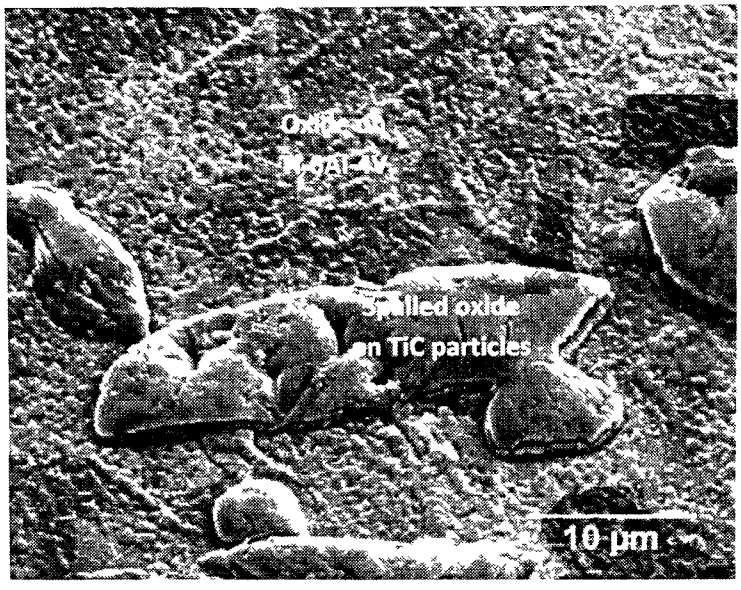

Figure 4.14. The SEM micrograph of the oxide scale formed on TMC samples that were oxidized at 600°C for 65h. This image is taken when the stage was tilted 50° relative to the SEM beam. The oxide is visibly thicker and is exfoliated on TiC particles.

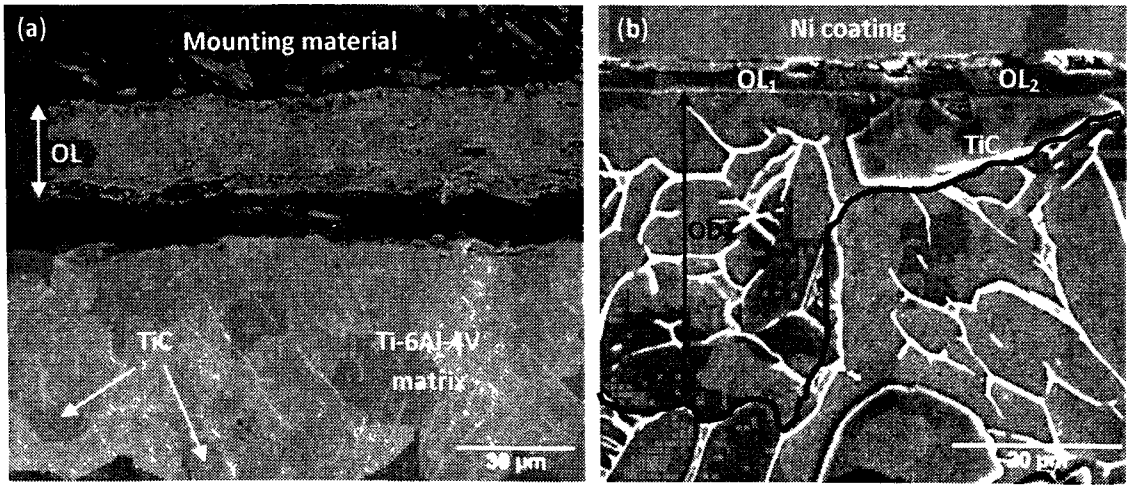

Figure 4.15. cross-sectional micrographs of the TMC samples oxidized at 800°C (a) for 20 h showing the spallation of the oxide (OL) spallation and (b) for 20 min showing the oxide layer formed on the substrate (OL_1) and on the particles (OL_2) and also the oxygen diffusion zone (ODZ) formed. Beneath the TiC particle no $\beta \rightarrow \alpha$ transformation has occurred.

Table 4.2. The thickness of oxide scale formed on the Ti-6Al-4V substrate and TiC particles, and the thickness of ODZ layers as measured from the SEM micrographs of the TMC samples oxidized at 600°C for 65h (6-65h) and at 800°C for 20 min (8-20min)

Oxidation condition	Thickness of the oxide layer		Thickness of ODZ
	On Ti-6Al-4V	On TiC particles	
600°C-65h	0.73±0.15	4.41±0.72	11.25±0.65
800°C -20min	2.60±0.35	4.07±0.35	31.19±11.60

The oxidation behaviour of TMC alloy at the temperatures of this study can be discussed based on the morphology of the oxide scales on substrate and TiC particles. As it is apparent from Figure 4.13 and from Table 4.2, at 600°C preferential oxidation of TiC particles dominates and the scale on the particles was 3.7 μm thicker than the scale on the substrate. This difference in thickness was compensated by growth of a thicker scale in two directions: i) in the direction shown by arrow "1" in Figure 4.13 which formed the lump of oxide on the surface and ii) in the direction shown by arrow "2" in Figure 4.13 which formed the penetrating dent of oxide. The stratification observed within the thick scale is mainly due to the growth stresses built up in the scale caused by: i) high Pilling-Bedworth ratio of the oxide and the substrate, ii) the great variations in lattice parameters at the interface caused by formation of the solid solution, and iii) the high ratio of coefficient of thermal expansions of the oxide and the substrate [70,71,88]. These stresses increase until a bearable maximum value is reached at a critical thickness, at which the crack nucleates. The oxide formed at 8-20min oxidation condition, however, was more uniform in thickness with no evidence of stratification.

4.4.2 Micro-Indentation on Tapered Cross-Section

Similar to Ti-6Al-4V samples, a series of micro-indentation tests were performed on the tapered cross-sections of TMC samples oxidized at 6-65h and 8-20min conditions, starting at 5 μm distance from the interface, with a 10 μm step and a total distance of 50 μm. The hardness values were calculated from the load penetration depth data according to Appendix A. The variations of the measured microhardness as a function of the depth below the oxide/ODZ interface is shown in Figure 4.16 for TMC-8-20min and TMC-6-

65h samples. The ODZ is defined as the depth where the hardness-depth plot levels out and becomes equal to the bulk hardness, which was approximately 10 μm and 40 μm for TMC-6-65h and TMC-8-20min samples, respectively. These values, considering the large steps between the indentations, were in agreement with the results of the microscopic depth measurements conducted on the cross-sections (Figure 4.13 and Figure 4.15).

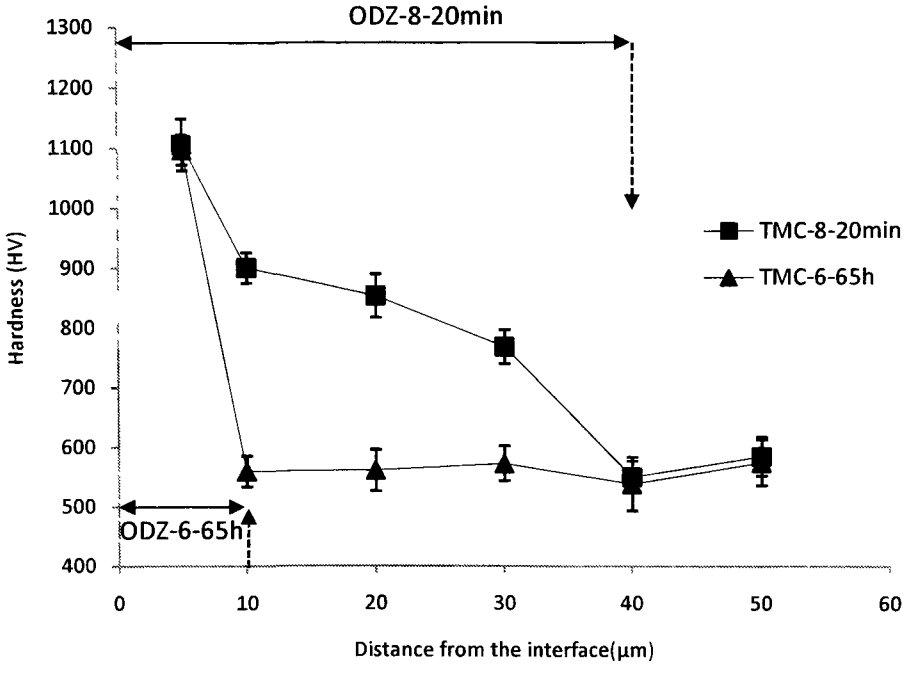

Figure 4.16. The micro-hardness vs. depth profile of the TMC-8-20min and TMC-6-65h samples showing the solid solution hardening effect of oxygen in titanium (ODZ: Oxygen Diffusion Zone and BM: Bulk Metal)

4.4.3 X-ray Diffraction of the Oxide Scale

The XRD patterns of the oxide scales developed at 6-65h and 8-20min oxidation condition are presented in Figure 4.17 and Figure 4.18 respectively. The main phase formed under both conditions was the rutile form of TiO_2. The peaks conforming to rutile pattern were more intensive for 8-20min condition while the peaks corresponding to α-Ti were more intensive for 6-65h condition. Since the oxide formed at 6-65h condition (0.73 μm) was thinner compared to the oxide formed at 8-20min condition (2.6 μm), the X-rays penetrated the α-phase of ODZ beneath the 6-65h-type oxide and the α-Ti peaks become stronger. Furthermore, the (200), (301), (411) and (312) reflections of rutile were absent in the XRD pattern of 6-65h-type sample (Figure 4.17). Other possible compounds on

both types of samples were anatase form of TiO_2 and Al_2O_3. In comparison to the pattern obtained from the oxide on TO-Ti-6Al-4V samples (Figure 4.4), the most intensive peak of anatase corresponding to (010) reflection was absent for TMC samples. However, the only possible match for the peaks located at 2θ=37.62 and 112.64 was anatase, and the existence of anatase cannot be ruled out. The probability of formation of alumina is even less likely since its first three most intensive peaks were absent in the patterns obtained from both 6-65h and 8-20min-type samples. The only possible match for the peaks located at 2θ=41.8, 52.46, 63.38 and 72.78 was alumina similar to the case of anatase. The oxide formed on the TiC particles at both conditions was, apparently, thick enough to eliminate any reflection from TiC particles beneath the oxide scale since none of the peaks in the spectra obtained from 6-65h and 8-20min-type oxides conformed to any of TiC peaks.

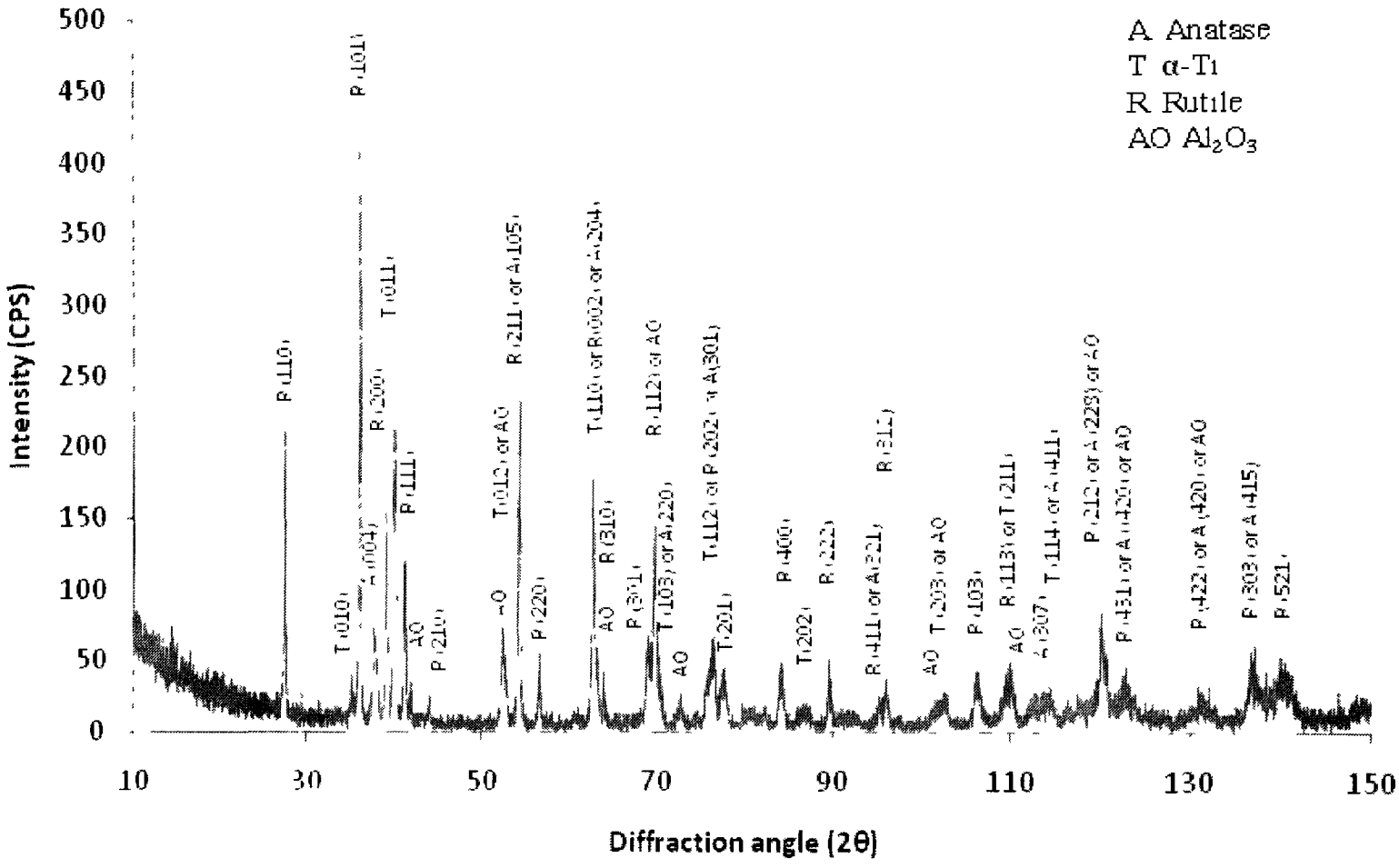

Figure 4.17 XRD pattern for TMC oxidized at 600°C for 65h.

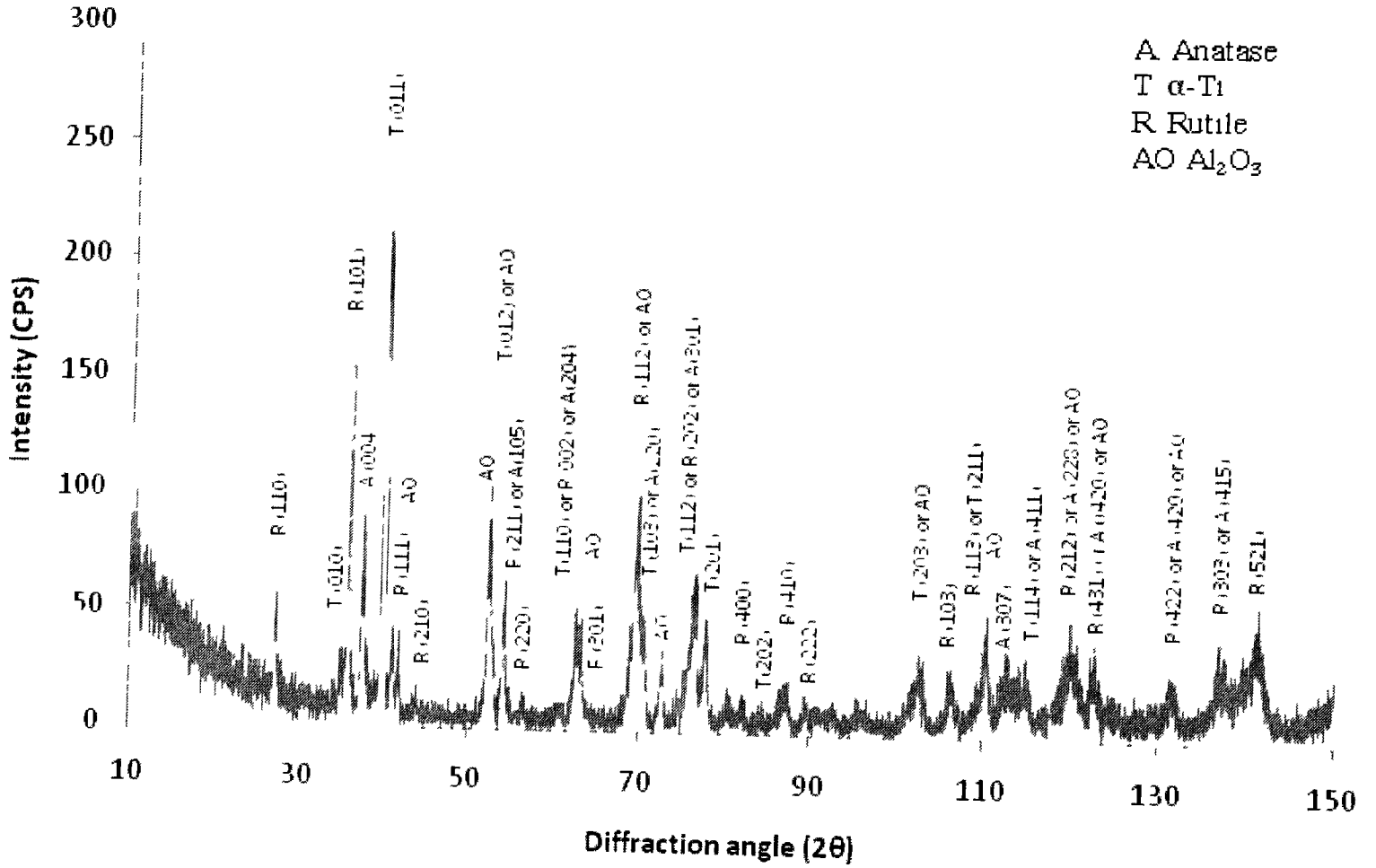

Figure 4.18 XRD pattern for TMC oxidized at 800°C for 20 min.

4.4.4 Scratch Test Results Performed on TMC, TMC-6-64 and TMC-8-20min

The scratch tests were performed under progressive normal load between 1-20 N. Ascribing $E_{TiO_2} = 192\ GPa, \vartheta_{TiO_2} = 0.3, E_{TMC} = 110\ GPa, \vartheta_{TMC} = 0.3, E_{Diamond} = 1141\ GPa$ and $\vartheta_{Diamond} = 0.07$, this range of load produces a contact pressure in the range of 5.33-14.47 GPa for the oxidized sample and 3.87-10.50 GPa for Ti-6Al-4V and TMC samples. A Rockwell C type indenter with 200 μm tip radius was pulled along the surface to create a 6 mm scratch. The rate of increase in normal load was of 6 N/min. Ti-6Al-4V and TMC samples were mirror polished prior to the test, while no post-treatment surface preparation was performed on TMC-6-65h and TMC-8-20min samples to preserve the oxide scales that were formed during oxidation.

Figure 4.19 illustrates the profile of penetration depth along the scratch length for Ti-6Al-4V, TMC, TMC-6-65h and TMC-8-20min samples. The spherical indenter penetrated into the TMC sample from 1,277 to 37,088 nm, and into Ti-6Al-4V from 2,861 to 59,798 while the corresponding depths for TMC-6-65h and TMC-8-20min samples were 715-23,210 nm and 966-18,423 nm. The penetration depth represents the degree of plastic and elastic deformation imposed on the surface due to the contact stresses. As can be seen in Figure 4.19, at the entire load range the deformation imposed on TMC was lower than Ti-6Al-4V, and it was also decreased by performing 8-20min oxidation condition. It should be noted that the contact pressure produced on oxidized-TMC samples was higher than the contact pressure on Ti-6Al-4V samples at the same load which was due to the higher stiffness of oxide coating compared to stiffness of TMCs (equation 4.9 and equation 4.10). The penetration depth on TMC and TMC-6-65h was roughly equal up to 4.93 N with larger fluctuations for TMC-6-65h sample. The improvement caused by 6-65h-type oxidation was apparent when the normal load increased to higher than 4.93 N. Even so, TMC-8-20min exhibited the lowest penetration depth of all that was lower than penetration depth produced on TMC-6-65h sample by an average factor of 0.66. Studying the penetration depth on TMC sample itself, a significant increase in the slope of the plot happened at 4.2 N—marked as point "1" in Figure 4.19—that was followed by a decrease in the slope at 9.7 N—marked as point "2" in Figure 4.19.

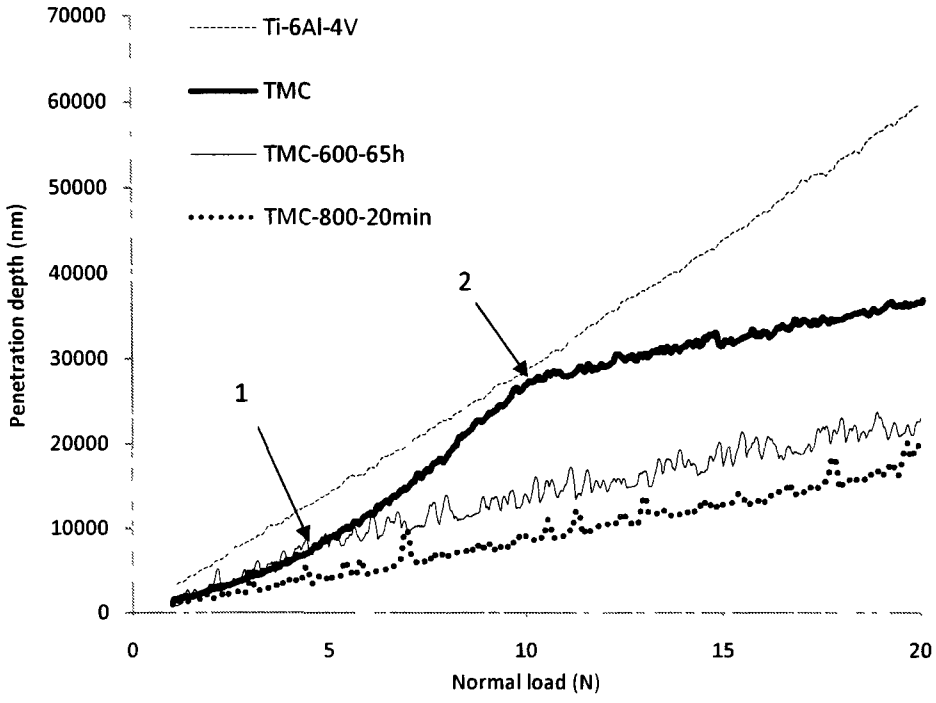

Figure 4.19. Variation of penetration depth with normal load of Ti-6Al-4V. TMC and oxidized TMC samples at different oxidation conditions of 600°C for 65 h and 800°C for 20 min during scratch test under increasing normal load of 1-20N. The scratch length was 6 mm.

The COF vs. normal load plots for Ti-6Al-4V, TMC, TMC-6-65h and TMC-8-20min samples are shown in Figure 4.20. For Ti-6Al-4V sample, the COF curve fluctuated around a constant average of 0.36 giving the highest value of COF at entire range of load. The COF curve of TMC-8-20min increased steadily from 0.1 to 0.18, giving the lowest COF value under the highest contact pressure. For TMC-6-65h sample, the COF rapidly increased from 0.1 to 0.38 giving a higher COF value at 20N normal load compared to TMC and TMC-8-20min. On the other hand, the COF curve for TMC sample showed a similar trend as its penetration depth curve, where it increased from a value of 0.1 to around 0.15 as the normal load increased to 4.2 N (marked as "1" in Figure 4.20) that was then followed by a rapid rise to a value around 0.3 at around 9.7 N (Marked as "2" in Figure 4.20) and stayed constant at that level. In order to identify the origin for the variations in penetration depth and COF values, the morphology of the scratches were studied under SEM which results are given in section 4.4.4.1.

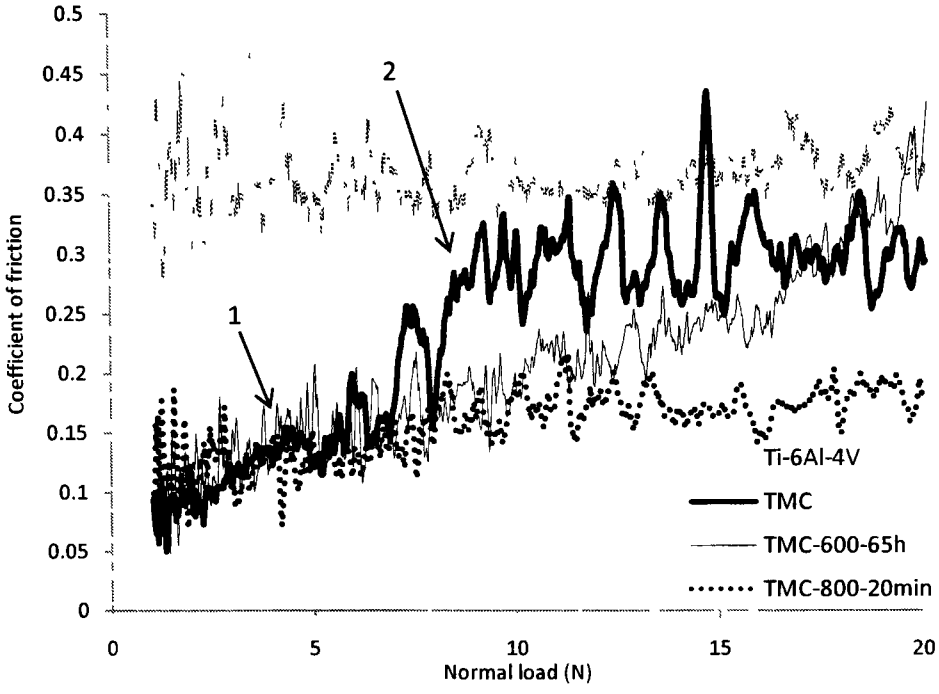

Figure 4.20. Variation of Coefficient of friction with normal load of Ti-6Al-4V, TMC and oxidized TMC samples at different oxidation conditions of 600°C for 65 h and 800°C for 20 min during scratch test under increasing normal load of 1-20N. The scratch length was 6 mm.

4.4.4.1 SEM Observations of the Scratch

The modes of failure and the values of critical loads for both oxidized and un-oxidized samples were revealed by close examination of the scratch surface under SEM. Figure 4.21 illustrates the SEM micrographs of various types of failure observed on TMC sample. As shown in Figure 4.21 (a), under 1.3 N normal load (4.22 GPa contact pressure) cracking within the particles commenced, however, the Ti-6Al-4V matrix below the TiC particles was able to withstand the indentation force transmitted by the particle under pressure and the particles were not pushed into the matrix. The cracking within the particles was similar to the half-circle type cracking that was evidenced on the oxide in Figure 4.9 (c). As mentioned before, this type cracking is induced by the maximum tensile stress at the trailing edge of the sliding stylus. Figure 4.21 (b) shows the cracked particles that completely sank into the matrix under 4.3 N (6.29 GPa contact pressure), and the Ti-6Al-4V matrix which was smeared over the particles. As the normal load increased to 9.6N (8.22 GPa contact pressure), cracking within the particles resulted in

fracture of particles at the edge of the scratch groove, and then fragments of TiC particle were formed (Figure 4.21 (c)).

The sudden increase in penetration depth and COF values at around 4.2 N—marked as point "1" in Figure 4.19 and Figure 4.20—occurred when the TiC particles lost their load bearing capacity, sank into the matrix and the penetration depth under of the sliding stylus into the TMC matrix increased considerably. The particles are less likely to be worn out at these low loads since no particle damage was observed up to the higher loads (The point marked as 2 in Figure 4.19 and Figure 4.20). The contact type, then, was changed from TiC/diamond to Ti-6Al-4V/diamond that was accompanied by a sudden increase in COF (marked as point 1in Figure 4.19 and Figure 4.20) caused by the higher adhesion tendencies of Ti-6Al-4V matrix, and the COF curve of TMC was shifted toward the COF curve of Ti-6Al-4V The fracture within the particles—evidenced at around 8.22 GPa—was accompanied by a drop in the slope of the penetration depth plot and larger fluctuations in COF (marked as point 2 in Figure 4.19 and Figure 4.20 respectively). Fracture within the particle put away some of the deformation energy and caused the depth of penetration to increase less rapidly under the rising contact pressure, and the TiC fragments formed caused larger fluctuations in COF.

The various types of failure that can happen during scratch test on a coated-system, which were previously described in section 4.2.5, are classified into 6 groups and shown schematically in Figure 4.8. Both angular and half-cone type cracking were observed on TMC-6-65h and TMC-8-20min samples as evidenced by SEM observations of the scratch groove that is depicted in Figure 4.22 (a) and (b). No indication of interfacial type failures was evidenced on either of the coatings. The compressive stresses at the leading edge of stylus, however, removed the lumps of oxides protruding from TMC-6-65h sample and formed the small oxide particles shown in Figure 4.8 (a). The thermally oxidized TMC samples, therefore, exhibited a better interfacial strength compared to the TO-Ti-6Al-4V samples, since chipping of the oxide coating under 12.2 GPa pressure was evidenced on the latter. The angular type cracking was commenced at 10.4 GPa pressure for TMC-8-20min sample while the first angular cracking occurred at 8.99 GPa for TMC-6-65h sample.

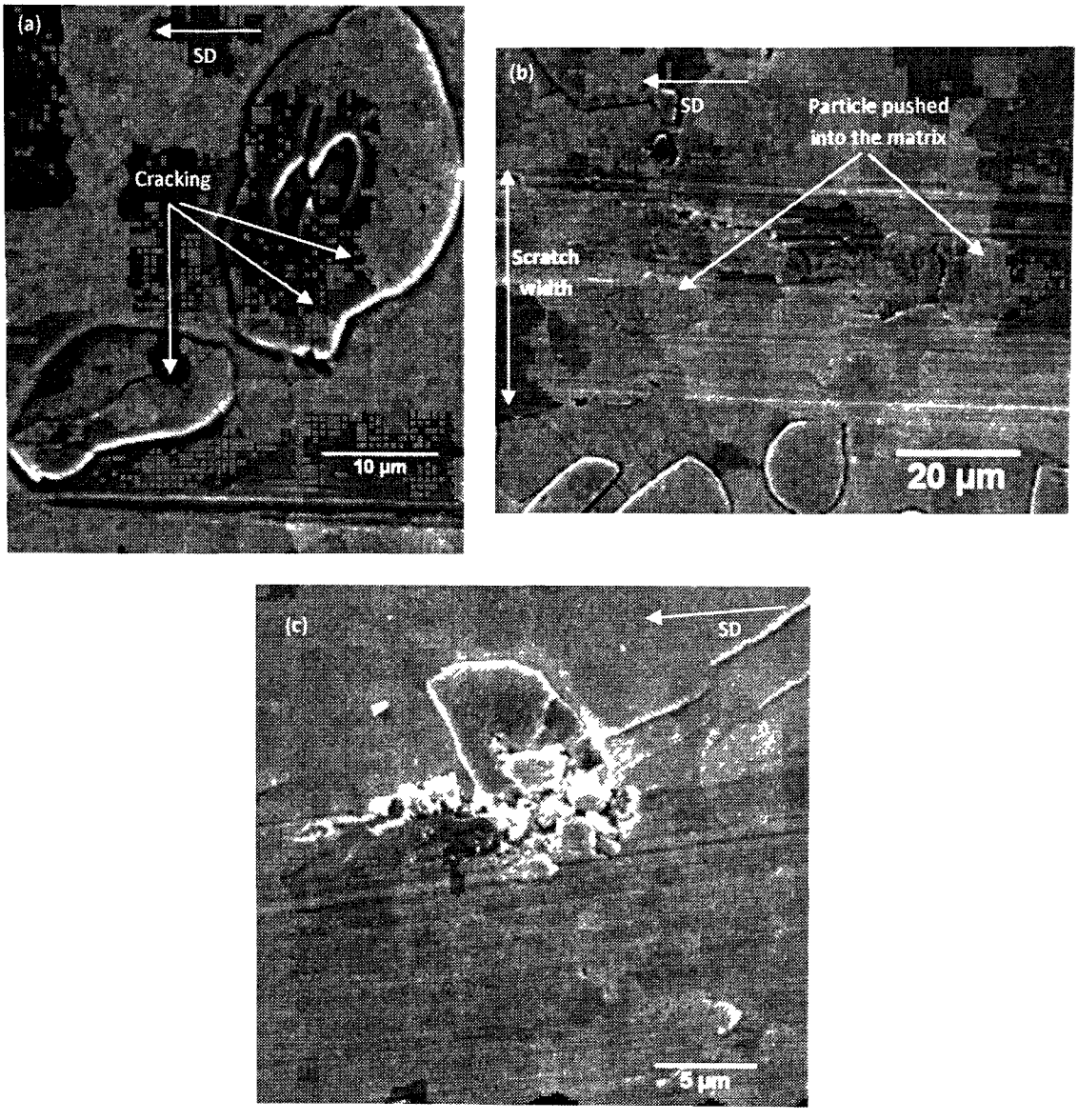

Figure 4.21. SEM micrograph of the various types of failures happened when scratch test was performed on mirror-polished-TMC sample: (a) cracking within the TiC particles at 4.22 GPa, (b) particles are pushed into the matrix and the Ti-6Al-4V matrix is smeared over the particles at 6.29 GPa, and (c) fracture of TiC particles at the edge of the scratch at 8.22 GPa. The arrow marked as "SD" shows the direction of sliding.

The relationship between the applied load and the density of the half-cone cracks has been studied by Keer et al [122]. They confirmed that the density of cracks depends on various parameters namely normal load, critical flaw size and fracture toughness. The cracking density of the 6-65h- and 8-20min-type coatings was compared based on the average interval of circular cracks that were formed under an equal contact pressure. The

SEM micrographs of Figure 4.22 illustrate the scratches formed under 14.2 GPa contact pressure on TMC-6-65h and TMC-8-20min.

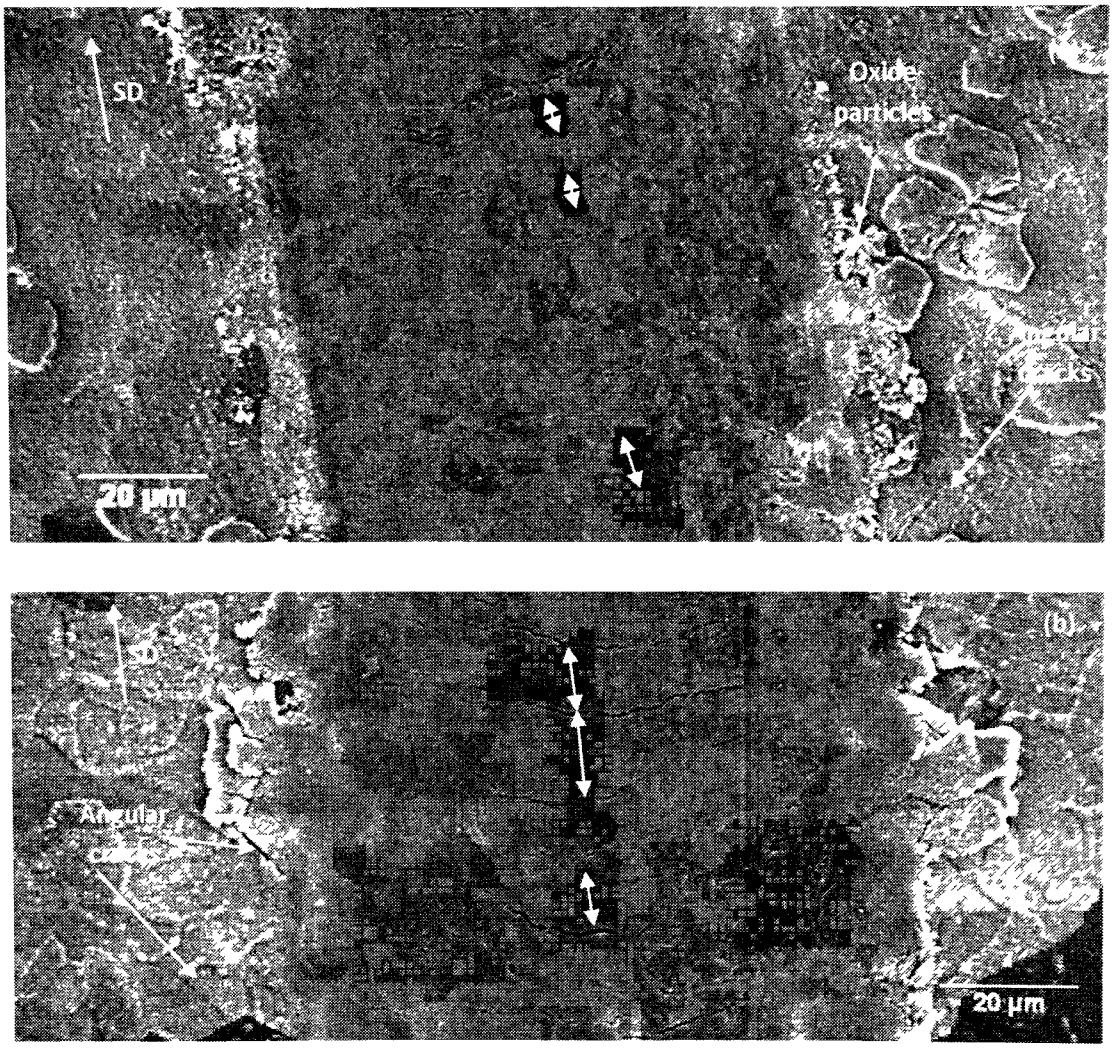

Figure 4.22. SEM micrograph of the scratch formed at 14.2 GPa on (a) TMC-6-65h and (b) TMC-8-20min showing the angular and half-cone cracks formed. The average spacing between the latter was 7.5 and 12.5 μm respectively. The arrow marked as "SD" shows the direction of sliding.

The average interval by which the cracks were repeated was measured parallel to sliding direction at the center of the scratch groove. The measured spacing was 7.5±1.9 and 12.5±3.4 μm for TMC-6-65h and TMC 8-20min respectively. The results of measurements confirmed that a higher crack density existed on TMC-6-65h. Due to the

approximate nature of this approach, the fracture toughness was calculated by indentation cracking method which results are presented in section 4.4.5.

4.4.5 Fracture Toughness Measured by Indentation Crack Length Method

A well-known method for estimating the fracture toughness of brittle materials is to measure the length of the cracks emanating from the corners of a Vickers-type indentation. Micro-indentation tests were performed on TMC-6-65h and TMC-8-20min samples under variable normal loads of 0.75, 1, 1.25, 1.5, 1.75, 2 and 3 N, with at least 30 indentations at each load. The crack length from the corners of indentation (l) and the indent half-diagonal (a) were measured using SEM and Ominemet image analyzing software. The measured values were used to determine whether Palmqvist or radial-median cracking is the prevailing mode, as previously described in section 2.3. The fracture toughness of the coatings was then calculated utilizing equations 2.17, 2.18 and 2.22. These equations will be referred to as Niharra [102], Shetty [104] and LEM [116] equations respectively. The SEM observations on the indents and the details of the calculations are described here.

Figure 4.23 (a) illustrates the indentation mark formed on TMC-6-65h sample under 1 N normal load. It is apparent that the lateral cracks—or the side edge cracks—were predominant, while radial cracking at the corners of the indentation was also evidenced (Figure 4.23 (b)). The crack length measurements were performed on perfect indentations which were defined as indentation with all 4 radial cracks which were not located on an oxidized particle. The length of the indent half diagonal (a) and the radial crack (l) were measured as shown in Figure 4.23 (a) and (b). The average and the standard deviation values of the crack and indent dimensions together with the length of crack from the center of indent ($c=l+a$) are given in Table 4.3. The hardness and elastic modulus values at each indentation load were calculated from the load-penetration depth curve utilizing the Oliver and Pharr method [119]—described in Appendix 1. These values as well as the values of maximum indentation depth under each load are also listed in Table 4.3. The average thickness of the coating on Ti-6Al-4V substrate was 0.73±0.15 (Table 4.2). Therefore the indenter penetrated the coating/substrate interface. It is known that the penetration depth of the indenter should be less than one tenth of the coating

thickness in order to measure the properties of the coating without significant interference of the substrate [116]. This means that the parameters obtained here are actually a combination of the properties of the coating and substrate, which are designated as composite hardness or elastic modulus.

The indentation mark formed on TMC-8-20min sample at 1N normal load is illustrated in SEM micrograph of Figure 4.24 (a) and the radial crack emanating from the corner of the indent is shown at higher magnification in Figure 4.24 (b). For 8-20min type of samples, radial cracking was predominant. At loads higher than 1.75 N, however, the lateral cracking predominant for 6-65h type samples became apparent in 8-20min type samples. Similarly, the radial crack and indent dimensions were measured as shown in Figure 4.24 (a) and (b). These values together with the composite hardness and elastic modulus values and the maximum indentation depths are listed in Table 4.4. The average thickness of the 8-20min type coating was 2.6 μm (Table 4.2). The indenter, therefore, penetrated beyond the coating/substrate interface.

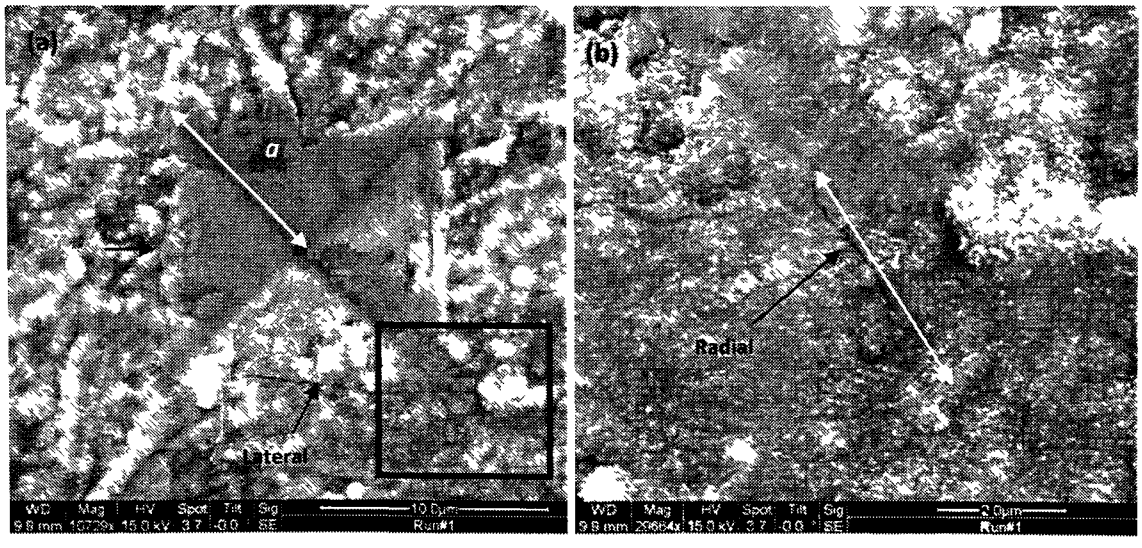

Figure 4 23. SEM micrographs of (a) the indentation mark formed on TMC-6-65h sample under 1 N load showing the lateral and radial cracks and (b) a higher magnification of the area enclosed by the black box in (a) The measured length of the crack (l), and the measured indent half diagonal (a) are shown

Table 4.3. The length of the radial crack from corners of indent mark (l), the indent half-diagonal length (a),and the length of the crack from the center of indent (c) as measured from the SEM micrographs of the indentations performed on TMC-6-65h sample. The composite Vickers hardness (Hv) and elastic modulus (E) and the maximum indentation depth (P_d) are also presented.

Load (N)	0 75	1.00	1.25	1.50	1 75	2.00
l (μm)	3.03±1.05	4.04±0.85	4.75±2.87	5.71±1.05	7.66±2.35	8.49±3 04
a (μm)	6.70±1.05	8.28±0.79	9.82±1.56	10 80±0.88	11 42±1 17	12.38±1 17
$C = l+a$ (μm)	9 74±0.96	12 34±0 88	14.57±4.34	16.51±1.27	19.08±2 55	20.86±2.66
Hv	847.2±251.3	936.2±147.0	604.5±144.3	590.6±89.6	550 3±94 4	521.6±76.5
E (GPa)	147 3±25.7	153.2±17 6	113.6±17.3	95.8±11.3	92 3±23 1	85 7±9.1
P_d (μm)	2.3±0.2	2.5±0.2	3 4±0 4	4.1±0.3	4.2±0.3	4 7±0 3

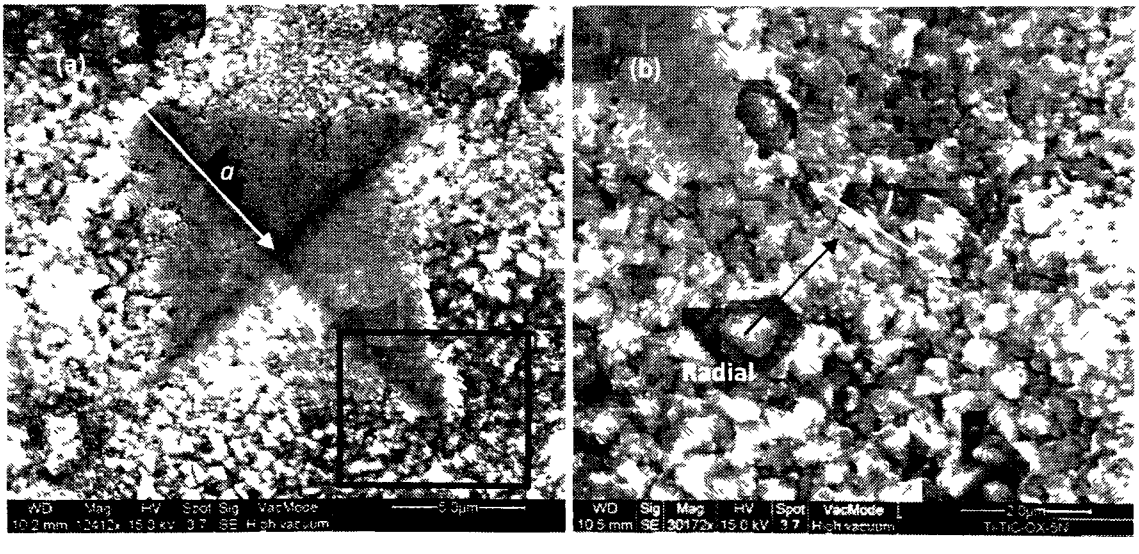

Figure 4.24. SEM micrographs of (a) the indentation mark formed on TMC-8-20min sample under 1 N load showing the radial crack and (b) a higher magnification of the area enclosed by the black box in (a). The measured length of the crack (l), and the measured indent half diagonal (a) are shown

Table 4.4 The length of the radial crack from corners of indent mark (l), the indent half-diagonal length (a),and the length of the crack from the center of indent (c) as measured from the SEM micrographs of the indentations performed on TMC-8-20min sample. The composite Vickers hardness (Hv) and elastic modulus (E) and the maximum indentation depth (P_d) are also presented.

Load (N)	1.00	1.25	1.50	1.75	2.00	3.00
l (μm)	2.76±0.27	4.64±0.85	5.08±1.07	7.01±1.01	8.02±1.31	9.95±1.79
a (μm)	7.38±1.46	8.73±1.35	9.67±0.89	11.27±0.73	12.28±1.68	14.25±1.31
c (μm)	10.14±1.51	13.48±1.35	14.75±1.67	18.28±1.01	20.29±2.40	24.20±2.35
Hv	1087.9±173.6	1211.7±193.9	1028.3±191.3	839.6±120.3	735.8±47.0	841.8±91.9
E (GPa)	160.9±18.4	170.6±20.8	144.6±9.6	117.2±16.0	109.9±10.3	130.3±9.0
P_d (μm)	2.4±0.2	2.6±0.1	3.1±0.0	3.7±0.1	4.0±0.1	4.6±0.2

In order to determine the type of the radial cracks, the load dependence of crack length was studied. As previously described in section 2.3, according to Shetty et al [104] Li et al [112] and Ponton et al [100], the plot of crack length from the center of the indentation ($c = l + a$), versus indentation load provides a criterion to identify the cracking type. For the radial-median cracks a relationship of type $c = AP^{2/3}$ and for Palmqvist cracks a relationship of type $c = AP + BP^{1/2} + D$ should fit the c-P data. The experimental data of crack length from the center of indent (c) was plotted as a function of indentation load (P) for TMC-6-65h and TMC-8-20min samples. These plots are presented respectively in Figure 4.25 and Figure 4.26, the least square fit predictions of the radial-median and Palmqvist equations were then generated using MATLAB software. For both types of the samples, the Palmqvist type equation gives a better fit overall than the median type since the R-square values were higher for Palmqvist type equation compared to median type equation. Therefore, Palmqvist type was the more probable geometry for radial cracking on both TMC-6-65h and TMC-8-20min. Nolan et al [99] suggested that for the thin brittle films on tough substrate it is reasonable to assume the Palmqvist morphology to dominate as this type of cracking initiates at the

surface (where the coating is more brittle) rather than at depth (where the more ductile substrate exists). This is in agreement with the results of the current study where the formation of Palmqvist type cracks was evidenced within the relatively brittle rutile scale rather than the formation of median type cracks within the more ductile Ti-6Al-4V substrate.

The equations based on the Palmqvist cracking geometry were previously described in section 2.3.2. Equations 2.27 and 2.18 has been proved to give fracture toughness values in agreement with conventional measurement techniques [112,113] which are repeated here:

$$K_{Ic} = 0.0122\left(\frac{E}{Hv}\right)^{\frac{2}{5}} P/(al^{\frac{1}{2}}) \qquad \text{Equation 2.17}$$

$$K_{Ic} = 0.0319P/(al^{\frac{1}{2}}) \qquad \text{Equation 2.18}$$

Equation 2.17 was proposed by Niharra [102] who considered the Palmqvist cracks as semi-elliptical, surface cracks, while in deriving equation 2.18 Shetty [104] et al assumed that the Palmqvist cracks are two-dimensional through cracks. It should be noted that these models are developed for monolithic materials and a suitable extension to coating/substrate system is not available. The hardness value in equation 2.17 is defined as load divided by the area. For a coating/substrate system the area of contact is modified by the fact that the compliance is influenced by the underlying substrate, and also the plastic zone underneath the indenter is penetrated the substrate [116]. The comparison between the indentation depth and the coating thickness confirmed that, for both types of coatings, the indenter penetrated beyond the coating/substrate interface (Table 4.3 and Table 4.4). Therefore, the lengths of the cracks were also modified by the presence of the oxygen diffusion zone beneath the coating scale. The composite hardness, therefore, should be incorporated into equation 2.17 and the estimated fracture toughness would represent the composite fracture toughness of the coating and the substrate. The composite hardness and elastic modulus values were calculated from the load-penetration depth data utilizing Oliver and Pharr method [119]—explained Appendix A— and are listed in Table 4.3 and Table 4.4. As a result of the load dependence of these effective

hardness values, the indentation size effect on the true hardness value cannot be discriminated here.

In order to determine the fracture toughness of TMC-6-65h and TMC-8-20min samples based on the Niharra's equation, the values of $(0.0122\left(\frac{E}{Hv}\right)^{\frac{2}{5}}P)$ were calculated from the data given in Table 4.3 and Table 4.4 which was then plotted against $(al^{\frac{1}{2}})$ data. These plots are shown in Figure 4.27 along with the linear fits that were generated using MATLAB software. The slope of the linear fit, according to equation 2.17, is equal to K_{IC}. The fracture toughness values were also determined based on equation 2.18 for which the values of $(0.0319P)$ were plotted against $(al^{\frac{1}{2}})$ data for TMC-6-65h and TMC-8-20min. These plots are depicted in Figure 4.28. Similarly, the slope of the generated linear fit represents the fracture toughness value (K_{IC}). The fracture toughness values obtained by these methods are tabulated in Table 4.5.

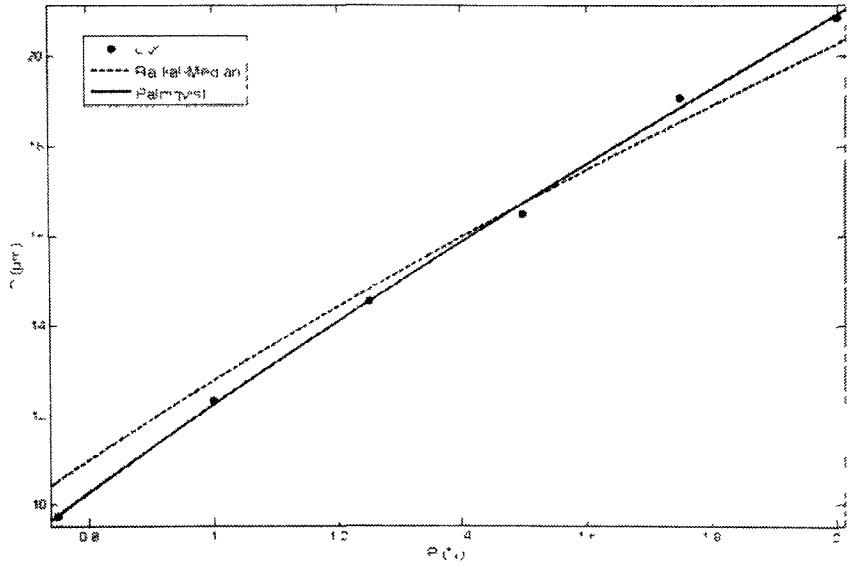

Figure 4.25. A comparison of the experimental data of measured crack length from the center of the indenter, c, and load data with the least square predictions of the Palmqvist and radial-median crack type equations for TMC-6-65h samples The R-square value is 0.9986 for Palmqvist and 0.9817 for radial-median fits.

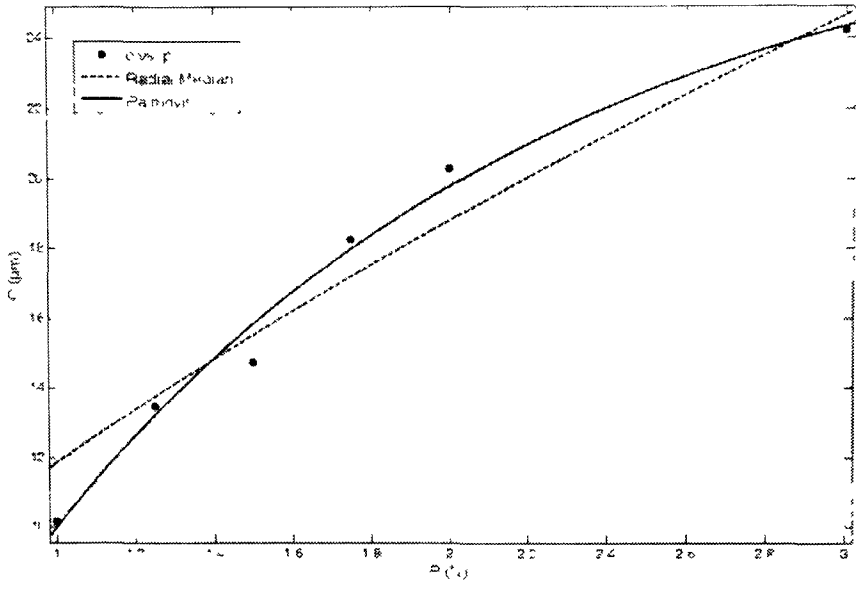

Figure 4.26. A comparison of the experimental data of measured crack length from the center of the indenter, *c*, and load data with the least square predictions of the Palmqvist and radial-median crack type equations for TMC-8-20min samples. The R-square value is 0.9872 for Palmqvist and 0.9445 for radial-median fits.

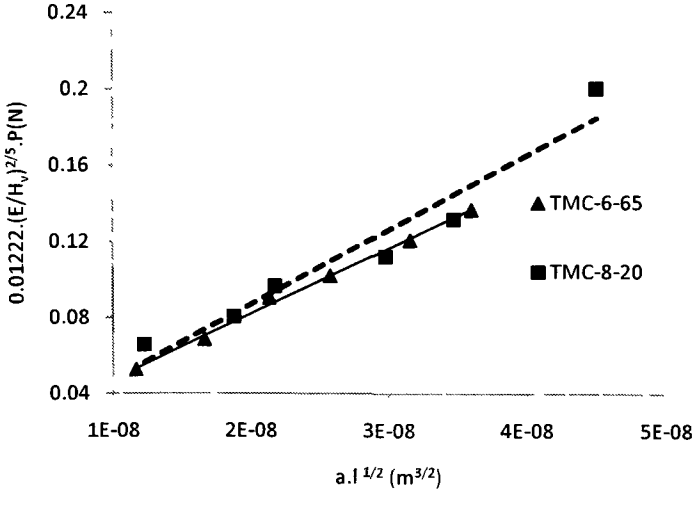

Figure 4.27 $\mathbf{0.0122}\left(\frac{E}{Hv}\right)^{2/5}\boldsymbol{P}$ as a function of $\boldsymbol{al^{\frac{1}{2}}}$ obtained according to equation 2.17 and using the data tabulated in Table 4.3 and Table 4 4. The solid and dashed lines represent the linear fit of data obtained by micro-indentations performed respectively on TMC-8-20mın and TMC-6-65h samples.

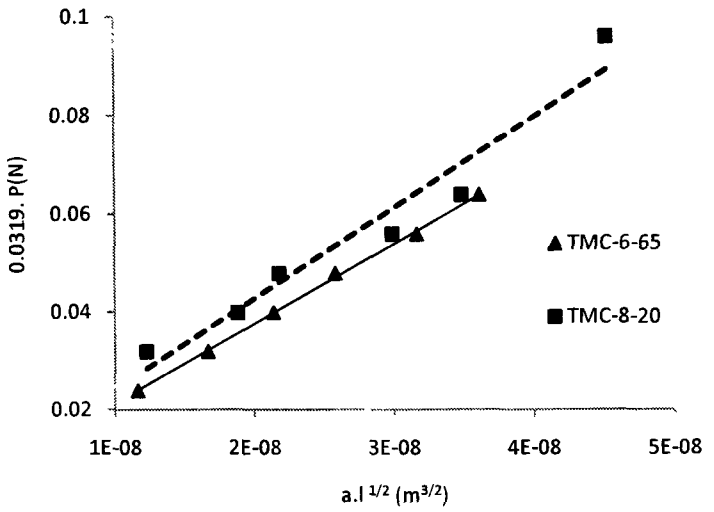

Figure 4.28. $\mathbf{0.0319}\boldsymbol{P}$ as a function of $\boldsymbol{al^{\frac{1}{2}}}$ obtained according to equation 2.18 and using the data tabulated in Table 4.3 and Table 4.4. The solid and dashed lines represent the linear fit of data obtained by micro-indentations performed respectively on TMC-8-20min and TMC-6-65h samples.

Since there is no apparent relationship for the effect of surface residual stresses on the fracture toughness data that had been developed based on Palmqvist crack models, equation 2.22 which was originally developed for radial-median crack configuration is employed here to estimate the residual stress with the oxide coatings.

$$K = X\frac{P}{c^{\frac{3}{2}}} - 2m\sigma_R\left(\frac{c}{\pi}\right)^{1/2} \qquad \text{Equation 2.22}$$

Where in the first term X is $0.016\left(\frac{E}{Hv}\right)^{1/2}$; and in the second term m is a dimensionless modification factor which is defined as follows:

$$m = 0.56\pi\frac{d/c}{(3\pi/8) + (\pi/8)(d/c)^2} \qquad \text{Equation 4.11}$$

Where d is the depth of the radial crack which can be determined by post-fracturing the sample or by FIB cross-sectioning. It is commonly assumed that the crack has a semi-circular shape and the value of m becomes unity when free-surface effects and stress gradients over the prospective crack depth are neglected [116]. When cracking happens in a coating/substrate system, the main influence of the substrate is, however, to change the

shape of the crack, and, therefore, a semi-circular shape crack can no longer be assumed. Prior knowledge of the exact value of m is only important when the value of residual stress is of interest, while the value of fracture toughness can be estimated from equation 2.22 without the knowing the correct crack shape. In our experiment, using equation 2.22 and substituting the crack length (c), the indentation load (P), the effective elastic modulus (E), and effective Vickers hardness (Hv) values from Table 4.3 and Table 4.4, $(X\frac{P}{c^{\frac{3}{2}}})$ was plotted against $(c^{1/2})$. This plot is shown in Figure 4.29 for TMC-6-65h and TMC-8-20min. A linear fit of the experimental data was then generated utilizing MATLAB software. From equation 2.22 the intercept with the ordinate axis for the linear fit is K_{IC} and the slope of the fit is $-(2m\pi^{-1/2}).\sigma_R$. Since according to equation 4.11 the value of m is always positive, the negative slope of the plots of TMC-6-65h and TMC-8-20min samples implies a tensile residual stress within the coating. The fracture toughness and the slope values measured by this model are also listed in Table 4.5.

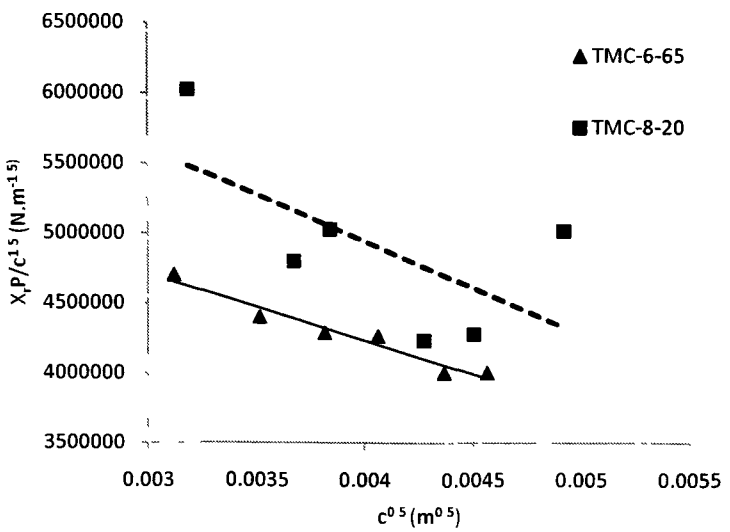

Figure 4.29. $(X\frac{P}{c^{\frac{3}{2}}})$ as a function of $c^{\frac{1}{2}}$ obtained according to equation 2.22 and using the data tabulated in Table 4.3. The solid and dashed lines represent the linear fit of the data obtained by micro-indentations performed respectively on TMC-8-20min and TMC-6-65h samples.

Table 4.5. The fracture toughness values measured by plotting experimental data according to equations 2.17 (Niharra), 2.18 (Shetty) and 2.22 (LEM) and generating the linear fit for TMC-6-65h and TMC-8-20min samples. The slopes of the LEM plots are also listed gives information about the type of residual stress within the coating.

Coating type	Fracture toughness, K_{IC}, measured by			$-(2m\pi^{-1/2}).\sigma_R$=slope of LEM fit (MPa)
	Niharra method ($MPa.m^{1/2}$)	Shetty method ($MPa.m^{1/2}$)	LEM method ($MPa.m^{1/2}$)	
TMC-6-65h	3.9	1.8	6.1	−478.4
TMC-8-20min	4.2	2.0	7.6	−663.3

The K_{IC} values calculated by means of equations 2.17, 2.18 and 2.22 are compared for TMC-6-65h and TMC-8-20min compounds in Figure 4.30. The values of K_{IC} calculated by Niharra model are somewhat 2 times higher than the values calculated by Shetty model, and the values calculated by LEM model are roughly 1.6 times higher the values by Niharra model. Because of the absence of experimental K_{IC} values for these coatings, however, it is impossible to determine which equation results in the most accurate approximation of fracture toughness value. The values obtained by Niharra and Shetty models are more reliable, since a Palmqvist morphology was the dominant mode of radial cracking in these coating/substrate systems.

These measurements are based on indentation tests where the indenter penetrated beyond the coating and therefore represent a combination of the fracture toughness of the coating and the substrate. The fracture toughness values obtained here, thus, should be interpreted with cautious since these equations are originally developed for monolithic materials and, to the author's knowledge, no apparent relationship exists that defines the effect of substrate on the measures values. These values, however, can be used to evaluate the performance of the combination of the oxide coating/ODZ layers—formed at 6-65h and 8-20min type conditions—under contact stresses during sliding.

In spite of the type of the equation used to estimate the composite fracture toughness, the values obtained for 6-65h-type oxide was always lower than the values for 8-20min-type oxide. Additionally, lateral type cracks were observed when indentation

was performed on TMC-6-65h sample at 0.75 N while the onset of lateral cracking on TMC-8-20min occurred at 1.75 N. The occurrence of lateral cracks contributes to the energy dissipated during the loading-unloading cycle and decreases the energy dissipated during radial type fracture. In estimation of fracture toughness values only the fraction of energy dissipated by radial type cracking was considered, and the lateral type cracks were neglected, and, therefore, the values calculated for TMC-6-65h overestimates the fracture toughness, and the difference between K_{IC} values of TMC-6-65h and TMC-8-20min should be even higher.

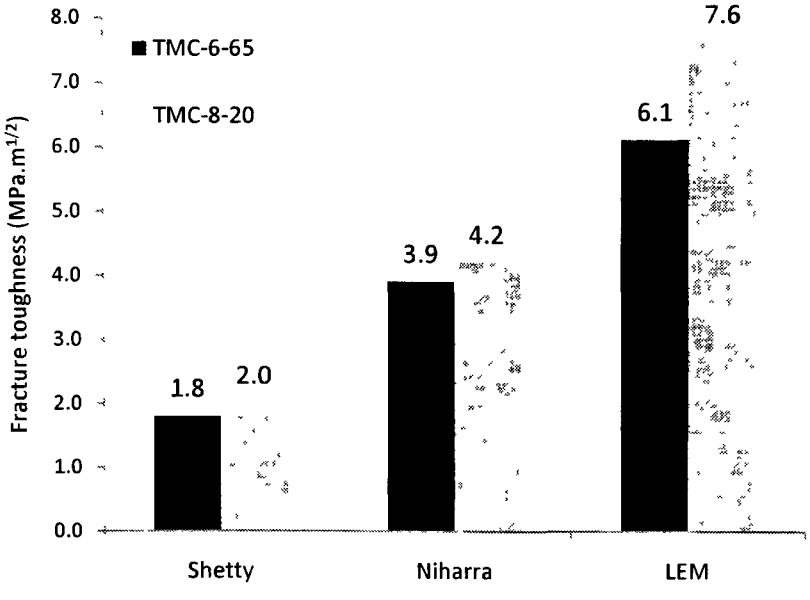

Figure 4.30. Fracture toughness of TMC-6-65h and TMC-8-20min samples calculated from equations 2.12 (Niharra), 2.18 (Shetty) and 2.22 (LEM).

4.5 Ball-on-Disk Tests and Characterization of Worn Surface

The tribological behaviour of TMC samples and thermally oxidized TMC samples under sliding wear was evaluated utilizing a ball-on-disk test configuration. The wear tests were performed on Ti-6Al-4V, TMC and TMC-8-20min samples under normal loads of 2, 3.5, 5, 7, and 10. All tests were run under dry condition, at room temperature, 30 %RH, at a sliding velocity of 0.3 m/s. The mechanical properties of Ti-6Al-4V are very sensitive to temperature;. for example the yield strength of this alloy decreases from 950 MPa at room temperature to 450 MPa at 500°C [50]. Thermal softening effects, on the

other hand, are often considered when explaining the increase in delaminative wear as the sliding velocity or the ambient temperature is increased [62]. Straffelini and Molinari [50] conducted a comprehensive study on the disk-on-disk sliding wear properties of Ti-6Al-4V against steel and Ti-6Al-4V counterfaces within a sliding velocity range of 0.3-0.8 m/s. The surface average contact temperature and the wear mechanism observations confirmed that the thermal softening effects are not of sufficient intensity when the sliding velocity is 0.3 m/s [50]. This sliding velocity was, therefore, adopted in the current study to prevent the thermal effects that occur during sliding contact. Each test involved a total sliding distance of 1,000 m, which proved to be sufficient for the attainment of a steady-state situation in all tests (section 4.5.1.1).

The variation of wear rates with load and sliding distance, SEM observation performed on the worn surface, worn subsurface and the wear debris generated from TMC samples are presented in section 4.5.1 and compared to Ti-6Al-4V samples. In section 4.5.2 the wear rate data and SEM observation results of TMC-8-20min sample are presented which are then compared to TMC samples.

4.5.1 Wear Rates and Wear Mechanisms of TMC Sample

4.5.1.1 Variation of Wear Rate with Load and Sliding Distance

The variation of wear rates with normal load for Ti-6Al-4V and TMC samples against chrome-steel (C/S) ball is shown in Figure 4.31. The Vickers hardness of the chrome-steel balls was 700 HV Ascribing the following values: $E_{Ti64} = 110\ GPa$, $\vartheta_{Ti64} = 0.3$, $E_{C/S} = 210\ GPa$ and $\vartheta_{C/S} = 0.0.3$, the contact pressure produced by 6mm diameter ball for the loads of 2, 3.5, 5, 7, and 10 N were 0.65, 0.78, 0.88, 0.98 and 1.11 GPa. In order to determine the wear rate of samples based on the definition given in section 2.1.6.1, the measured mass loss values were converted into volume loss, which was then divided by the total sliding distance (1,000 m). It can be seen in Figure 4.31 that the wear rate of Ti-6Al-4V and TMC samples increased by increasing normal load. The negative value of wear rate of TMC sample at 2 N normal load, i.e. $-3.16 \times 10^{-5}(mm^3/mm)$, implies that the mass was gained by this sample. The wear rate of TMC sample increased moderately when load increased to 5 N, followed by an abrupt

increase from 841.9×10^{-6} to 1808.1×10^{-6} (mm^3/mm) as the load rose from 5 to 7 N. Despite of this sudden increase, the wear rate of TMC samples remained lower than the wear rate of Ti-6Al-4V samples provided that the load remained lower than 7 N. The wear rate of TMC sample tested at 10 N normal load was somewhat 2 times higher than the wear rate of Ti-6Al-4V sample.

Based on the load dependence of wear rate values, three regimes were distinguished for TMC sample, namely the low load (<2 N), the moderate loads (3.5-5 N)which data is fitted by thick dashed line in Figure 4.31 and high loads (7-10 N) which data is fitted by thick solid line.

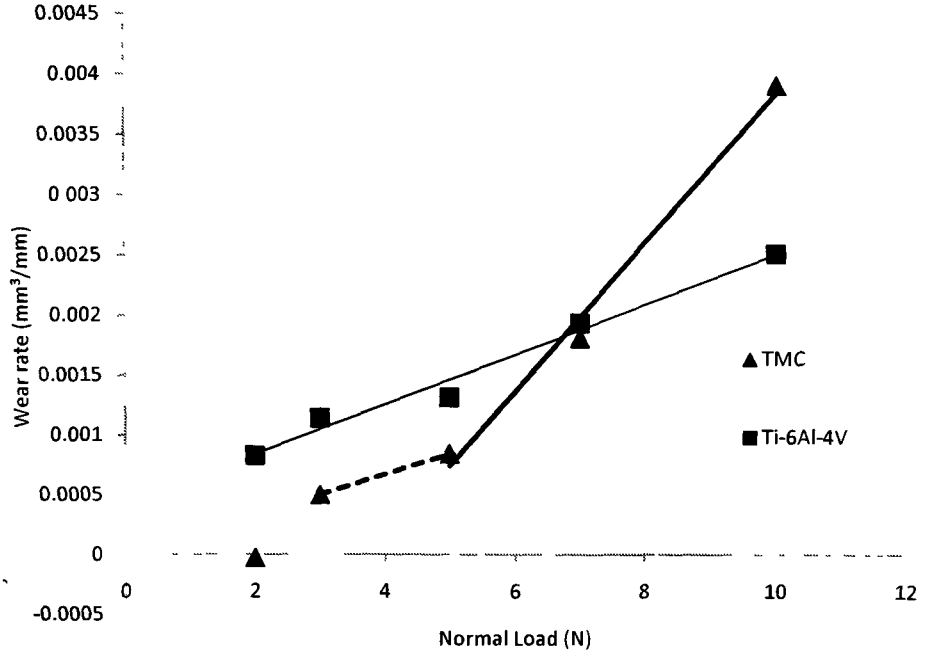

Figure 4.31. The wear rate of TMC and Ti-6Al-4V samples within the normal load range of 2-10N based on the weight loss measurement. The thin line is the linear fit generated for Ti-6Al-4V data. The thick dashed and solid lines represent the linear fit for the moderate loads and the high loads distinguished for TMC samples.

As previously described in section 3.6.3, the vertical position of the ball was also continuously recorded with an electrical transducer and the wear rate was deducted from the variations in the depth of penetration. The volume loss vs. sliding distance graphs for TMC and Ti-6Al-4V samples are presented in Figure 4.32 (a), (b) and (c) for the constant normal loads of 2, 5 and 10 N which represent the low loads, the moderate loads and high

loads, respectively. As can be seen in these plots, except for the short initial running in period (lower than 200 m) which is excluded from the graph, a linear fit can be generated for both TMC and Ti-6Al-4V data up to the highest load studied. This assured that a steady state condition was achieved in all the tests. For the low loads (Figure 4.32 (a)), not only the slope of the plot is lower for TMC sample, but also the volume loss is somewhat half of the volume loss of Ti-6Al-4V When the load increased to 10 N, however, the volume loss of TMC sample rose to around 1.5 times the volume loss of Ti-6Al-4V (Figure 4.31 (c)). For the moderate loads of 5 N (Figure 4.32 (b)) both the slope of the plot and the volume loss values of TMC and Ti-6Al-4V were roughly equal.

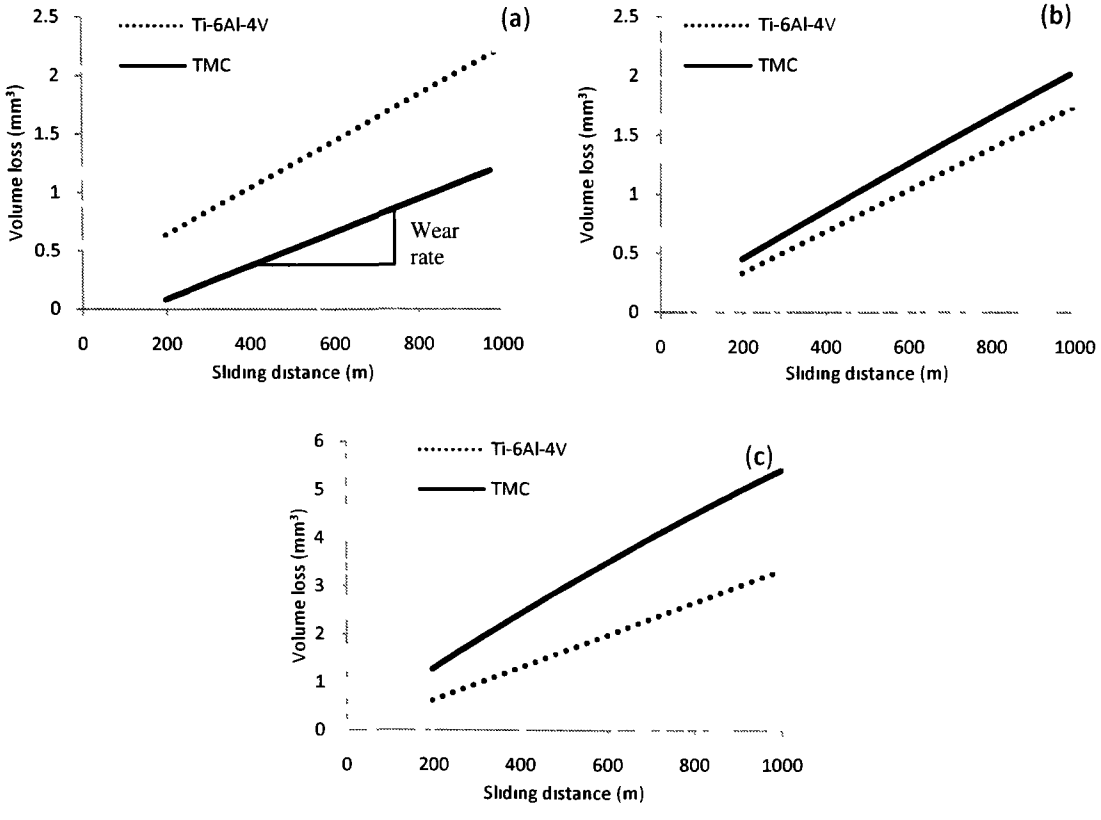

Figure 4.32. Variation of volume loss of Ti-6Al-4V and TMC samples with sliding distance at constant normal loads of (a) 2, (b) 5 and (c) 10N. The volume loss data are calculated based on the recorded depth data.

The variation of volume loss of TMC samples with sliding distance is compared for various normal loads in Figure 4.33. The three load regimes, which were identified based on the mass loss method, are confirmed by the slope of these graphs.

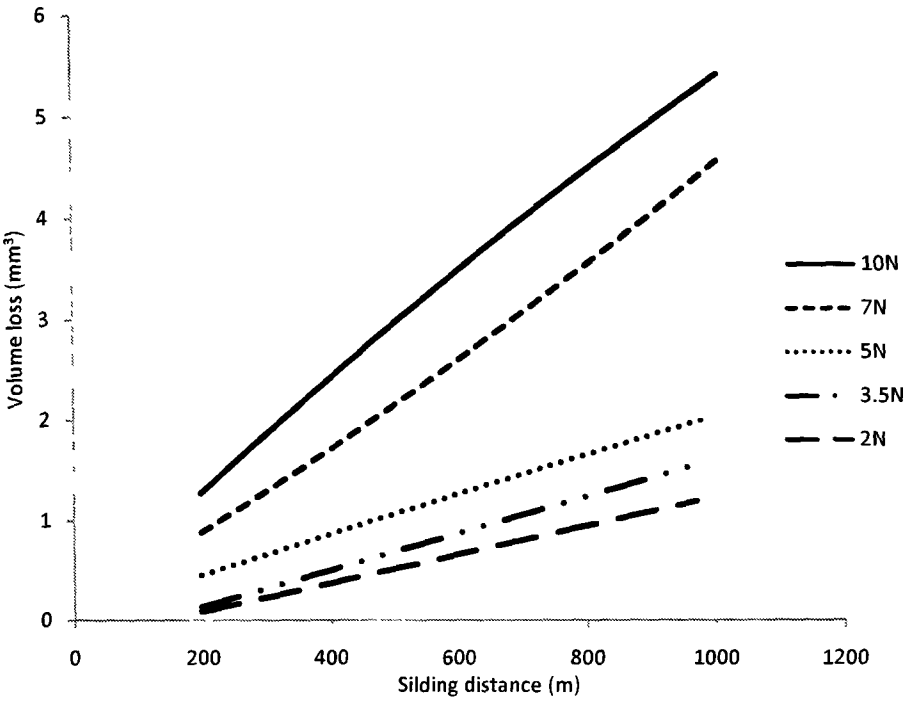

Figure 4.33. Variation of volume loss of TMC with sliding distance at constant normal loads within the range of 2-10 N. The volume loss data are calculated based on the depth change data.

The steady state wear rates were determined based on the linear fit of the depth-based volume loss data, and are presented in Figure 4.34 for Ti-6Al-4V and TMC samples. According to Figure 4.31 and Figure 4.34, the wear rate values that were obtained from depth changes were higher than the wear rate values that were determined from the mass loss data for both Ti-6Al-4V and TMC samples, and the difference was higher for TMC samples. It should be noted that a fraction of the counterface material that is worn away and removed from the contact area contributes to the recorded depth change data, and the depth based wear rate data represent both the volume loss of the disk and a fraction of the volume loss of the ball. The higher values of depth based wear rate can be therefore justified based on the contribution of counterface wear rate to the recorded depth data. The higher difference between the depth based and mass loss based wear rate data of TMC samples compared to Ti-6Al-4V samples were caused by either or both of the following factors: i) abrasion of counterface by TMC sample caused by the presence of abrasive TiC particles or ii) material transfer from Ti-6Al-4V alloy to the steel counterface. It is also interesting to note that the ratio of the depth based wear rate to the mass loss based wear rate of TMC samples was 3.48 at 2 N and 1.35 at 10 N. The larger

difference at lower loads was attributed to a more severe abrasion occurred at 2 N compared to 10 N. All these factors contributed to a larger shift in wear rate data of TMC sample to higher values compared to the shift in the wear rate data of Ti-6Al-4V sample and the displaced graphs of TMC and Ti-6Al-4V cross each other at lower loads compared to the mass loss based graphs. The critical load at which the wear rate of TMC samples increased over Ti-6Al-4V sample was consequently 5 N for depth based type measurements and 7 N for mass loss type measurements. Despite of these observed shifts in the wear rate of TMC samples relative to Ti-6Al-4V sample, the wear behaviour of TMC sample remained the same and similarly three load regimes were identified from the depth based wear measurements, namely the low loads (< 2 N), the moderate loads (3.5-5 N) and the high loads (7-10 N).

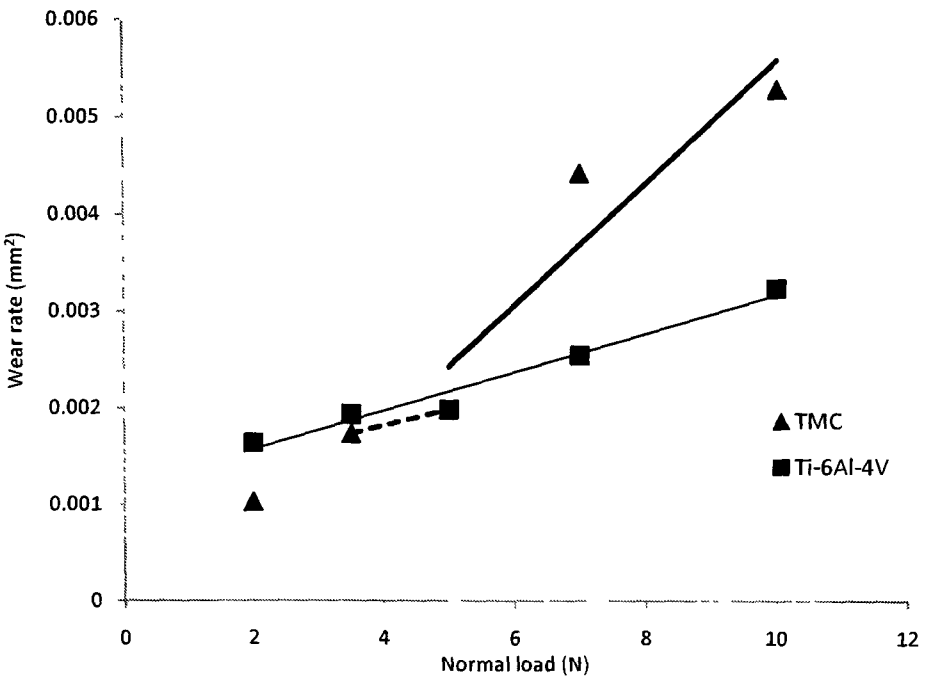

Figure 4.34. The wear rate of TMC and Ti-6Al-4V samples within the normal load range of 2-10N based on the depth changes measured at each load. The thin line is the linear fit generated for Ti-6Al-4V data. The thick dashed and solid lines represent the linear fit for the low loads and the high loads identified for TMC samples.

4.5.1.2 Variation of Coefficient of Friction by Sliding Distance and Load

Typical COF plots representing dry sliding of the TMC and Ti-6Al-4V samples against C/S balls at the constant normal loads of 2, 5 and 10 N are shown in Figure 4.35

to Figure 4.37 In all instances the friction behaviour exhibited a short initial running-in period of approximately 100-200 m sliding distance that was followed by steady state behaviour. The longest running-in period belonged to TMC sample when tested at 2 N where COF rose from an initial value of 0.7 to 0.95 at the beginning of the test (150 m) followed by a sudden drop to an average value of 0.75 with large fluctuations (± 0.1), and then stayed constant at that level. As can be seen from Figure 4.36 and Figure 4.37 the shape of the COF plot is different for TMC samples tested at 5 and 10 N normal load. At these loads COF increased to a value of 0.55 and remained constant at this level. However the running-in period lasted longer for the TMC sample tested at 10N compared to 5N. Figure 4.35 to Figure 4.37 confirmed that the shape of the COF plots of Ti-6Al-4V samples tested at 2, 5 and 10 N were similar. For Ti-6Al-4V samples tested at 2 and 5 N, within a short running in period of 100m COF increased to a steady state value of around 0.6, and for Ti-6Al-4V samples tested at 10N once a sliding distance of 200m was reached, COF attained a steady state COF of 0.52.

The steady state COF levels were similar for TMC and Ti-6Al-4V samples when tested at high or moderate loads while the COF values of the TMC samples tested at low loads (2 N) was higher than the COF values of Ti-6Al-4V sample tested at the same load.

The initial rise that was observed for Ti-6Al-4V samples at all the loads and TMC samples tested at 5 and 10 N loads were attributed to the small amount of surface oxides, which were then worn away, and caused a greater degree of adhesion and a rise in friction. The initial rise in COF value of TMC samples tested at low loads was due to the initial high roughness of the surface, which produced a momentary rise in friction until surface conformity and smoothing occurred which induced the drop in COF

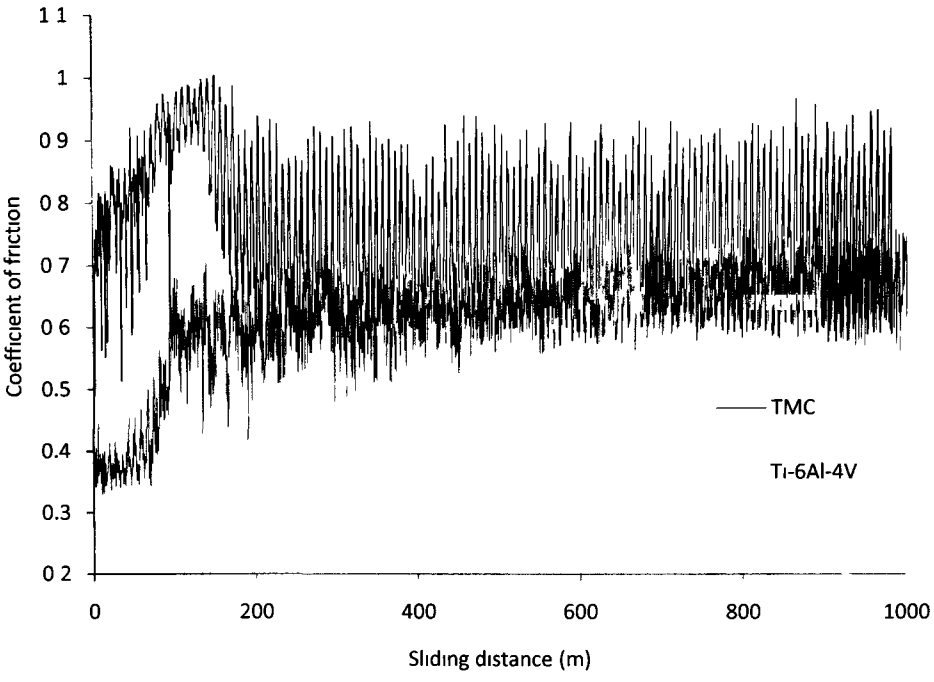

Figure 4.35. Variations of coefficient of friction with sliding distance for TMC and Ti-6Al-4V samples tested at constant normal load of 2N representing the low load regime.

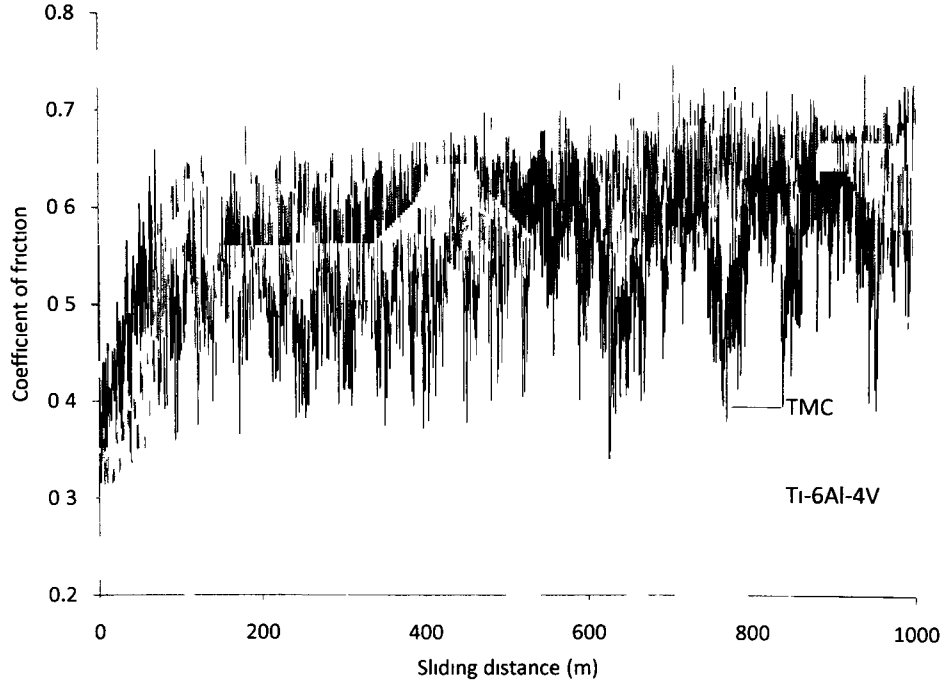

Figure 4.36. Variations of coefficient of friction with sliding distance for TMC and Ti-6Al-4V samples tested at constant normal load of 5N representing the transition load.

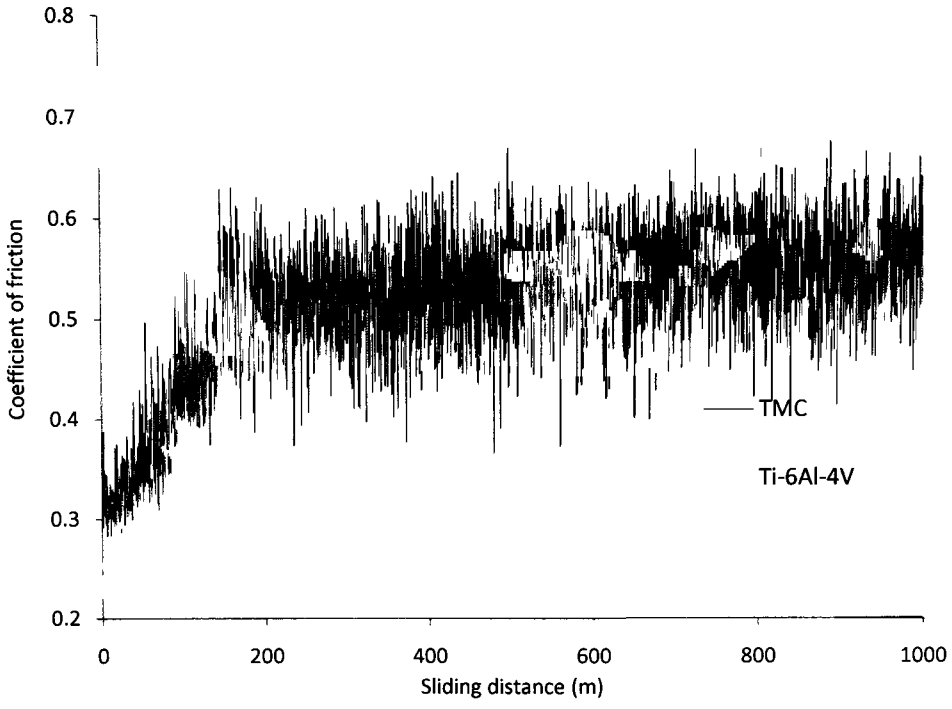

Figure 4.37. Variations of coefficient of friction with sliding distance for TMC and Ti-6Al-4V samples tested at constant normal load of 10N representing the high load regime.

4.5.1.3 SEM Observation of the Worn Surface

Worn Surface in the Low Loads (<2N)

Figure 4.38 shows the back-scattered image (BEI) of the worn surface of TMC sample tested against chrome steel ball at 2N normal load, 0.3 m/s sliding speed and to a sliding distance of 1000 m which represents the low loads. The samples were rinsed with acetone prior to microscopic examination in order to remove any loose debris. The majority of the contact area was covered by a layer which appeared darker than the substrate in back-scattered image. Regions of TMC substrate were evidenced between the dark layers—area marked as "1"—that were neither deformed nor covered by the dark layer.

A higher magnification secondary image of the wear track is shown in Figure 4.39. Surface plastic deformation in the form of grooves with 6 μm width was evidenced on the worn surface. The dark layer evidenced in Figure 4.38 was in two forms; namely patches of material smeared over the leading edge of protruding TiC particles (marked as "1" in Figure 4.39 (a)) and fine particles (marked as "2" in Figure 4.39 (a)), and the size

of the fine particle was in the range of 0.1-1 μm. Several fine scratches were also observed which were similar to the scratches formed on the matrix of TMC sample during micro-scratch test that was previously discussed in Figure 4.21 (a). The contact pressure calculated by means of Hertzian equation was 4.22 GPa for micro-scratch test while the contact pressure produced during the wear test at 2N load was 0.65 GPa. In both cases, the main contact happens at the protruding TiC particles. During the wear test, however, if the fine debris particles carry a fraction of the load, a relatively high pressure would be produced that is caused by their small size (0.1-1 μm). The pressure transformed by the oxide particles to the matrix would consequently rise to the range of the pressure produced during micro-scratch test, and this justifies the similar types of plastic deformation observed in both cases.

Figure 4.38. A low magnification back-scattered micrograph of the worn surface of TMC sample tested at 2 N normal load, 0.3 m/s sliding speed after 1000 m sliding distance. The majority of the surface was covered by a darker layer which left the uncovered areas undeformed.

In order to better identify the nature of the dark patches and the fine particles, EDS analysis on areas marked as "1" and "2" in Figure 4.39 (a) was performed. The EDS results, which are illustrated in Figure 4.39 (b), showed that the patches and the fine particles consisted mainly of Fe (70 at %) and O (27 at %) with minor amount of Ti (2 at %). The dark layer was, therefore, mainly composed of iron oxide and the peaks of Ti could be picked up from the Ti substrate beneath the iron oxide layer.

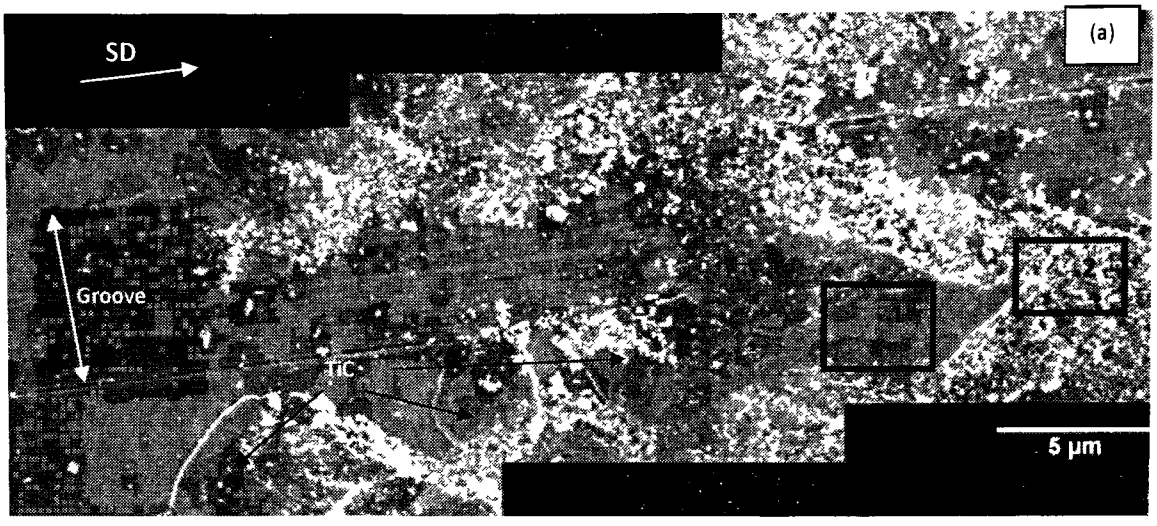

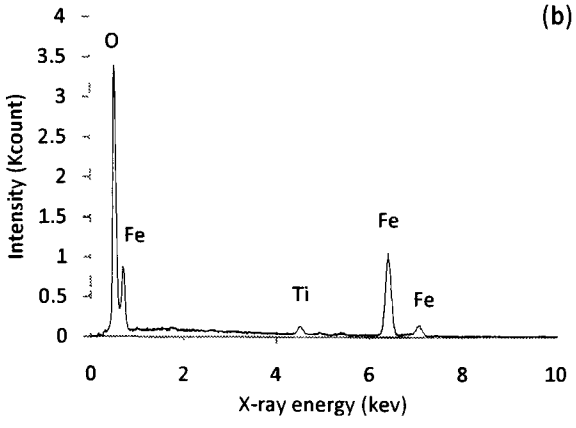

Figure 4.39. (a) A high magnification SEM micrograph of the worn surface of TMC sample tested at 2 N normal load. Area "1" shows the patches of dark layer smeared over TiC particle and "2" shows the small particles mostly on the leading edge of particles. This micrograph also illustrates formation of a large groove with smaller scratches within the groove. The EDS spectrum of regions marked as "1" and "2" in (a) is given in (b).

Figure 4.40 shows a higher magnification SEM micrograph of the TiC particles that were covered by iron oxides at their leading edge. This image was taken by tilting the SEM stage 50° relative to the beam, and revealed some of the common features of the TMC samples tested at low loads which includes: i) some scratches were formed on Ti-6Al-4V substrate that were stopped at TiC particles, ii) the main contact with the steel ball happened on the TiC particle, which were protruding from the matrix as a result of the mirror-polished surface finish prior to test and iii) patches and small particles of iron oxide covered, mainly, the leading edge of the TiC particles. Surface deformation occurred also by formation of large grooves, in addition to these small scratches. It is

noteworthy that no evidence of cracking or fracture was found within the TiC particles. In summary, at these low loads the abrasion of the steel counterface occurred by protruding TiC particles and, consequently, the TMC surface was covered by a layer of iron oxide. This was accompanied by occasional third-body abrasion of the Ti-6Al-4V by the loose oxide particles.

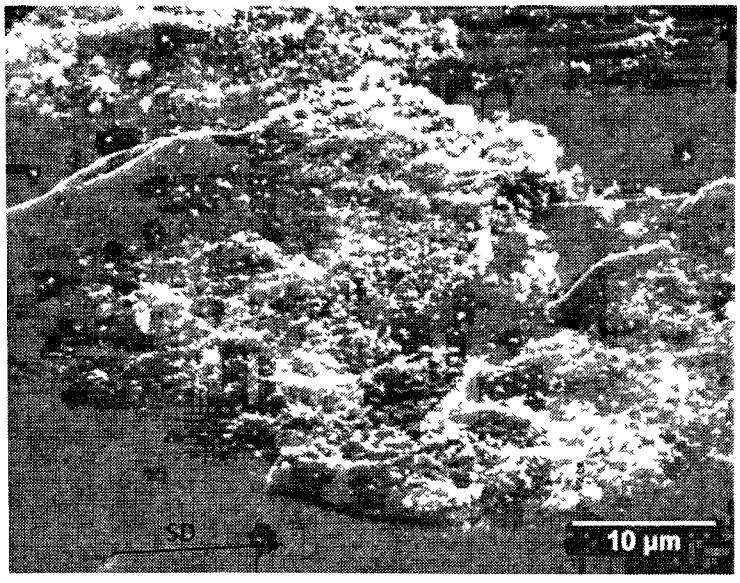

Figure 4.40. SEM micrograph of the worn surface of TMC sample tested at 2 N normal load. This image was taken by tilting the SEM stage 50° relative to the beam, and shows the TiC particles that stand higher than the Ti-6Al-4V matrix, the oxide particles that covered the leading edge of TiC and the small scratches on the matrix alloy that were stopped at the TiC particles.

Worn Surface in the high loads (7-10N)

The surface morphology of the worn surface of the TMC sample tested against chrome steel ball at 10N normal load, 0.3 m/s sliding speed and to a sliding distance of 1000 m, which represents the highs, is demonstrated in the BE image of Figure 4.41. A significant area of the wear track was covered by patches of material that looked darker in the back-scattered image. The Ti-6Al-4V matrix was heavily deformed by ploughing and cutting. The SEM micrograph in Figure 4.42 (a) illustrates the morphology of the patches of the dark material and the deformed matrix. The EDS spectrum that was obtained from area marked as"1" (Figure 4.42 (b)), revealed that these dark patches consisted of a mixture of Ti (41 at %), Fe (5 at %), Al (5 at %) and V (2 at %) oxides. A tribolayer was, therefore, formed from the mixture of TMC and the counterface oxides stacked on top of

the heavily deformed Ti-6Al-4V matrix (area marked as "2" in Figure 4.42 (a)). The EDS spectrum of the latter is depicted in Figure 4.42 (c). The atomic fraction of Fe in the tribolayer was significantly lower when the test was performed at high loads compared to low loads. The examination of area "3", which EDS spectrum is presented in Figure 4.42 (d), revealed that the TiC particles were buried under Ti-6Al-V matrix, since this area gives a high fraction of C (40 at%), and the relatively strong Al peak (4 at %) can only be justified if a layer of Ti-6Al-4Vexisted over the particles.

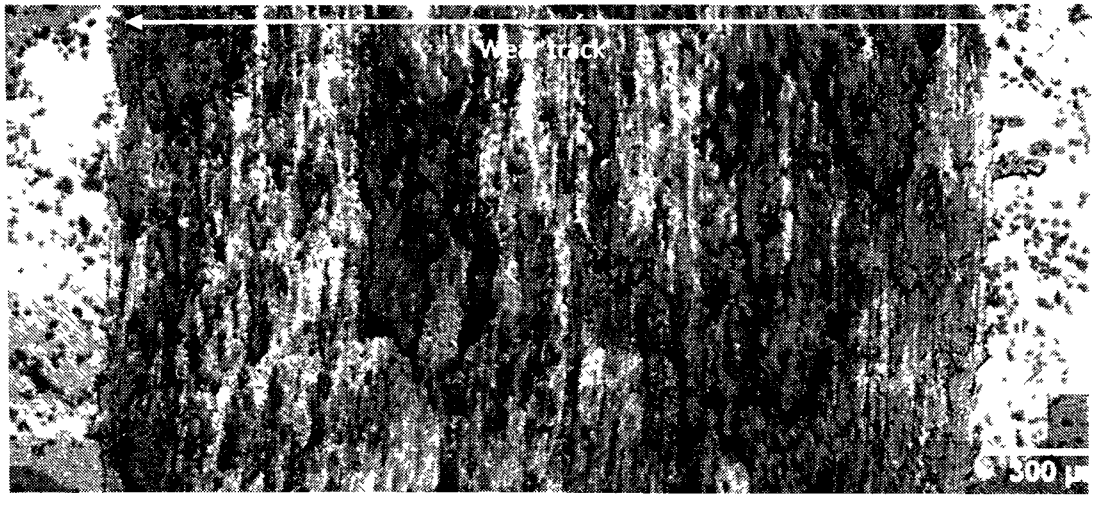

Figure 4.41. The low magnification back-scattered micrograph of the worn surface of TMC sample tested at 10 N normal load, 0.3 m/s sliding speed after 1000 m sliding distance, showing patches of a dark layer and severe deformation of the matrix by ploughing and cutting.

The morphologies of the oxide patches and the heavily deformed TMC are demonstrated in SEM micrograph of the edge of the wear track that is shown in Figure 4.43. This image was taken by tilting the SEM stage 50° relative to the beam. The tribolayer was consisted of two layers of oxide stacked loosely on top of the heavily deformed Ti-6Al-4V matrix. The morphology of these layers is described more precisely by subsurface SEM observation that is described in section 4.5.1.4. A crater is formed on the surface after the tribolayer was delaminated and both the tribolayer and the TMC substrate are heavily deformed by ploughing and shear. In summary, severe plastic deformation of Ti-6Al-4V matrix in the form of deep grooves, fractured and buried TiC particles and oxidation of the severely deformed substrate constituted the wear characteristics of the worn surface at high loads.

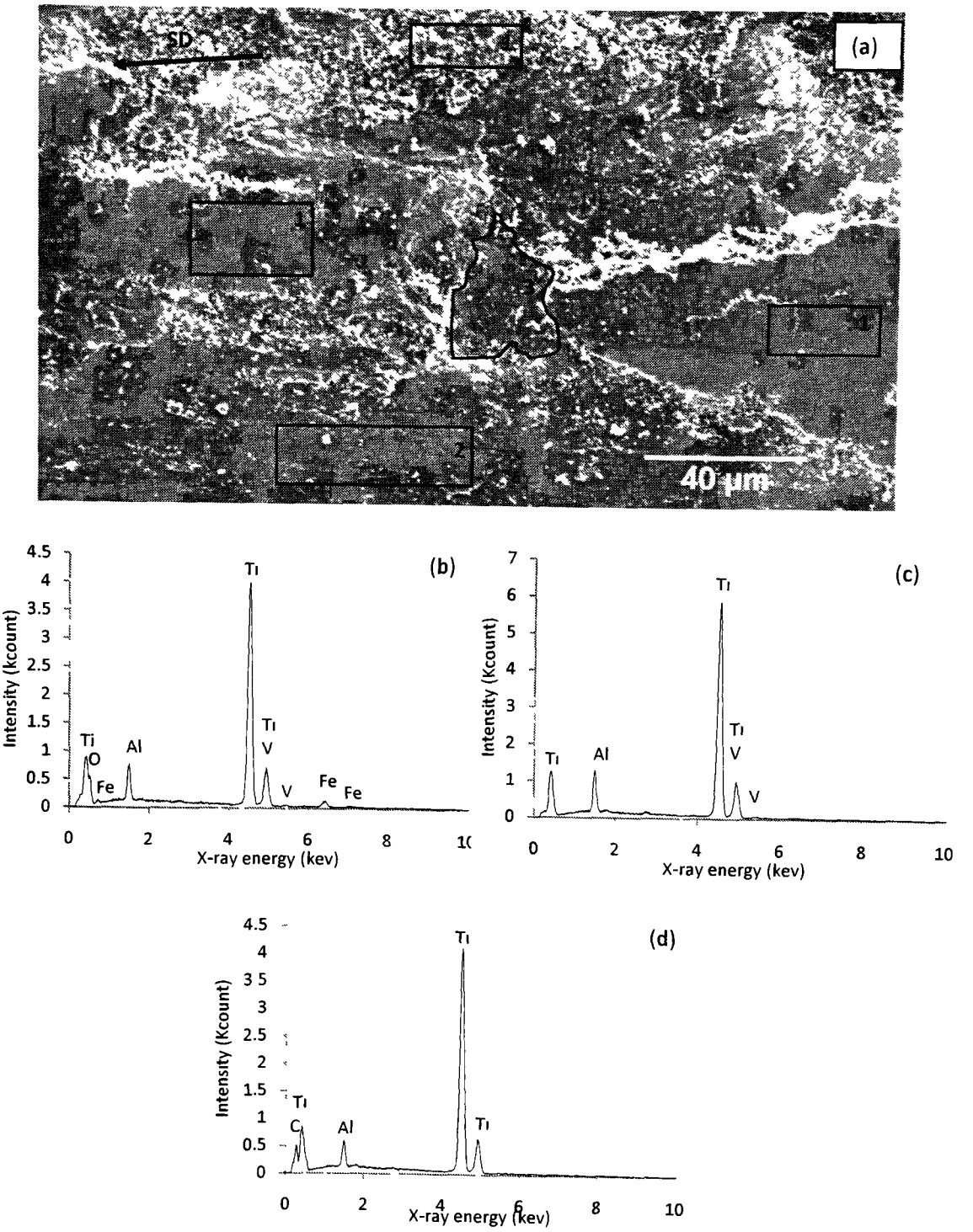

Figure 4.42. (a) SEM micrograph of the worn surface of TMC sample tested at 10N normal load. Area "1" shows a mixture of Ti, Al, Fe and V oxides in the form of patches smeared over the largely deformed matrix and particles. Area "2" shows the deformed TMC substrate and area 3 is a TiC particle sank into the Ti-6Al-4V matrix. The EDS spectra of these regions are shown in (b), (c) and (d) respectively.

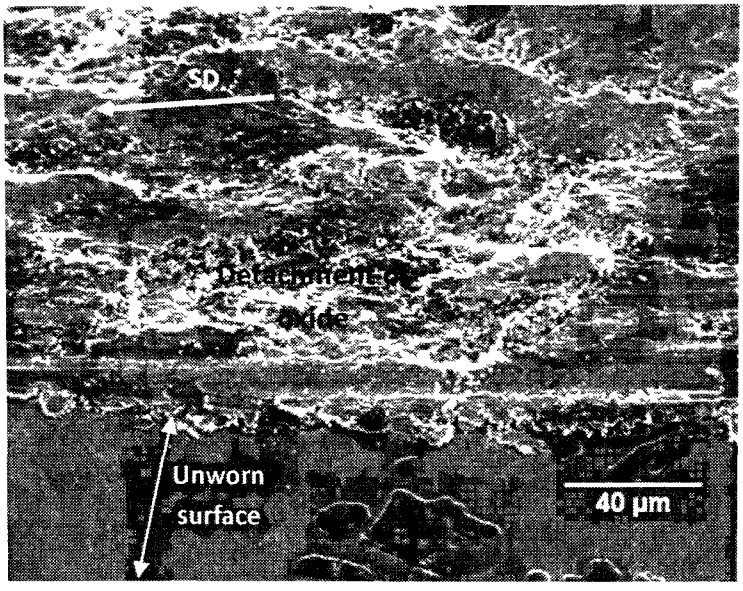

Figure 4.43. SEM micrograph of the worn surface of TMC sample tested at 10 N normal load. This image was taken by tilting the SEM stage 50° relative to the beam showing the patches of sheared oxide stacked on top of the deformed matrix and a crater formed as a result of oxide delamination.

Worn Surface at Moderate Loads (3.5-5N)

Figure 4.44 shows the morphology of the worn surface of the TMC sample tested against chrome steel ball at 5 N normal load, 0.3 m/s sliding speed and to a sliding distance of 1000 m, which represents the moderate loads. Continuous sliding marks with relatively deep grooves were the characteristic features of the worn surface. The extent of ridges and grooves was more severe than the low loads, but not as severe as the high loads. Flattened patches of a layer which appears darker than the substrate in the back-scattered mode were also evidenced. The fraction of the contact area that was covered by these layers was smaller than the high loads.

A closer inspection of the worn surface—shown in Figure 4.45 (a) —and EDS analysis of the area marked as "1" revealed that plastic deformation of Ti-6Al-4V substrate happened with ploughing in the direction of sliding and formation of tongue shaped wedges. EDS spectrum of the dark patches (marked as "2" in Figure 4.45 (a)), which is given in Figure 4.45 (b), indicated that these layers consisted of a mixture of Ti (36 at %), Fe (9 at %), Al (6 at %) and V (3 at %) oxides. The fraction of Fe oxides was higher in the tribolayer formed on the sample tested at moderate loads compared to high

loads. The EDS analysis performed on the fine particles which were located inside the grooves and around the oxide patches (marked as "3" in Figure 4.45 (a)) confirmed that the particles had a composition similar to the oxide patches.

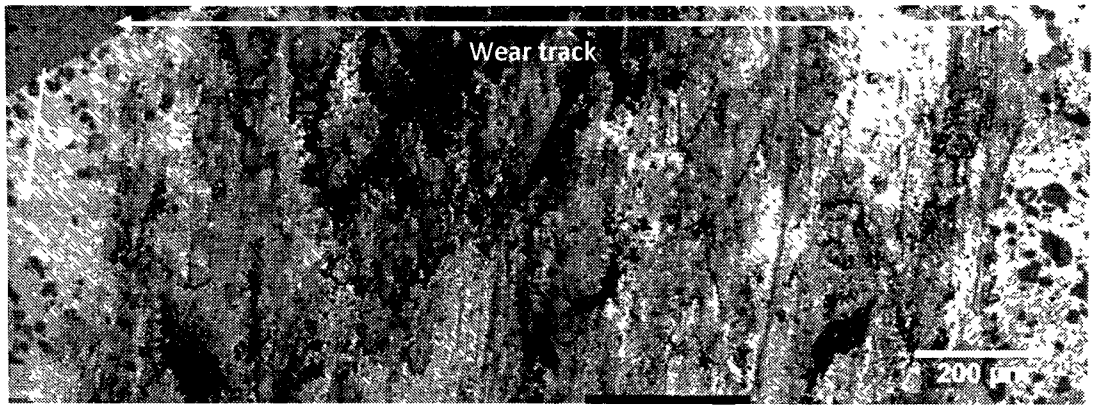

Figure 4.44. The low magnification back-scattered micrograph of the worn surface of TMC sample tested at 5 N normal load, 0.3 m/s sliding speed after 1000 m sliding distance showing patches of a dark layer, grooves and scratches on the surface.

The SEM micrograph of the typical morphology of the TiC particle within the wear track is shown in Figure 4.46, which demonstrates that for moderate loads (3.5-5 N) the particles were no longer remained intact. The contact pressure produced by the 6 mm steel ball during the wear test was in the range of 0.78-0.88 GPa, which is lower than the critical pressure identified by micro-scratch test for the onset of semi-circular type cracking within the TiC particle (5.8 GPa). These discrepancies in contact pressure can be explained based on a surface fatigue phenomenon which is characterized by surface cracking and flaking of material caused by repeated, alternating loading of solid surfaces [34]. Despite of the aforementioned differences in the contact pressures, the morphology of damaged-TiC particles in Figure 4.46 was originated from a type of cracking similar to the semi-circular cracking that was evidenced in Figure 4.21 (a), since the walls of the particle remnant render somewhat a similar geometry.

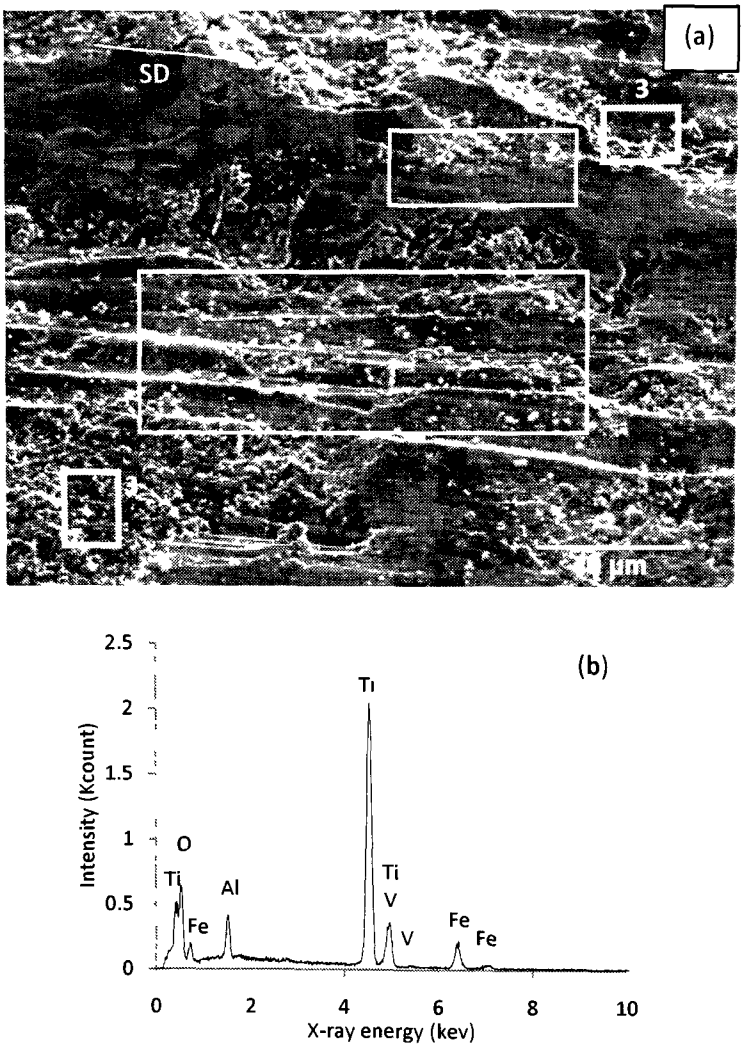

Figure 4.45. (a) SEM micrograph of the worn surface of TMC sample tested at 5 N normal load. Area "1" shows the deformed Ti-6Al-4V substrate, area "2" shows a mixture of Ti, Al, Fe and V oxides in the form of patches smeared over the matrix. Area "3" shows the fragments of the same oxide. The EDS spectrum of regions "2" and "3" is shown in (b).

In summary, as the contact pressure increased to higher than low load regime, the TiC particles were no longer the real area of contact, and the surface damage of the reinforcements placed the Ti-6Al-4V in real contact with the steel counterface. The pressure was not, however, high enough to push the particles into the matrix or completely destroy the particles, and the damaged particles maintain their role to impede plastic deformation—occurred by ploughing and scratching (Figure 4.46).

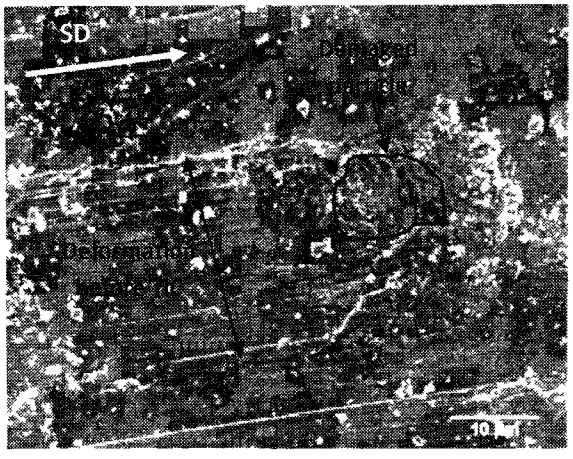

Figure 4.46. A high magnification SEM micrograph showing the morphology of damaged-TiC particles when TMC sample tested at 5N. The groove aligned with the sliding direction is stopped at the particles.

4.5.1.4 Cross-sectional SEM Observations of the Worn Subsurface

The morphology of the tribolayers formed and the degree of subsurface damage were studied by sectioning the wear track of TMC samples tested at 2, 5 and 10N which represent respectively the low, moderate and high loads. The details of SEM observations performed on prepared cross-sections of these samples are presented here.

Worn Subsurface at Low Load (<2N)

The SEM micrograph of the subsurface microsctructure of TMC sample tested at 2N normal load 0.3 m/s sliding speed and to a sliding distance of 1000 m is illustrated in Figure 4.47. The thickness of the iron oxide layer was in the range of 0.45-0.55 μm. There was a gap between the TMC substrate and the Fe-oxide layer that confirms that these layers are non-adherent. The average height distribution of the TiC particles protruding from the surface was 1.25 μm prior to the test. The height of the particles after the test was measured from subsurface observations which confirmed that the TiC particles tolerated up to 0.65 GPa nominal contact pressure and maintained their elevation over the substrate. A limited number of voids were observed at the TiC/matrix interface. The particles were, however, neither pulled out nor pushed into the substrate. The degree of rotation of the β phase close to the surface can represent the negligible plastic deformation of the subsurface. It was not possible, however, to estimate the exact dept of

deformed zone and the amount of deformation since the direction of the β phase prior to the test was unidentified.

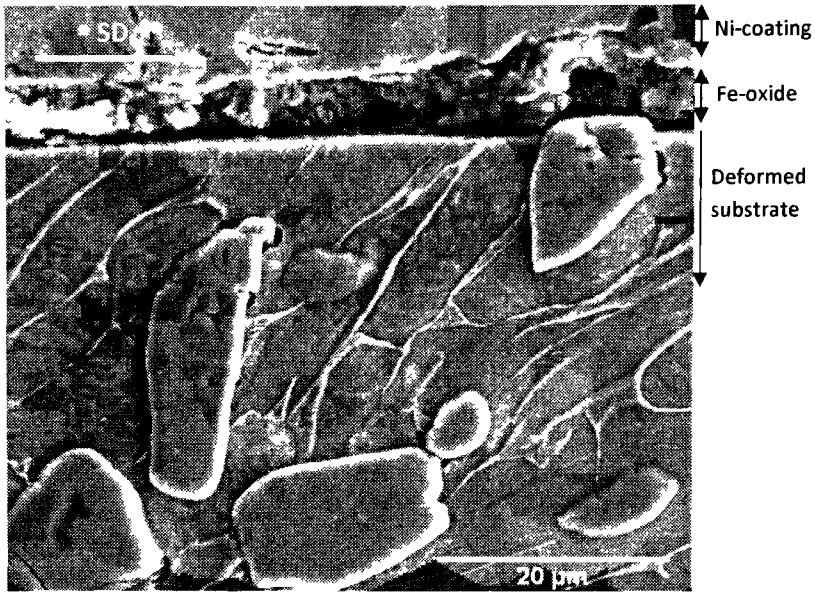

Figure 4.47 SEM micrograph of the worn subsurface of TMC sample tested at 2 N normal load. The surface was Ni-coated prior to finial surface preparation followed by etching. A thin Fe oxide layer laid over the TiC particles which were protruding out of substrate are the common features observed in low loads.

Worn Subsurface at High Loads (7-10N)

The typical morphology of the worn subsurface encountered at high loads is shown in Figure 4.48 (a). The tribolayer consisted of two separate scales, namely the inner compact scale with a thickness in the range of 1.1-5.8 μm and an outer scale composed of small fragments with 3.7-5.6 μm thickness. The EDS analysis on both layers, which is shown in Figure 4.48 (b), confirmed that these layers consisted of a mixture of Ti (50 at%), Fe (4 at%), Al (6 at%) and V (2 at%) oxides. A layer of severely deformed Ti-6Al-4V alloy existed adjacent to the oxide layer. A closer inspection of the morphology of the deformed substrate and tribolayers is shown in Figure 4.49. The microstructure of the outermost layer of the substrate was altered and a lower fraction of β-phase were evidenced. Notably, no evidence of equiaxed β-phase was found at the outermost layer of deformed substrate. A longitudinal crack was also extended from the tribolayer/substrate interface to the substrate passing through the particle/substrate interface. Wear loss occurred by delamination of the inner tribolayer and/or delamination

of severely deformed substrate along with the fragmentation of the outer tribolayer. The outer tribolayer contained a relatively large fragment of TiC particle, which was pulled out of the substrate. This micrograph also shows evidence for the fracture of TiC particles within a depth of approximately 2 μm in the deformed substrate. No evidence of TiC particles that had survived the contact pressure on the surface was found. At high loads, therefore, the TiC particles on the surface were fractured and pulled out of the matrix, and left Ti-6Al-4V matrix unreinforced.

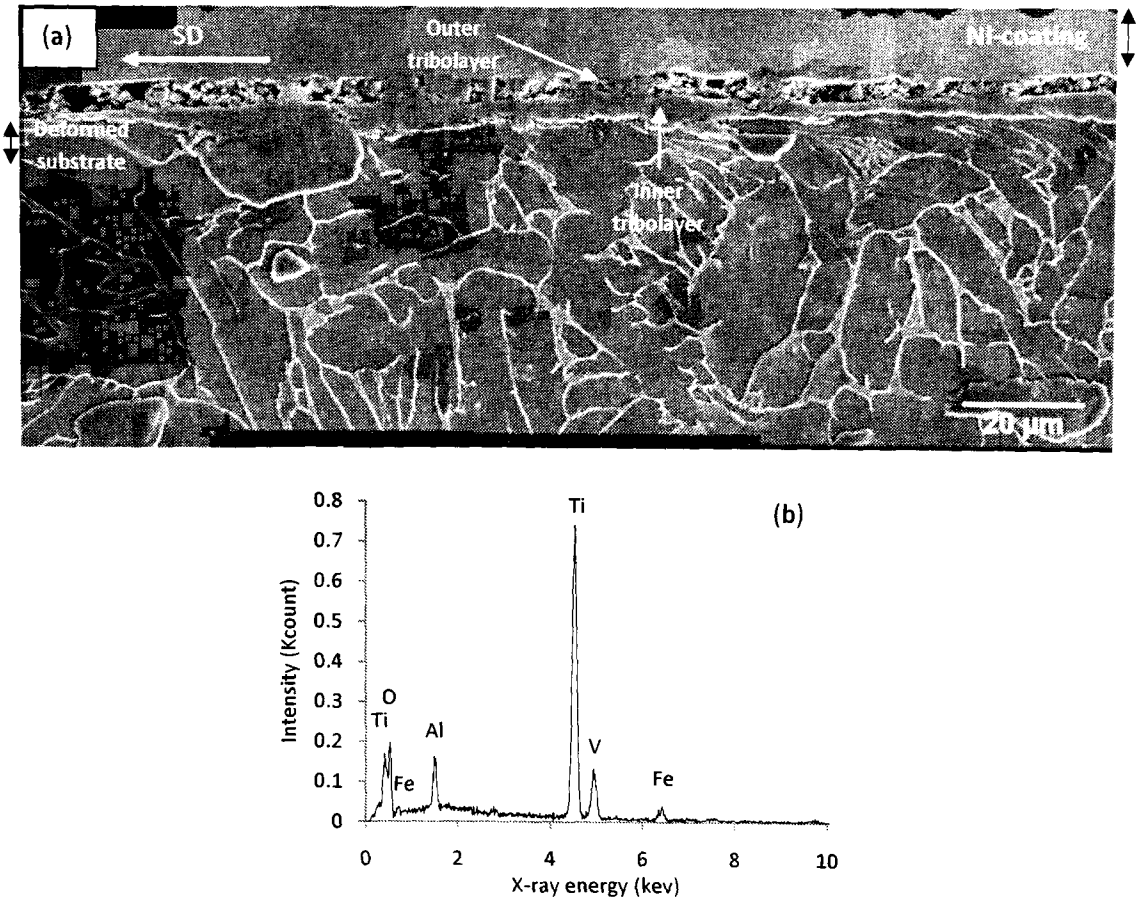

Figure 4.48. (a) SEM micrograph of the worn subsurface of TMC sample tested at 10 N normal load, 0.3 m/s sliding speed after 1000 m sliding distance. The surface was Ni-coated prior to finial surface preparation followed by etching. The tribolayer was twofold: inner compact layer and outer scale consisted of small particles which EDS spectra were similar and shown in (b).

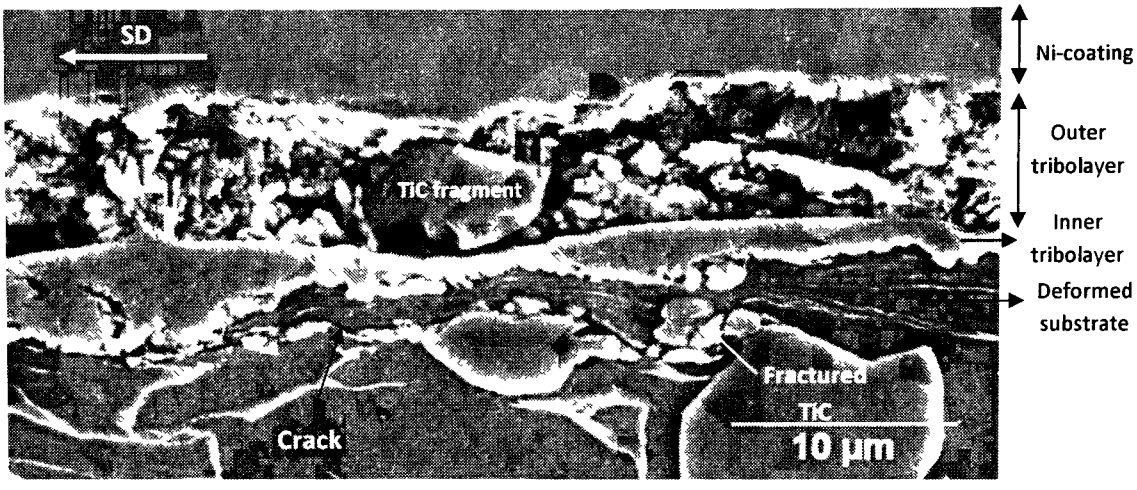

Figure 4.49. A typical worn subsurface morphology observed for TMC sample tested at 10N. The surface was Ni-coated prior to finial surface preparation followed by etching. The tribolayer was two-fold: the inner compact layer and the outer layer consisted of small oxide particles and TiC fragments. A crack was propagated within the substrate and through the tribolayer/substrate interface as into particle/substrate interface.

Worn Substrate at Moderate Loads (3.5-5N)

Figure 4.50 (a) depicts the typical morphology of the worn subsurface of TMC sample tested at 5N which represents moderate load regime. The tribolayer formed at this load consisted of a mixture of Ti (35 at %), Fe (9 at %), Al (5 at %) and V (3 at %) oxides (Figure 4.50 (b)). The fraction of Fe in this mixture was therefore higher than the high load regime. The thickness of the tribolayer varied between 0.7 and 5 µm. Three characteristic features of the tribolayer formed at moderate loads made it different than the high load regime; i) the higher fraction of Fe, ii) the un-continuous, and ii) single layer morphology of the tribolayer. This micrograph also reveals the delamination mechanism of tribolayer which occurred by cracking at the tribolayer/substrate interface. This crack was, however, confined to the interface and unlike the high load regime did not propagate into the Ti-6Al-4V substrate. The TiC particles, which were protruding from the surface prior to the test, were damaged on the surface resulted in surface conforming. Nevertheless, the particle remnants were not pulled out of the matrix. This was confirmed by the observation of preserved TiC particles at the surface compared to the high load regime where even particles at 5µm below the tribolayer were fractured. A closer inspection of the morphology of the tribolayer is illustrated in Figure 4.51, which provided evidence for the layered morphology of the scale similar to the inner tribolayer

that was formed at high load regime. The evidenced gaps between the tribolayer/substrate interface and within the tribolayer can enhance delamination of the oxide tribolayer. The equiaxed microstructure of the Ti-6Al-4V substrate was altered adjacent to the surface and no equiaxed β-phase was observed within 1 μm of the surface. This thickness was around 3 μm for the TMC sample tested at 10N normal load.

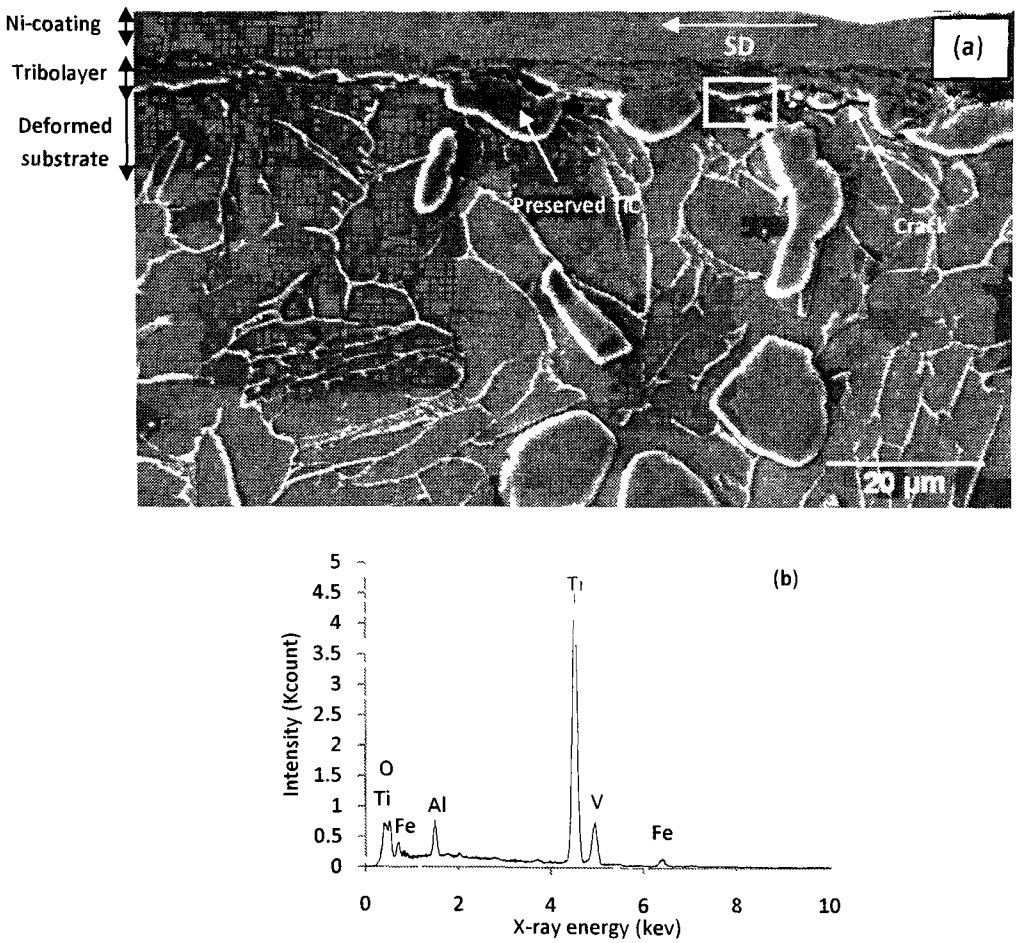

Figure 4.50. (a) SEM micrograph of the worn subsurface of TMC sample tested at 5 N normal load. The surface was Ni-coated prior to the finial surface preparation followed by etching. EDS spectrum of the un-continuous tribolayer is shown in (b). A crack is visible at the tribolayer/substrate interface.

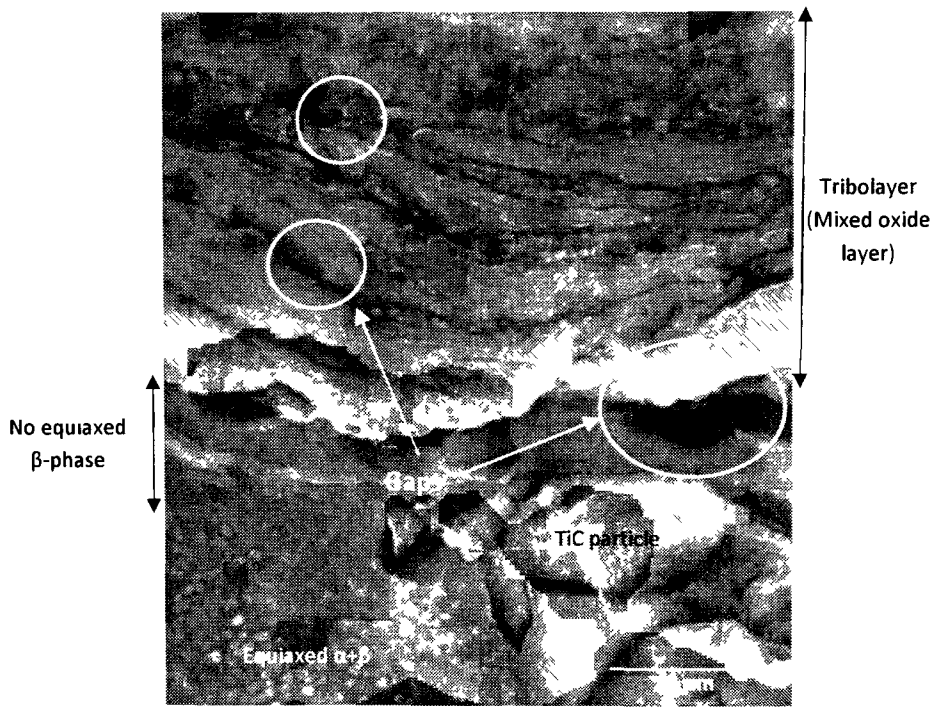

Figure 4.51. A high magnification SEM micrograph of the area enclosed by the rectangle in Figure 4.50. The tribolayer had a multilayered structure. No equiaxed β-phase was found within the layer adjacent to the surface.

4.5.1.5 SEM Observation of the Wear Debris

Wear Debris at Low Load (<2N)

The wear debris generated during the sliding of TMC sample against chrome steel counterface at 2 N normal load after 1000m sliding distance was brownish in colour to the naked eye. The SEM observation—depicted in Figure 4.52 (a) —confirmed that the brownish wear debris mainly consisted of large plate-like particle (10-40 μm) with some fine powder-like particles. The size of powder-like particles varied from sub-micron to 6μm. when carefully examined, at least two types of plate-like debris were identified. One which was shiny with no sliding mark (marked as "1" in Figure 4.52 (a)) and the other one which was dull and grayish in appearance (marked as "2" in Figure 4.52 (a)). EDS analysis revealed that both types of shiny and dull plates consisted of iron oxide which spectrum is shown in Figure 4.52 (b). The presence of large amount Fe in the wear debris provided evidence for abrasion of counterface by the protruding TiC particles that was then followed by oxidation and transfer of iron oxide to TMC substrate. This is

consistent with the SEM observation of the worn surface and subsurface in which a layer of iron oxide was evidenced on the TiC particles. Figure 4.52 (c) illustrates the EDS spectrum of the loose debris marked as "3" which were oxide particles rich in Fe (74.7 at%) with minor amount of Ti (1.3 at%). The scratches observed on the worn surface of TMC were therefore produced by abrasive action of these fine particles. It is noteworthy that the carbon tape used to hold the debris particles on the holder added an intensive peak of carbon to the spectra which made it difficult to identify any TiC fragment in the wear debris.

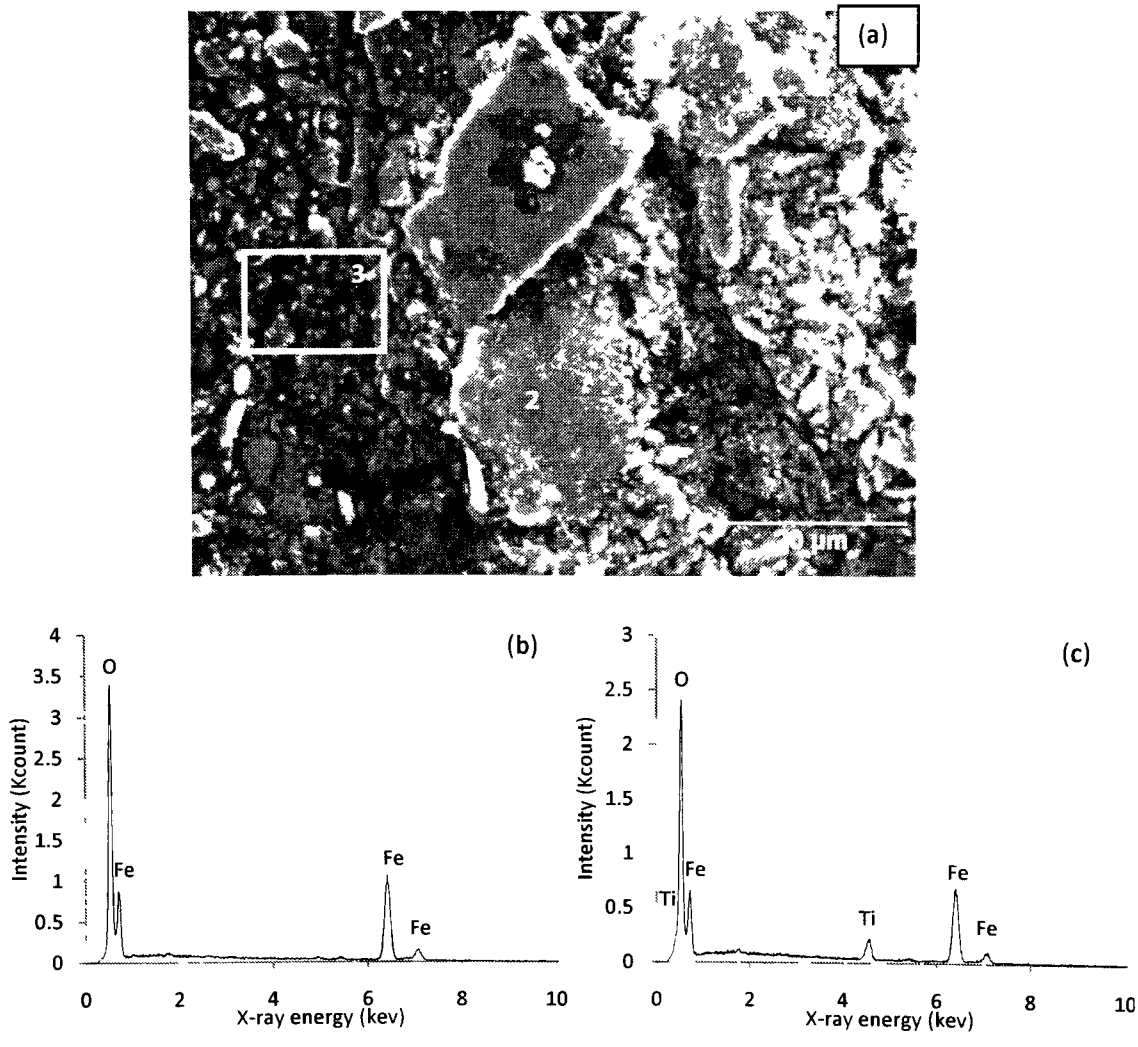

Figure 4.52. (a) SEM micrograph of the wear debris generated during sliding of TMC sample at 2 N. Three types of debris were identified: shiny and dull plate-like marked respectively as "1" and "2" along with fine particles marked as "3" The EDS spectra of the plate-like and the fine debris are given respectively in (b) and (c).

Wear Debris at High Loads (7-10N)

The SEM micrograph in Figure 4.53 (a) and (c) depicts the two types of wear debris generated during the sliding of TMC against chrome steel ball under 10 N normal load. The oxide form of the debris shown in Figure 4.53 (a) consisted mainly of Ti (64.7 at%) with minor amounts of Al (4 at%), Fe (4.5 at%) and V (2.4 at%) which is indicated by EDS spectrum of this type of debris in Figure 4.53 (b). Clusters of fine particle with a size in the range of 0.3-0.5 μm or plate-like laminates with a maximum length between around 50-100 μm were identified as two types of oxide loose debris. The thickness of the plate-like oxide debris was roughly between 1.3-4 μm which is fairly close to the thickness range of the inner tribolayer that was evidenced by subsurface observations at high loads (Figure 4.49 (a)). The fine oxide particles were therefore generated by abrasion of the outer tribolayer, while the plate-like oxide was formed by crack nucleation and propagation at the inner tribolayer/substrate interface.

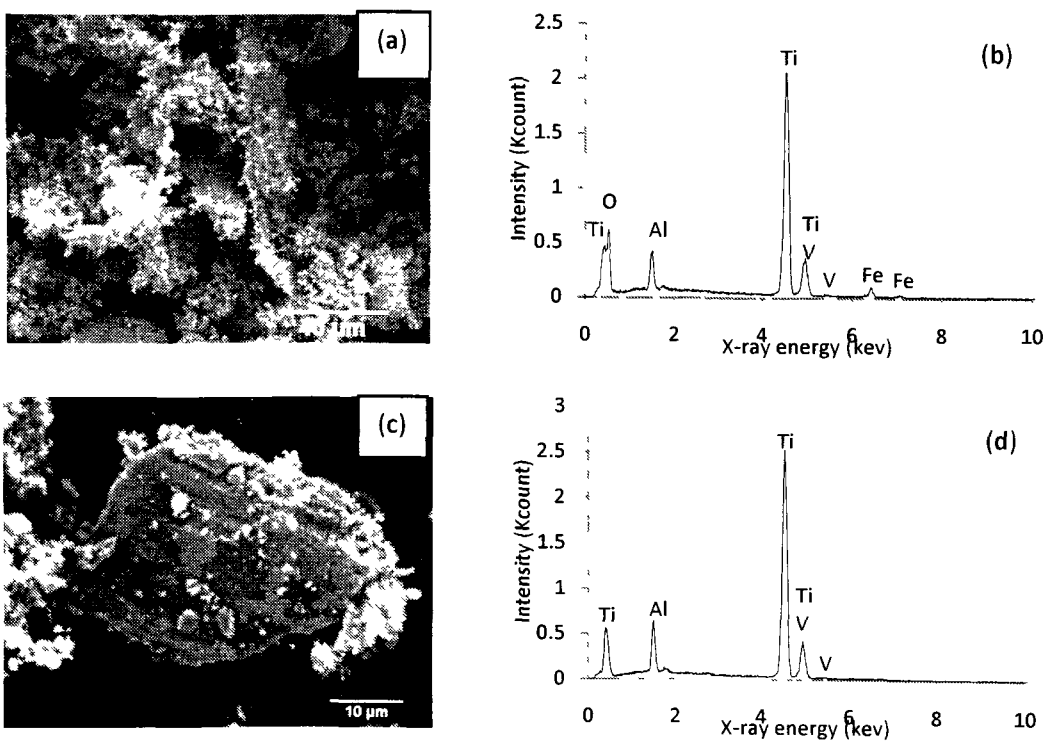

Figure 4.53. SEM micrographs of the two types of wear debris generated during sliding of TMC sample at 10 N; (a) oxide type debris in the form of fine particles and plate-like laminates with corresponding EDS spectrum shown in (b); (d) plate-like metallic debris with the corresponding EDS spectrum shown in (d).

Some metallic plates were also identified within the loose debris produced at high loads. The SEM micrograph and corresponding EDS analysis of this type debris are shown in Figure 4.53 (c) and (d). Severe sliding marks were evidenced on the surface of these plates that consisted of Ti, Al and V Delamination of Ti-6Al-4V substrate had, therefore, occurred as a result of crack nucleation and propagation within the severely deformed subsurface layer.

Wear Debris at Moderate loads (3.5-5N)

The morphological analysis of the wear fragments generated during sliding of TMC against chrome steel ball at 3.5 and 5 N normal load revealed that two types of debris were formed. Figure 4.54 (a) and (b) illustrate the two morphologies observed for oxide debris, which were respectively the fine particles and the plate-like debris. The size of particles was between 1 and 3 μm which is apparently larger than the fine particles formed at high loads. The maximum length of the plate-like oxide debris (9-40 μ) was smaller than the length of the loose debris formed at high loads (50-100 μm). The result of EDS analysis performed on these particles is given in Figure 4.54 (c) which confirmed that the composition of the oxide was similar to the composition of the tribolayer formed at this loads: Ti (43 at %), Fe (6 at %), Al (4 at %) and V (1.3 at %). The oxide laminates were therefore generated by delamination of tribolayer which was induced by cracking at the tribolayer/substrate interface and followed by further fragmentation of the delaminated layer from which the fine particles were formed.

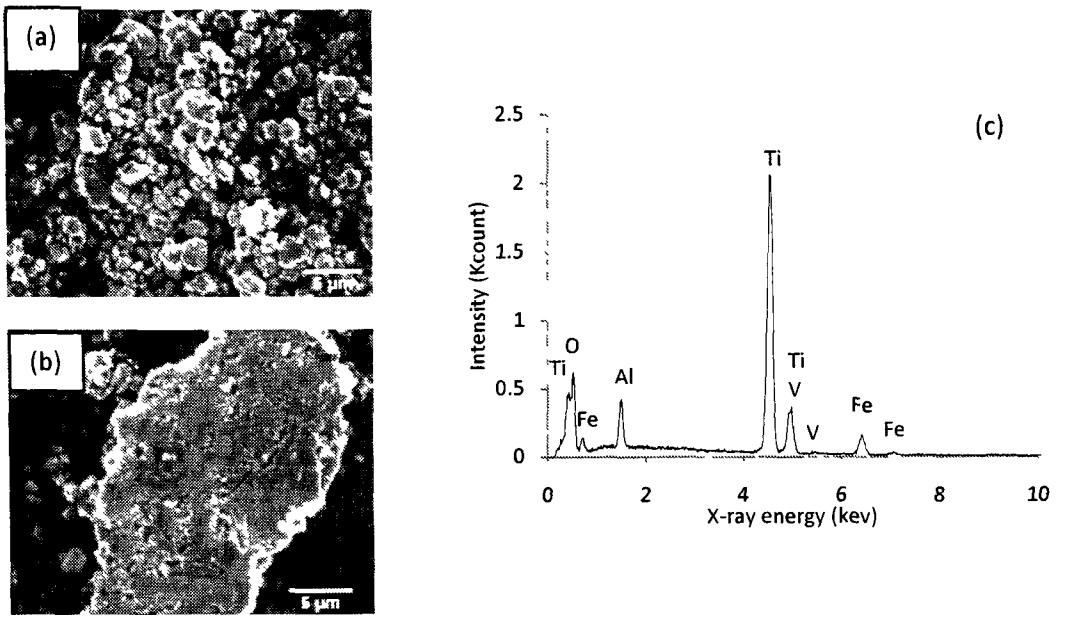

Figure 4.54. SEM micrographs of the two types of wear debris generated during sliding of TMC sample at 5 N; oxide type debris in the form of (a) fine particles and (b) plate-like laminates with corresponding EDS spectrum shown in (c).

4.5.2 Wear Rates and Wear Mechanisms of Oxidized TMC Samples

4.5.2.1 Variation of Wear Rate with Load and Sliding Distance

The variation of wear rate with normal load for TMC samples thermally oxidized at 800°C for 20 min (TO-TMC) was measured by two methods similar to TMC samples; namely the mass loss based and depth based methods. The tests were performed under normal loads of 2, 3.5, 5, 7 and 10 N. Ascribing the following values: $E_{TiO_2} = 192\ GPa, \vartheta_{TiO_2} = 0.3, E_{C/S} = 210\ GPa$ and $\vartheta_{C/S} = 0.03$, the contact pressures produced under a 6mm C/S ball were 0.806, 0.971, 1.09, 1.22 and 1.38 GPa respectively. Figure 4.31 was updated by adding the wear rates of TO-TMC samples—which were obtained by mass-loss method—and re-plotting the graph as a function of contact pressure instead of normal load. The values of wear rates were negative when TO-TMC sample were tested at 0.806, 0.971 and 1.09 GPa contact pressures, and increased as the normal load increased. The negative values of wear rate provided evidence for the severity of material transfer from counterface which was higher for TMC sample tested under 0.65 GPa ($-3.16 \times 10^{-5} mm^3/mm$) compared to the TO-TMC sample tested under 0.806 GPa ($-2.43 \times 10^{-5} mm^3/mm$). The mass loss based wear rate of TO-TMC sample increased

as the contact pressure increased. Despite this increase, the wear rate of TMC samples tested at 1.11 GPa was around 126 times higher than the wear rate of TO-TMC sample tested under 1.23 GPa pressure. Therefore, thermal oxidation at 800°C for 20 min has significantly improved the wear resistance of TMC sample in terms of mass loss, especially at high pressures.

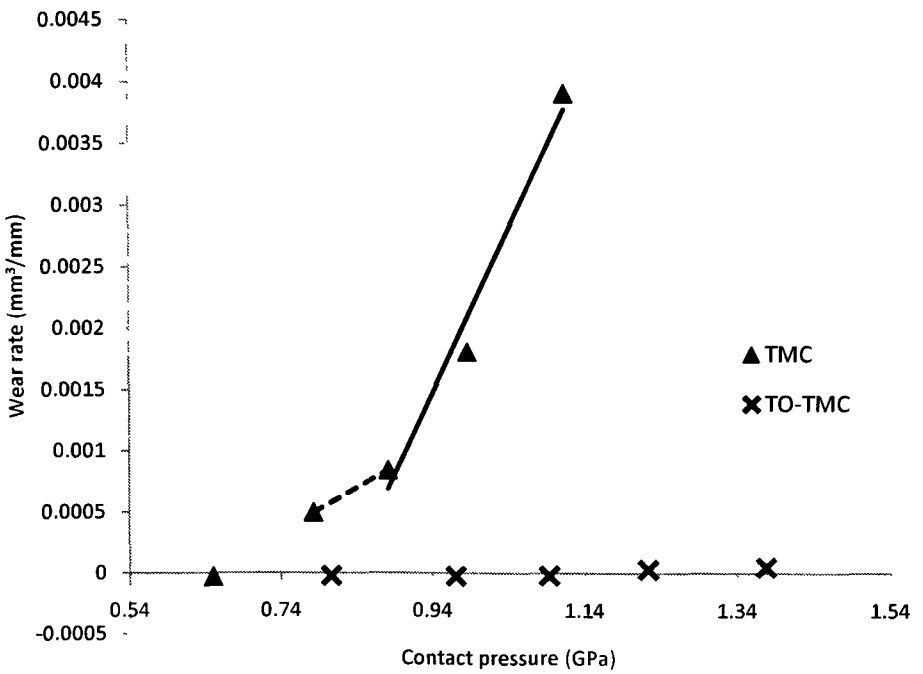

Figure 4.55. The wear rates of TMC and TO-TMC samples within contact pressure range of 0.64-1.38 GPa based on the weight losses measured at each load. The thick dashed and solid lines represent the linear fit for the low load and high load regimes that were identified for TMC samples.

The variation of the depth based volume loss with sliding distance was plotted and compared for various normal loads—shown in Figure 4.56— in order to distinguish the wear regimes for TO-TMC samples sliding against C/S ball. Steady state condition was achieved for all the tests once an initial running in period of 300 m was established. The running in data was excluded from the volume loss graphs. At the start of the steady state condition the volume loss of the sample tested at 2 N was between around 3 to 4 times lower than the samples tested at higher loads. The slopes of the plots, however, increased linearly with load. The depth based wear rate of TO-TMC samples that was determined from the slope of the graphs in Figure 4.56 increased linearly with contact pressure. This

plot is illustrated in Figure 4.57. The wear rate of TO-TMC samples, however, remained lower than the wear rates of TMC and Ti-6Al-4V at all the pressures. Analyzing the wear rate values, it was revealed that the improvement in the wear resistance of TMC sample that was accomplished by thermal oxidation was more significant at higher pressures, and the wear resistance of TMC sample was enhanced by a factor of 3.4 at 1.11 GPa compared to an enhancement by a factor of 3 at lower pressures (0.88 GPa). Similar to TMC and Ti-6Al-4V samples, the wear rate of TO-TMC samples measured based on the depth were higher that the wear rate values measured from the mass loss method. As previously discussed in section 4.5.1.1, the difference in the wear rate values measured by these two methods is attributed to the contribution of counterface wear rate and material transfer from counterface to the sample. The former increases the depth based wear rate values while the latter decreases the mass loss-based wear rate values, and both result in a larger difference. The large difference between the depth-based and mass loss-based wear rate values for TO-TMC was caused by the severe abrasion of C/S counterface by the hard-oxide layer that was superimposed by the material transfer from counterface to TO-TMC sample.

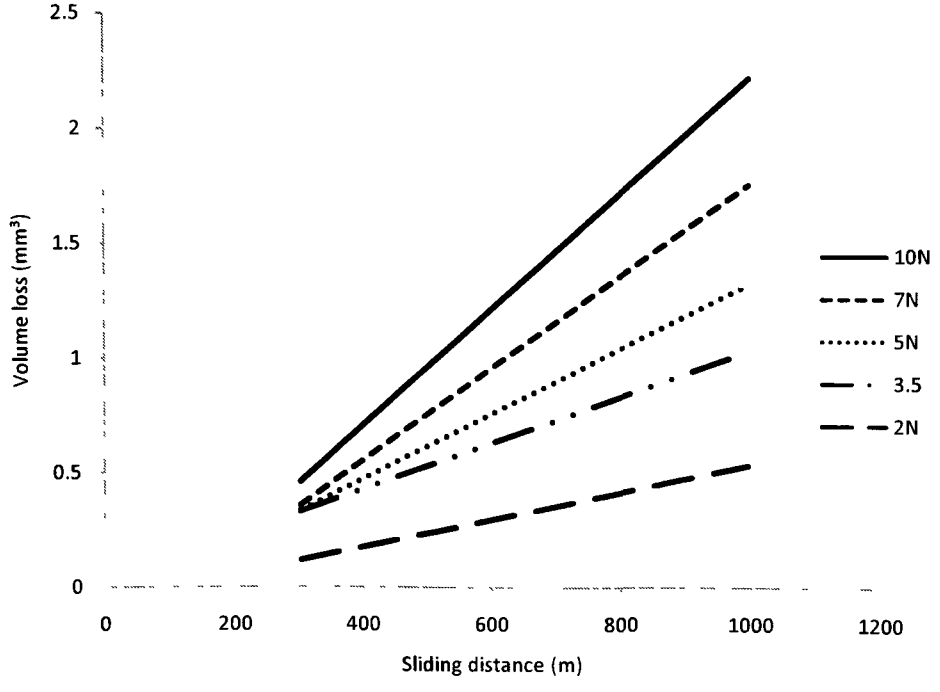

Figure 4.56. Variation of volume loss of TO-TMC with sliding distance at constant normal loads within the range of 2-10 N. The volume loss data are calculated based on the depth change data.

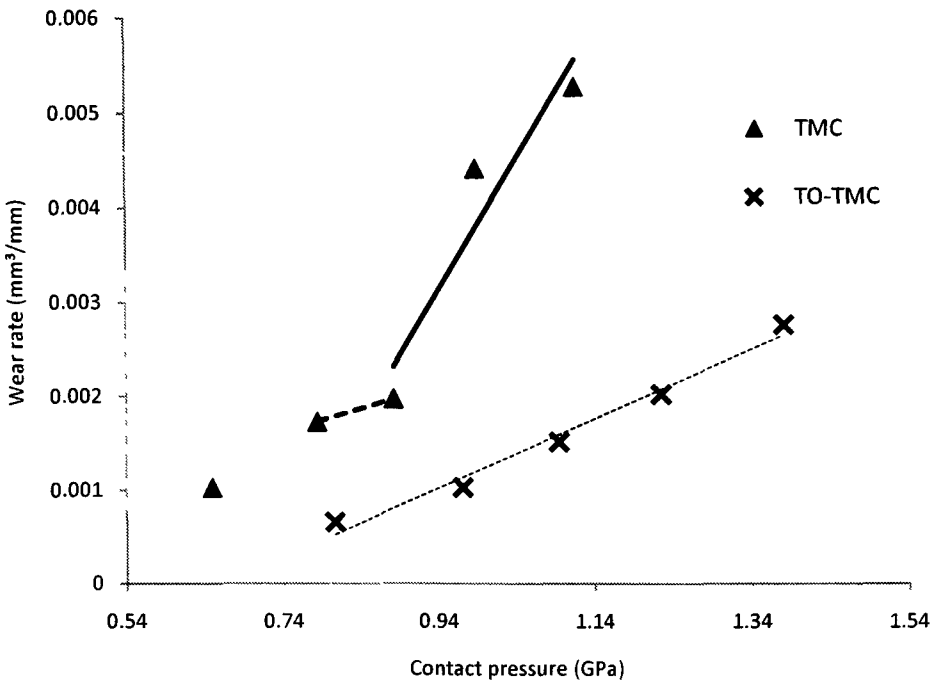

Figure 4.57. The wear rate of TMC and TO-TMC samples within the contact pressure range of 0.64-1.38 GPa based on the depth changes measured at each pressure. The thin dashed line is the linear fit generated for TO-TMC data. The thick dashed and solid lines represent the linear fit for the low load and high load regimes which were identified for TMC samples.

In summary, in terms of the changes in mass loss based wear rates, two different wear regimes can be distinguished; i) low loads (2- 5 N) at which wear rates were negative and ii) high load regime (7-10 N) with positive values of wear rates. Based on the wear rate values measured by depth method, however, no significant change in the wear could be discriminated and the wear rates increased linearly as normal load increased. The SEM observations on the worn surface and subsurface—discussed in sections 4.5.2.3 and 4.5.2.4—confirmed the existence of two wear regimes, which were suggested based on mass loss measurements.

4.5.2.2 Variation of Coefficient of Friction by Sliding Distance and Load

Figure 4.58 represents the typical COF plot observed at low loads. At this loads COF fluctuated around an average value with relatively small fluctuations (±0.05), and remained constant at this level during the test. The average steady state COF value was 0.52 at 2N and increased to 0.55 at 5N. At low loads, the average value of COF for TO-TMC sample was lower and it exhibited smaller fluctuations compared to the COF

obtained for TMC samples. Figure 4.59 illustrates the typical COF plot that was obtained for high loads, which exhibited a short initial running in period of approximately 300 m followed by steady state behaviour. At 7N normal load COF rose from an initial value of 0.6 to 0.87 at the beginning of the test (115m) followed by a sudden drop to an average value within the range of 0.6-0.62 with relatively large fluctuations (±0.08), and remained constant at that level for the rest of the test. The average value of the steady state period was higher for 10N normal load (0.65), and the steady state COF values obtained for TO-TMC at high loads was higher compared to TMC samples tested at the same load.

The sudden drop in COF at the initial stages of sliding at 7 and 10N were due to the surface conformity that was obtained by asperity removal process and formation of a relatively continuous iron oxide layer on the surface. At 2, 3.5 and 7 N normal loads, the asperities of hard oxide layer were not smoothen out and the iron oxide layer existed intermittently between the asperity tips, and therefore the momentary rise in friction and the sudden drop were not observed for the low loads. The large fluctuations at higher loads were attributed to the frequent formation and destruction of the iron oxide layers.

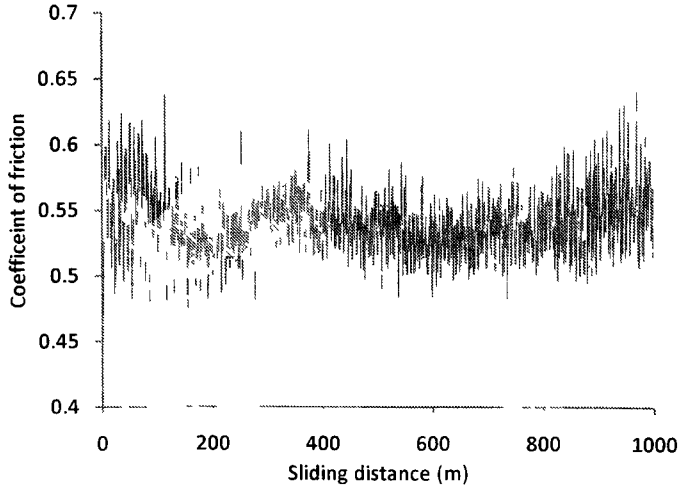

Figure 4.58. Variations of coefficient of friction with sliding distance for TO-TMC sample tested at constant normal load of 2N representing the low loads.

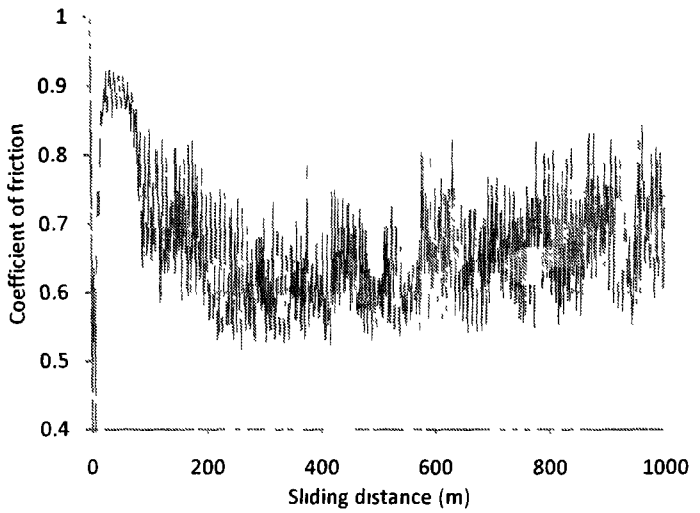

Figure 4.59. Variations of coefficient of friction with sliding distance for TO-TMC tested at constant normal load of 7N representing the high loads.

4.5.2.3 SEM Observation of the Worn Surface

Worn Surface in the Low Loads (2-5N)

The typical morphology of the worn surface of TO-TMC at low loads is shown in Figure 4.60, which depicts the back-scattered micrograph of the sample tested at 2 N normal load, 0.3 m/s sliding speed and to a sliding distance of 1000 m. The real contact happened at the tip of the asperities of the oxide scale, and these asperities were slightly worn due to the sliding action of counterface. A layer which appeared lighter in back-scattered mode was also covered the surface. Close examination of the worn surface revealed the nature and morphology of the white layer. This layer was in two forms which SEM micrographs and the associated EDS spectra are presented in Figure 4.61.

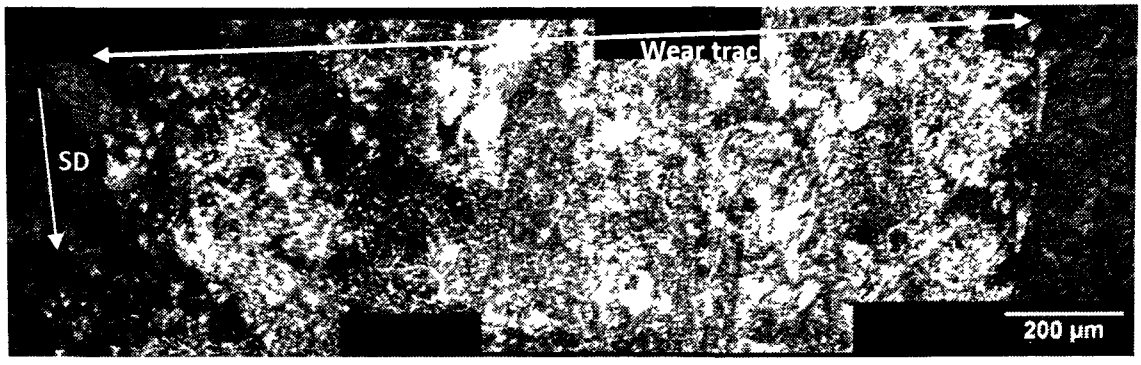

Figure 4.60. The low magnification back-scattered micrograph of the worn surface of TO-TMC sample tested at 2 N. The majority of the surface is covered by a whiter layer and the titanium oxide retained its original surface features.

The majority of the contact area was covered by a mixture of Fe oxides (14 at %), Ti oxides (14 at %) and Al oxides (5 at %) for which the SEM micrograph and the corresponding EDS spectrum are given in Figure 4.61 (a) and (b). The oxide scale exhibited a layered morphology that was attributed to the frequent abrasion of counterface by the hard rutile asperities, and formation of a fresh layer of iron oxide in each cycle. This iron oxide was then mixed with the minor amount of titanium oxide removed from the asperity tips and formed the multilayered oxide morphology. The iron oxide layer was also smeared over the substrate without further mixing with titanium oxide and formed patches of oxide that is depicted in Figure 4.61 (c). This image was taken when the SEM stage was tilted 50° relative to the beam. The EDS spectrum of the aforementioned patches is given in Figure 4.61 (d) which confirms that these patches were mainly consisted of Fe (40 at %) oxides with minor amounts of Ti (2 at%). It was possible that the Ti peaks were picked up from the rutile layer beneath the thin iron oxide layer.

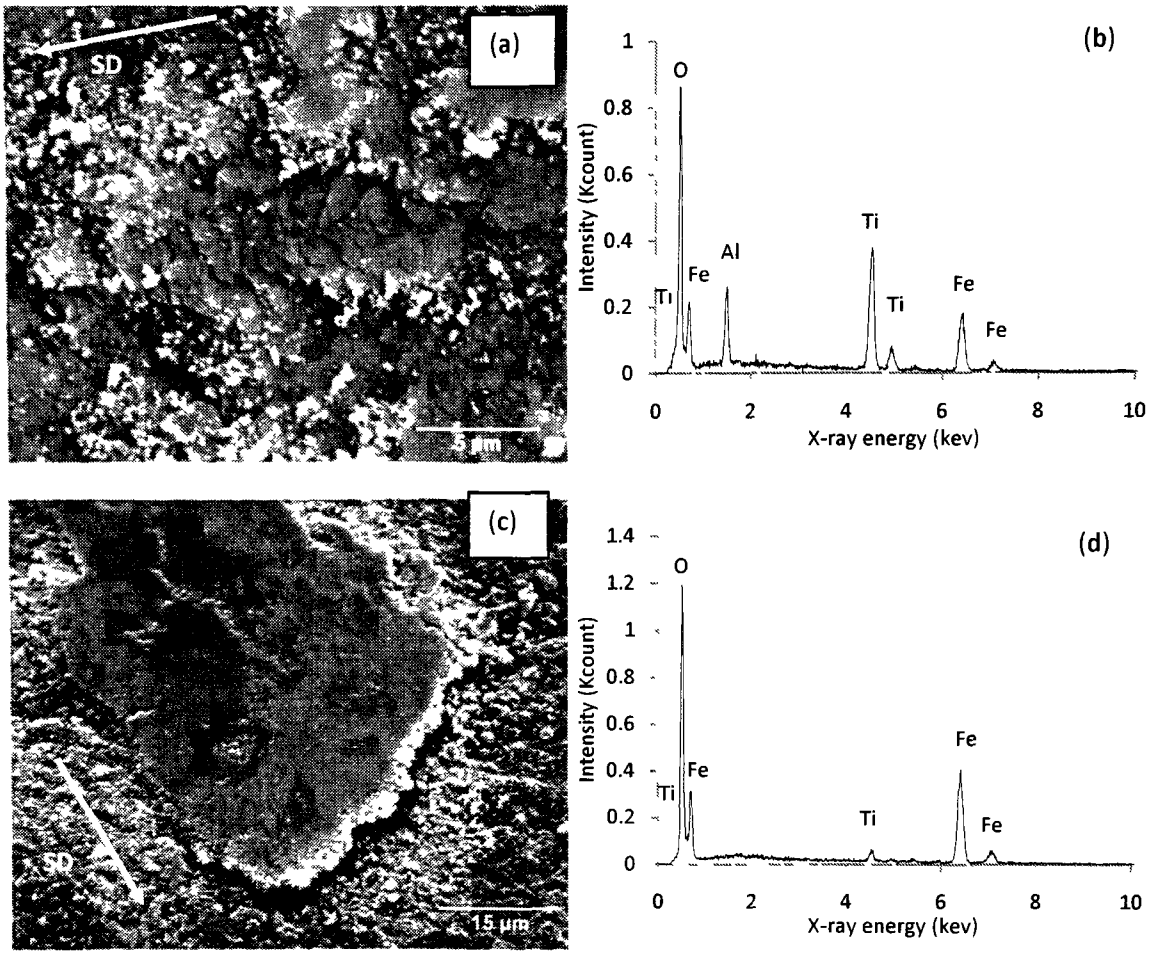

Figure 4.61. SEM micrograph of the two morphologies of the iron oxide scale formed on the worn surface of TO-TMC sample tested at 2 N; (a) a mixture of Ti, Al, Fe and V oxides in the form of a multilayered scale and (c) patches of mainly Fe oxides smeared over the surface. The latter is taken by tilting the SEM stage 50° relative to the beam. The EDS spectra associated with these layers are given in (b) and (d).

Worn Surface in the High Loads (7-10N)

Figure 4.62 shows the back-scattered image of the worn surface of the TMC sample tested against chrome steel ball at 5 N normal load, 0.3 m/s sliding speed and to a sliding distance of 1000 m which represents the typical morphology observed in high loads. The majority of the contact area was uniformly covered by a white layer. Unlike the low loads, TO-TMC did not retain its surface features at this load and, and the rutile scale—created by thermal oxidation—was removed at some spots as a result of the sliding action of C/S ball. The white layer was also exfoliated at some infrequent spots, and left the TO-TMC matrix in direct contact with the counterface.

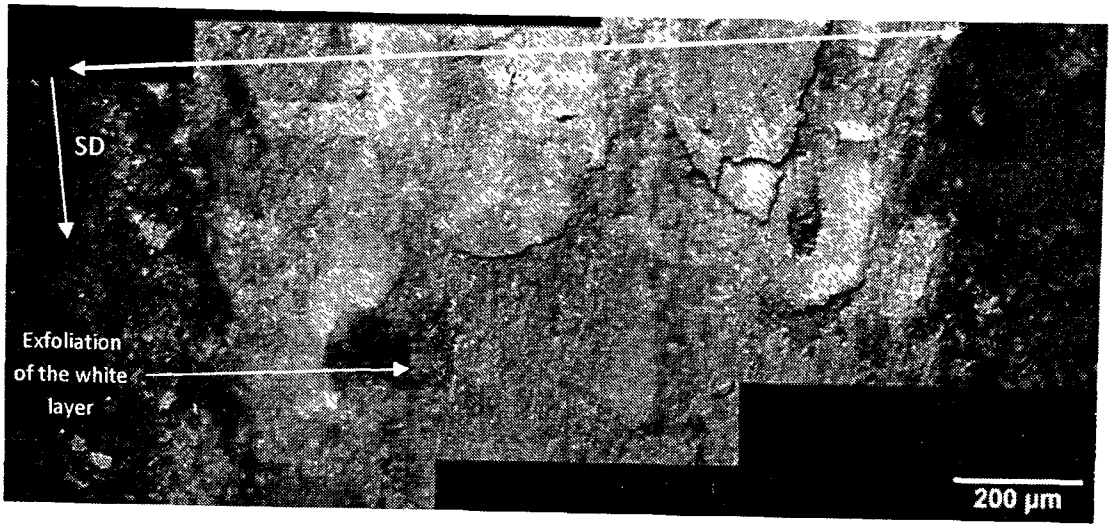

Figure 4.62. The low magnification back-scattered micrograph of the worn surface of TO-TMC sample tested at 10 N. The majority of the surface is covered by a whiter layer which is exfoliated at some occasional spots.

A higher magnification secondary image of the white layer is shown in Figure 4.63 (a). The majority of the white layer was consisted of layers of oxide stacked on top of each other (marked as "1"). The EDS spectra of this homogeneous layer that is marked as "1" and the adjacent non-homogenous layer that is marked as "2" are presented respectively in Figure 4.63 (b) and (c). At high loads, similar to low loads, the white layer consisted of two forms of oxide; namely the homogeneous layer that was consisted mainly of Fe oxide (40 at %) with minor amounts of Ti oxide (2.5 at%) and the non-homogenous form which was a mixture of Fe (20 at%) and Ti (14 at%). The fraction of Fe in the mixture of oxides was, however, higher at higher loads, so was the fraction of the surface area that was covered with the homogeneous layer of iron oxide, while at low loads the fraction of non-homogeneous layer was higher.

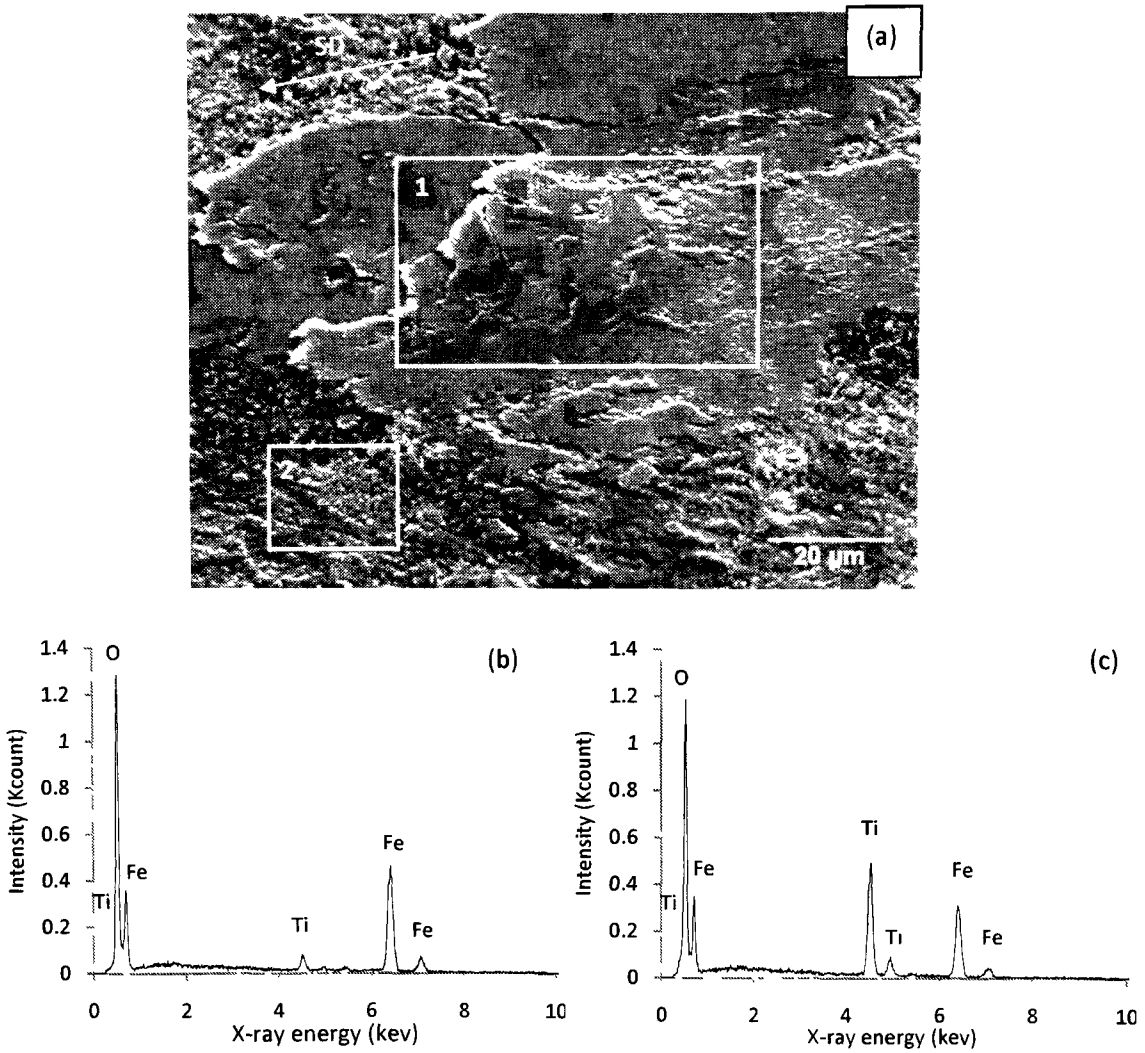

Figure 4.63. SEM micrograph of the two morphologies of the iron oxide scale formed on the worn surface of TO-TMC sample tested at 10N; the area marked as "1" is a homogeneous layer of iron oxide and the area marked as "2" is a mixture of Fe and Ti oxides. The micrograph was taken when the SEM stage was tilted 50° relative to the beam. The EDS spectra obtained from "1" and "2" are given in (b) and (c).

The SEM micrograph in Figure 4.64 illustrates an iron oxide scale which is about to be exfoliated. This micrograph was taken when the stage was tilted relative to the beam and depicts the oxide scale that was buckled out due to the tensile stress field at the trailing edge of the sliding ball. A number of sliding marks in the form of shallow scratches were also apparent on the surface of the oxide scale. EDS analysis on the occasional areas where the oxide scale was delaminated revealed that the cracking can include either only the iron oxide scale or both the titanium oxide scale along with the iron oxide. Spallation of titanium oxide scale due to cracking at the oxide/substrate

interface or within the substrate was the characteristic feature of high loads compared to the low loads where the titanium oxide scale retained its integrity on the surface. A detailed description of the different types of spallation of the coating is presented in section 4.5.2.4.

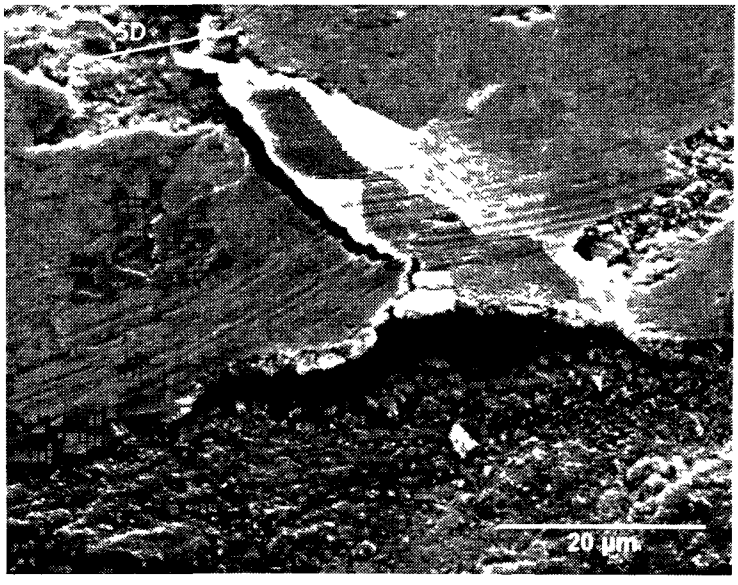

Figure 4.64. SEM micrograph of the iron oxide layer formed on TO-TMC sample tested at 10 N. The oxide is buckled up due to the sliding action of the counterface and then fractured.

4.5.2.4 Cross-Sectional SEM Observations of the Worn Subsurface

In order to better understand the microstructure changes and the response of the titanium oxide scale and the underlying substrate to deformation during sliding wear tests, cross-sections of the wear track were cut and prepared parallel to the sliding direction. The cross-sectional features of the samples tested at low load regime differed from the samples tested at high load regimes, and are separately discussed in this section.

Worn Subsurface at Low Loads (2-5N)

The cross-sectional morphologies of the TO-TMC sample tested at 2 N and 5 N normal loads, 0.3 m/s sliding speed and to a sliding distance of 1000 m are shown in Figure 4.65 and Figure 4.66. No evidence of the iron oxide layers—observed at the worn surface—was found at the cross-section. This confirms the thin and non-adherent nature of these layers that were removed by surface cutting process, even though the surface was

Ni-coated prior to performing any surface preparation process. The prepared subsurface cross-sections, however, provided useful information regarding the roles of titanium oxide and oxygen diffusion zone (ODZ). The titanium oxide scale that was created by 8-20min type oxidation remained attached to the substrate, in spite of the nucleation of voids and cracks. The subsurface plastic deformation—evidenced by the rotation of β phase in TMC samples— was not observed for TO-TMC which was due to the hard nature of the oxide scale and the adjacent ODZ. It is apparent from Figure 4.65 that at 2 N a limited number of voids were nucleated within the hard and brittle ODZ that were located at a depth range of 0.8-4 μm below the oxide. Due to the simultaneous action of the shear and tensile stress components, the nucleated voids were stretched and became oblate. The larger axis of the voids was rotated towards the sliding direction which is depicted in Figure 4.65. The titanium oxide scale retained its surface features at 2N normal load (0.805 GPa) and fragmentation of oxide was not observed.

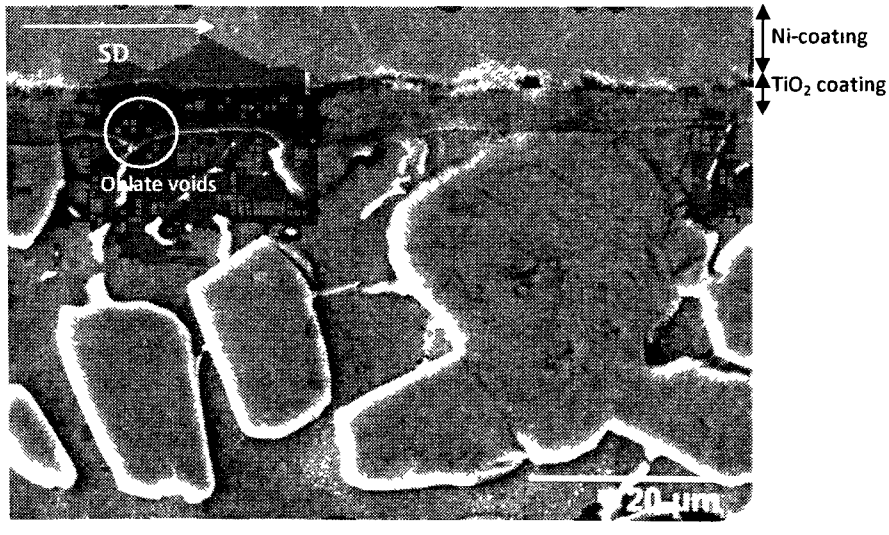

Figure 4.65. SEM micrograph of the worn subsurface of TO-TMC sample tested at 2N. The surface was Ni-coated prior to finial surface preparation followed by etching. A number of oblate voids were evidenced.

Nucleation of cracks from the voids located closest to the interface but not at the interface was evidenced at 5 N which SEM micrograph is depicted in Figure 4.66. This confirms the outstanding interfacial strength of the scale formed at 800 °C which was consistent with the micro-scratch results discussed in section4.4.4. It is important to note that the retained-β phase within ODZ acted as a ductile fiber that bridges the two faces of

the crack when the crack passed through it. The cracks were also stopped at the TiC particles. It was evident that even though the oxide remained integrated to the subsurface at 5N normal load, the sliding action of the counterface ball fragmentised the oxide on the surface. Since the oxide formed at 8-20min oxidation condition was thick (3.3 μm) and relatively uniform, the scale was not removed entirely by fragmentation process. The characteristic features of worn subsurface at low loads was the nucleation and coalescence of voids, and formation of cracks that was accompanied with partial fragmentation of oxide scale at 5 N.

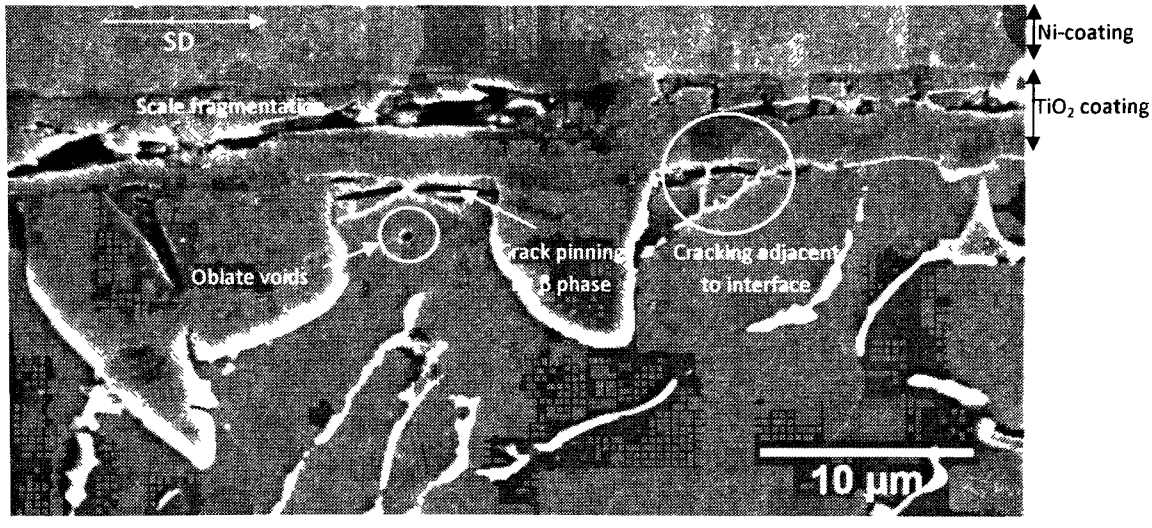

Figure 4.66. SEM micrograph of the worn subsurface of TO-TMC sample tested at 5N. The surface was Ni-coated prior to finial surface preparation followed by etching. Oblate voids and cracks which are both bridged by the β phase and were stopped at TiC particles are visible besides the scale fragmentation.

Worn Subsurface at High Loads (7-10N)

The typical subsurface morphology observed for TO-TMC tested at high load regime is shown in Figure 4.67 A significant number of voids were formed within around 6.4 μm depth below the interface. The voids formed at 7N were oblate similar to low load regime, and their larger axis was rotated towards the sliding direction. Cracks were also formed by coalescence of these voids. At high load regime, however, the nucleation of voids and cracks was more frequent which resulted in occasional delamination of the oxide scale, and not only the oxide scale was fragmentised on the surface but also it was delaminated by cracking adjacent to the interface within ODZ.

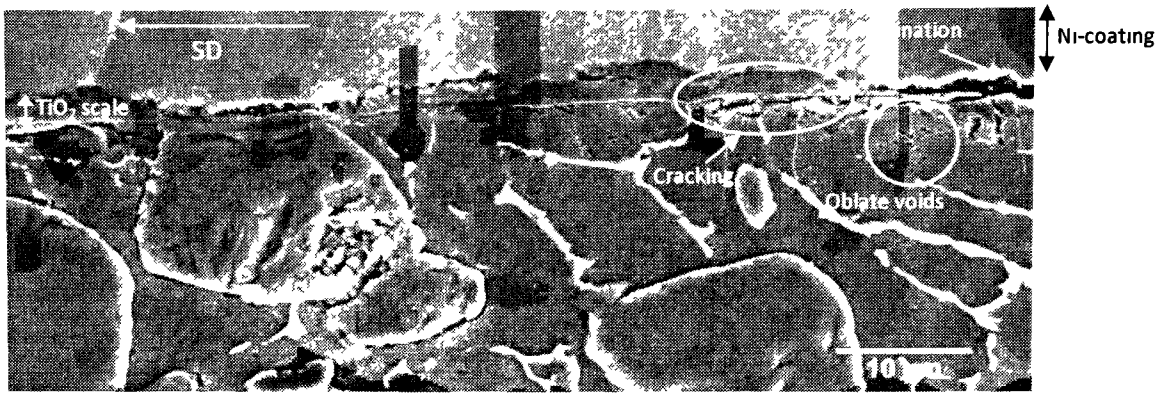

Figure 4.67 SEM micrograph of the worn subsurface of TO-TMC sample tested at 7N. The surface was Ni-coated prior to finial surface preparation followed by etching. Oblate voids and cracks were drastically frequent. The area where TiO_2 is delaminated is marked.

Figure 4.68 illustrates the SEM micrograph of an area of oxide which was about to be spalled at 10N normal load. This image provides evidence for the mechanism of spallation of the titanium oxide scale. The cracks formed within the ODZ layer and adjacent to the interface propagated towards the surface, forming debris with oxide on one side and Ti-6Al-4V on the other side. The retained β phase deflects the path of the crack within ODZ layer and also bridges the faces of the propagating crack, and, therefore, there were several cracks within the spalled layer which were either confined by this phase or stopped at the oxide/substrate interface. Eventually, when the crack reached a critical length, which is a function of the fracture toughness of the ODZ material, it broke through the oxide scale towards the surface—accompanied by rupture of the fiber-like β phase.

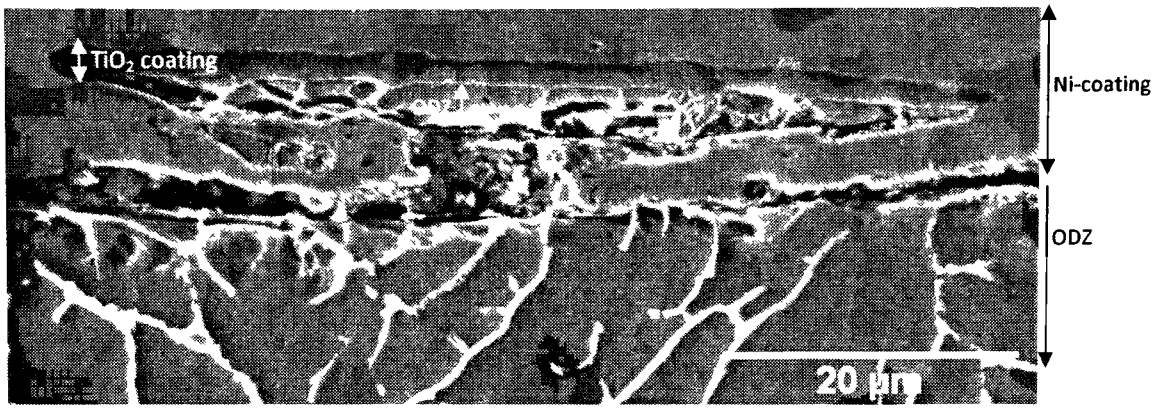

Figure 4.68. A high magnification SEM micrograph of the scale spallation that was occurred when TO-TMC tested at 10 N. The cracking occurred within the brittle ODZ layer adjacent to the interface and propagated towards the surface.

4.5.2.5 SEM Observation of the Wear Debris

Wear Debris at Low Loads (2-5N)

SEM observation on the wear debris generated during sliding of TO-TMC against chrome steel ball at the low loads revealed that two types of debris were formed. Figure 4.69 (a) depicts the morphologies of loose debris formed at 2 N normal load which includes the ultrafine particles (marked as "1") and thin laminates (marked as "2"). The particles were within a size range of 0.02-0.1 µm. EDS analysis performed on ultrafine particles revealed that they consisted of mainly Fe (38 at%) oxides with slight amounts of Ti (2.5 at%) oxides (Figure 4.69 (b)). Moderate abrasion of the multilayered mixture of Fe and Ti oxides—evidenced on the surface—was responsible for the formation of these particles. The particles formed by this process were then fractured and got smaller as a result of pressure by the hard sliding couple. The loose particles simultaneously abraded the steel counterface and generated more Fe oxide. The second type of debris illustrated in Figure 4.69 (a) was in the form of thin plate-like laminates of Fe oxide which length was within a size range of 15-55 µm. The EDS spectrum of these particles is given in Figure 4.69 (c). This type of debris was generated by delamination of the patches of iron oxide scale that were evidenced on the worn surface.

The majority of the loose debris generated at 2 N consisted of ultrafine type particles. As the load increased within the low loads, the ratio of the ultrafine particles to

the plate-like debris decreased, and a higher fraction of plate-like particles was observed at 5 N The size of the ultrafine particles did not change significantly with normal load, yet, the average size of plate-like debris increased to around 54-145 μm at 5 N normal load The larger size of the laminates and the higher frequency of delamination at 5 N were consistent with the lower weight gain of this sample compared to TO-TMC sample tested at 2 N

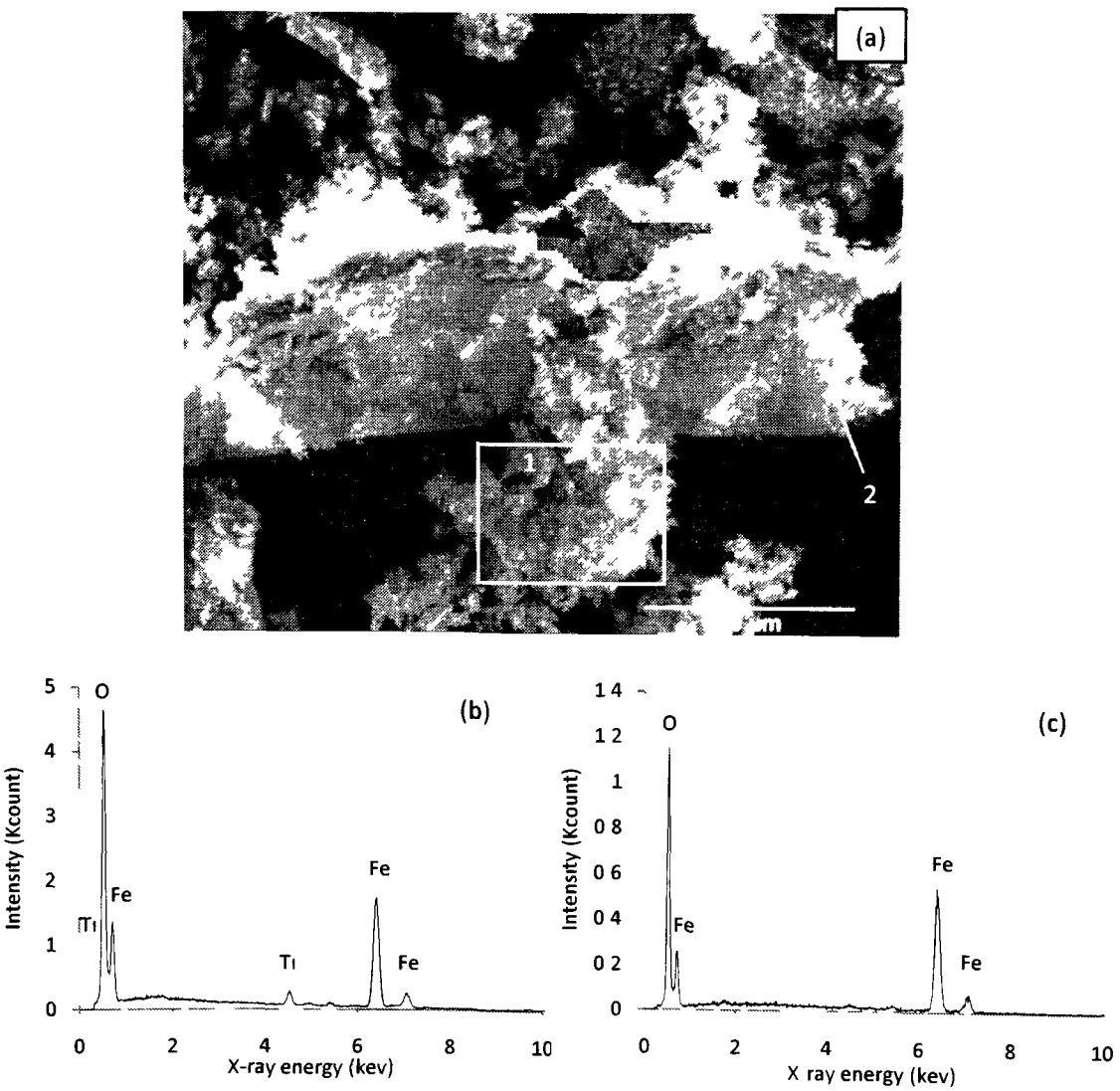

Figure 4 69 (a) SEM micrograph of the wear debris generated as a result of wear test on TO-TMC sample at 2 N Two types of debris were identified ultrafine particles and plate-like which are marked respectively as "1" and "2" The corresponding EDS spectra are given in (b) and (c)

Wear Debris at High Loads (7-10N)

The SEM micrographs of the two types of loose debris generated as a result of wear test on TO-TMC sample at 10 N normal load are shown in Figure 4.70 (a) and (c). Ultrafine particles and plate-like laminates, similar to the low loads, were the typical types of loose debris at high loads. The size and morphology of the ultrafine particles were quite similar when the samples tested at low and high loads. The EDS analysis—given in Figure 4.70 (b) —confirmed that the source of these particles was the non-homogeneous layer of Fe and Ti oxides that were evidenced on the worn surface. The fraction of the fine particles was, however, considerably inferior to the fraction of plate-like laminates.

EDS analysis was performed on the surface of nearly all of the plate-like debris that were collected during sliding in either 7 or 10 N, to identify any wear debris that confirms the mechanism described in Figure 4.68. A strong peak of Ti was not found in any of the EDS spectra. This was necessary to verify the nucleation of cracks within ODZ layer which resulted in formation of loose debris with the morphology explained in section 4.5.2.4, i.e. Ti-6Al-4V on one face, and iron or Ti oxides on the other face. The EDS spectra obtained were generally verified two types of composition: i) Fe oxide which is depicted in Figure 4.70 (d) and ii) Fe (40 at%) oxide with a slight amount of Ti (2.5 at%) which is depicted in Figure 4.70 (e). It can be stated that even though spallation of TiO_2 was evidenced to occur as a result of cracking within ODZ, the majority of the TiO_2 scale remained attached to the substrate, and the fraction of the loose debris specified in section 4.5.2.4 was too low to be identified.

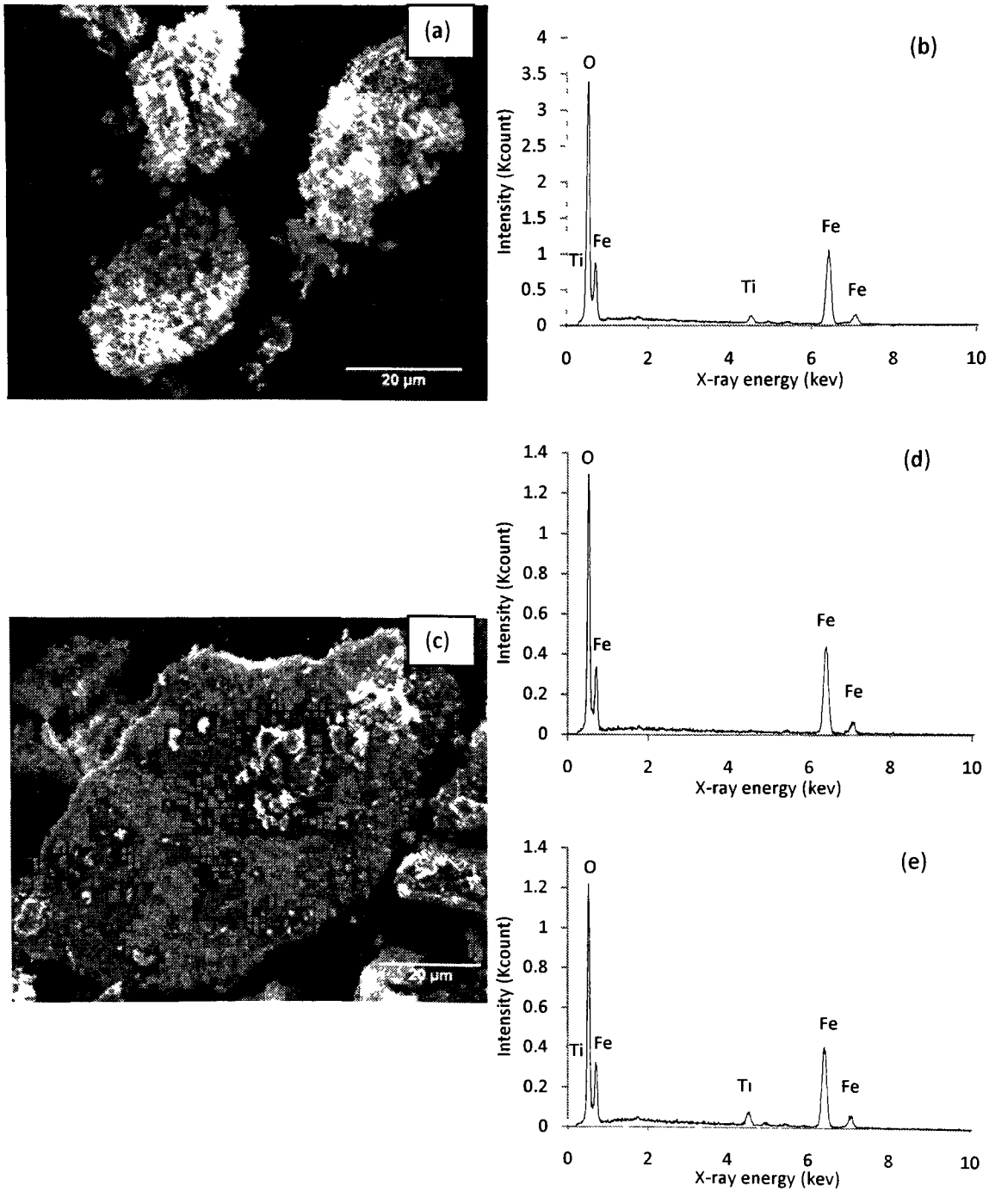

Figure 4.70. SEM micrographs of the two types of wear debris generated when TO-TMC was tested at 10 N; (a) ultrafine particles and (c) plate-like laminates. The EDS spectrum of (a) is given in (b). The EDS spectra shown in (d) and (e) represent two types of composition obtained from the plate-like laminates.

4.5.3 Wear Rates and Wear Mechanisms of the Counterface Ball

The variation of the wear rate of chrome steel (C/S) ball that were tested against TMC and TO-TMC samples were measured by weighting the balls before and after the test. The surface of the balls was rinsed with acetone prior to weight measurement to remove any loose debris that was generated during the wear test. Figure 4.71 illustrates the variation of the wear rates of the C/S ball that was measured based on the mass loss at different contact pressures when tested against TMC and TO-TMC samples. The wear rates of the balls tested against TMC samples was consistent with the characteristic features of the three regimes of wear that are described in section 4.5.1. At the low contact pressure (0.65 GPa) the wear rate of C/S ball was slightly higher than the moderate contact pressure of 0.78 GPa, which was attributed to the abrasive action of the protruding TiC particles. The wear rate of the ball was increased suddenly as the pressure increased from moderate loads (0.88 GPa) to the high loads (0.98 GPa), and at the highest contact pressure (1.11 GPa) the wear rate of the ball was 3 times higher than the moderate contact pressure of 0.88 GPa, which was due to the abrasive action of the fractured and loose TiC fragments with sharp edges at high loads.

The wear rate of the chrome steel ball tested against TO-TMC sample increased linearly when the contact pressure increased from 0.805 to 1.05 GPa (low loads). As the pressure increased to the high loads (1.22-1.37 GPa), the wear rate increased sharply which evidenced the higher abrasion of the steel counterface by the TiO_2 oxide at high pressures. The wear rate of the ball slide against TO-TMC remained lower than the ball slide against TMC samples, for example the wear rates of the balls slide against TMC under the pressures of 0.98 and 1.11 GPa was 7.7 and 5.4 times higher than the wear rate of the ball slide against TO-TMC. The abrasive nature of TMC samples, therefore, was significantly improved by performing thermal oxidation at 800°C for 20 min.

The wear rate of the counterface ball were deducted from the wear rates of the TMC disk measured via the depth based method to better elucidate the contribution of the counterface wear loss on the measured value. The calculated values are plotted in Figure 4.72 and compared to the wear rate values measured via the mass loss method. The depth based measured wear rates were lower as the contribution of the ball counterface was

deleted from these measurements. These calculated difference values were, however, not equal to the wear rate values measured via the mass loss method. The existed difference was attributed to the contribution of material transfer to the mass loss based measurements, which further decreases the weight gained by the sample. The wear rate difference values plotted in Figure 4.72, therefore, represents a more precise estimation of the wear rate of the disk samples. The wear rates of the TMC and TO-TMC sample calculated based on the wear rate difference of the disk and the ball are compared in Figure 4.73. The wear regimes previously indentified for TMC and TO-TMC samples and the significant improvement in the wear resistance of TMC samples—achieved by thermal oxidation— are also confirmed by this method calculation (similar to the mass-loss and depth based methods).

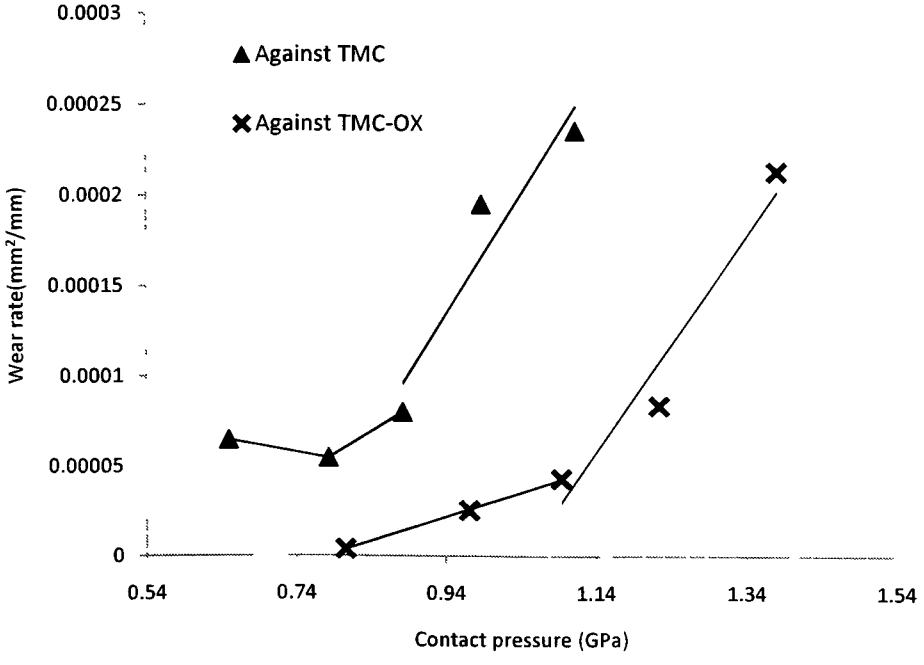

Figure 4.71. The wear rate of the chrome steel ball tested against TMC and TO-TMC samples within the contact pressure range of 0.64-1.38 GPa which was measured based on the mass loss at each pressure.

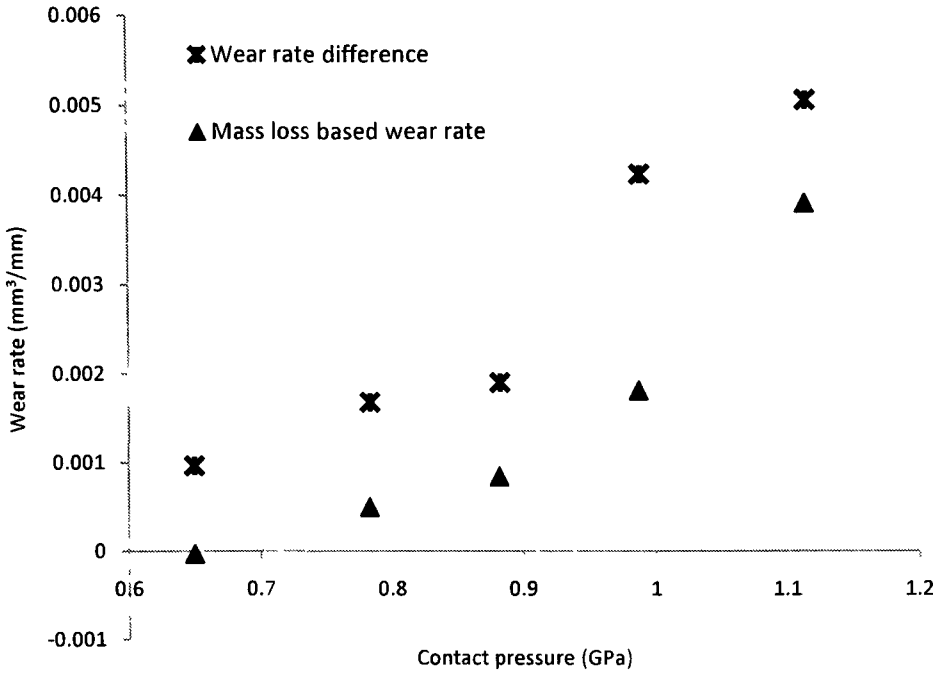

Figure 4.72. The difference between the wear rate of the TMC disk measured based on the depth-based method and the wear rate of ball counterface. These values are compared with the wear rate of TMC samples measured based on mass loss method.

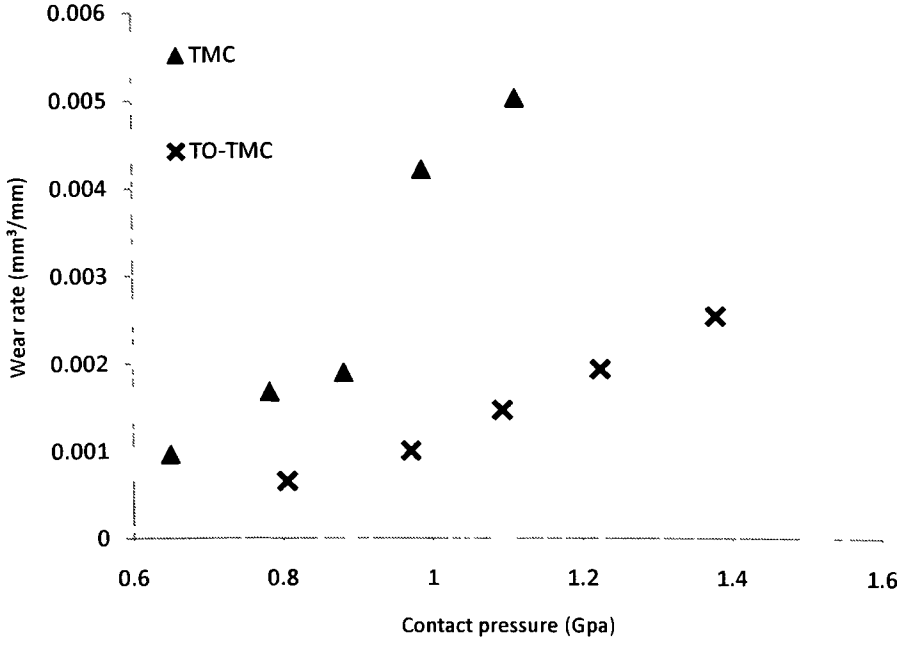

Figure 4.73. The wear rate of TMC and TO-TMC samples within the contact pressure range of 0.64-1.38 GPa calculated based on the difference between the depth-based wear rate of the disk and the wear rate of the counterface ball.

Chapter 5

5 Discussion

5.1 Evaluation of Mechanical Performance of TMC Samples

In this study, the mechanical properties of TMCs were evaluated based on their performance during tensile and micro-scratch tests. The incorporation of TiC particles into Ti-6Al-4V alloy increased the yield and tensile strength at the expense of the tensile ductility at room temperature, which was impaired by a factor of 3.3 compared to the unreinforced alloy (Figure 4.11). The tensile ductility of the composites was, however, significantly increased at elevated temperature, which satisfies the high-temperature service condition as an exhaust valve [1]. The strengthening effect of the particles was inferior at high temperatures, and the tensile strength of TMC samples was 24 % higher than the unreinforced alloys at 400°C compared to a 9% increase in strength at 25°C. SEM observations of fracture surface of the sample tested at room temperature (Figure 4.12) confirmed that the TiC particles act as stress raisers during mechanical loading, giving rise to failure of composites via cracking within the particles, followed by the final failure of the matrix via void coalescence. According to Tjong and Mai [7], ex-situ fabricated TMCs generally do not have a clean interface, which promotes a weak bonding between the particles and the matrix [7]. In this study, however, a clean and strong interfacial bonding was achieved by MIM process. The observed cracking within the particles during mechanical loading was believed to be due to the large size of the reinforcements (1-10 μm), which then promotes stress concentration within the particles.

It is known that the strength of Ti-6Al-4V is very sensitive to temperature [50]: it decreases from 839 MPa, at room temperature, to 414 MPa at 400°C (Figure 4.11). The mechanical strength of the TiC particles, on the other hand, is not affected by the temperature [9]. The significant enhancement in the high temperature strength achieved by incorporation of TiC particles was, therefore, due to the inherent high temperature stability of the carbide particles.

The mechanical performance of the composites was further evaluated by performing micro-scratch test and studying the types of failure during sliding contact (Figure 4.21). Particle cracking also occurred during scratch test, commenced at 4.22 GPa contact pressure, and exhibited a semi-circular morphology that was previously evidenced on the coatings. Particle cracking was followed by sinking in at 6.29 GPa which was accompanied by a sudden increase in the depth of penetration of indenter. Finally, at 8.22 GPa particle fracture occurred at the edges of the scratch groove which caused a sharp shift in coefficient of friction to higher values with larger fluctuations.

The results of micro-scratch test, therefore, confirmed the strong interfacial bonding achieved by MIM process where no indication of pulled-out particle was found. Failure of the TMC samples via cracking within the particles, however, occurred during scratch test based on which the role of particles as stress raisers during mechanical loading was concluded. A perfect interfacial bonding is a prerequisite condition for transfer of load from matrix to the particle. Consequently, the load is carried by the carbide particles—as a result of their higher elastic modulus— and the tensile and yield strength of the material is improved significantly. The improvement in the high temperature mechanical properties of the composites was, on the other hand, a result of the stability of TiC at high temperatures.

5.2 Discussion of Wear Mechanisms of TMC Alloy

The wear mechanisms of TMC samples are discussed and compared with the unreinforced Ti-6Al-4V alloy in terms of the changes in wear rate of the samples and the ball counterface, the changes in the coefficient of friction, the worn surface and subsurface morphologies and the structure and morphology of the loose debris. Three wear regimes were distinguished, namely the low, the moderate and the high loads. The TMC samples exhibited weight gain at low load (<2 N), while the wear rate increased to a positive value as the wear tests was performed at moderate load regime (3.5-5 N). When tested at moderate loads, the wear rate of the TMC samples, however, was lower than the wear rate of Ti-6Al-4V samples. The wear rate of TMC samples increased sharply at high loads and the composite samples lost their wear resistance compared to Ti-6Al-4V samples. In this section, the series of phenomenon associated with these wear regimes are

discussed, and then the role of TiC particles during sliding contact is inspected based on the micro-scratch and the wear test results.

5.2.1 Characteristics and Wear Mechanisms of Low Loads (<2N)

The characteristic features of the worn surface of TMC samples at low loads—previously described in section 4.5.1.3—are as follows:

i) Patches of iron oxide mainly concentrated at the leading tip TiC particles,

ii) Fine particles of iron oxide (0.1-1 μm) that even after rinsing with acetone were remained on the surface,

iii) Virtually undeformed Ti-6Al-4V matrix between the TiC particles with occasional surface deformation in the form of grooves with an average width of 6μm and sub-micron scratches which were both stopped at TiC particles,

iv) Protruding TiC particles which were not damaged or sank into the matrix, the average height of the TiC particles over the surface measured by optical profilometery prior to the test (section 3.6.2) remained unchanged after the test (Figure 4.47).

The various types of running-in in terms of changes in microstructure, surface topography, transfer films, third body agglomerates, etc have been discussed by Blau [124]. The typical COF plot observed for TMC samples tested at low load is described in section 4.5.1.2. According to the classification made by Blau [124], the initial momentary rise at the start of the wear test followed by the sudden drop in COF is generally attributed to the high initial surface roughness followed by surface conformity and smoothing [124]. The average surface roughness of the TMC samples prior to wear test was 0.4 μm compared to an average of 0.04 μm for Ti-6Al-4V, and the average height distribution of TiC particles was 1.25μ. Surface conformity was achieved by formation of iron oxide layer on the surface. The large fluctuations superimposed upon the general curve (Figure 4.35) were caused by spallation of the iron oxide layer and then formation of a new layer (Figure 4.47).

Abrasion of the steel counterface with protruding TiC particle, followed by oxidation of iron has been frequently evidenced by other researchers [10,11,94] under the

conditions similar to this study (0.3 m/s, 0.65 GPa). The Vickers hardness of the particles was measured via micro-indentation test on the reinforcements which was 3653±554 (*Hv*), while the Vickers hardness of chrome steel ball was 700 (reported by the supplier). The initial contact at the protruding, hard TiC particle was, therefore, followed by severe abrasion of counterface, oxidation and transfer of iron to the leading edge of TiC particles. A lubricant layer of iron oxide covered the surface which smoothen out the surface and caused the sudden drop in COF The oxidation of iron can be explained by the work of Lim and Ashby [54] according to which mild oxidational wear happens due to elevated flash temperature at the asperity tips. In this case the transferred iron layer comprised the asperity tips. The oxide spalled off once its thickness reached a critical thickness [54]. The plate-like wear debris (Figure 4.52) was, therefore, formed by oxide spallation causing large fluctuation in the steady state stage of COF plot. The loose oxide particles were retained within the wear track where they were comminuted and were fractured by repeated plastic deformation, and the fine oxide particles were then generated (Figure 4.52). This model for formation of oxide debris particles was first suggested by Stott [55] which is shown in the schematic illustration of Figure 2.11 [55]. These small fragments of oxide abraded the ductile Ti-6Al-4V matrix—evidenced by formation of grooves on the substrate (Figure 4.40).

The wear rate at the low loads was, accordingly, determined by the rates of following processes:

i) Transfer and oxidation of iron,
ii) Agglomeration of oxide particles and formation of layers of oxide,
iii) Break down of the layers,
iv) Abrasion of Ti-6Al-4V substrate.

The negative value of the wear rate measured by mass loss method (section 4.5.1.1) confirmed that the transfer and oxidation of iron was the controlling process at the low loads. Incorporation of TiC particles, therefore, improved the wear resistance of the Ti-6Al-4V matrix via the load carried by the ceramic reinforcements. This was confirmed also by the results of micro-scratch and tensile tests (discussed in section 5.1).

5.2.2 Characteristics and Wear Mechanisms of High Loads (7-10N)

As a results of the studies performed on the worn surface and subsurface of TMCs tested at high loads (sections 4.5.1.3 and 4.5.1.4), the following features were found:

i) Two layers of tribolayer formed successively on the worn surface:
   a. An inner compact layer (1.1-5.8 μm) consisted of Ti (50 at%), Fe (4 at%), Al (6 at%), and V (2at%) oxides. This layer exhibited a stratified morphology,
   b. An outer layer (3.7-5.6μm) formed by agglomeration of oxide particles and TiC fragments. The composition of the oxide was similar to the inner layer,

ii) Brittle detachment of large particles of oxide from the tribolayers which exposed the Ti-6Al-4V matrix into more deformation,

iii) Fractured and plucked-out TiC particles which left the unreinforced Ti-6Al-4V unprotected.

iv) Severely deformed Ti-6Al-4V substrate below the tribolayer which exhibited several features:
   a. The microstructure of the Ti-6Al-4V substrate within an average depth of 3 μm was changed, which was believed to be due to either deformation induced transformation of β phase to α or dynamic recrystallization [125].
   b. Rotation of the lamellar β phase towards the sliding direction in the layer beneath the abovementioned layer. The thickness of the β lamella was also significantly reduced.
   c. Fracture of TiC particles within a depth of 2 μm below the tribolayer,

v) Cracking within Ti-6Al-4V substrate parallel to the sliding direction.

The plot of coefficient of friction at the high loads increased from an initial low value to an steady state value of 0.55 (Figure 4.37), which was roughly equal to the steady state COF value for Ti-6Al-4V This was attributed to the initial contact at the protruding TiC particles immediately followed by the fracture of TiC particles, and then metallic contact which caused the jump in friction. The contact pressure produced under 6mm C/S ball at the high loads was within a range of 0.98-1.11 GPa, while fracture of

particles under micro-scratch test was first evidenced under 8.22 GPa (section 4.4.4). These discrepancies between the critical pressure of failure can be justified based on a surface fatigue phenomenon that is characterized by surface cracking and flaking of material caused by repeated, alternating loading of solid surfaces [34].

The metallic contact that occurs after destruction of particles induced a wear process similar to unreinforced Ti-6Al-4V with an additional contribution of TiC fragments as third body abrasives. Molinari et al [58], Straffelini [50] and Qu et al [61] studied the dry sliding wear of Ti-6Al-4V against steel. The operative mechanisms were oxidative wear of a plastically strained subsurface at low sliding speed, and metallic delamination at high sliding speed. The inner compact tribolayer observed in this study was similar to the oxide layer formed on the worn surface of unreinforced Ti-6Al-4V The minor amount of iron oxide was added by the abrasive action of TiC fragments on counterface. The multilayered morphology of the inner tribolayer can be explained based on the mild oxidational wear mechanism proposed by Lim and Ashby [54], and described in section 2.1.6.1. Similar to unreinforced alloy, even when the oxidative wear predominates plastic shearing of the subsurface layers was evidenced.

The similar thickness, morphology and composition of the inner tribolayer and the plate-like oxide debris together with the observed cracking at the tribolayer/substrate interface (Figure 4.49 and Figure 4.53) confirmed that this type debris was generated via brittle detachment of the inner tribolayer. The small oxide particles—shown in Figure 4.53—were then produced via abrasion of the oxide tribolayer by TiC particles. The significantly small size of these particles, i.e. 0.3-0.5 μm, confirmed the abrasive action of hard particles on a hard scale (oxide). The outer tribolayer was then formed by agglomeration and compaction of the oxide particles, which conforms to the mechanism proposed by Stott [55] (Figure 2.11). After this stage wear proceeded by the following processes:

i) Fragmentation of outer tribolayer by any of the following mechanisms:
   a. Brittle fracture that left relatively large craters (50-100 μm) behind,
   b. Abrasion by TiC fragments.

ii) Delamination of the inner tribolayer as a result of cracking at the tribolayer/substrate interface,

iii) Metallic delamination of Ti-6Al-4V substrate.

The damage accumulation model proposed by Zhang and Alpas [43] for an Al-7%Si alloy can be adopted here to explain the metallic delamination of Ti-6Al-4V matrix. According to this model the critical depth of crack propagation is below the surface and determined by the opposing effect of plastic strain (flow stress σ_f) and hydrostatic pressure (σ_H) [43]. As described earlier, severe deformation of Ti-6Al-4V substrate changed the microstructure of the subsurface which probably caused by a $\beta \rightarrow \alpha$ transformation. Fracture of TiC particles within a 2 μm depth was also evidenced. Stress concentration provided by the martensitic transformation [1] and/or fractured particles, enhanced crack nucleation at the critical depth within the deformed substrate.

The following mechanisms were, therefore, cooperative at the high loads and contributed to the high wear rate of Ti-6Al-4V-10Vol%TiC compared to Ti-6Al-4V: Oxidative wear of the severely deformed substrate, third-body abrasion by TiC fragments and/or oxide particles, and metallic delamination.

5.2.3 Characteristics and Wear Mechanisms of Moderate Loads (3.5-5N)

The prominent characteristic features that were observed on the worn surface and subsurface of Ti-6Al-4V-10Vol%TiC alloy tested at the moderate loads are as follows:

i) A discontinuous tribolayer that exhibited the following characteristics:
   a. Comprised a single layer morphology (0.7-5 μm) similar to the inner tribolayer evidenced at the high loads,
   b. Consisted of a mixture of Ti (36 at%), Fe (9 at%), Al (6 at%) and V (3 at%) oxides,
   c. Provided void nucleation sites at the interface with the substrate or between its own sub-layers,
   d. Provided intermittent coverage of the TMC matrix,

ii) Surface damage of TiC particles which was not followed by fracture or particle pull-out.

iii) Plastic deformation of Ti-6Al-4V substrate that occurred by ploughing and scratching. The deformation was impeded by the damaged TiC particles.

iv) A plastically strained layer below the tribolayer which exhibited the following features:

   a. Similar to high loads, the microstructure was varied within 1 μm depth below the contact surface, namely no equiaxed β phase was observed in this layer.
   b. The lamellar β phase at the region underneath the abovementioned layer became finer while rotated towards the sliding direction.
   c. Unlike the high loads, the TiC particles endured the shear strain and no particle fracture was observed at the subsurface regions.

Similar to the high loads, the initial increase in COF (Figure 4.37) was due to the surface conformity achieved by particle damage followed by metallic/metallic contact. The higher iron content of the tribolayer compared to the high loads was a consequence of a longer running-in period. This led to an initial abrasion of the counterface by protruding TiC particles—prior to any particle damage—which lasted longer at moderate loads. Formation of the multilayered oxide tribolayer can be explained based on the mechanism proposed by Lim and Ashby [54] for mild oxidational wear of a plastically deformed layer. Detachment of the plate-like wear debris (which is shown in Figure 4.54) occurred by cracking started from the voids at the oxide/substrate interface or within the tribolayer (Figure 4.51). The loos debris particles formed at moderate loads (1-3μm (Figure 4.54)) outsized the fine oxide particle evidenced at higher loads. The size of these particles provides evidence for their source of formation, which was fragmentation of detached plate-like loose debris and not abrasion by TiC fragments—evidenced at high loads. According to Stott [55], the prerequisite for agglomeration of the oxide particles is that they should be small enough for the adhesion forces arising from the surface energy to come into play. The relatively large size of the oxide particles at moderate loads, therefore, explains the single layer morphology of the tribolayer.

Another distinction in wear performance of TMCs at moderate loads can be made based on the absence of metallic delamination compared to high loads. As described in

section 5.2.2, the nucleation of cracks can happens at a critical depth which is determined by the opposing effect of plastic strains and hydrostatic pressure that introduces a maximum in the damage rate at a critical depth. The value of critical depth has been proved to increase with increasing load and velocity [43]. Cracking at high loads was, on the other hand, enhanced by the martensitic, deformation-induced $\beta \rightarrow \alpha$ phase transformation and/or particle fracture. Therefore, two factors contributed to the absence of metallic delamination at moderate loads: i) the smaller critical depth of crack nucleation caused by lower load and better protection exerted by oxide tribolayer and ii) lack of points of stress concentration for crack nucleation confirmed by the absence of any particle fracture at the subsurface zone.

In summary, at moderate loads wear of TMCs proceeded by oxidation of the plastically deformed layers, which was followed by brittle detachment and fragmentation of the oxide tribolayer. The oxide layer formed at these loads, however, provided an outstanding protection for the substrate compared to the tribolayer formed at higher loads. The conserved TiC particles within the matrix, additionally, impeded severe deformation of Ti-6Al-4V matrix and annihilated any metallic delamination.

5.2.4 Evaluation of TiC Particles Performance during Sliding Contact

The TiC particles incorporated by MIM process into Ti-6Al-4V matrix were damaged via cracking that occurred at 0.78 GPa during wear test and at 4.22 during micro-scratch test, however, they remained intact under this pressure and impeded the surface plastic deformation of the Ti-6Al-4V matrix up to 0.88 GPa pressure. These particles lost their load bearing capacity via particle fracture that happened at 0.98 GPa pressure during wear test, at 8.22 GPa during micro-scratch test, and in the course of tensile test. Particle fracture, which was believed to be mainly due to their large size (1-10 μm), preceded any type of particle pull-out. This confirmed a good particle/substrate interfacial bonding achieved by MIM process.

5.3 Oxidation Mechanisms of Ti-6Al-4V and TMC Alloys

The oxidation mechanism of Ti-6Al-4V and the effect of incorporating TiC particles on oxidation mechanism of Ti matrix are discussed in this section. The

morphology, composition and mechanical properties of the oxide scale formed on Ti-6Al-4V as a result of thermal oxidation are discussed in section 5.3.1, and are used as a reference for discussion of oxidation mechanism of TMC alloys. The oxidation behaviour of TMC samples at various temperature and times are discussed in section 5.3.2 in terms of the structure, morphology and composition of the scale. The mechanical properties of the coating are also determined and discussed which include their performance under micro-scratch test and their fracture toughness. Based on these discussions the optimum oxidation condition for TMC samples is then determined (section 5.3.3).

5.3.1 Oxidation Mechanism of Ti-6Al-4V Alloy

The studies on the TO-Ti-6Al-4V samples revealed that the morphology, thickness and compositions of the oxide scale and ODZ were similar for bimodal and Widmanstätten microstructures. The thicknesses of the oxide scale and the ODZ, which were measured by microscopic observations and micro-indentation on tapered cross-sections, are listed in Table 4.1 and Table 4.2. Theoretically, diffusion through α-Ti is one to three orders of magnitude slower than diffusion through β-Ti [87]. The diffusion in both microstructures, therefore, is controlled by the thickness of the α-case (ODZ) and also the thickness of the oxide scale, and once a thin layer of oxide and α-case were formed on the surface, the effect of microstructure on diffusion mechanism became negligible. The effect of primary microstructure on oxidation was only via the primary hardness of the bulk sample that was 540 (*Hv*) for bimodal and 650 (*Hv*) for Widmanstätten samples (Figure 4.3). As a result, the hardness diffusion zone adjacent to the interface (at a 5μm distance) was 989 for bimodal microstructure while it was 1072 (*Hv*) for Widmanstätten microstructure. This higher value of hardness can be explained in terms of the hardening effect of the martensitic structure formed during heat-treatment within β-phase field—performed to produce the Widmanstätten type microstructure [1].

X-ray diffraction studies were performed to reveal the composition of the oxide (Figure 4.4) followed by FIB cross-sectioning and EDS mapping to find out the distribution of the compounds within the oxide scale (Figure 4.5). The major phase formed during oxidation at 600°C was rutile form of TiO_2, and the patterns obtained for anatase and alumina were weak with many of the high intensity reflections absent. The

existence of these oxides, however, cannot be ruled out. The EDS mapping on the oxide cross-section (Figure 4.5) revealed that an Al-rich layer—consisted of an alumina compound—was generated at the gas/oxide interface, while the inner scale consisted of a Ti-rich layer in the form of rutile. The thermodynamics of formation of alumina and titania oxides as well as the diffusion mechanisms that are responsible for the layered morphology of the oxide are described here.

The layered structure of the oxide scale and the XRD results indicates that two reactions took place during the oxidation process of Ti-6Al-4V alloy:

$$Ti + O_2 \rightarrow TiO_2 \qquad \text{Equation 5.1}$$

$$4/3Al + O_2 \rightarrow 2/3Al_2O_3 \qquad \text{Equation 5.2}$$

The values of free Gibbs energies associated with these reactions can be obtained from the following equations [98]:

$$\Delta G^o_{5.1} = -943500 + 179.1T \qquad \text{Equation 5.3}$$

$$\Delta G^o_{5.2} = -1115500 + 209.2T \qquad \text{Equation 5.4}$$

where T is the temperature. Ascribing 873 to T, the free Gibbs energy of formation of alumina at this temperature is -787.1 KJ while the energy if formation of titania would be -932.9 KJ, and therefore alumina is more stable at this temperature. However, in this study preferential oxidation of Ti at the oxide/substrate interface was observed. The free Gibbs energies can be determined from the following equations:

$$\Delta G^o_{5.1} = -RTlnK_{5.1} = -RTln\frac{a_{TiO_2}}{a_{Ti}.P_{O_2}} \qquad \text{Equation 5.5}$$

$$\Delta G^o_{5.2} = -RTlnK_{5.2} = -RTln\frac{(a_{Al_2O_3})^{2/3}}{(a_{Al})^{4/3}.P_{O_2}} \qquad \text{Equation 5.6}$$

where $K_{5.1}$ and $K_{5.2}$ are the equilibrium constants for reactions 5.1 and 5.2, R is the gas constant, and a_{TiO_2}, a_{Ti}, $a_{Al_2O_3}$, and a_{Al} are the activities of titania, titanium, alumina and

aluminum respectively. If unit activities are ascribed to Al_2O_3 and TiO_2 and atmospheric pressure for P_{O_2}, then equations 5.5 and 5.6 become:

$$\Delta G^o_{5.1} = RT\ lna_{Ti} \qquad \text{Equation 5.7}$$

$$\Delta G^o_{5.2} = 4/3\ RT\ lna_{Al} \qquad \text{Equation 5.8}$$

From these equations and by substituting T=873 K in equations 5.3 and 5.4, the minimum values of aluminum and titanium activities were calculated: $a_{\min Al} = 1.3 \times 10^{-42}$, and $a_{\min Ti} = 7.5 \times 10^{-48}$ Accordingly, the values of minimum aluminum activity required for the formation of alumina is higher than the minimum required Ti activity for the formation of TiO_2. Du et al [83] and Ignatov et al [81], on the other hand, suggested that the activation of Al (a_{Al}) is about 4 orders of magnitude smaller than the activation of Ti (a_{Ti}) for binary Ti-Al alloys. Therefore, in the course of inward diffusion of O species and outward diffusion of cation species, preferential oxidation of Ti can happen at the oxide/substrate interface as oxygen anions meets titanium cations, in spite of the higher free Gibbs energy of formation of alumina. This allows the Al cations to leave the substrate and diffuse outward to the gas/oxide interface, and an external Al-rich compound layer will be formed consequently. A schematic illustration of the diffusion mechanisms described here is shown in Figure 5.1.

In summary, as described in section 2.2.1.1, TiO_2 in an n-type conductor. As a result the disorder of TiO_2 oxide scale at high oxygen pressure and low temperatures is dominated by oxygen anion vacancies. Once a thin layer of rutile is formed at the beginning of oxidation, the oxygen required for oxidation of substrate is provided by inward diffusion of oxygen anions that is accompanied by the outward diffusion of anion vacancies as schematically depicted in Figure 5.1. Since the preferential oxidation of Ti happens at the oxide/substrate interface, Al species can leave the interface and form the external Al-rich layer. Nevertheless, as diffusion of metal ion vacancies are not possible in n-conductors, the vacancies left behind by diffusion of Al cations form a porous interface (Figure 4.5).

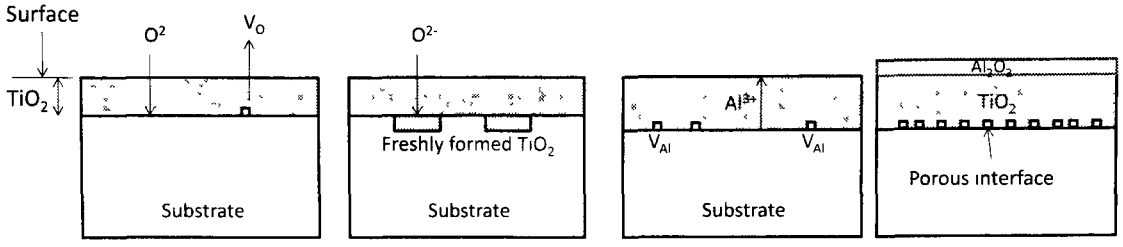

Figure 5.1. Schematic illustration of the diffusion mechanism responsible for the formation of Al_2O_3+TiO_2-scale on Ti-6Al-4V alloy; V_O is the oxygen vacancy and V_{Al} is the aluminum vacancy.

5.3.2 Oxidation Mechanism of TMC Alloys

The microscopic observation on the cross-sections of the oxidized TMC samples revealed that the oxidation had to be continued for at least 65 h to attain an integrated scale at 600 C. The scale formed at 800 C, however, reached its critical thickness, once the oxidation process prolonged for more than 20 min. Based on these observations, the oxidation behaviour of TMCs was studied at two conditions, namely at 600 C for 65 h and at 800 C for 20 min. The thicknesses of the oxide scales formed on Ti-6Al-4V substrate, on TiC particles and the thickness of ODZ are listed in Table 4.2. The oxidation of TiC particles at 600 C resulted in a thick (4.41 μm) but stratified scale. The stratification observed within the scales is mainly due to the growth stresses built up in the scale caused by: i) high Pilling-Bedworth ratio of the oxide and the substrate, ii) the great variations in lattice parameters at the interface caused by formation of the solid solution, and iii) the high ratio of coefficient of thermal expansions of the oxide and the substrate. These stresses increase until a bearable maximum value is reached at a critical thickness, at which a crack nucleates [70,71,88].

X-ray diffraction analysis (section 4.4.3) revealed that the composition and the element distribution of the scale formed on TMC samples at 600 C and 800 C was similar to the scale on TO-Ti-6Al-4V Oxidation of the Ti matrix alloy resulted in an inner TiO_2 layer—mainly rutile—that was covered by an outer alumina scale. The EDS analysis (section 4.4.1) together with XRD results (section 4.4.3) also confirmed that a rutile scale was formed as a result of oxidation of TiC particles. The oxide formed at both conditions was, however, thick enough to eliminate any reflection from TiC particles beneath the oxide scale.

The temperature dependence of oxidation behaviour of TMCs is discussed here based on the morphologies of the oxide on TiC particles and on Ti-6Al-4V substrate (Figure 4.13, Figure 4.15 and Figure 4.14). At 600 °C, preferential oxidation of TiC particles was dominated, and the scale on TiC particles (4.41 μm) was thicker than the scale on Ti-6Al-4V (0.73 μm). At 800°C, a thicker and more uniform scale was formed. As previously discussed in section 2.2.1.1, rutile is an n-conductor for which at low pressure and high temperature interstitial titanium ions are the major defects, while at high oxygen pressure and low temperatures disorder is dominated by oxygen anion vacancies [20] In the case of oxidation at 600°C, inward diffusion of oxygen species controls the oxidation mechanism since otherwise the oxidation reaction cannot penetrate oxide/substrate interface (in the direction shown by arrow "2" in Figure 4.13). Outward diffusion of interstitial titanium ions is, however, more likely to happen at 800°C. The latter is confirmed by the outward growth of the scale evidenced by the uniform thickness of the scale on the particles and substrate (Figure 4.15 (b)). The cationic diffusion mechanism at 800°C promotes oxide growth at the gas/oxide interface, where the CO_2 gas—produced during oxidation of TiC particle according to equation 2.6—can leave the system, and avoid cracking within the scale. Additionally, the outward diffusion of the oxide provides the ability to heal cracks. A more uniform and adherent oxide can, therefore, form at 800°C.

5.3.3 Determination of Optimum Oxidation Condition for TMC Samples

The performance of the oxide scales formed on TMCs at 800°C after 20 min (8-20min) and at 600°C after 65 h (6-65h) were evaluated by micro-scratch tests and SEM observations on the scratch groove (section 4.4.4), and their fracture toughness was then measured by indentation cracking length method (section 4.4.5). The properties of these coatings were compared to the coating on TO-Ti-6Al-4V samples, which has already been proved to successfully create an adherent, and integrated oxide scale [4,5,64].

The degree of surface deformation created by the sliding stylus on the coating was studied based on the penetration depth profile along the scratch (Figure 4.19). The coefficient of friction was also studied as a function of the normal load (Figure 4.20). The lowest values of depth and coefficient of friction were observed for TMC-8-20min type

coating, which impeded the deformation of TMC sample by a factor of 2 and decreased the coefficient of friction by a factor of 1.6. The TMC-6-65h sample resulted in the highest coefficient of friction at the highest contact pressure compared to TMC and TMC-8-20min samples.

The types of failure were studied based on the classification made by Holmberg et al [120], which is schematically illustrated in Figure 4.8. The critical pressure for each type of failure was detected by SEM observations on scratch groove which is shown in Figure 4.9 for TO-Ti-6Al-4V and in Figure 4.22 for TMC-8-20min and TMC-6-65h samples. All of the following types of failure were evidenced for TO-Ti-6Al-4V sample: i) angular and parallel cracking (at 8.02 GPa), ii) chipping of the coating at the edges of the scratch (12.2 GPa), and iii) half-cone cracks (12.4 GPa). On TMC-8-20min and TMC-6-65h samples, however, only the angular and the half-cone cracks were evidenced. The lumps of oxide protruding from TMC-6-65h were also removed by the sliding action of the stylus. Another criterion used for the evaluation of the coatings is the density of the half-cone cracks at a constant load which is, according to Keer et al [122], affected by the fracture toughness of the coating, normal load and the critical flaw size. These types of failures, the critical pressures, and the average interval of half-cone cracks for TO-Ti-6Al-4V, TMC-6-65h and TMC-8-20min samples are summarized in Table 5.1. It is apparent that the TMC-8-20min samples exhibited the highest resistance to deformation, cohesive and interfacial type failures and the lowest density of half-cone cracks when it was compared to TMC-6-65h and TO-Ti-6Al4V samples.

The modes of failure and the value of the critical load depends on various parameters, namely, the properties of the substrate, the coating, and the coating/substrate interface, the coating thickness, and the friction between the coating and the scratch tip [116]. The angular cracking is a cohesive type failure, which is caused by the substrate pile-up around the sliding indenter [120]. The higher value of critical load for angular cracking in TMC-8-20min samples was attributed to the following factors: i) the thicker scale, ii) the higher fracture toughness of the coating by the lower density of the half-cone cracks, iii) a better support provided for the TiC particles by formation of ODZ (compared to unreinforced Ti-6Al-4V sample). The elastic modulus of the ODZ was 156

GPa while the elastic modulus of non-oxidized Ti-6Al-4V was 105 GPa (as measured by micro-indentation under 400 mN) The difference between the elastic modulus of the TiC particles and the substrate was, therefore, decreased by the thermal oxidation process Consequently, the stress concentration was lower on the particles and they were supported by the stiff ODZ layer Chipping of the coating, on the other hand, is obviously related to an interfacial type failure [120] According to Table 5.1, a better coating/substrate interfacial bonding was achieved by oxidation of TMC samples compared to Ti-6Al-4V samples

Table 5 1 The types of failures, the critical pressures, and the half-cone cracks' interval evidenced during micro-scratch test performed on TO-Ti-6Al-4V, TMC-6-65h, and TMC-8-20min samples

Type of coating	TO Ti-6Al-4V	TMC-6-65h	TMC-8-20min
Maximum penetration depth (μm)	25 94	23 21	18 42
Critical pressure for angular cracking (GPa)	8 02	8 99	10 4
Critical pressure for delamination (GPa)	12 2	Was not observed	Was not observed
Average interval of half-cone cracks at 14 2 GPa	5 5±1 6 μm	7 5±1 9 μm	12 5±3 4 μm

It is generally known that the oxide phases formed during oxidation have substantially lower fracture toughness than the underlying substrate which can adversely affect the wear performance of the components [99] The fracture toughness of the coatings was, therefore, determined based on an indentation techniques Lateral cracks became prevalent for TMC-6-65h samples at 0 75N while the predominant mode for TMC-8-20min samples was radial cracking up to an indentation load of 1 75 N The type of the radial cracks was determined based on the generated best fits of the experimental data for Palmqvist and median geometry (Figure 4 25 and Figure 4 26), which revealed that the Palmqvist geometry dominated This was reasonable since according to Nolan et al [99] for the thin brittle films on tough substrates Palmqvist morphology is more dominant as this type of cracking initiates at the surface where the coating is more brittle The fracture toughness values were then estimated based on three equations, two of which

have been developed for Palmqvist geometry, and the results are listed in Table 4.5 and compared for TMC-8-20min and TMC-6-65h in Figure 4.30. As with the results of micro-scratch test, the coating formed at 800°C after 20 min rendered a higher critical intensity factor compared to the coating formed at 600°C after 65 h, and this result was independent of the type of equation used.

The effect of thermal oxidation on the surface residual stress was also studied based on equation 2.22, which was originally developed by Marshal and Lawn for median type cracking [115]. The negative value of the slope of the graphs—plotted based on this equation (Figure 4.29 and Table 4.5)—should imply the existence of a tensile residual stress for both of the oxide scales. However, according to Ponton and Rawling [107] the slope of these plots has been observed to depend on both the equation used to calculate K_{Ic} data and the type of material, and the existence of a tensile stress within the coating cannot be assured.

In summary, the oxidized TMC samples exhibited a better resistance to chipping and angular cracking compared to the oxidized Ti-6Al-4V samples, which was believed to be due to the role of the particles in hindering the cracks and impeding the substrate pile up. Thermal oxidation at 800°C for 20 min resulted in a thick and adherent oxide which produced the lowest friction trace and the lowest penetration depth under scratch test. The fracture toughness and the oxide/substrate interface strength were higher than the oxide formed at 600°C after 65 h. With these in mind, thermal oxidation at 800°C for 20 h was selected as the optimum condition for TMCs, which was expected to perform satisfactory in wear tests.

5.4 Discussion of Wear Mechanisms of Oxidized TMC Samples

The wear mechanisms of oxidized TMC samples are discussed and compared with TMC samples in terms of the changes in wear rate of the samples and the ball counterface, the changes in the coefficient of friction, the worn surface and subsurface morphologies and the structure and morphology of the loose debris. Two wear regimes were identified, namely the low load (2-5 N) and the high load (7-10 N). The oxidized TMC samples gained weight when tested at low loads, while the wear rate was increased,

albeit so small, and attained a positive value at high loads. The wear mechanisms associated with these load regimes are discussed separately in sections 5.4.1 and 5.4.2.

5.4.1 Characteristics and Wear Mechanisms of Low Loads (2-5N)

The characteristic features of the worn surface and subsurface of oxidized TMC samples at low load (2-5 N) —described in sections 4.5.2.3 and 4.5.2.4— can be listed as follows:

i) The Rutile coating remained integrated and attached to the substrate.

ii) Layers of Iron oxide covered the worn surface which displayed the following two forms:
   a. Patches of homogeneous iron oxide smeared over the rutile coating,
   b. A mixture of Fe (14 at%), Ti (14 at%) and Al (5 at%) oxides,

iii) No plastic deformation occurred at the subsurface oxygen diffusion zone (ODZ) beneath the coating.

iv) Infrequent nucleation of voids within ODZ (at a depth range of 0.8-4 μ), which were rotated and stretched towards the sliding direction as a result of the tensile stress at the trailing edge of sliding ball.

v) Formation of cracks via a void coalescence mechanism adjacent to the coating/ODZ interface,

vi) Higher density of voids and cracks at 5N compared to 2N,

vii) Crack arrest at the retained β phase which acted as a ductile fiber and bridged the faces of the crack.

The negative values of mass loss-based wear rate of TO-TMC at 2, 3.5 and 5N along with the significantly larger value of depth-based wear rates (section 4.5.2.1) confirmed abrasion of the chrome steel counterface by the hard asperities of the oxide coating. This coating had an average thickness of 3.33 μm and mainly consisted of rutile and alumina oxides (section 5.3.2). The Vickers hardness of the oxide coating was 1347±190—measured by micro-indentation under 0.2 N load—, while the Vickers hardness of C/S ball (provided by the supplier) was 700 (*Hv*). Patches of homogeneous iron oxide were formed by severe abrasion of the counterface that was followed by

oxidation of freshly transferred iron. The loosely attached iron oxide layer (Figure 4.61) was exfoliated and formed the plate-like wear debris that is shown in Figure 4.69. The mixture of Fe (14 at%), Ti (14 at%) and Al (5 at%) oxides were then formed by a sequence of events: fragmentation of the oxide laminates that was followed by mixing with the minor amount of rutile and alumina—removed from the asperity tips—, and then agglomeration of the oxides mixture. The ultrafine (0.02-0.1μm) oxide debris—shown in Figure 4.69—confirms this mechanism.

As described in section 2.2.1.1, oxygen dissolution in α-Ti increases the CRSS of prismatic planes more than the other systems which accounts for the preference of pyramidal and basal planes over the prismatic planes [28,75,76]. Several models, such as the non-planar core structure of $\langle a \rangle$ type screw dislocations [76] or ordering of oxygen atoms on slip planes [25] are proposed to explain the change in the preferred slip system. Moreover, plastic deformation by twinning has been proved to be completely suppressed as the oxygen content of Ti increases [26,77]. The significant enhancement of strength and the deterioration of ductility—caused by oxygen dissolution in α-Ti—, therefore, can be explained in terms of the suppressed modes of plastic deformation.

The geometry of the tensile stress at the trailing edge of a rigid sliding sphere has been studied by Lawn et al [126] according to which the superposition of a tangential force rotates the tensile stress axis towards the sliding direction. The relationship between the angle of rotation (θ) and the coefficient of friction (μ) (which is shown in Figure 5.2) has the following form:

$$\theta = Arctan(\mu) \qquad \text{Equation 5.9}$$

Formation of the oblate voids—voids which were rotated and stretched towards the sliding direction—can be explained based on the fracture theory of ductile materials in a tensile stress field. The voids which are the basic source of ductile fracture are nucleated at sites where compatibility of deformation is difficult [29]. These sites are provided via the restricted plastic deformation of ODZ that is caused by the aforementioned effect of oxygen dissolution. The crack growth in ductile fracture is essentially by a process of void coalescence. The direction of tensile stress and elongation of voids relative to the

sliding direction are shown in the schematic illustration of Figure 5.2. Void coalescence occurs by elongation of voids and elongation of bridges of materials between the voids in a direction perpendicular to the tensile stress which makes an angle of $\varphi=\theta+90^{\circ}$ with the sliding direction. The average value of steady state COF at low load increased from 0.52 at 2N to 0.55 at 5N which gives a value of θ within a range of 27.5-28.8° However the direction of oblate voids measured from subsurface observations (Figure 4.65 and Figure 4.66) gives an average value of 60°for θ. Equation 5.9 has originally been developed for monolithic materials and the differences between the theoretical and analytical directions can be due to the effect of the elastic modulus of the coating on the tensile stress distribution. Nevertheless the trend of change in the direction and density of the voids and cracks are consistent with a ductile mechanism of void nucleation.

It is noteworthy that the retained β-phase within ODZ acted as bridging points and confined the crack that was propagating through it. This mechanism is similar to the crack wake toughening that is one of the various toughening mechanisms operative in fiber reinforced composites. According to this mechanism as the crack opens under the action of the applied stress, some of the stress will be transferred to the fibers which will deform elastically. The stresses in the bridging fibers are viewed as crack closure tractions which reduce the stresses at the crack tip. There is a corresponding reduction in the stress intensity factor at the crack tip and hence crack propagation is hindered [92].

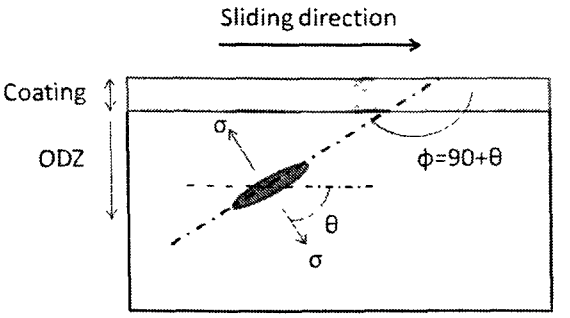

Figure 5.2. Schematic illustration showing elongation of voids with an angle of φ relative to the sliding direction due to the tensile stress (σ) at the trailing edge of sliding ball, θ is the degree of rotation of tensile stress when $\mu \neq 0$.

Despite the nucleation and propagation of voids and cracks within ODZ, no evidence of delamination was found at the low loads. The cracks were, therefore,

predominantly confined by β-phase and/or arrested at the coating/substrate interface and wear of the samples was controlled by the following processes:

i) Transfer and oxidation of iron,
ii) Spallation of iron oxide layer,
iii) Moderate abrasion of the coating with the oxide particles,
iv) Partial fragmentation of the coating observed at the highest load of this regime (5N).

The transfer of iron from counterface, however, controlled the wear process which resulted in the negative value of wear rate measured by mass loss method, and abrasion of the C/S counterface ball that was also confirmed by the considerable wear loss of the counterface bal (Figure 4.71).

5.4.2 Characteristics and Wear Mechanisms of High Loads (7-10)

The prominent characteristic features of the worn surface and subsurface of the oxidized TMC alloy common to the high loads (sections 4.5.2.3 and 4.5.2.4) can be listed as follows:

i) An iron oxide layer which—similar to the low loads—exhibited two different morphologies:
   a. Patches of iron oxide that covered the majority of the surface,
   b. A mixture of Fe (20 at%) and Ti (14 at%) oxides,
ii) A higher area fraction was covered by the iron oxide layer compared to the low loads. This layer can be exfoliated more easily.
iii) Considerably high density of oblate voids whose angle with the sliding direction increased as the load increased.
iv) Formation of cracks via a void coalescence mechanism at the coating/substrate interface, and/or within the hard and brittle ODZ,
v) Occasional failure of the rutile coating either via fragmentation caused by compressive stresses at the surface or via delamination caused by cracking at the interface.

The COF plot, typical to the high loads, exhibited an initial rise (Figure 4.59) which was attributed to the initial high surface roughness—0.6 μm as measured by optical surface profilometery—of the rutile coating. The surface conformity achieved by fragmentation of the rutile coating and formation of the iron oxide layer created the sudden drop in COF As shown in Figure 4.64, the homogeneous iron oxide layer was, occasionally, buckled out as a result of the tensile stress field generated by the sliding ball, and then a crack formed at the surface of the delaminated layer perpendicular to the sliding direction. Exfoliation of the iron oxide layer generated the plate-like loose debris (Figure 4.70). The predominant difference between the high load and low loads can was the spallation of the coating (Figure 4.68). As the contact pressure raised over 1.09 GPa, the value of elastic strain energy released by the voids coalescence became large enough for the crack to break through the arrest points; namely the ductile retained β fibers and the substrate/coating interface. Consequently, a "cup-and-cone" or "dimpled rupture" type morphology [29] was created on the fracture surface which is evident on the SEM micrograph of the delaminated surface of a TO-TMC sample tested at 10N (Figure 5.3). On the other hand, the angle of the axis of elongation of the voids with the sliding direction (φ) increased as the load increased. Considering equation 5.9, this was consistent with the rise in the value of steady state COF from an average of 0.52 at low loads to around 0.65 at high loads.

In summary, destruction of the rutile coating via simultaneous operation of fragmentation—started from the surface—and delamination—started from the subsurface—were the distinctive features of wear at high loads. Additionally, a higher area fraction of the contact surface was covered by the iron oxide layer compared to the low loads. This layer can be exfoliated more quickly compare to the mixture oxide layer. The frequently observed spallation of the iron oxide layer accompanied by a high rate of destruction of rutile coating justified the positive value of wear rate of TO-TMC sample—measured based on mass loss method—despite the evidenced severe abrasion of C/S counterface that was significantly higher than the counterface wear loss at low loads (Figure 4.71).

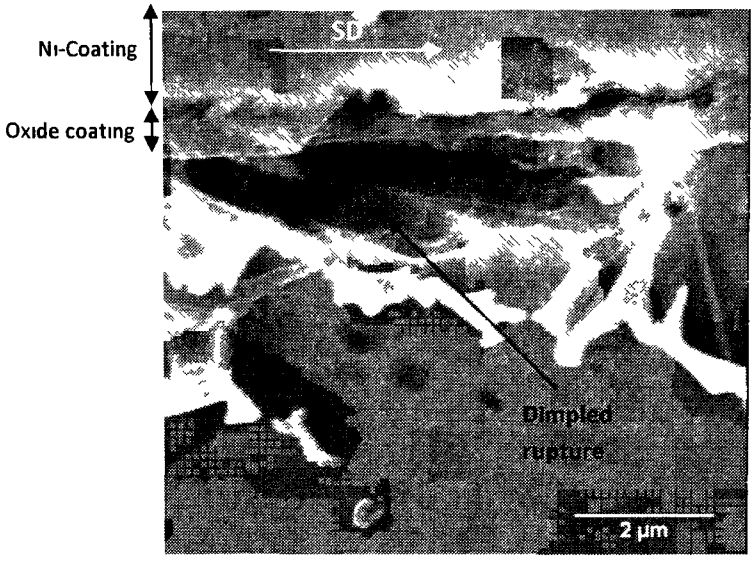

Figure 5.3. SEM micrograph of the worn subsurface of TO-TMC sample tested at 10N normal load, 0.3 m/s sliding speed after 1000m sliding distance. The surface was Ni-coated prior to final surface preparation followed by etching. Dimpled rupture-type fracture morphology is evident on the surface of crack at the coating/substrate interface.

5.5 Comparison of Wear Behaviour of TMCs with Oxidized TMCs

Based on the changes in wear rates and the worn surface features, three wear mechanisms were characterized for TMCs, namely abrasive wear of counterface at low loads, mild oxidative wear at moderate loads, and severe oxidative wear and metallic delamination at high loads. Thermal oxidation at 800°C for 20 min significantly improved the surface properties of TMCs during ball-on-disk and micro-scratch tests. After oxidation was carried out, the depth of penetration of the Rockwell diamond stylus into TMC was decreased by 50%, and the coefficient of friction was also decreased by 40%. The wear rate of TMCs tested at 1.11 GPa was around 126 times higher than the wear rate of TO-TMC sample tested under 1.23 GPa pressure. It should be noted that the contribution of material transfer from the counterface ball induces a false decrease in the wear rate values measured based on mass loss method, and increase the degree of uncertainty of wear rate values. Even so, the superior wear resistance of TO-TMC samples was confirmed by the depth-based wear rate values (Figure 4.57). The depth-based wear rate results also confirmed that the wear resistance of TMCs was enhanced more significantly at higher pressures, namely a 71% increase at 1.11 GPa compared to a 66% increase at lower pressures (0.88 GPa). On the other hand, the wear rate of the C/S

ball tested against TO-TMC remained lower than the wear rate of the ball tested against TMC at all the pressures, for example 81% lower at 1.11 GPa. Therefore, not only the surface properties of TMCs was significantly improved by means of the thermal oxidation process developed in this study, but also the abrasive nature of the TiC particles, which causes the severe abrasion of the counterface, was hindered.

The poor tribological characteristics of TMCs under contact pressures higher than 0.98 GPa has been attributed to two factors: i) inherent surface characteristics of Ti-6Al-4V matrix and ii) third-body abrasion caused by TiC fragments. The inherent surface characteristics of Ti include:

- The low d-bond character of Ti as an element (27%) which makes it extremely active, and promotes adhesion

  The extremely ductile nature of Ti which is because of the increased number of the possible slip systems of α-Ti structure compared to an ideal HCP structure owing to its low value of c/a ratio [4,56].

On the other hand, the incorporation of TiC particle into Ti matrix has been frequently observed to be accompanied by particle cracking and fracture at a critical pressure which in turn increases the wear rate of Ti matrix alloy [10-12,93]. With these factors in mind, the superior wear resistance of oxidized TMCs can be correlated to the contribution of the following factors:

- The nature of the surface contact is changed from metallic/metallic to metallic/ceramic contact, and the ratio of the elastic modulus to the hardness of the surface—measured under 0.2 N load—was decreased from 241 for Ti-6Al-4V substrate to 141 for the oxidized samples. The smaller value of this ratio for oxidized samples promotes elastic deformation and impedes adhesion during wear.
- The hardness of the oxygen diffusion zone adjacent to the oxide was 1042 (*Hv*), and the support provided by this layer prevents the oxide from bending in and penetrating the ductile Ti matrix.

- The diffusion of oxygen into Ti matrix increased the modulus of elasticity (E) of the matrix by a factor of 1.5, and therefore the difference between the stiffness of TiC particle and the stiffness of ODZ became smaller. Assuming a linear elastic behaviour during loading ($\sigma = E\varepsilon$), the stress concentration on the TiC particles was therefore reduced after oxidation, followed by less frequent particle cracking.

In summary, thermal oxidation in an air furnace at 800°C for 20 min, followed by furnace cooling, altered the surface characteristics of the Ti substrate and provided a better support for the carbide particles via formation of diffusion zone, and consequently improved the tribological behaviour of the TMC alloy.

6 Chapter 6

6.1 Summary and Conclusions

The developments in the full potential industrial applications of Ti-6Al-4V alloy have been restricted by the poor tribological properties of this alloy together with the significant loss of mechanical strength of the alloy at high temperature. The aim of this study was, therefore, to evaluate the current available methods for improvement in mechanical properties together with the tribological properties of this alloy, namely thermal oxidation and incorporation of TiC particle by means of metal injection moulding method. The mechanism of oxidation of Ti-6Al-4V alloy was studied using XRD, SEM observations and EDS mapping of the oxide cross-section, micro-scratch and micro-indentation tests. The mechanical performance of the Ti-6Al-4V-10Vol%TiC composites was then studied using tensile test, surface fractography, and micro-scratch tests. Ball-on-disk test configuration was then adopted to characterize and compare the tribological performance of Ti-6Al-4V and Ti-6Al-4V-10Vol%TiC under various normal loads. The wear resistance of the matrix alloy was improved via incorporation of TiC particles provided that the pressure remained lower than 0.98 GPa. In order to improve the high pressure wear resistance of the composite samples, thermal oxidation was adopted. The oxidation mechanism and the optimum oxidation condition for composites were characterized using XRD, SEM observations and EDS mapping of the oxide cross-section, and micro-scratch tests. The fracture toughness of the coatings was measured by indentation cracking length method. In order to further evaluate the performance of the oxide coating generated by the optimum oxidation condition (at 800°C for 20 min), wear tests were performed on oxidized samples. Based on these series of works the following conclusions can be drawn:

1) The effect of the microstructure of Ti-6Al-4V alloy on the oxidation mechanism was negligible. The thickness and the composition of the oxide and the ODZ were analogous for Widmanstätten and bimodal microstructures, since the oxidation mechanism was controlled by diffusion through the oxide scale and ODZ, which was similar for both microstructures. The scale consisted of an outer alumina layer

and an inner rutile layer. Rutile is an n-conductor, and its disorder is dominated by oxygen anion vacancies. The minimum required activities of Al and Ti for oxidation were determined in terms of thermodynamic calculations which offered a higher minimum activity for Al. The outer alumina layer and the porous interface were therefore generated by outward diffusion of Al species, while inward diffusion of oxygen species formed the inner rutile layer.

2) The TiC particles exhibited a strong interfacial bonding with Ti-6Al-4V substrate during tensile and micro-scratch tests, and no interfacial failure was observed. Particle cracking was, however, detected on the fracture surface of tensile samples and during scratch test when the contact pressure reached 4.22 GPa. The yield and tensile strength at room temperature were increased at the expense of ductility. The difference between the tensile ductilities of the unreinforced Ti-6Al-4V alloy and composites was, however, lower at higher temperature. The incorporation of ceramic particles, therefore, significantly improved the high-temperature properties of the matrix alloy, which satisfies the properties required in applications such as exhaust valves of the car engines or in the engines of the aircrafts.
3) Based on their wear rate, characteristic features of worn surface, subsurface and loose debris, and wear of the chrome steel counterface ball, three different wear regimes were identified for the composite samples:
    a. At low loads severe counterface abrasion by protruding TiC particles accompanied by formation of an iron oxide layer on the worn surface of TMC disk, followed by frequent spallation of the iron oxide were the main wear mechanisms. The TiC particle remained intact up to the contact pressure of 0.65 GPa, and virtually no surface deformation was imposed on Ti-6Al-4V matrix.
    b. At moderate loads the wear rate of TMC sample increased to a positive value, but it remained lower that the wear rate of unreinforced alloy. The wear of the TMCs occurred by oxidation of the plastically deformed Ti-6Al-4V substrate, followed by brittle detachment and fragmentation of the oxide layer. The TiC particles were damaged on the surface. The strong

particle/substrate interfacial bonding—also evidenced by the tensile and micro-scratch tests—diminished particle pull-out, which in turn restrained the deformation of the Ti substrate and annihilated any metallic delamination.

c. At high loads, incorporation of TiC particles deteriorated the wear resistance of the matrix alloy. The TiC particles did not withstand a contact pressure of 0.98 GPa, and fragments of fractured TiC particle severely abraded the Ti-6Al-4V substrate. Two mechanisms were cooperative at these loads, namely severe oxidative wear and metallic delamination of the severely deformed Ti-6Al-4V alloy. Metallic delamination occurred via damage accumulation at a critical depth, and cracking. Fracture of particles at the subsurface area promoted crack nucleation.

4) Comparison of the wear rates of Ti-6Al-4V and composite sample—considering the role of particles—led to the following conclusion: the incorporation of TiC particle by MIM process improved the wear resistance of the matrix alloy provided that the particles withstand the contact pressure (critical pressure = 0.98 GPa), and they are not fractured and/or pulled out of the matrix. Thermal oxidation was then adopted to annihilate the role of particles as stress raisers at high contact pressures.

5) Based on the morphological analysis of the oxide scale formed on TMC samples, as a result of oxidation at 600°C and 800°C for various times, the following two conditions were selected for further coating characterizations: at 600°C for 65 h (6-65h) and at 800 °C for 20 min (8-20min). Oxidation at 8-20min condition resulted in a thick, adherent and more uniform oxide. Similar to Ti-6Al-4V samples, an inner rutile layer was sandwiched between the oxygen diffusion zone and an outer alumina layer. The oxide formed on TiC particle at 600 °C was spalled due to the stresses built up in the scale, and preferential oxidation of TiC particles predominated via an inward diffusion of oxygen anions. At 800 °C, however, cationic diffusion promoted the oxide growth at gas/oxide interface, which provided the ability to heal cracks and resulted in an intact scale.

6) The TMC-8-20min type coating exhibited the maximum resistance to deformation during scratch test and the lowest value of coefficient of friction compared to TMC-6-65h and oxidized Ti-6Al-4V samples. Additionally, any cohesive and interfacial type failure were delayed and happened at higher pressures when oxidation at 800°C for 20 min was performed. The better support of the scale provided by the TiC particle (compared to the unreinforced alloy), and the formation of a thicker scale were believed to contribute to the better performance of TMC-8-20min type sample compared to TMC-6-65h and oxidized Ti-6Al-4V samples. Additionally, the fracture toughness of the coatings was estimated using indentation crack length method. For TMC-8-20min type coating, radial cracks were the predominant type which exhibited Palmqvist morphology, while for TMC-6-65h lateral cracking dominated at low loads. The fracture toughness of TMC-8-20min type sample was higher than the TMC-6-65h samples regardless of the type of equation used to estimate the fracture toughness. Subsequently, wear tests were performed on TMC-8-20min type samples.
7) Based on their wear rate, characteristic features of worn surface, subsurface and loose wear debris, and wear of the chrome steel counterface ball, two different wear regimes were identified for oxidized TMC samples (TO-TMC):
    a. At low loads, abrasion of the steel counterface by hard rutile asperities, followed by oxidation and transfer of iron resulted in weight gain of the TO-TMC samples. Moderate exfoliation of the iron oxide layer, and formation of oblate voids and cracks within ODZ were also the evidenced at low loads. The cracks were confined by the ductile retained β-phase and the oxide/substrate interface, and therefore did not propagate toward the surface.
    b. At high loads, occasional fragmentation and delamination of the rutile coating cooperated with the abrasion of the counterface—also observed at low loads—, and resulted in a slight increase in the wear rate of TO-TMC samples. Delamination of the rutile coating was started from subsurface cracks that were formed via a void coalescence mechanism. Several cracks were stopped at the oxide/coating interface or were arrested by the ductile

β-phase, until; eventually the elastic energy released by crack propagation became large enough for the crack to break through the arrest points.

8) The surface treatment developed in this study, therefore, enhanced the tribological performance of the TMC samples in two ways: i) the wear resistance of the TMC sample was significantly improved and ii) abrasion of the steel counterface by TiC particle was entirely terminated and replaced with a more moderate abrasion by asperities of the rutile coating. This improvement was believed to be attributed to the following factors:
    a. The oxide coating changed the nature of the contact from metallic/metallic to ceramic/metallic, and also decreased the ratio of hardness to elastic modulus by a factor of 2 which promotes elastic deformation and prevents any adhesion.
    b. The increase in the hardness and elastic modulus of the adjacent ODZ as a result of oxygen dissolution provided a better support for the oxide coating and TiC particles.

6.2 Suggestions for Future Work

- Since formation of an outer layer of alumina was observed during oxidation of Ti-6Al-4V and TMC samples, it would be interesting to study the effect of this scale on the tribological behaviour of the oxidized samples. For example this layer can be removed with a surface polishing procedure and a series of surface characterizations similar to this study can be performed to evaluate the effect of the presence of the alumina layer.
- The TiC particles were proved to act as stress raisers as a result of their relatively large size. Composite samples can be fabricated with a lower average particle size in order to study the effect of particle size on the wear performance of the composite samples.
- During the wear tests on TMC samples an interesting microstructure was developed beneath the contact surface where no equiaxed β phase was observed. Either a deformation induced martensitic transformation of β to α or a dynamic recrystallization process was believed to be responsible for the formation of this

microstructure. Therefore, it can be interesting to study the nature of this severely deformed layer by TEM analysis.

- An interesting phenomenon that has been observed by Shimada et al [97] is formation of an amorphous carbon layer as the TiC pallets were oxidized in water vapour. This process should be associated with a low oxygen pressure at the reaction interface that cannot oxidize the carbon component of TiC, but does oxidize Ti. Therefore, TMC samples can be oxidized in an atmosphere with high relative humidity, or a very low oxygen pressure. Formation of a layer of amorphous carbon can significantly improve the wear performance of TMCs.

Appendices

A. Instrumented Indentation

Instrumented indentation has been developed over the last decade, and allows the force to be recorded as a function of penetration depth during the indentation process. The mechanical properties of the coating may be extracted from the force-penetration depth curves obtained during loading and unloading (Figure 1). The elastic modulus can be estimated from the slope of the beginning of the unloading curve (S) which is assumed to be purely elastic:

$$S = \frac{2}{\pi} E^* \sqrt{A} \qquad \text{Equation 1}$$

Where A is the projected contact area and E^* is the reduced elastic modulus that is defined by:

$$\frac{1}{E^*} = \frac{1-\vartheta^2}{E} + \frac{1-\vartheta_i^2}{E_i} \qquad \text{Equation 2}$$

Where E_i, ϑ_i and E, ϑ are the Young's modulus and Poisson s ration of the diamond indenter and the specimen, respectively. The slop of the plot (S) can be computed by fitting the unloading curve to a power law as suggested by Oliver and Pharr:

$$F = a(a - h_f)^m \qquad \text{Equation 3}$$

Where h_f is the residual depth shown in Figure 1. For a conical indenter, the projected contact area is related to the contact height (h_c) which can be determined by the following formula:

$$h_c = h_m - \varepsilon \frac{F_{max}}{S} \qquad \text{Equation 4}$$

Where ε is a geometric factor, which depends on the geometry of the indenter and h_m is the maximum penetration depth shown in Figure 1. The Vickers hardness (Hv) of the material can be estimated by the following formula:

$$Hv = \frac{F_{max}}{9.81A(h_c)} \text{ in Vickers} \qquad \text{Equation 4}$$

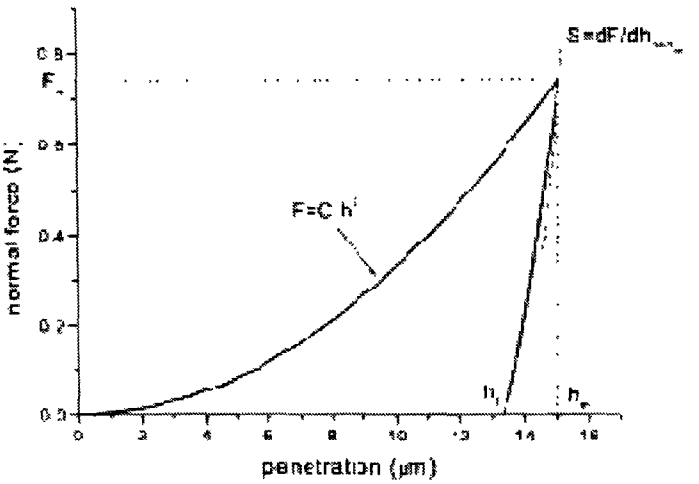

Figure 1. Loading and unloading response of an elasto-plastic material to sharp indentation. The normal force, F, during loading is proportional to the square of the penetration, h, through the loading curvature, C.

List of References

[1] G Lutjering, JC Williams, Titanium, Springer, Germany, 2003, p. 177.

[2] JD Donachie, Understanding the metallurgy of titanium, Titanium, a technical guide, 2nd ed., ASM International, USA, 2000, p. 13.

[3] H Güleryüz, H Çimenoğlu. Effect of thermal oxidation on corrosion and corrosion-wear behaviour of a Ti-6Al-4V alloy, Biomaterials. 25 (2004) 3325-3333.

[4] H Dong, T Bell. Enhanced wear resistance of titanium surfaces by a new thermal oxidation treatment, Wear. 238 (2000) 131-137

[5] H Dong, A Bloyce, PH Morton, T Bell. Surface engineering to improve tribological performance of Ti-6Al-4V, Surface Engineering. 13 (1997) 402-406.

[6] PA Dearnley, KL Dahm, H Çimenoğlu. The corrosion-wear behaviour of thermally oxidised CP-Ti and Ti-6Al-4V, Wear. 256 (2004) 469-479.

[7] SC Tjong, Y- Mai. Processing-structure-property aspects of particulate- and whisker-reinforced titanium matrix composites, Composites Science and Technology. 68 (2008) 583-601.

[8] R Zhang, J Kruszewski, J Lo. A study of the effect of sintering parameters on the microstructure and properties of PIM Ti6Al4V alloy, Powder Injection Moulding International. 2 (2009) 74-78.

[9] DB Miracle, ST Donaldson, ASM International handbook committee, ASM Handbook, Composites, ASM International, USA, 2006.

[10] C Poletti, A Merstallinger, T Schubert, W Marketz, HP Degischer. Wear and friction coefficient of particle reinforced Ti-alloys, Materialwissenschaft und Werkstofftechnik. 35 (2004) 741-749.

[11] F Wang, J Mei, H Jiang, X Wu. Laser fabrication of Ti6Al4V/TiC composites using simultaneous powder and wire feed, Materials Science and Engineering A. 445-446 (2007) 461-466.

[12] DE Alman. JA Hawk. The abrasive wear of sintered titanium matrix-ceramic particle reinforced composites, Wear. 225-229 (1999) 629-639.

[13] XN Zhang, C Li, XC Li, LJ He. Oxidation behavior of in situ synthesized TiC/Ti-6Al composite, Materials Letters. 57 (2003) 3234-3238.

[14] Y Qin, D Zhang, W Lu, W Pan. Oxidation behavior of in situ-synthesized (TiB+TiC)/Ti6242 composites, Oxidation of Metals. 66 (2006) 253-268.

[15] Y Qin, D Zhang, W Lu, W Pan. Oxidation behavior of in situ synthesized (TiB + TiC)/Ti-Al composites, Materials Letters. 60 (2006) 2339-2345.

[16] Y Qin, W Lu, D Zhang, J Qin, B Ji. Oxidation of in situ synthesized TiC particle-reinforced titanium matrix composites, Materials Science and Engineering A. 404 (2005) 42-48.

[17] Y Qin, W Lu, D Xu, D Zhang. High-temperature OM investigation of the early stage of (TiC+TiB)/Ti oxidation, Journal of Materials Science. 40 (2005) 687-692.

[18] JD Donachie, Introduction to selection of titanium alloys, Titanium, a technical guide, 2nd ed., ASM International, USA, 2000, p. 7.

[19] KHJ Buschow, RW Cahn, MC Flemings, B Ilschner, EJ Kramer, S Mahajan, Encyclopedia of materials: science and technology, Elsevier, Netherlands, 2001.

[20] M Peters, J Hemptenmacher, J Kumpfert, C Leyens, Structure and properties of titanium and titanium alloys, Wiley-VcCH GmbH&Co, Germany, 2003.

[21] M Long, HJ Rack. Titanium alloys in total joint replacement A materials science perspective, Biomaterials. 19 (1998) 1621-1639.

[22] FA Crossley. Effects of the ternary additions: O, Sn, Zr, Cb, Mo, and V on the $\alpha/\alpha+Ti_3Al$ Boundary of Ti-Al base alloys, Met Soc of AIME-Trans. 245 (1969) 1963-1968.

[23] JD Donachie, Titanium and titanium alloys, in: Chesnutt JC, Rhodes CG, Williams JC (Eds.), Relationship between mechanical properties, microstructure, and fracture topography in $\alpha+\beta$ titanium alloys, ASTM International, USA, 1976.

[24] JA Ruppen, CL Hoffmann, VM Radhakrishnan, AJ McEvily. The effect of environment and temperature on the fatigue behavior of titanium alloys, Fatigue, Environment and Temperature Effects. (1980) 265-300.

[25] S Naka, A Lasalmonie, P Costa, LP Kubin. The low-temperature plastic deformation of α-Ti and the core structure of a-type screw dislocations, Philosophical Magazine. A57 (1988) 717-740.

[26] S Zaefferer. A study of active deformation systems in titanium alloys: Dependence on, Materials Science and Engineering A. 344 (2003) 20-30.

[27] F Bridier, P Villechaise, J Mendez. Analysis of the different slip systems activated by tension in a α/β titanium alloy in relation with local crystallographic orientation, Acta Materialia. 53 (2005) 555-567.

[28] AT Churchman. The slip modes of titanium and the effect of purity on their occurrence during tensile deformation of single crystals, Proc. Roy. Soc. A. 226 (1954) 216-226.

[29] GE Dieter, Mechanical metallurgy, Mc Graw-Hill Book Co, USA, 1987.

[30] Z Liu, G Welsch. Literature survey on diffusivities of oxygen, aluminum, and vanadium in alpha titanium, beta titanium, and in rutile, Metallurgical Transactions A. 19 (1988) 1121-1125.

[31] O Kubaschewski, P Habil, BE Hopkins, Oxidation of Metals and Alloys, Butterworths Scientific, UK, 1953.

[32] JF Archard, W Hirst. "The wear of metals under unlubricated conditions", Proc. Royal Soc, Vol A. (2006).

[33] IM Hutching, Tribology, friction and wear of engineering materials, CRC Press Inc., USA, 1992.

[34] Zum Gahr, K. H., Microstructure and wear of materials, Elsevier, Netherlands, 1987

[35] Peterson, M.B. and Winer, W.O., Wear control handbook, ASME, USA, 1980.

[36] DA Rigney, Invited:Microstructural evolution during sliding, Proceeding from Materials Solutions '97 on Wear of Engineering Materials. (1997) 3-12.

[37] DA Rigney. Transfer, mixing and associated chemical and mechanical processes during the sliding of ductile materials, Wear. 245 (2000) 1-9.

[38] XY Li, KN Tandon. Microstructural characterization of mechanically mixed layer and wear debris in sliding wear of an Al alloy and an Al based composite, Wear. 245 (2000) 148-161.

[39] L Kenny, H Sang. Effect of particles on scoring and friction in ironing, Met. Trans. Gall. Met. Syst. (1986) 117-130.

[40] MM Shoukry, MA Fakhry, M Kassem, MM Farag. Sheet to metal transfer in two phase aluminium alloys, Proceedings of a Symposium Sponsored by the NFMC of Met. Soc. and Erosion and Wear G2 of ASTM. (1986) 131-153.

[41] CM Smith, RB Griffin, ST Noah. A statistical approach to modeling the compound wear of steels, Proceedings of a Symposium Sponsored by the NFMC of Met. Soc. and Erosion and Wear G2 of ASTM. (1986) 227-246.

[42] EP Whitenton, MB Peterson, LK Ives. Method for quantitative measurement of galling damage, Proceedings of a Symposium Sponsored by the NFMC of Met. Soc. and Erosion and Wear G2 of ASTM. (1986) 155-170.

[43] J Zhang, AT Alpas. Delamination wear in ductile materials containing second phase particles, Materials Science and Engineering A. 160 (1993) 25-35.

[44] DA Rigney, LH Chen, MGS Naylor, AR Rosenfield. Wear processes in sliding systems. Wear. 100 (1966) 195-219.

[45] SM Kuo, DA Rigney. Sliding behavior of aluminum, Materials Science and Engineering A. 157 (1992) 131-143.

[46] DA Rigney, Flow, mixing and evolution of tribomaterial, Proceeding of the 16th International Conference on Wear of Materials. (2007) 1-3.

[47] SK Biswas. Some mechanisms of tribofilm formation in metal/metal and ceramic/metal sliding interactions, Wear. 245 (2000) 178-189.

[48] Y Wang, T Lei, J Liu. Tribo-metallographic behavior of high carbon steels in dry sliding I. Wear mechanisms and their transition, Wear. 231 (1999) 1-11.

[49] NC Welsh. The dry wear of steels II. Interpretation and special features, Philosophical Transactions of the Royal Society of London.Series A, Mathematical and Physical Sciences. 257 (1965) 51-70.

[50] G Straffelini, A Molinari. Dry sliding wear of Ti-6Al-4V alloy as influenced by the counterface and sliding conditions, Wear. 236 (1999) 328-338.

[51] MB Peterson, LK Ives, KJ Bhansali. A literature review of the galling process, Proceedings of a Symposium Sponsored by the NFMC of Met. Soc. and Erosion and Wear G2 of ASTM. (1986) 1-25.

[52] NP Suh, Tribophysics, Prentice-Hall Inc, USA, 1986.

[53] SS Akarca, WJ Altenhof, AT Alpas. Subsurface deformation and damage accumulation in aluminum-silicon alloys subjected to sliding contact, Tribology International. 40 (2007) 735-747

[54] SC Lim, MF Ashby. Wear-mechanism maps, Acta Metallurgica. 35 (1987) 1-24.

[55] FH Stott. The role of oxidation in the wear of alloys, Tribology International. 31 (1998) 61-71.

[56] H Dong, XY Li. Oxygen boost diffusion for the deep-case hardening of titanium alloys, Materials Science and Engineering A. 280 (2000) 303-310.

[57] Y Liu, DZ Yang, SY He, WL Wu. Microstructure developed in the surface layer of Ti-6Al-4V alloy after sliding wear in vacuum, Materials Characterization. 50 (2003) 275-279.

[58] A Molinari, G Straffelini, B Tesi, T Bacci. Dry sliding wear mechanisms of the Ti6A14V alloy, Wear. 208 (1997) 105-112.

[59] M Long, HJ Rack. Friction and surface behaviour of selected titanium alloys during reciprocating-sliding motion, Wear. 249 (2001) 158-168.

[60] MO Alam, ASMA Haseeb. Response of Ti-6Al-4V and Ti-24Al-11Nb alloys to dry sliding wear against hardened steel, Tribology International. 35 (2002) 357-362.

[61] J Qu, PJ Blau, TR Watkins, OB Cavin, NS Kulkarni. Friction and wear of titanium alloys sliding against metal, polymer, and ceramic counterfaces, Wear. 258 (2005) 1348-1356.

[62] J Singh, AT Alpas. Elevated temperature wear of Al6061 and Al6061-20%Al2O3, Scripta Metallurgica et Materialia. 32 (1995) 1099-1105.

[63] S Wilson, AT Alpas. Thermal effects on mild wear transitions in dry sliding of an aluminum alloy, Wear. 225-229 (1999) 440-449.

[64] H Guleryuz, H Cimenoglu. Surface modification of a Ti-6Al-4V alloy by thermal oxidation, Surface and Coatings Technology. 192 (2005) 164-170.

[65] S Frangini, A Mignone, F de Riccardis. Various aspects of the air oxidation behaviour of a Ti6Al4V alloy at temperatures in the range 600-700 °C, Journal of Materials Science. 29 (1994) 714-720.

[66] O Kubaschewski, BE Hopkins, Oxidation of metals and alloys, ButterWorths Scientific, 1953, p. 166.

[67] Z Liu, G Welsch. Literature survey on diffusivities of oxygen, aluminum, and vanadium in alpha titanium, beta titanium, and in rutile, Metallurgical Transactions A. 19 (1988) 1121-1125.

[68] A Jostson, P Mcdougall, Phase relationships in titanium-oxygen alloys, The science, technology and application of titanium. (1968) 745-763.

[69] S Weissmann, A Shrier, Strain distribution in oxidized alpha titanium crystals, The science, technology and application of titanium. (1968) 441-451.

[70] MN Gardos. The effect of anion vacancies of the tribological properties of rutile (TiO2-x). STLE Tribology Trans. 32 (1989) 30-31.

[71] AE Jenkins. Oxidation of titanium at high temperatures in an atmosphere of pure oxygen, Journal of The Institue of Metals. 82 (1953-54) 213-221.

[72] EM Levin, CR Robbins, HF McMurdie, Phase diagrams for ceramists, ACS, USA, 1979.

[73] RJ Brook, Concise Encyclopedia of advanced ceramic materials, Pergomon Press, UK, 1990.

[74] S Murugesan, P Kuppusami, N Parvathavarthini, E Mohandas. Pulsed laser deposition of anatase and rutile TiO_2 thin films, Surface and Coatings Technology. 201 (2007) 7713-7719.

[75] TR Cass, Slip modes and dislocation substructures in titanium and titanium-aluminum single crystals, The Science, Technology and Application of Titanium. (1968) 459-477.

[76] G Welsch, W Bunk. Deformation modes of the α-phase of Ti-6Al-4V as a function of oxygen concentration and aging temperature, Metallurgical Transactions A. 13 (1982) 889-899.

[77] JC Williams, AW Sommer, PP Tung. The influence of oxygen concentration on the internal stress and dislocation arrangements in α titanium, Metallurgical Transactions. 3 (1972) 2979-2984.

[78] WR Tyson, Interstitial strengthening of titanium alloys, The science, technology and application of titanium. (1968) 479-487.

[79] AM Chaze, C Coddet. Influence of aluminium on the oxidation of titanium between 550 and 750 °C, Journal of The Less-Common Metals. 157 (1990) 55-70.

[80] AM Chaze, C Coddet. Influence of alloying elements on the dissolution of oxygen in the metallic phase during the oxidation of titanium alloys, Journal of Materials Science. 22 (1987) 1206-1214.

[81] DV Ignatov, EM Lazarev, ZI Kornilova, Structural and kinetic investigation of oxidation process of titanium and its alloys, and their protection against high temperature gas corrosion, Titanium science and technology. 2 (1972) 1089-1096.

[82] AE Jenkins. A further study of the oxidation of titanium and its alloys at high temperatures, Journal of The Institue of Metals. 84 (1955-56) 1-9.

[83] HL Du, PK Datta, DB Lewis, JS Burnell-Gray. Air oxidation behaviour of Ti-6Al-4V alloy between 650 and 850°C, Corrosion Science. 36 (1994) 631-642.

[84] K Rudinger, HH Weigand, On the scalling behaviour of commercial titanium alloys, Titanium science and technology. 4 (1972) 2554-2570.

[85] MN Mungole, N Singh, GN Mathur. Oxidation behaviour of Ti6Al4V titanium alloy in oxygen, Materials Science and Technology. 18 (2002) 111-114.

[86] H Garbacz, M Lewandowska. Microstructural changes during oxidation of titanium alloys, Materials Chemistry and Physics. 81 (2003) 542-547

[87] F Pitt, M Ramulu. Influence of grain size and microstructure on oxidation rates in titanium alloy Ti-6Al-4V under superplastic forming conditions, Journal of Materials Engineering and Performance. 13 (2004) 727-734.

[88] G Bertrand, K Jarraya, JM Chaix. Morphology of oxide scales formed on titanium, Oxidation of Metals. 21 (1984) 1-19.

[89] B Feng, JY Chen, SK Qi, L He, JZ Zhao, XD Zhang. Characterization of surface oxide films on titanium and bioactivity, Journal of Materials Science: Materials in Medicine. 13 (2002) 457-464.

[90] I Vaquila, LI Vergara, MCG Passeggi Jr., RA Vidal, J Ferrón. Chemical reactions at surfaces: Titanium oxidation, surface and coatings technology. 122 (1999) 67-71.

[91] GR Wallwork, AE Jenkins. Oxidation of titanium, zirconium, and hafnium, Journal of The Electrochemical Society. 106 (1959) 10-14.

[92] FL Matthews, RD Rawlings, Composite materials:Engineering and science, Chapman&Hall, UK, 1993.

[93] B Liu, Y Liu, XY He, HP Tang, LF Chen, BY Huang. Preparation and mechanical properties of particulate-reinforced powder metallurgy titanium matrix composites, Metallurgical and Materials Transactions A: Physical Metallurgy and Materials Science. 38 A (2007) 2825-2831.

[94] PJ Blau, BC Jolly, J Qu, WH Peter, CA Blue. Tribological investigation of titanium-based materials for brakes, Wear. 263 (2007) 1202-1211.

[95] R Riedel, Handbook of ceramic hard material, Wiley-VCH, Germany, 2000,.

[96] VA Lavrenko, LA Glebov, AP Pomitkin, VG Chuprina, TG Protsenko. High-temperature oxidation of titanium carbide in oxygen, Oxidation of Metals. 9 (1975) 171-179.

[97] S Shimada, K Mochidsuki. The oxidation of TiC in dry oxygen, wet oxygen, and water vapor, Journal of Materials Science. 39 (2004) 581-586.

[98] EA Brands, Smithells metals reference book, ButherWorths, UK, 1968,.

[99] D Nolan, V Leskovsek, M Jenko. Estimation of fracture toughness of nitride compound layers on tool steel by application of the Vickers indentation method, Surface and Coatings Technology. 201 (2006) 182-188.

[100] CB Ponton, RD Rawlings. Vickers indentation fracture toughness test. Part 1. Review of literature and formulation of standardised indentation toughness equations, Materials Science and Technology. 5 (1989) 865-872.

[101] M Dietz, H- Tietz. Characterization of engineering ceramics by indentation methods, Journal of Materials Science. 25 (1990) 3731-3738.

[102] K Niihara. A fracture mechanics analysis of indentation-induced Palmqvist crack in ceramics, Journal of Materials Science Letters. 2 (1983) 221-223.

[103] K Niihara, R Morena, DPH Hasselman. Evaluation of K_{Ic} of brittle solids by the indentation method with low crack-to-indent ratios, Journal of Materials Science Letters. 1 (1982) 13-16.

[104] DK Shetty, IG Wright, PN Mincer, AH Clauer. Indentation fracture of WC-Co cermets, Journal of Materials Science. 20 (1985) 1873-1882.

[105] AG Evans, TR Wilshaw. Quasi-static solid particle damage in brittle solids-I. Observations analysis and implications, Acta Metallurgica. 24 (1976) 939-956.

[106] AG Evans, EA Charles. Fracture toughness determination by indentation, Journal of American Ceramic Society. 59 (1976) 371372.

[107] CB Ponton, RD Rawlings. Vickers indentation fracture toughness test part 2 application and critical evaluation of standardised indentation toughness equations, Materials Science and Technology. 5 (1989) 961-976.

[108] AG Evans. Fracture toughness: The role of indentation techniques. ASTM Special Technical Publication. (1979) 112-135.

[109] BR Lawn, AG Evans, DB Marshall. Elastic/plastic indentation damage in ceramics: The median/radial cracks system. Journal of the American Ceramic Society. 63 (1980) 574-581.

[110] GR Anstis, P Chantikul, BR Lawn, DB Marshall. Indentation techniques for measuring toughness of ceramics. Proceedings - Australian Ceramic Conference. (1980) 32-34.

[111] MT Laugier. New formula for indentation toughness in ceramics, Journal of Materials Science Letters. 6 (1987) 355-356.

[112] Z Li, A Ghosh, AS Kobayashi, RC Bradt. Indentation fracture toughness of sintered silicon carbide in the Palmqvist crack regime, Journal of the American Ceramic Society. 72 (1989) 904-911.

[113] V Milekhine, MI Onsøien, JK Solberg, T Skaland. Mechanical properties of FeSi (ε), FeSi2 (ζα) and Mg2Si, Intermetallics. 10 (2002) 743-750.

[114] J Gong. Determining indentation toughness by incorporating true hardness into fracture mechanics equations, Journal of the European Ceramic Society. 19 (1999) 1585-1592.

[115] DB Marshall, BR Lawn. Residual stress effects in sharp contact cracking - Part 1 Indentation fracture mechanics, Journal of Materials Science. 14 (1979) 2001-2012.

[116] J Malzbender, JMJ Den Toonder, AR Balkenende, G De With. Measuring mechanical properties of coatings: A methodology applied to nano-particle-filled sol-gel coatings on glass, Materials Science and Engineering: R: Reports. 36 (2002).

[117] W Feng, D Yan, J He, G Zhang, G Chen, W Gu, et al. Microhardness and toughness of the TiN coating prepared by reactive plasma spraying, Applied Surface Science. 243 (2005) 204-213.

[118] ZX Zhang, H Dong, T Bell, B Xu. The effect of treatment condition on boost diffusion of thermally oxidised titanium alloy, Journal of Alloys and Compounds. 431 (2007) 93-99.

[119] WC Oliver, GM Pharr. Measurement of hardness and elastic modulus by instrumented indentation: Advances in understanding and refinements to methodology, Journal of Materials Research. 19 (2004) 3-20.

[120] K Holmberg, A Laukkanen, H Ronkainen, K Wallin, S Varjus. A model for stresses, crack generation and fracture toughness calculation in scratched TiN-coated steel surfaces, Wear. 254 (2003) 278-291.

[121] B Bhushan, Principles and applications of tribology, John Wiley, USA, 1999.

[122] LM Keer, CH Kuo. Cracking in a loaded, brittle elastic half-space, International Journal of Solids and Structures,. 29 (1992) 1819-1826.

[123] AF Bower, NA Fleck. Brittle fracture under a sliding line contact, Journal of the Mechanics and Physics of Solids,. 42 (1994) 1375-1396.

[124] PJ Blau. On the nature of running-in, Tribology International. 38 (2005) 1007-1012.

[125] J Zhang, AT Alpas. Transition between mild and severe wear in aluminium alloys, Acta Materialia. 45 (1997) 513-528.

[126] BR Lawn, SM Wiederhorn, DE Roberts. Effect of sliding friction forces on the strength of brittle materials, Journal of Materials Science. 19 (1984) 2561-2569.

VITA AUCTORIS

Name	Neda Dalili
Place of Birth	Tehran, Iran
Year of Birth	1981
Education	Bachelor of Science, Materials Science and Engineering, Sharif University of Technology, Tehran, Iran, 1999-2005
	Master of Applied Science, Engineering Materials, University of Windsor, Windsor, Ontario, Canada, 2007-2009